Aus dem Institut für Robotik und Kognitive Systeme
der Universität zu Lübeck

Direktor:
Prof. Dr.-Ing. Achim Schweikard

Centre-Surround Suppression: Computational Modelling and Neural and Perceptual Correlates in Humans

Inauguraldissertation
zur
Erlangung der Doktorwürde
der Universität zu Lübeck
— Aus der Sektion Informatik/Technik —

Vorgelegt von Christoph Metzner
geboren in Rodalben, Rheinland-Pfalz (Deutschland)

Lübeck 2014

1. Berichterstatter: Prof. Dr.-Ing. Achim Schweikard

2. Berichterstatter: Prof. Dr. rer. nat. Ulrich Hofmann

Tag der mündlichen Prüfung: 14.04.2014

Zum Druck genehmigt. Lübeck, den 22.04.2014

1. Zusammenfassung

Ein wichtiges Problem der sensorischen Informationsverarbeitung im allgemeinen und der visuellen Informationsverarbeitung im speziellen, ist die Frage, wie sich das Gehirn an drastisch sich verändernde äußere Bedingungen anpasst. Folgerichtig spielt die Untersuchung der, der Kontextintegration zugrunde liegenden Mechanismen eine wichtige Rolle bei der Erforschung der sensorischen Systeme der Säugetiere. In dieser Arbeit wurde das Problem der Kontextintegration im visuellen System auf zwei komplementären Ebenen behandelt: der neuronalen und der perzeptuellen.

Auf der neuronalen Ebene wurde ein detailliertes, biologisch inspiriertes neuronales Netzwerkmodell der Eingangsschicht des primären visuellen Kortex entwickelt und implementiert. Dieses Modell wurde anhand von anatomischen und elektro-physiologischen Daten erstellt und umfangreich mittels Daten experimenteller Tierstudien validiert. Es zeigte 'centre-surround suppression', eine bestimmte Form der Kontextintegration im visuellen System, in guter Übereinstimmung elektro-physiologischen und psychophysischen Experimenten. Das Modell wurde dazu benutzt, die der 'centre-surround suppression' zugrunde liegenden Mechanismen zu untersuchen und es konnte gezeigt werden, dass die lokale, laterale Inhibition maßgeblich zur 'centre-surround suppression' beiträgt. Das Modell unterstützt die Theorie, dass 'centre-surround suppression' möglicherweise ausreichend durch lokale, laterale Inhibition erklärt werden kann. Obwohl es nicht im Fokus dieser Arbeit lag, ermöglichte das Modell außerdem eine Erforschung der Mechanismen, die den klassischen Eigenschaften der rezeptiven Felder zugrunde liegen. Auch hier konnte ein maßgeblicher Einfluss lokaler, lateraler Inhibition nachgewiesen werden.

Auf der perzeptuellen Ebene wurde die 'centre-surround suppression' und ihre neurochemischen und neuronalen Korrelate in einer Studie untersucht, die psychophysische Messungen, Magnetresonanzspektroskopie und funktionelle Magnetresonanztomographie umfasste. Zusätzlich zu den gesunden Probanden wurden in dieser Studie auch Patienten mit Schizophrenie untersucht, da bei diesen Defizite in der Kontextintegration und speziell in der 'centre-surround suppression' bekannt sind. Die Studie konnte eine signifikant reduzierte 'centre-surround suppression', wie sie in vorangegangen Studien für Untergruppen von Patienten nachgewiesen wurden, in der heterogenen Patien-

tengruppe nicht bestätigen, obwohl sowohl signifikant reduzierte GABA (ein wichitger inhibitorischer Neurotransmitter) Konzentrationen als auch BOLD Aktivierungen gefunden wurden. Darüber hinaus wurden, entgegen vorangegangener Befunde, keinerlei Korrelationen zwischen 'centre-surround suppression', Neurotransmitter-Konzentrationen und BOLD Aktivierungen gefunden, was darauf schließen lässt, dass die perzeptuelle 'centre-surround suppression' auf komplexere Weise von den lokalen, neuronalen Schaltkreisen abhängt, als bisher angenommen.

Die Modellierungsresultate und die experimentellen Ergebnisse dieser Arbeit tragen zu einem besseren Verständnis der 'centre-surround suppression' bei. Darüber hinaus bietet diese Arbeit eine exzellente Basis für die modellbasierte Erforschung aller Aspekte der klassischen und nicht-klassischen Eigenschaften rezeptiver Felder.

2. Abstract

One major issue in sensory information processing and, particularly, in visual information processing is the question of how the brain adapts to drastically differing external conditions. Consequently, the exploration of the mechanisms of context or surround integration plays a key role in the quest for an eventual understanding of mammalian sensory systems. In this work, the problem of context integration in the visual system was approached on two complementary scales: the neural, microcircuit scale and the perceptual scale.

On the neural, microcircuit scale, a detailed, biologically inspired, neural network model of the input layer of the primary visual cortex was designed and implemented. The model was based on anatomical and electrophysiological data, and was extensively validated against experimental animal studies. It showed centre-surround suppression, a particular form of context integration in the visual system, well in accordance with electrophysiological and psychophysical experiments. The model was used to explore the mechanisms underlying centre-surround suppression and could identify short-range, lateral inhibition as a factor crucially contributing to centre-surround suppression. Therefore, the model supported the theory that centre-surround suppression might be sufficiently explained in terms of local, lateral inhibition. Although not of primary interest, the model also enabled an exploration of the mechanisms underlying classical receptive field properties, that is, basic response properties of neurons in the primary visual cortex. Again, local, lateral inhibition was identified as a major factor contributing to these phenomena.

On the perceptual scale, centre-surround suppression and its neurochemical and neural correlates were investigated in a study combining psychophysical measurements, magnetic resonance spectroscopy and functional magnetic resonance imaging. Participants in the study not only included healthy subjects, but also patients suffering from schizophrenia, because of their known deficits in context integration and, particularly, centre-surround suppression. The study found that reduced centre-surround suppression in schizophrenic patients, previously demonstrated for certain subgroups of patients, did not generalise to a heterogeneous patient group, although significantly re-

duced GABA (an important inhibitory neurotransmitter) levels and BOLD activations were found for the patient group. Furthermore, for both groups, previously established correlations between centre-surround suppression, neurotransmitter levels and BOLD activations could not be replicated, suggesting a more complex dependence of perceptual centre-surround suppression on the underlying neural circuits than previously thought.

The model and experimental results presented in this work contribute to a better understanding of centre-surround suppression. Furthermore, this work provides an excellent basis for a model-based investigation of all aspects of classical and extra-classical receptive field phenomena.

Contents

1. Zusammenfassung **5**

2. Abstract **7**

3. Introduction and Motivation **1**

3.1. Purpose of this Work 1

3.2. Scientific Motivation 3

3.3. Structure of this Work 7

4. Computational Foundations **9**

4.1. Electrical Properties of Neurons 9

4.2. Computational Units 13

4.2.1. Firing-Rate Models 13

4.2.2. Integrate-and-Fire Neurons 14

4.2.3. Hodgkin-Huxley Type Neurons 17

4.2.4. Multi-Compartment Neuron Models 18

4.2.5. Comparison and Evaluation 19

4.3. Modelling Networks 21

4.3.1. Connections in Rate-Based Models 21

4.3.2. Connections in Spiking Models 22

4.4. Implementation and Efficiency 23

4.4.1. Numerical Solutions to Coupled Differential Equations 23

4.4.2. Neural Simulators 26

5. Theories of Computation in the Primary Visual Cortex **27**

5.1. Classical Receptive Field Properties 27

5.2. Neural Centre-Surround Suppression 32

6. A Computational Model of the Primary Visual Cortex **37**

6.1. Introduction 37

6.2. Methods . . . 38
6.2.1. A Detailed Multi-Compartment Neural Network Model of the Primary Visual Cortex . . . 38
6.2.2. Single Neurons - Validation I . . . 47
6.2.3. Classical Receptive Field Properties of Network Model Neurons - Validation II . . . 48
6.2.4. Neural Centre-Surround Suppression . . . 53
6.2.5. Mechanisms of Emergent Classical Receptive Field Properties . . . 57
6.2.6. The Role of Recurrent Inhibition in Classical Receptive Field Properties and Centre-Surround Suppression . . . 58
6.3. Results . . . 59
6.3.1. Single Neurons - Validation I . . . 59
6.3.2. Classical Receptive Field Properties of Network Model Neurons - Validation II . . . 62
6.3.3. Neural Centre-Surround Suppression . . . 75
6.3.4. Mechanisms of Emergent Classical Receptive Field Properties . . . 78
6.3.5. The Role of Recurrent Inhibition in Classical Receptive Field Properties and Centre-Surround Suppression . . . 87

7. Experimental Studies **99**
7.1. Introduction . . . 99
7.2. Methods . . . 103
7.2.1. Subjects . . . 103
7.2.2. MR Spectroscopic Measures of Neurotransmission . . . 105
7.2.3. Functional MR Imaging of Contrast Processing . . . 108
7.2.4. Psychophysical Measurement of Centre-Surround Suppression . . . 110
7.3. Results . . . 112
7.3.1. MR Spectroscopic Measures of Neurotransmission . . . 112
7.3.2. Functional MR Imaging of Contrast Processing . . . 121
7.3.3. Psychophysical Measurement of Centre-Surround Suppression . . . 124
7.3.4. Interactions between Modalities . . . 128

8. Discussion **137**
8.1. Computational Models . . . 137
8.1.1. Feature Selectivity . . . 137
8.1.2. Contrast Response Properties . . . 142
8.1.3. Centre-Surround Suppression . . . 142

8.1.4. Modelling Considerations . . . 147
8.2. Experimental Studies . . . 150
8.2.1. Psychophysical Measures . . . 150
8.2.2. MR Spectroscopy . . . 152
8.2.3. Functional MR Imaging . . . 153
8.2.4. Relations Between Neurotransmission, Contrast-Evoked BOLD Signal and Context Perception . . . 154
8.3. Modelling vs. Experiments . . . 157

9. Conclusion and Outlook **159**
9.1. Contributions . . . 159
9.2. Outlook . . . 160
9.2.1. A Community Model of the Primary Visual Cortex . . . 160
9.2.2. Theory of Receptive Field Properties . . . 161
9.2.3. Theory of Centre-Surround Suppression . . . 162

A. The Visual System **163**
A.1. Functional Neuroanatomy . . . 163
A.1.1. The Eye - Phototransduction and Retinal Processing . . . 164
A.1.2. The Thalamus . . . 168
A.1.3. The Primary Visual Cortex . . . 169
A.1.4. Higher Visual Areas . . . 170

B. Results - The Role of Recurrent Inhibition in Feature Selectivity and Centre-Surround Suppression **171**
B.1. Weight of Inhibitory Connections on Excitatory Cells . . . 171
B.2. Weight of Excitatory Connections on Inhibitory Cells . . . 175
B.3. Number of Inhibitory Cells . . . 180
B.4. Number of Inhibitory Connections to Excitatory Cells . . . 182
B.5. Number of Excitatory Connections on Inhibitory Cells . . . 185
B.6. Decay Times at GABAergic Synapses . . . 187

Bibliography **193**

List of Figures **205**

List of Tables **209**

3. Introduction and Motivation

This chapter explains the development of a detailed, biologically inspired neural network model of the primary visual cortex, as well as neuroimaging and psychophysical experiments to examine the neural basis of centre-surround suppression in the visual system. It begins delineating the purpose of this work, describing the necessity for and the potential of such a network model to aid understanding the neural mechanisms of classical and, especially, of centre-surround suppression. The possibilities offered by neuroimaging and psychophysical methods for this topic are also covered . Such an understanding might not only advance the knowledge of the human visual system, but could also help to identify pathophysiological mechanisms in severe neurological and psychiatric disorders such as schizophrenia.

3.1. Purpose of this Work

The mammalian visual system has been studied extensively over the past decades, and an enormous amount of experimental and theoretical work has been accomplished [149]. However, a full understanding of visual processing is not on the horizon.

In his seminal work [138], David Marr describes vision as an information processing task:

> "The study of vision must therefore include not only the study of how to extract from images the various aspects of the world that are useful to us, but also an inquiry into the nature of the internal representations by which we capture this information... ."

This task consists of two aspects: the extraction of useful information and the internal representation of this information. At the heart of his analysis was the distinction between three levels of understanding [138]:

- The computational level: what does the system do and why?
- The algorithmic/representational level: how does the system do what it does?

- The physical level: how is the system physically realized?

Although, a good understanding of the computational level has been reached, both the algorithmic and the physical level and especially their correspondence remains elusive [149].

One approach to understand the algorithmic level is to analyse the simple features and properties of the building blocks of the system, that is, for the visual system, the single neurons, and from there, move to more and more complex features. Starting with the discoveries of Hubel and Wiesel [98], a great variety of features and properties of single neurons in the visual cortex have been discovered [e.g. 54, 59, 98, 99, 195]. The emergence of these so-called **classical receptive field properties**, that is, the specificity of a neuron to stimuli within a distinct spatial region of the visual field, is one important first step in the cortical processing of information. It is thought that these properties build the foundation for all higher-level processing in the visual system, such as object recognition, face recognition, motion detection and colour perception [46]. However, there is still no coherent theory including all features and the neural mechanisms implementing this processing are still under debate [166, 187]. That is, neither the algorithmic nor the physical level are understood sufficiently well.

Even less understood are the mechanisms underlying the so-called **extra-classical receptive field properties** of neurons in primary visual cortex [3, 97, 99, 222]. These properties result from a stimulation outside of the classical receptive field, which leads to a modulation of the neurons response to stimulation of the classical receptive field. An important example is the so-called **(neural) centre-surround suppression**, i.e. the suppression of neural activity in response to a stimulus, by a simultaneously applied stimulus in the surround of the neuron's classical receptive field [43].

Since experimental methods to investigate extra-classical receptive field properties are still challenging and centre-surround suppression can only be inferred indirectly [222], rigorous computational support for theories of extra-classical field properties is crucial in electrophysiological and psychological studies. However, to the author's knowledge, no biologically inspired, detailed model for centre-surround suppression exists so far and only a few simplified, more abstract models exist [198, 222]. There is a clear demand for such models, especially keeping in mind that the timing of inhibition and also spatial location of the inhibitory input might play an important role, as will be explained later (see Chapter 5). The proposed network model provides a starting point for more realistic and biophysically constraint modelling of centre-surround suppression, that is, a deeper investigation of the physical level.

Therefore, the objectives of this work were threefold. The first objective was to de-

velop a detailed, neural network model of the V1 input layer, grounded on anatomical and physiological data, which could be used to investigate the intracortical mechanisms of classical and extra-classical receptive field properties of V1 neurons. The proposed network model was developed to reproduce not just one but a multitude of classical properties, making it closer to data from electrophysiological recordings. Furthermore, a highly flexible, extensible and simulator-independent design was also a high priority, so that the model could be changed, exchanged and extended very easily.

The second objective was to use the model to show that neural centre-surround suppression phenomena can be produced by short-range intracortical mechanisms without long-range interactions and extrastriate feedback, as recent studies suggest [161, 222]. Moreover, the role of intracortical inhibition in the emergence of neural centre-surround suppression sought to be investigated and the influence of different factors governing inhibition on neural centre-surround suppression was to be tested.

The third and last objective was to explore neural substrates of perceptual centre-surround suppression combining psychophysical and neuroimaging methods.

3.2. Scientific Motivation

Visual Processing Sensory perception, in general, and visual perception, in particular, massively depends on **gain control**, i.e. the ability to adapt to drastically differing surround conditions [119]. In the visual system, this surround adaptation leads to a high responsiveness to changes in the stimulus and thus to an increased detection of salient features. The integration of surround information in the visual system takes place at different stations along the visual pathway and has diverse effects on different modalities such as luminance, contrast, orientation and motion. However, on the algorithmic level, in all cases gain control can be explained theoretically by some form of suppression (subtractive or divisive) [19, 86, 176]. Nonetheless, the biophysical mechanisms, that is, the physical level, underlying this suppression remain poorly understood. Several candidate mechanisms, local and multi-stage, have been proposed, such as **lateral inhibition**, **feed-forward mechanisms** or **feed-back mechanisms**, which have been shown to contribute to gain control in specific cases at some stage of the visual processing [65, 98, 166, 187]. A comprehensive theory explaining gain control at all stages along the pathway of visual information processing is still to be developed and several questions remain unanswered: *Do different mechanisms work at different scales (from the scale of single neurons/small circuits up to the perceptual/behavioural scale) of the processing? Are different mechanisms responsible for gain control at different modalities? Do they work at different stages along the pathway? How*

are they implemented computationally and neurochemically?

Furthermore, several neurological and psychiatric disorders are associated with deficits in visual gain control, for example, schizophrenia, major depressive disorder, photosensitive epilepsy, and migraine [51, 78, 142, 164]. Since the mechanisms of gain control in the healthy brain are not fully understood, it also remains elusive how these mechanisms change with disorder: whether they express a fundamental change in information processing, whether they appear as epiphenomena or whether they point to compensatory mechanisms.

Finally, surround suppression as a form of gain control is an ubiquitous principle in information processing in the brain [119]. Thus, a theory of the neural mechanisms implementing surround suppression in the visual system might easily be generalized to a theory of surround suppression for the whole brain. Similarly, a comprehension of the visual deficits in disorders like schizophrenia might contribute to an understanding of the more general disorder's mechanisms.

Suppression Mechanisms in the Visual System V1 neurons are sensitive to a specific spatial region within the visual field, the **classical receptive field (CRF)**, meaning that a stimulus presented in this region elicits a neural response [e.g. 98]. Many properties or feature selectivities have been shown to exist for V1 neurons, such as orientation, direction, spatial frequency and temporal frequency selectivity [54, 98, 99, 174]. These feature selectivities are restricted to the CRF in the sense that the elicited response is maximal if the stimulus exactly covers the CRF, and are thus referred to as **classical receptive field properties**. However, although a stimulus beyond the CRF does not elicit a spike response, V1 neurons are not 'blind' to stimuli beyond their CRF. How is this possible? V1 neurons integrate information from a large region outside the CRF in a modulatory way, that is, if a stimulus is presented in the CRF simultaneously with a second stimulus beyond it, this surround stimulus modulates the response of the neuron [e.g. 182]. In most cases this modulation is suppressive and is known as **neural centre-surround suppression** or simply **centre-surround suppression**. Since this phenomenon is based on stimulation outside the CRF it is termed an **extra-classical receptive field property**. The phenomenon of centre-surround suppression is also known on the perceptual/behavioural level, where the perception of a centred stimulus is changed by a surrounding stimulus [e.g. 43], and it is known for different modalities such as luminance, contrast, orientation or size of the stimulus [43, 150, 161]. In order to avoid confusion with neural centre-surround suppression, it will be referred to as **perceptual centre-surround suppression**. Obviously, neural and perceptual centre-surround suppression are related to

each other, since perception is based on neural activity. Thus, perceptual centre-surround suppression is an emergent property of neural centre-surround suppression, such as any change of the neural network properties potentially results in a change on the perceptual level. However, it is still not clear what mechanisms are responsible for both phenomena, and how centre-surround suppression on the neural level translates to centre-surround suppression on the perceptual level. Nevertheless, it seems to be a close relation, since the same type of response functions are employed to fit experimental data from single cell recordings of neural centre-surround suppression as to fit experimental data from human psychophysical studies investigating perceptual centre-surround suppression [226].

As mentioned above, several candidate mechanisms have been proposed to contribute to neural centre-surround suppression. In 1994, DeAngelis et al. [56], proposed that neural centre-surround suppression is the result of long-range horizontal connections and argued that the spatial extent of short-range intra-cortical connections would be insufficient to produce the surround sizes observed experimentally. This theory was further supported by other studies [61, 102, 202]. However, Sceniak et al. [182] argued that even the range of horizontal connections (< 5 mm) did not suffice for the surround sizes they found experimentally. They concluded that extrastriate feedback was necessary to account for their results. This theory was supported by subsequent experimental studies measuring surround sizes [37], but also from tracer injection [6] and timing experiments [10], which concluded that intra-cortical suppression was not fast enough to explain the onset times of suppression. Still, neither the theory of DeAngelis et al. nor the theory of Sceniak et al. can account for one important experimental finding: Neural centre-surround suppression is found throughout all layers of the visual cortex, even those layers that do not have long-range horizontal connections or that do not receive extra-striate feedback [181, 182]. In addition, investigating neural centre-surround suppression experimentally still poses an enormous challenge for the experimenter, and inferences about surround sizes and timing can only be made indirectly [222]. Interestingly, neural centre-surround suppression has been found to exist in thalamic nuclei, specifically in the **lateral geniculate nucleus (LGN)**, which projects to V1. What is more, there is evidence that V1 might partially inherit this property from LGN by simple feed-forward mechanisms [161, 196]. In the same vein, a recent computational model has provided support for the hypothesis that neural centre-surround suppression might be produced by both partial inheritance from the LGN and short-range, recurrent connections [222].

To sum up, the exact mechanisms behind neural centre-surround suppression are still incompletely understood. It is not clear whether extra-striate effects and horizontal mechanisms are necessary for surround suppression to be observed or if they can be

explained by local, lateral mechanisms alone. The current experimental techniques can only indirectly measure the mechanisms behind neural and perceptual centre-surround suppression. Therefore, building computational models is an essential step in the process of understanding neural centre-surround suppression, its links to perceptual centre-surround suppression and its impairments in neurological and psychiatric disorders on the algorithmic level. Building biophysically detailed models additionally allows for an investigation of the implementation of these mechanisms, that is, the physical level.

3.3. Structure of this Work

The subsequent chapters of this work are organized as follows:

Chapter II (Computational Foundations) introduces the mathematical techniques needed to build computational models of the visual system and reviews currently available software packages for the simulation of such models.

Chapter III (Theories of Computation in the Primary Visual Cortex) introduces the current theories of classical receptive field properties in detail. It describes the interdependence of classical receptive field properties with extra-classical field properties with a focus on neural centre-surround suppression.

Chapter IV (A Computational Model of the Primary Visual Cortex) describes the computational model developed in this work and presents the results of its validation. The model is then used to investigate the neural mechanisms underlying orientation selectivity. Further, the results of the exploration of the model's neural centre-surround suppression properties are presented and the influence of short-range, lateral inhibition on these centre-surround suppression as well as on classical receptive field properties is studied.

Chapter V (Experimental Studies) describes the experimental studies performed to investigate perceptual centre-surround suppression and its neural basis. Results from psychophysical experiments, proton magnetic resonance spectroscopy and functional magnetic resonance imaging are presented.

Chapter VI (Discussion) analyses the results presented in Chapters IV and V and their implications for the current understanding of computational mechanisms underlying both levels: neural and perceptual centre-surround suppression.

Chapter VII (Conclusion and Outlook) summarises the presented work and its contributions to the fields of visual and computational neuroscience. It delineates interesting and promising possibilities for future research: Extensions and applications of the model in new research scenarios as well as further options for the psychophysical and neuroimaging methods used.

4. Computational Foundations

This chapter provides an overview of the existing techniques to model networks of neurons. Basically, two factors determine the computations in a neural network like the brain. The first one is the basic units of computations, that is, the neurons. The second one is the way these basic computational units are connected and how they transfer information, in this case, the way neurons communicate via axons, dendrites and synapses. Naturally, these two essential building blocks of the nervous system have to be mathematically modelled. However, a third question arises, when trying to build network models of the brain, namely, how to solve the mathematical descriptions analytically or numerically.

4.1. Electrical Properties of Neurons

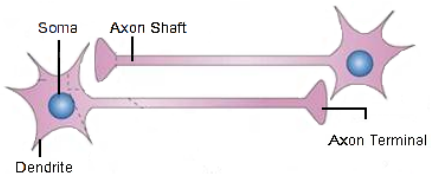

Figure 4.1.: Depiction of the different units of a neuron (modified after [29]).

Neurons are the essential building blocks of the brain and can be seen as its computational units [46, 52]. A neuron is composed of a cell body or **soma**, a **dendritic tree** and an **axon** (see figure 4.1). The neuron's **cell membrane** is a bi-lipid layer which is almost impermeable for charged particles. This insulation property makes the membrane act like a capacitor. By convention, the electrical potential of the fluid surrounding the cell membrane is 0 mV and thus the intracellular membrane potential at rest, the **resting potential**, is negative, between -95 mV and -55 mV [46]. Specific **ion channels** are found throughout the membrane, which control the in- and out-flux of ions. Most of them are voltage-dependent although other dependencies exist (e.g. Ca^{2+}-dependent potassium channels). Furthermore, the membrane has a lot of **ion pumps** that transport ions

through it in order to sustain concentration gradients between the intra- and extracellular space [23, 46, 52]. The most important ion types are **sodium (Na^+)**, **potassium (K^-)**, **calcium (Ca^{2+})** and **chloride (Cl^-)** [46]. The membrane potential can have different values in different parts of the neuron, which causes ion flux in order to equalize these differences. The intracellular space of the neuron exhibits a longitudinal resistance to such ion movements, often called the **intracellular resistance (R_L)**. As mentioned before, the neuronal membrane acts like a capacitor having a specific capacitance C_m, which is coupled to the voltage across the membrane V and the charge Q of the inside of the membrane surface by

$$Q = C_m V. \tag{4.1}$$

The time derivative of this basic equation gives

$$C_m \frac{dV}{dt} = \frac{dQ}{dt}, \tag{4.2}$$

which plays an important role in the modelling of neurons [52]. While the membrane capacitance determines the amount of current to change the membrane potential at a given rate, the **membrane resistance** R_m defines the current needed to hold the membrane potential at a value different from the resting value. The product of this resistance and the membrane capacitance is called the **membrane time constant**, $\tau_m = R_m C_m$. This constant defines the basic time frame for changes in the membrane potential and typically lies between 10 ms and 100 ms [52].

The two forces determining the flux of ions through the ion channels are electric charges and diffusion. The current flow that is due to diffusion is conveniently characterized by the so-called **equilibrium potential**, that is, the membrane potential at which the current flow produced by electric charges cancels the flow produced by concentration gradients. The equilibrium potential E can be calculated using the **Nernst equation**, given by

$$E = \frac{V_T}{z} \ln\left(\frac{[outside]}{[inside]}\right), \tag{4.3}$$

where $[outside]$ and $[inside]$ are the ion concentrations outside and inside the cell, respectively, z is the charge of the ion divided by the charge of a proton and V_T is the potential difference across the membrane ($V_T = \frac{k_B T}{q}$, q charge of a proton, T temperature and k_B the Boltzmann constant). Typical equilibrium potentials for ion channels are listed in Table 4.1.

An ion channel with an equilibrium potential E produces a current flow that will move the membrane potential towards E, that is, an outward flow of positive current if $V > E$ and inward flow of positive current if $V < E$. As can be seen in Table 4.1

Table 4.1.: Equilibrium potentials for the four electrophysiologically most important ions: sodium, potassium, chloride and calcium at their physiological concentrations.

Ion	Sodium	Potassium	Chloride	Calcium
Equilibrium Potential (mV)	50	-70 to -90	-60 to -65	150

sodium and calcium have positive equilibrium potentials; hence, sodium and calcium channels tend to depolarize a neuron. Potassium channels have negative equilibrium potentials, which are below the resting membrane potential of most neurons and thus tend to hyperpolarise neurons. Since the equilibrium potential of chloride channels is very close to the resting membrane potential of most neurons, the net effect of these channels is small.

The **membrane current** is the sum of all currents going through all channels of the membrane. Since the neuron membranes vary in shape and size, the **membrane current per unit area (I_m)** needs to be defined, which is the membrane current divided by the surface area of the cell. Since I_m is the sum of all the currents flowing through the channels of the membrane it can be written as

$$I_m = \sum_i g_i(V - E_i), \tag{4.4}$$

where V is the membrane potential, g_i is the conductance per unit area of channel i and E_i is the equilibrium potential of channel i.

Neurons receive information via their dendritic tree, integrate this information on the way to the soma and then produce action potentials that travel along the axon to other neurons. The neuron's electrophysiological properties, that is, how it reacts to incoming information from its dendrites, are determined by its morphology and its ion channels, which determine the ion flux through the membrane and the passive properties of the neuron. All neuron models describe the flow of charged particles between the intra- and extracellular space and their effects on the membrane potential.

Equation 4.2 shows that the rate of change of the neuron's membrane potential is proportional to the rate of charge accumulating on the inside of the cell's membrane. Again, this is proportional to the current entering the cell. Combined, this results in the basic equation for a neuron model

$$c_m \frac{dV}{dt} = -I_m + \frac{I_e}{A}, \tag{4.5}$$

where $c_m = C_m/A$ is the **specific membrane capacitance**, A is the total surface area of the

cell and I_e any external current entering the cell. This structurally resembles an electric circuit, where the membrane is the capacitor, and different variable and non-variable resistances corresponding to the different ion channels contribute to the membrane current I_m (Figure 4.2).

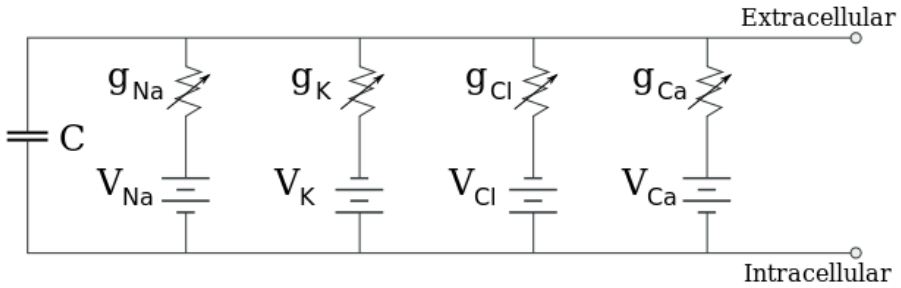

Figure 4.2.: Equivalent circuit representation of a neuron model comprising four ionic channels, sodium (Na^+), potassium (K^+), chloride (Cl^-) and calcium (Ca^{2+}). Here the membrane current I_m from Equation 4.5 would be the sum of the four. The variable resistances illustrate the voltage-dependence of these ion channels. ([94], License: GFDL).

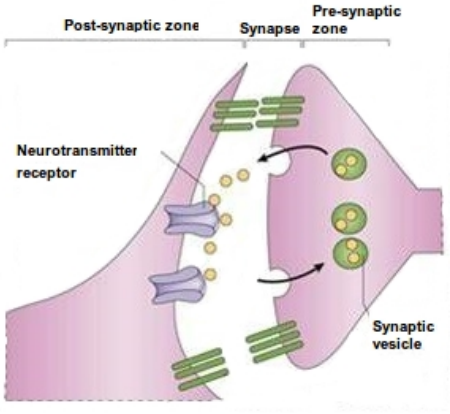

Figure 4.3.: Depiction of a chemical synapse connecting two neurons (modified after [29]).

Synapses are the interface between an axon from one neuron and a dendrite from another one. Since information flows from the axon to the dendrite, the **pre-synaptic** neuron is the one sending information through its axon and the **post-synaptic** neuron is the one receiving information at its dendrite (see Figure 4.3). Generally, the action potential arriving at the synapse triggers ion channels that cause the release of neurotransmitters into the synaptic cleft. The neurotransmitter travels to the receptors at the post-synaptic dendrite and causes a so-called **post-synaptic potential** (PSP). There are two types of

synapses: synapses that cause a depolarising PSP, called **excitatory post-synaptic potential** (EPSP), and synapses that cause a hyperpolarising PSP, called **inhibitory post-synaptic potential** (IPSP). Most of the time, but not always, an EPSP leads to facilitation of the spiking in the post-synaptic neuron [109] and, hence, these synapses are called **excitatory** synapses. Analogously, synapses that prevent spiking, mostly because they create an IPSP, are called **inhibitory** synapses. This can also be described in terms of equilibrium potentials as for the other ion channels in the membrane described earlier. The two main neurotransmitter in cortical areas are glutamate and γ-amino-butyric acid (GABA) [46]. Both bind to different kinds of receptors, 2-amino-3-(3-hydroxy-5-methyl-isoxazol-4-yl)propanoic acid (AMPA) and N-methyl-D-aspartate (NMDA) being the two most important glutamatergic receptors, and GABA_A and GABA_B the two most prominent GABAergic ones.

4.2. Computational Units

In this section, state-of-the-art models of neuronal computation are reviewed starting with abstract population models and gradually introducing more detailed models. Their design is discussed, as well as their properties and drawbacks, based on their applicability to the problems addressed in this work.

4.2.1. Firing-Rate Models

Firing-rate models put an emphasis on the overall activity of neurons and discard information on temporal interactions within populations of neurons. Firing-rate models, therefore generalise distinct firing events of single neurons to the activity level of the neuron under consideration.

Firing-rate models consider the activity level s of a neuron and describe its evolution as the weighted sum of the activity levels η_k of all neurons connecting with this neuron [149]:

$$s = \sum_k \eta_k \cdot w_k, \tag{4.6}$$

where the weights w_k describe the strength of the connection from the connecting neurons k to this neuron. This activity level can still be interpreted as the neuron's membrane potential and is often further abstracted into a firing rate η depending on s. The abstraction is done using a sigmoid activation function σ [149]:

$$\eta = \sigma(s) = \frac{1}{1 + e^{-s}}. \tag{4.7}$$

η is then limited between 0 and 1.

Firing-Rate models are computationally very efficient and are often used to simulate large populations of neurons, up to whole neural systems. It is even possible to use a piecewise linear approximation of the activation function σ, making the model even more efficient. They are preferred in simulations of high-level behaviour such as language processing, memory and reasoning [e.g. 4] and in simulations of developmental and organisational processes [e.g. 149].

However, over the past few years years growing experimental evidence has accumulated showing that the mean firing rate of a neuron might not be the only quantity carrying information [27, 108]. For example, in many tasks, the reaction times of humans and animals are so short that a transmission of information via average firing rates seems impossible regarding the many processing steps involved. Furthermore, studies suggest temporal correlations between spikes of different neurons as well as stimulus-dependent synchronisation of populations of neurons [e.g. 193]. These studies suggest that the temporal information cannot be discarded without loosing valuable information and the concept of coding by mean firing rates oversimplifies the computations in the brain [27].

4.2.2. Integrate-and-Fire Neurons

Leaky Integrate-and-Fire The **integrate-and-fire** model goes back to the early work of Lapicque [122] and uses a single variable to describe neuronal dynamics. Neurons are modelled with a basic circuit consisting of a capacitor C in parallel with a resistor R driven by a current $I(t)$ [201, 212] (see Equation 4.5). The potential variable v can be regarded as the membrane potential and the model integrates incoming spikes until a membrane threshold is reached, fires an action potential and resets the potential afterwards. It can be formulated in the so-called standard form of the leaky integrate-and-fire model [74]

$$\tau_m \cdot \frac{\mathrm{d}v}{\mathrm{d}t} = -v(t) + R \cdot I(t), \tag{4.8}$$

where the variable v is regarded as the membrane potential, τ_m as the membrane time constant, $I(t)$ represents the incoming activity that builds up the membrane potential over time and R is the resistance of the membrane [31, 74, 154]. Note that this model does not explicitly generate action potentials. Instead, whenever the membrane potential exceeds a 'spiking threshold' θ, the formal event 'spike' and its time are noted, and the membrane potential is reset to a value $v_{reset} < \theta$. The simplicity of this model often allows for analytical examinations of the problem at hand.

Non-Linear Integrate-and-Fire A non-linear generalisation, the **non-linear integrate-and-fire** neuron, can be formulated as follows

$$\tau \cdot \frac{\mathrm{d}v}{\mathrm{d}t} = F(v) + G(v) \cdot I(t), \tag{4.9}$$

where F and G are nonlinear functions and, as above, the membrane potential is reset after it reaches a certain threshold θ [74].

Quadratic Integrate-and-Fire One prominent example of the non-linear integrate-and-fire neuron is the **quadratic integrate-and-fire** neuron. For the **quadratic integrate-and-fire** neuron the function F in Equation 4.9 is set to be $F(v) = v^2$. This results in

$$\tau \cdot \frac{\mathrm{d}v}{\mathrm{d}t} = v^2 + G(v) \cdot I(t), \tag{4.10}$$

with a reset of the membrane potential v whenever $v = v_{peak}$. Note that this model is able to generate the upstroke of an action potential and that the membrane potential is reset when a certain peak value of the action potential is reached.

The quadratic integrate-and-fire neuron has some advantages over the linear integrate-and-fire neuron. First of all, as mentioned above, it is able to generate the upstroke of an action potential, i.e. it really is a 'spiking' neuron model. Furthermore, it has some dynamical properties which can also be found in mammalian neurons [74]. The quadratic integrate-and-fire model often allows for analytical examinations [109].

However, the quadratic integrate-and-fire neuron has some severe limitations with regard to capturing the biological diversity. Mammalian neurons do not only show the behaviour of integrators but many of them have the property of being a resonator with many functional consequences. The quadratic integrate-and-fire model is, for every choice of parameters, an integrator and thus not able to capture the dynamics of resonator neurons. Moreover, the model is not able to capture another important feature of some mammalian neurons, the so-called **bursting**, that is to say, the ability to fire pulses or **bursts** of several spikes with a high frequency followed by a period of quiescence [105, 109].

Simple Model of Izhikevich One of the two major disadvantages of the quadratic integrate-and-fire neurons is its inability to produce burst firing, a property seen in many mammalian neurons which is hypothesised to have important functional consequences [106]. To overcome this shortcoming, Izhikevich [105] proposed a generalisation of the quadratic integrate-and-fire model that has nearly the same computational efficiency but is capable of producing biologically plausible firing patterns. At the heart of this model

lies the fact that intrinsic burst firing, that is, resulting from intrinsic currents not from a time-dependent input, is typically achieved by the interplay of time scales, fast spiking and a slower modulation by a resonant current [109].

Therefore, Izhikevich [105] proposed the following model

$$\frac{\mathrm{d}v}{\mathrm{d}t} = 0.04 \cdot v^2 + 5 \cdot v + 140 - u + I \tag{4.11}$$

$$\frac{\mathrm{d}u}{\mathrm{d}t} = a \cdot (b \cdot v - u), \tag{4.12}$$

with a reset $v \leftarrow c$ and $u \leftarrow u + d$ whenever

$$v \geq 30 \text{ mV}. \tag{4.13}$$

Again, v describes the membrane potential and u is now the recovery variable enabling burst firing. Furthermore, the model has four dimensionless parameters a, b, c, d which determine the firing behaviour of the neuron. Note that both variables are dimensionless, but the model is scaled (see Equation 4.11) so that the membrane potential has mV scale and the time scale is ms. The model reproduces the most common firing behaviours seen experimentally.

Adaptive Exponential Integrate-and-Fire Similar to the simple model of Izhikevich discussed above, the **adaptive exponential integrate-and-fire** model, introduced by Brette and Gerstner [28], is a non-linear generalisation of the integrate and fire model. It is given by

$$\frac{\mathrm{d}v}{\mathrm{d}t} = -\frac{1}{C}(g_L(v - E_L) + g_L\Delta_T\, e^{\frac{V - V_T}{\Delta_T}} - u + I), \tag{4.14}$$

$$\frac{\mathrm{d}u}{\mathrm{d}t} = \frac{1}{\tau_u}(a(v - E_L)) - u, \tag{4.15}$$

where C is the membrane capacitance, u is an adaptation variable, I the synaptic current, E_L is the resting potential, Δ_t is the slope factor and V_t is the threshold potential. Again, if a threshold is reached, in this case $V_{peak} = 20\,\mathrm{mV}$, the model is said to fire a spike and the membrane potential and the adaptation variable are reset to

$$v \leftarrow E_L \tag{4.16}$$

and

$$u \leftarrow u + b, \tag{4.17}$$

respectively.

The behaviour of the adaptive exponential integrate-and-fire model is very similar to the simple model of Izhikevich. It is also able to reproduce a large variety of different firing behaviours of biological neurons, such as burst firing, sub-threshold oscillations and spike-frequency adaptation, if the parameters are adapted reasonably [28].

4.2.3. Hodgkin-Huxley Type Neurons

The original model proposed by Hodgkin and Huxley in 1952 described the generation of an action potential in the axon of the giant squid [91]. The original model is given by

$$C\frac{\mathrm{d}v}{\mathrm{d}t} = \bar{g}_L(v - E_L) + \bar{g}_K n^4(v - E_K) + \bar{g}_{Na} m^3 h(v - E_{Na}) + I, \tag{4.18}$$

where C is again the membrane capacitance, E_i and $\bar{g}_i$ ($i \in \{L, K, Na\}$) are the reversal potentials and maximum conductances for the ionic currents, respectively. The variables m, n and h describe activation and inactivation of the ionic currents, sodium and potassium in this case, and are called **gating variables**.

Hodgkin-Huxley (HH) type models use activation and inactivation variables as well as maximum conductances, as in Equation 4.18, to describe the contributions of ionic currents to the temporal evolution of the membrane potential [87]. Again, the evolution of these gating variables, describing the influence of specific ionic currents, is described by differential equations of the form

$$\frac{\mathrm{d}n}{\mathrm{d}t} = \alpha_n(v)(1 - n) - \beta_n(v)n, \tag{4.19}$$

where $\alpha_n(v)$ describes the voltage-dependent transition of a channel from a closed to an open state, and $\beta_n(v)$ the transition from open to closed. Another way of expressing these relations is

$$\tau_n(v)\frac{\mathrm{d}n}{\mathrm{d}t} = n_\infty(v) - n, \tag{4.20}$$

where

$$\tau_n(v) = \frac{1}{\alpha_n(v) + \beta_n(v)} \tag{4.21}$$

and

$$n_\infty(v) = \frac{\alpha_n(v)}{\alpha_n(v) + \beta_n(v)}. \tag{4.22}$$

Consequently, if the voltage v is fixed, n approaches the limit $n_\infty(v)$ exponentially with the time constant $\tau_n(v)$. The functions α and β, which play a key role in the description of the ionic currents, are usually fit to experimental data. However, to get a feel for the form these functions, it is useful to take a closer look at them. Thermodynamic arguments

suggest that these functions are exponential, thus making the functions in Equation 4.22 a sigmoid function of the form:

$$n_\infty(v) = \frac{1}{1 + (A_\beta/A_\alpha)exp((B_\alpha - B_\beta)V/V_T)}, \tag{4.23}$$

where $A_\alpha, A_\beta, B_\alpha$ and B_β are constants [74]. Still, in a lot of practical cases, the best fit might not be a sigmoid function and other forms are used.

4.2.4. Multi-Compartment Neuron Models

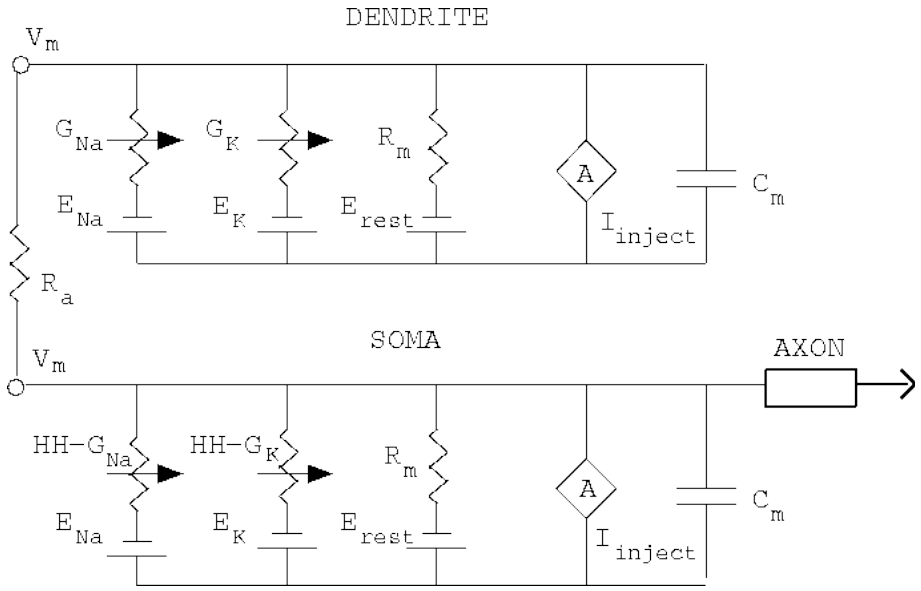

Figure 4.4.: Depiction of an equivalent circuit model describing the coupling of a somatic, a dendritic and an axonal compartment.

So far, single-compartment neuron models have been presented, that is to say neuron models that do not consider the structural morphology of the neurons. However, in animal and human brains, neurons have evolved into complex and elaborate structures with intricate dendritic trees. It is obvious that such an evolution must have functional implications and, in order to fully capture these consequences, more realistic neuron models need to be investigated. Constructing morphologically more detailed neuron models than single-compartment neurons requires splitting the neuronal morphology into sections or compartments. For every compartment, the membrane potential along it is assumed constant. The number of compartments used determines how realistic the

representation of the neuron is. So for every compartment k, the temporal evolution of the membrane potential is described by

$$C\frac{\mathrm{d}v_k}{\mathrm{d}t} = -i_k + I_k/A_k + g_{k,k+1}(v_{k+1} - v_k) + g_{k,k-1}(v_{k-1} - v_k), \tag{4.24}$$

where i_k is the total ionic current, I_k is the inward current, A_k is the surface area of the compartment and the two last terms describe the current flow between compartment k and its adjacent compartments $k+1$ and $k-1$ [52]. If the compartment only has one neighbouring compartment, there is only one term in Equation 4.24. For a branch this results in three terms in Equation 4.24. The constants $g_{i,j}$ determine the coupling strength of two adjacent compartments and are calculated using Ohm's law [52]. They depend on the lengths L_i and L_j and the radii a_i and a_j, respectively, of the two compartments and are given by [52]:

$$g_{i,j} = \frac{a_i a_j^2}{r_L L_i (L_i a_j^2 + L_j a_i^2)}. \tag{4.25}$$

Efficient ways to numerically integrate multi-compartment neurons are discussed in Section 4.4.1.

4.2.5. Comparison and Evaluation

The choice of the model for the computational units strongly depends on the purpose of the model and the type of the problem. The HH-type model is the best model to study how neuronal behaviour depends on neurophysiological parameters because it is the only type of model that combines biophysically meaningful parameters with a wide variety of neurocomputational properties (Table 4.2, [109]). However, the main drawback of the HH-type models is the computational complexity with an approximate number of 1200 floating point operations (FLOPS) to simulate the model for 1 ms (see Table 4.2). The simulation of large networks (> 1000 neurons) of these types of neurons has become possible over the last decade, but is still very time-consuming [105, 106, 109].

Numerous more efficient models are available to simulate large networks of neurons, which however sacrifice the physiological reference to the parameters. The most efficient models are the simple and quadratic integrate-and-fire models (see Table 4.2). However, neither can fully replicate fundamental properties of spiking neurons, the integrate-and-fire model even failing to exhibit almost all of these properties [109]. The simple model proposed by Izhikevich [105] gives a very good trade-off between rich neurocomputational properties and low computational costs, it can reproduce a wide variety of spiking patterns and is only slightly more expensive than the integrate-and-fire model. The

exponential integrate-and-fire model has similar properties as the simple model and a comparable computational complexity [28].

Table 4.2.: Comparison of the computational properties and complexity of different neuron models (data from [106]). The integrate-and-fire model is the most commonly used neuron model and the quadratic integrate-and-fire neuron the most commonly used generalisation. The Izhikevich neuron model can reproduce these important features with little additional computational complexity, but it still does not have biophysically meaningful parameters. The Hodgkin-Huxley type neuron models do have meaningful parameters, while reproducing the important characteristics. However, this comes at the expense of dramatically increased computational costs.

Models	Integrate-and-Fire	Quadratic Integrate-and-Fire	Izhikevich	Hodgkin-Huxley Type
Biophysically Meaningful	NO	NO	NO	YES
Regular Spiking	YES	YES	YES	YES
Bursting	NO	NO	YES	YES
Spike Frequ. Adaptation	NO	NO	YES	YES
Resonator	NO	NO	YES	YES
Integrator	YES	YES	YES	YES
Sub-threshold Oscillations	NO	NO	YES	YES
FLOPS/ms	5	7	13	1200

4.3. Modelling Networks

4.3.1. Connections in Rate-Based Models

In firing rate network models the activity of a computational unit is described by its firing rate η. In order to connect these units, it has to be defined how the time-varying firing rates η_{pre} of N pre-synaptic neurons determine the firing rate η_{post} of one particular post-synaptic neuron. Starting with one action potential from one pre-synaptic neuron b, the synaptic current arriving at the post-synaptic neuron a at time $t = 0$ is defined by two factors: the **weight** w_{ba}, which describes the strength of the connection between these two neurons and the **synaptic kernel** $K_s(t)$, which describes the current produced by a single spike arriving at neuron a. For all pre-synaptic neurons $b_1 \cdots b_N$ projecting to the neuron a, all the weights can be written into a single weight vector w. Furthermore, if the linear summation of spikes at one synapse is assumed, the total synaptic current I_s at neuron a at time t for a sequence of spikes arriving at times t_j is defined as:

$$I_s = \sum_{i=1}^{N} w_{b_i a} \sum_{t_j < t} K_s(t - t_j) \tag{4.26}$$

To find out the firing rate that results from this synaptic current, the temporal evolution of the synaptic input current can be written as

$$\tau_s \frac{dI_s}{dt} = -I_s + w \cdot \eta_{pre} \tag{4.27}$$

with the firing rate $\eta_{post} = F(I_s)$, where F is the steady-state firing rate as a function of the somatic current (see [52]). Note that in equation 4.27, w and η_{pre} are vectors and the $\cdot$ denotes the inner product between these vectors. This formulation, however, assumes that the post-synaptic firing rate follows the synaptic current instantaneously. If it is assumed that this is not the case, this results in the membrane potential being a low-pass filtered version of the synaptic current (see [52]). Therefore, a low-pass filtered version of the steady-state firing rate is often taken as the time-dependent firing rate, resulting in

$$\tau_r \frac{d\eta_{post}}{dt} = -\eta_{post} + F(I_s(t)). \tag{4.28}$$

Here, the time constant τ_r determines how the firing rate follows the fluctuations of the synaptic current. If $\tau_r << \tau_s$, it can be approximated that equation 4.28 rapidly relaxes to its equilibrium, and this model is reduced to the instantaneous steady-state firing model. On the contrary, if $\tau_r >> \tau_s$, I_s can be replaced by $w \cdot \eta_{pre}$, resulting in

$$\tau_r \frac{d\eta_{post}}{dt} = -\eta_{post} + F(w \cdot \eta_{pre}). \tag{4.29}$$

4.3.2. Connections in Spiking Models

In the brain, information is exchanged by neurons via axons and dendrites, which are connected by synapses. Although there are other types of synapses, such as gap junctions, this work focusses on chemical synapses, since only those play an important role in the questions addressed here and were implemented in the models.

In most models, the axon is modelled as a delay line and, if the details of the synapse properties are not relevant, a certain function is taken to relate the incoming of a spike to a resulting post-synaptic potential.

A simple approach to model chemical synapses, is to increase the conductance g at a synapse every time a spike arrives by a certain amount g_{max} and, in the absence of spikes, letting the conductance g decay exponentially:

$$\frac{dg}{dt} = -g/\tau, \tag{4.30}$$

where the time constant τ governs the time course of the decay and can vary as much as from $3 - 5\,ms$ for fast glutamatergic synapses (e.g. AMPA receptors) to $150\,ms$ for slow glutamatergic (e.g NMDA receptors), or slow GABAergic synapses (e.g. GABA_B receptors) [52, 107].

Instead of assuming an instantaneous effect as above, a slightly more realistic approach is modelling the changing conductance with a so-called **alpha function** given by the equation

$$g(t) = g_{max}\frac{t}{\tau}e^{(1-t/\tau)}, \tag{4.31}$$

where the peak of the conductance is not reached instantaneously, but at time $t = \tau$ after the arrival of the spike.

Most of the available neural simulators use an even more general form, the so-called **double exponential function** given by

$$g(t) = \frac{A\,g_{max}}{\tau_1 - \tau_2}(e^{-t/\tau_1} - e^{-t/\tau_2}), \tag{4.32}$$

for $\tau_1 > \tau_2$. A is a normalisation factor chosen so that the maximum of g is g_{max}. The two time constants describe the rise and the decay time of the PSP.

4.4. Implementation and Efficiency

This section deals with the analysis and simulation of networks of neurons. Existing software packages for construction, simulation and analysis of network models are also reviewed.

4.4.1. Numerical Solutions to Coupled Differential Equations

The numerical techniques to solve the systems of coupled differential equations arising in the context of network models are described. For the sake of brevity, only methods that are commonly used in neural network modelling and neural simulators are considered.

The differential equations arising in the context of modelling neurons and networks of neurons, typically are of the following form (see 4.2,4.3):

$$\frac{dy_i}{dt} = f(t, y_1, y_2, \ldots, y_N), i = 1, \ldots, N. \tag{4.33}$$

For the sake of simplicity, this subsequently will be abbreviated to

$$\frac{dy}{dt} = f(t). \tag{4.34}$$

There are various numerical methods to solve this kind of coupled equations [22, 89, 140], which can be divided into two categories: **explicit** and **implicit** methods. While explicit methods only make use of old, previously calculated values, implicit methods are formulated with the new values expressed in a function of the new value that still has to be calculated. This implies that an additional method to solve these equations is needed.

Explicit Methods

Explicit or Forward Euler The **forward Euler** method is a very simple numerical method for the solution of Equation 4.34. For a time step Δt, the solution y at time $t + \Delta t$ is given by

$$y(t + \Delta t) = y(t) + f(t)\Delta t. \tag{4.35}$$

This is equal to an approximation by a Taylor series expansion

$$y(t + \Delta t) = y(t) + \frac{dy}{dt}\Delta t + \frac{1}{2}\frac{d^2y}{dt^2}(\Delta t)^2 + \frac{1}{6}\frac{d^3y}{dt^3}(\Delta t)^3 + \ldots, \tag{4.36}$$

where the terms of higher order than 1 have been neglected. In Equation 4.35 only previously known values of y are used, hence, this is an explicit method.

The advantages of the forward Euler method are its simplicity, making it very easy to implement, and its low computational complexity, because no costly operations must be performed [22, 89, 140]. However, the method suffers from instability and inaccuracy if, the chosen time step Δt is too large [22, 89, 140]. This means that the time step has to be chosen carefully and has to be quite small compared to other methods, thus reducing the speed of the overall simulations.

Adams-Bashforth As explained above, the forward Euler method cuts a Taylor series expansion after order one, which results in a coarse approximation, and leads to instability and inaccuracy. One way to approximate the truncated higher order derivatives is to use past values of $f(t)$. The **Adams-Bashforth** method does exactly this and can be written as

$$y(t + \Delta t) = y(t) + \Delta t(c_0 f(t) + c_1 f(t - \Delta t) + c_2 f(t - 2\Delta t) + \ldots + c_n f(t - n\Delta t)). \quad (4.37)$$

The used number n of previous time steps determines the order of the Adams-Bashforth method, that is, if n previous time steps are used then until the $(n + 1)$th derivative is approximated in the Taylor series expansion. Thus, the Adams-Bashforth method is said to be of $(n + 1)$th order. However, the coefficients c_i in equation 4.37 have to be determined. This can be done by expanding $f(t - i\Delta t)$ in a Taylor series and then comparing equation 4.37 with equation 4.36. Higher order Adams-Bashforth methods reduce the error introduced by the truncation of the Taylor series expansion and thus the error introduced at each time step. Still, the overall cumulative error over many time steps may be large because of the extrapolation from past values, which might not be related to the future value. This strongly depends on the function $f(t)$: If $f(t)$ varies smoothly in time, a higher order method usually gives more accurate results; but if $f(t)$ changes rapidly and sharply, an Adams-Bashforth method of lower order is more beneficial [22, 140].

Exponential Euler Another explicit integration method is the **exponential Euler** method [133]. This is an efficient and accurate method, which relies on the fact that the typical equations can be rewritten in the form

$$\frac{dy}{dt} = A - By, \quad (4.38)$$

where A and B might depend on y and t. Afterwards, the solution can be approximated, for time step Δt, by

$$y(t + \Delta t) = y(t)D + (A/B(1 - D), \quad (4.39)$$

where D is defined as

$$D = e^{-B\Delta t}. \tag{4.40}$$

Equation 4.39 holds if A and B are constants [22]. However, if A and B are assumed not to change much from t to $t+\Delta t$, the equation is an approximation of the solution even for non-constant A and B. A rigorous analysis of the error introduced by the exponential Euler scheme is difficult. Nonetheless, in practice, this method shows very accurate results for most types of models and allows for larger time steps than the above-mentioned methods [22].

Implicit Methods In contrast to the explicit methods covered before, in implicit methods, the right-hand side of the equation not only depends on old function values, but also on the new value that still has to be determined.

Backward Euler The **backward Euler** method is one example for an implicit method. It uses

$$y(t + \Delta t) = y(t) + f(t + \Delta t)\Delta t. \tag{4.41}$$

Since the right hand side of the equation does not explicitly give an expression that can be evaluated, an additional method is needed to solve this equation. Furthermore, the truncation error in 4.41 is the same of that from equation 4.35, except for the sign. This leads to the question, why implicit methods should be used at all, if the error is the same as for explicit methods, but an additional method is needed to solve it. However, the cumulative error of implicit methods is usually considerably smaller [104].

Crank-Nicholson The **Crank-Nicholson** method exploits the trapezoidal rule of numerical integration. This results in a mixture of the forward and backward Euler methods. Since the sign of the second order derivatives, neglected in forward and backward Euler schemes, have opposite signs for these two methods, an average of both leads to a cancellation of error terms. Hence, the **Crank-Nicholson** method is given by

$$y(t + \Delta t) = y(t) + (f(t) + f(t + \Delta t))\frac{\Delta t}{2}. \tag{4.42}$$

4.4.2. Neural Simulators

Numerous different software programs and libraries exist for the construction, simulation and analysis of networks of neurons at all different levels of abstraction.

The neuroConstruct software tool [76] was chosen to built the model and Neuron [88, 89] was used to run the simulations. neuroConstruct is a software package specifically dedicated to the design of biologically detailed, multi-compartment 3-D neuron models and networks, but it is not a neural simulator, that is, it does not provide routines to solve the system of differential equations to simulate a network of neurons. Nevertheless, it offers some distinct advantages over the use of a plain neural simulator for the design and simulation of our network. Firstly, it has a powerful, yet user-friendly, graphical user interface to design the network. Secondly, it offers a Python interface allowing automation of parameter searches or large numbers of simulations, as it is the case for the work presented here. Thirdly, it has a large pool of example projects to build on from. Finally, most importantly, it offers the possibility to generate simulator code for most of the generally used neural simulators, such as Genesis [22, 23], Neuron [88, 89] or Moose [62, 169, 170], and a simulator-independent representation of the network model in neuroML [77]. All simulations presented in this work were performed using Neuron, with its default numerical integration method, which is an optimisation of the Crank-Nicholson method for branching cables [88].

5. Theories of Computation in the Primary Visual Cortex

This chapter reviews the state-of-the-art of theories and models of the primary visual cortex (V1). The chapter is subdivided into two sections. First, existing theories of the emergence of classical receptive field properties are discussed, followed by theories of extra-classical receptive field properties, with a focus on centre-surround suppression.

5.1. Classical Receptive Field Properties

Along the visual pathway there are two early, non-cortical processing stages (hereupon early processing stages), the retina and the thalamic nuclei, until the signal reaches V1 (depicted in Figure 5.1). V1 is the first stage where highly selective cells are found and conducts the basic pre-processing for the two fundamental questions in vision: what (comprising object recognition) and where (comprising localisation and motion detection). These two features are then processed in higher visual areas segregated in two streams, the ventral stream (*what*) and the dorsal stream (*where*), as shown in Figure 5.2. However, since the models implemented in this work focus on V1, theories and models of higher visual areas are not reviewed. Since the early processing stages in the pathway provide the sensory input to V1, the concepts of early processing needed to understand the processing of information in V1 are shortly reviewed. For further details on anatomy and function of the visual system see Appendix A and [46, 138].

Early Processing Stages Photoreceptors transduce the incoming light to electrical activity. The first processing of visual information then happens at the retinal ganglion cells, where the so-called ON-centre and OFF-centre cells, along with other retinal nerve cells, perform an edge detection by responding most strongly to changes in luminance. An interesting point is that two distinct pathways emerge already in the retina, represented by magnocellular (M-type) and parvocellular (P-type) ganglion cells, which are kept segregated throughout the visual system, which functionally divides the **what** from

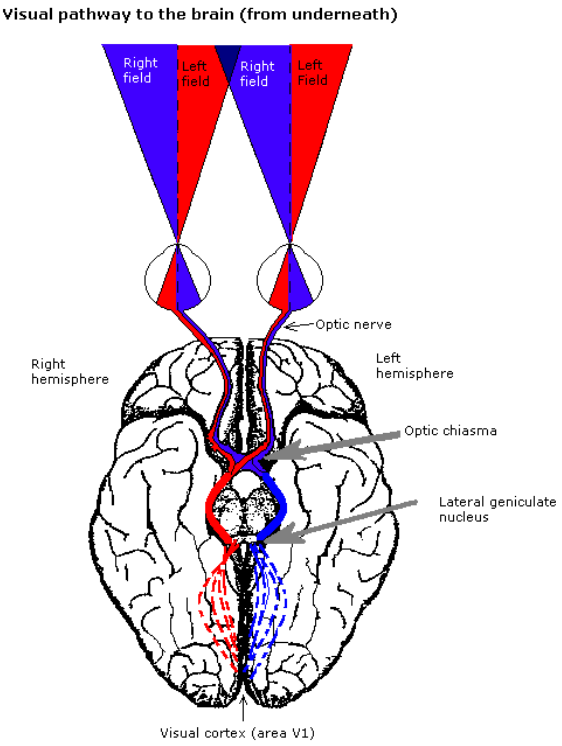

Figure 5.1.: The visual pathway from the eye to the cortex. Incoming light is converted in the retina of both eyes. The signal travels along the optic nerve through the optic chiasm to the LGN in the thalamus. Here it is relayed to the cortical visual areas, starting with the V1 ([93] License: GFDL).

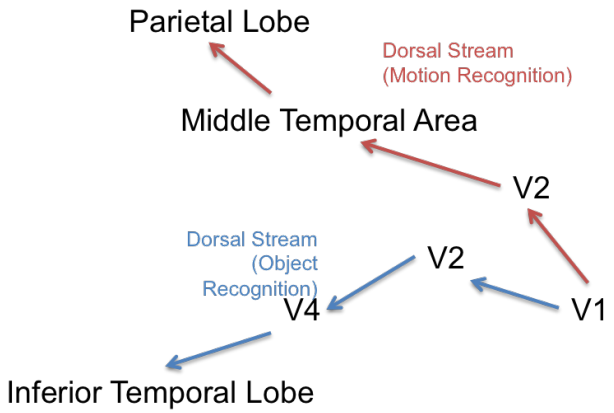

Figure 5.2.: The two streams in higher visual processing: the *ventral stream*, also called the *what stream*, and the *dorsal stream*, also called the *where stream* ([95] License: GFDL).

the **where** information. Important for the scope of this work is the M-pathway. Therefore, throughout this work, whenever retinal, thalamic or cortical processing is mentioned, it refers to the processing within the M-pathway (see Appendix A for further details on the anatomy and function of the retina).

The next stage, the thalamus, is mostly considered as relay station that transfers the retinal signals to the cortex, namely layer 4C (4Cα for the M-pathway to be exact) of V1. Similar to the retina, there are again ON-centre and OFF-centre cells. It is important to note that cells in thalamus, that is, the LGN, have little or no selectivity regarding orientation, spatial frequency and temporal frequency [54, 98, 99, 183, 184].

Processing in V1 V1 is the first stage in visual processing where highly selective cells emerge. This appearance of specificity is thought to underlie many important visual functions such as motion detection, edge detection and object recognition. This specificity is also found in higher visual areas. However, there is still a debate about the exact mechanisms underlying the emergence of feature selectivities [187].

The proposed theories and models explaining high selectivity in V1 can be categorised in two classes: theories attributing emergent selectivity to the convergence of a weakly selective input from the thalamus (**feed-forward models**), and theories explaining selectivity as a result of recurrent network activity (**recurrent models**).

The three main features of V1 neurons are: their specific response to moving stimuli (bars or gratings) of a given orientation, their specific response to stimuli with low spatial frequencies, and their linear (simple) or non-linear (complex) response to moving sinusoidal gratings.

Feed-Forward Model The division of cells into simple and complex cells dates back to the seminal work of Hubel and Wiesel [98]. Hubel and Wiesel explained simple cells as cells receiving a direct afferent input, which then converge onto a distinct class of cells that show complex behaviour (as illustrated in Figure 5.3 (a)). Note that distinct classes here means the cells have different computational functions or show different functional behaviour arising from different embeddings in the network structure, which does not necessarily mean different morphological and electrophysiological properties of the neurons, to wit, different cell types. Thus, this theory falls into the category of a feed-forward theory.

Similarly, the emergence of orientation and spatial selectivity can be explained by a theory of this type. The spatial arrangement of LGN cells providing convergent input to a simple cell (the **receptive field** of the cell), results in a preference for a certain orientation

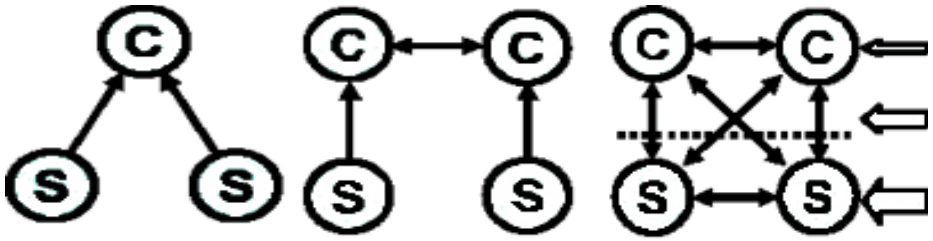

(a) (b) (c)

Figure 5.3.: Different models explaining the emergence of simple and complex cells in V1. (a) Schematic representation of the feed-forward model of Hubel and Wiesel. (b) Schematic representation of the model of Chance et al., where simple cells only receive feed-forward LGN input and only complex cells have recurrent connections. (c) The model of Tao et al. where recurrent connectivity is isotropic and the balance between recurrent and feed-forward drive determines whether cells are simple or complex. (modified from [204].)

or for a certain spatial frequency. In case of orientation selectivity, it is the elongated shape of the receptive field that generates preference for orientations perpendicular to its main axis. In case of spatial frequency selectivity, the size and the arrangement of the ON and OFF regions of the receptive field determines the preference. Directional preference can also be explained by the position of the ON and OFF regions relative to the direction of the movement. In addition to the Hubel and Wiesel data [98], there is experimental support for this theory [40, 44, 66, 171].

Notwithstanding researchers agree that the orientation selectivity predicted by this kind of architecture would be rather weak [144, 187, 210], and it does not reflect recent experimental data [199, 210]. Especially the dramatic drop in firing rate of cells in response to gratings orthogonal to their preferred orientation, seen in many neurons *in vivo* [e.g. 173, 174], cannot be sufficiently explained by this theory [187]. Another factor is that feed-forward models can be tuned to show high orientation selectivity [34], but this is only possible for one contrast and produces broadly tuned cells at stimuli having different contrasts [15, 199, 210]. Furthermore, new experiments on the dynamics of orientation selectivity are also inconsistent with purely feed-forward models [187]. In the same vein, it can be argued that the attenuation of response to not preferred spatial frequencies seen in V1 neurons can also not be fully explained by the feed-forward model. The feed-forward model also predicts a clear distinction of the two classes of simple and complex cells, that is, a clear bimodal distribution. However, recent experiments point to a continuum, which cannot be fully explained by the feed-forward model [174, 232].

A different model, depicted in Figure 5.3 (b), has been proposed by Chance et al. [39].

The distinction between simple and complex cells in this model stems from the differences in connectivity. Whereas simple cells only receive feed-forward LGN input, complex cells receive feed-forward input from simple cells and also from recurrent connections from other complex cells. Therefore, this model is not a pure feed-forward model. Nonetheless, since simple cells mostly show stronger selectivity than complex cells, the explanation for the emergence of orientation and spatial frequency selectivity is the same as for the Hubel and Wiesel type model, and hence the same objections hold.

Recurrent Model Many theories have been proposed that attribute the high selectivity of cells mainly to recurrent network activity, be it either excitatory [e.g. 15, 197, 211] or inhibitory [e.g. 64, 144, 210, 231, 232].

The idea behind inhibitory recurrent models is that inhibition is more broadly tuned than the excitation, arising from feed-forward convergence, and thus a significant sharpening at the preferred frequency is obtained. Two variations exist: phase-sensitive inhibition (often also called push-pull inhibition, [210]) and phase-insensitive inhibition (also called cross-orientation inhibition [144, 231, 232]). It could be argued that a broadly tuned inhibition could also be fed forward from the LGN, but there is strong experimental evidence that thalamo-cortical synapses are purely excitatory [30, 70], implying a cortical origin of inhibition. There is some experimental evidence for this theory from a study blocking inhibition pharmacologically (extracellularly) with bicuculline, a GABA-antagonist, resulting in a significant loss of orientation selectivity [189]. More recent pharmacological experiments using GABA antagonists have shown similar results [48, 126, 163, 179]. On the other hand, Nelson et al. reported that inhibition on a single neuron did not affect its orientation tuning, measured intra-cellularly, by blocking inhibitory currents [153].

The difference between the two types of models, push-pull and cross-orientation recurrent inhibition, is that, in the former, inhibition only occurs in phase with the drifting grating, whereas in the latter inhibition is phase-insensitive. Still, the phase-sensitivity in the push-pull model seems unnecessary from a theoretical point of view, and recent experimental and modelling studies indicate that the inhibition arriving at one neuron is the sum of many inhibitory neurons with different phase-sensitivities, resulting from their spatial distribution, and thus phase-insensitive [20, 187, 220].

5.2. Neural Centre-Surround Suppression

Neurons in V1 however, do not remain 'blind' to stimulation outside of their CRF, even though a stimulation does not directly elicit action potentials. Neurons do integrate information from a large area surrounding their CRF and this information modulates the neuron's behaviour in response to a stimulation of its CRF. These modulatory effects are called **extra-classical receptive field properties** since they originate from a stimulation outside of the CRF. One important example of an extra-classical receptive field property is **neural centre-surround suppression**, that is to say, the suppressive modulation of the response to a sinusoidal grating in the CRF by a sinusoidal grating placed in the surround (strongest suppression for parallel oriented gratings).

The neural mechanisms behind these extra-classical receptive field properties are less understood than those of classical receptive field properties. On the one hand, they pose greater challenges to experimenters to be reliably measured and, on the other hand they depend on the incompletely understood classical phenomena.

Currently, there are three main hypotheses for the emergence of extra-classical receptive field properties, which will be reviewed here, with a focus on neural centre-surround suppression.

Long-Range Intra-Cortical Connections Probably the oldest theory for the emergence of centre-surround suppression phenomena was formulated by DeAngelis et al. in 1994 [56]. They proposed that centre-surround suppression was produced by a pool of inhibitory neurons connecting to one excitatory, which had spatially offset receptive fields that surrounded the excitatory neuron and thus created the surround suppression. They argued that horizontal long-range connections were a plausible candidate for this intracortical inhibition (see Figure 5.4 (a)). This theory gained further support by studies reporting that lateral short-range connections might not have the spatial extent to produce experimentally observed surround field sizes. Furthermore, studies have argued against extrastriate feedback, and thus in favour of horizontal connections, as the origin of surround suppression by excluding significant influences of visual area V2 on surround suppression [102, 202]. However, these ignore that feedback might also come from visual areas V3 or MT and also they do not consider the possibility that lateral inhibition might underlie surround suppression. Another important point is, that centre-surround suppression is even seen in layers that do not receive horizontal connections at all [60, 222].

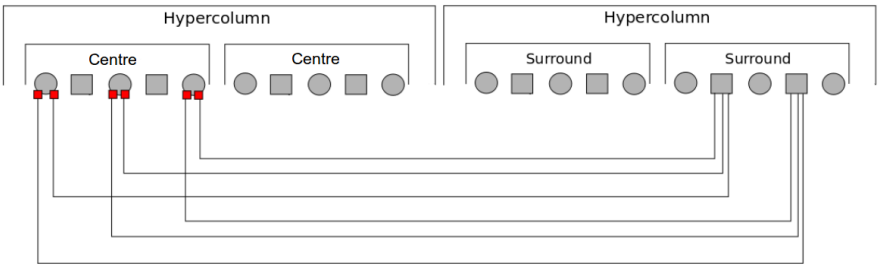

(a)

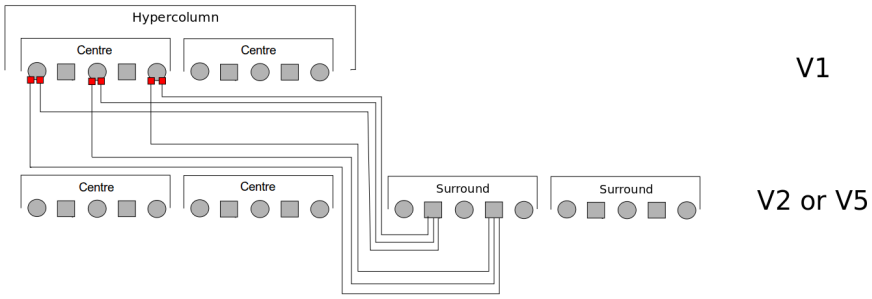

(b)

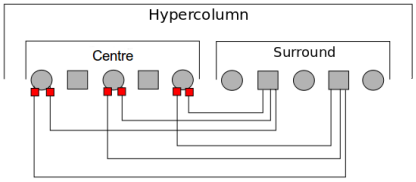

(c)

Figure 5.4.: Theories of the emergence of centre-surround suppression. (a) The suppression is mediated by long-range horizontal connections from different hypercolumns. (b) The suppression is provided by feed-back projections from extra-striate visual areas, such as V2 or V5. (c) The suppression comes from local, short-range connections within the same hypercolumn.

Extrastriate Feed-back Another theory for the emergence of extra-classical receptive field phenomena and, especially, for neural centre-surround suppression is fast feed-back from higher visual areas, such as V2, V3 or MT (see Figure 5.4 (b)). There is some experimental evidence for this theory as well. Firstly, it is argued that the short-range lateral connections, but also long-range horizontal connections, cannot fully account for the reported sizes of the suppression fields [6]. Furthermore, strong suppression seems to act as fast − sometimes also faster than − feed-forward excitation and thus long-range horizontal connections are most likely not delivering this early strong suppression [10]. Suppression propagates for up to 6-8 mm at a high velocity of 1 m/s, which exceeds both the length of horizontal connections (3.5-4 mm [202]) and also the typical speed of horizontal connections (up to 0.4 m/s [79]), but is comparable to feed-back velocities from, for example, area MT (1 m/s [103]). Furthermore, feed-back from higher visual areas is spatially aligned with the feed-forward input from the LGN, and blocking feed-back from area MT results in reduced suppression strengths [101].

However, there is also experimental evidence against this theory. For example, for iso-orientation suppression, horizontal and even short-range lateral connections can account for most of the experimentally observed data [6]. Another factor is that monosynaptic, inhibitory feed-back to V1 is very rare, at least in rats [143], making it unlikely to be the main factor in centre-surround suppression. Moreover, it has been shown that centre-surround suppression is partially inherited from the LGN [161], and thus the fast suppression component could merely be a misinterpretation of this forwarded suppression, keeping in mind that experimental techniques are not yet fully able to distinguish the different contributions to the centre-surround suppression phenomenon. Also, Webb et al. [218] have reported centre-surround suppression at spatial and temporal frequencies outside of the preferred range, which is unlikely to elicit responses, and thus feedback, in higher areas. Additionally, the studies of Hupe et al. [102] and of Stettler et al. [202] argue against extrastriate feed-back, as mentioned above. They reported that centre-surround suppression does not depend on V2 feed-back, and that V2 feed-back connections do not connect domains of similar orientation preference, thus contradicting the orientation-dependence of centre-surround suppression seen experimentally. Finally, probably the most important point is that centre-surround suppression is seen throughout all layers of V1 including those that do not receive extra-striate feed-back [60, 222].

Short-Range Intra-cortical Connections Recently, the long ignored hypothesis that centre-surround phenomena might be the result of lateral, short-range, intra-cortical connections has gained more attention (see Figure 5.4 (c)). Wielaard and Sajda [222] showed

with an integrate-and-fire model that centre-surround suppression can be explained by lateral, recurrent connections and a partial inheritance of surround suppression from the LGN. This is in accordance with centre-surround suppression being present in all layers of V1. Furthermore, centre-surround suppression is also present in the LGN [161]. This theory explains centre-surround suppression in a similar way as the recurrent model for classical receptive field properties explained above. V1 inherits centre-surround suppression partially from the LGN and afterwards recurrent, lateral, short-range mechanisms refine the suppression.

6. A Computational Model of the Primary Visual Cortex

6.1. Introduction

The network model presented in this work was built around three main design principles. First, whenever possible, the model should be founded on anatomical and electrophysiological data. Second, Hodgkin-Huxley (HH) type neuron models were chosen, despite their computational complexity, since the model was designed to serve as a starting point for a detailed, biophysically plausible community model of the primary visual cortex. Third, high flexibility and extensibility are necessary in order to be the starting point for a community model. Therefore, the model was designed with *neuroConstruct*, which allows for the use of all common neural simulators as well as a simulator-independent description of the model.

The presented model builds on two already existing models of primary visual cortex (V1) [160, 204, 205, 231, 232]. The modelling of the lateral geniculate nucleus (LGN) input and its convergence pattern onto V1 cells was adopted from a previously developed model [204, 205, 231, 232]. The pattern of intra-cortical connections was taken from the model of Oliveira and Roque [160]. Both of these models have similar intra-cortical connectivity profiles, such that the lateral connectivity is isotropic and there is no explicit distinction between simple and complex cells with regard to the connectivity profile. The latter model differs from the former in that the connections from excitatory to inhibitory cells are not primarily local short-range but rather in rings of mid-range connections. This connectivity scheme was adopted due to its important role in the centre-surround suppression, something that was not addressed in either of the mentioned models. The ring shaped connectivity leads to higher transfer of inhibition between centre and surround. Thus, the influence of the surround on the centre activity increases. However, the number of connections used by Oliveira and Roque [160] was adapted to match recent anatomical data on cortical connectivity [17].

With regard to the design principles mentioned above, the presented model also extends the two existent models of Zhu et al. [232] and of Oliveira and Roque [160]. The

neuron models used here are structurally and dynamically more complex than in the previous models, which use integrate-and-fire point neurons and simpler multi-compartment HH-type neurons, respectively. In comparison with the integrate-and-fire point neurons, the neuron model used here has the advantage of having biophysically meaningful parameters and is thus more strongly constraint by experimental data. In comparison with the simpler HH-type neurons, the inclusion of more active ion channels allows for more realistic neuronal dynamics and a better extensibility of the neurons. Furthermore, the use of *neuroConstruct* and thus the possibility to generate code for different simulator systems, as well as a simulator-independent description, makes it possible to exchange the model between different research groups, simplifying result replication and validation. What is more, it is uncomplicated to exchange the neuron model used in this network within the *neuroConstruct* environment allowing for both the incorporation of more anatomical or electrophysiological details, and the incorporation of more abstract neuron models.

6.2. Methods

6.2.1. A Detailed Multi-Compartment Neural Network Model of the Primary Visual Cortex

6.2.1.1. Single Cell Models

Two different types of neurons were implemented in the model: an excitatory spiny stellate cell, typically found in layer 4 of V1, and an inhibitory basket cell, found throughout all layers of V1. The spiny stellate neuron was chosen because layer 4 serves as a first cortical stage of visual information processing [132]. So, strictly speaking, the present model represents the input layer of V1. The basket cell was chosen because it is the predominant inhibitory interneuron in V1 [46]. Both single neuron models are multi-compartment HH-type with twelve and eight compartments, respectively. Figure 6.1 shows a schematic depiction of the two neuron models.

Ion Channels All model neurons were equipped with a set of 11 active ion channels, as implemented in the *neuroConstruct* model of Traub et al. [209] (developed in [208] and [50]). These ion channels were chosen over other types [e.g. 160] since they represent a generic set, which is found throughout cortex, and they allow for a wide variety of different firing behaviours [209], thus making the single cell models easily generalisable.

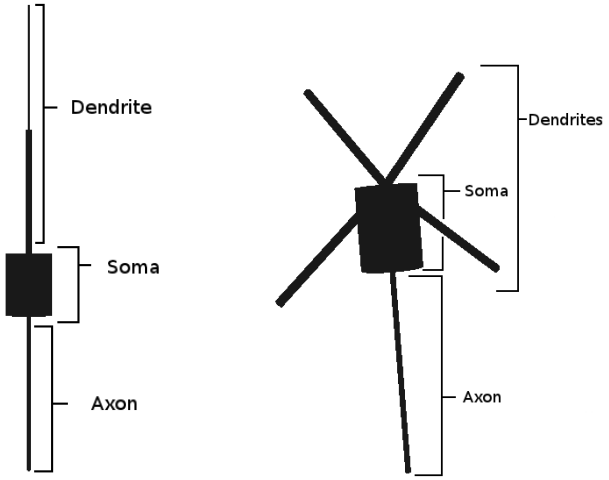

(a) (b)

Figure 6.1.: Schematic view of the two model neurons. (a) The inhibitory basket cell consisted of eight compartments in total, divided into two somatic, four dendritic and two axonal compartments. NMDA receptors target soma and dendrites. (b) The excitatory spiny stellate cell consisted of 12 compartments in total, divided into two somatic, eight dendritic and two axonal compartments. AMPA and GABA receptors target soma and dendrites.

These 11 active conductances were the following:

1. Sodium conductances
   - Fast, transient sodium ($g_{Na(F)}$)
   - Persistent sodium ($g_{Na(P)}$)
2. Potassium conductances
   - Delayed rectifier potassium ($g_{K(DR)}$)
   - Transient, inactivating A-type potassium ($g_{K(A)}$)
   - Slow after-hyper-polarising potassium ($g_{K(AHP)}$)
   - Fast voltage- and calcium-dependent potassium ($g_{K(C)}$)
   - M-type potassium ($g_{K(M)}$)
3. Calcium conductances
   - High-threshold calcium ($g_{Ca(T)}$)
   - Low-threshold calcium ($g_{Ca(L)}$)

4. Mixed conductances
    - Anomalous rectifier conductance (g_{AR})

Electrotonic Parameters and Reversal Potentials The membrane resistivities for the soma and the dendrites were 50,000 Ω/cm^2 and 25,000 Ω/cm^2 for spiny stellate neurons and basket cells, respectively. Axonal membrane resistivity was smaller, with 1,000 Ω/cm^2 for both cell types. Internal resistivity was also the same for soma and dendrites, and was set to 250 Ω/cm and 200 Ω/cm for spiny stellate neurons and basket cells, respectively. Again, internal resistivity was lower for the axons and set to 100 Ω/cm in both cell types [209]. The reversal potentials for the different ionic conductances are summarised in table 6.1.

Spiny Stellate Neurons Layer 4 spiny stellate cells were modelled to be regular spiking (RS) neurons with spike frequency adaptation, although some of these neurons may have intrinsic bursting (IB) properties [47]. Nevertheless, the majority of spiny stellate neurons in layer 4 are RS [14]. Firing rate adaptation was achieved by an adjustment of the muscarinic K_M and the afterhyperpolarising K_{AHP} current. Table 6.2 shows the membrane conductance densities for the spiny stellate neuron in soma, dendrite and axon compartments.

Basket Cell The basket cell was chosen as the model cortical inhibitory neuron because it represents the predominant interneuron type found in layer 4 [46]. These cells show so-called fast spiking (FS) behaviour, that is, basket cells respond to an activating input with a very regular high frequency train of spikes [47]. Table 6.3 shows the membrane conductance densities for the basket cells in soma, dendrite and axon compartments.

Table 6.1.: Reversal Potentials for the different ions: sodium (Na), calcium (Ca), potassium (K), as well as the anomalous rectifier (AR) and the leakage (L).

	V_{Na}	V_{Ca}	V_L	V_{AR}	V_K
Reversal Potential (mV)	50	125	-65 (basket cells) -70 (spiny stellate cells)	-40	-100

Table 6.2.: Membrane conductance densities for the RS spiny stellate neuron (mS/cm^2).

	$g_{Na(F)}$	$g_{Na(P)}$	$g_{K(DR)}$	$g_{K(C)}$	$g_{K(A)}$	$g_{K(M)}$	g_{K2}
Soma	562.5	0.15	375.0	40.0	65.0	4.5	0
Dendrites	28.125	0.075	281.25	40.0	65.0	0.45	0
Axon	1500.0	0.4	1500.0	0	4.33	0	0

	$g_{K(AHP)}$	$g_{Ca(L)}$	$g_{Ca(T)}$	g_{AR}
Soma	0.575	0.5	0.1	0.05
Dendrites	0.575	0.5	0.1	0.05
Axon	0	0	0	0

Table 6.3.: Membrane conductance densities for the FS basket cell (mS/cm^2).

	$g_{Na(F)}$	$g_{Na(P)}$	$g_{K(DR)}$	$g_{K(C)}$	$g_{K(A)}$	$g_{K(M)}$	g_{K2}
Soma	65.0	0	1100.0	71.2	0.6	0	0
Dendrites	65.0	0	1105.0	71.2	0.6	0	0
Axon	390.0	0	275.0	0.6	4.33	0	0

	$g_{K(AHP)}$	$g_{Ca(L)}$	$g_{Ca(T)}$	g_{AR}
Soma	0	0.1	0	0
Dendrites	0	0.1	0	0
Axon	0	0	0	0

6.2.1.2. Network Structure and Synaptic Connections

Network Architecture The network model consisted of $N_e = 1024$ excitatory spiny stellate neurons and $N_i = 256$ inhibitory basket cells arranged in a two-dimensional grid (see Figure 6.2), corresponding to the anatomically found 4:1 ratio of excitatory to inhibitory cells [17]. A visualisation of the three-dimensional network is shown in Figure 6.3 and a visualisation of different states of network activity can be found in Figure 6.4. Excitatory cells connected to other excitatory cells in their first, second and third surrounding rings via α-Amino-3-hydroxy-5-methyl-4-isoxazolepropionic acid (AMPA) synapses, and to inhibitory cells in their third, fourth and fifth surrounding rings via N-Methyl-D-aspartic acid (NMDA) synapses. Inhibitory cells connected to excitatory cells in their first, second, third and fourth surrounding rings via γ-Amino-butyric acid synapses of type A ($GABA_A$). The probability of a connection depended on the distance of the post-synaptic cell from the pre-synaptic cell. For further reference, the number of excitatory-to-excitatory connections shall be denoted with n_{ee}, the number of excitatory-to-inhibitory connections with n_{ei} and the number of inhibitory-to-excitatory connections with n_{ie} and their respective weights with w_{ee}, w_{ei} and w_{ie}. The number of connections for each type of cell was chosen to match the experimental data presented in [17].

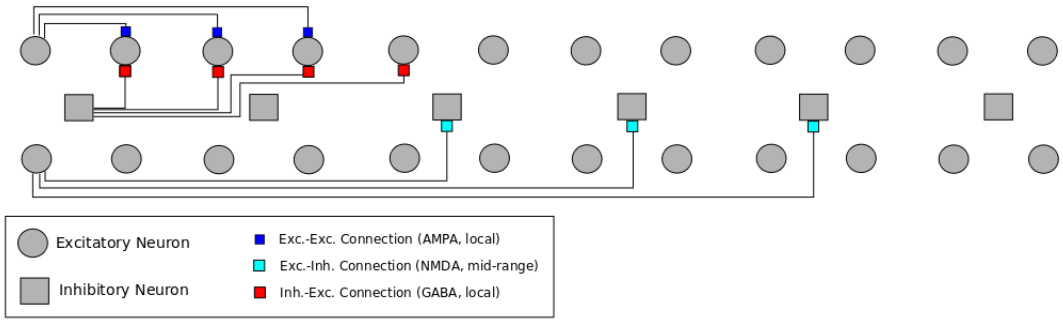

Figure 6.2.: 2-D network structure. Excitatory spiny stellate and inhibitory basket cells are arranged in a regular two-dimensional grid with the basket cells placed in between the spiny stellate neurons. Connectivity ranges are illustrated for all three different types of connections: excitatory-to-excitatory (blue), excitatory-to-inhibitory (cyan) and inhibitory-to-inhibitory (red).

Synaptic Connections Spiny stellate neurons are excitatory and glutamatergic, thus activate AMPA and NMDA receptors on post-synaptic cells. Basket cells are inhibitory interneurons and therefore activate $GABA_A$ synapses. Activation of $GABA_B$ receptors was not modelled here.

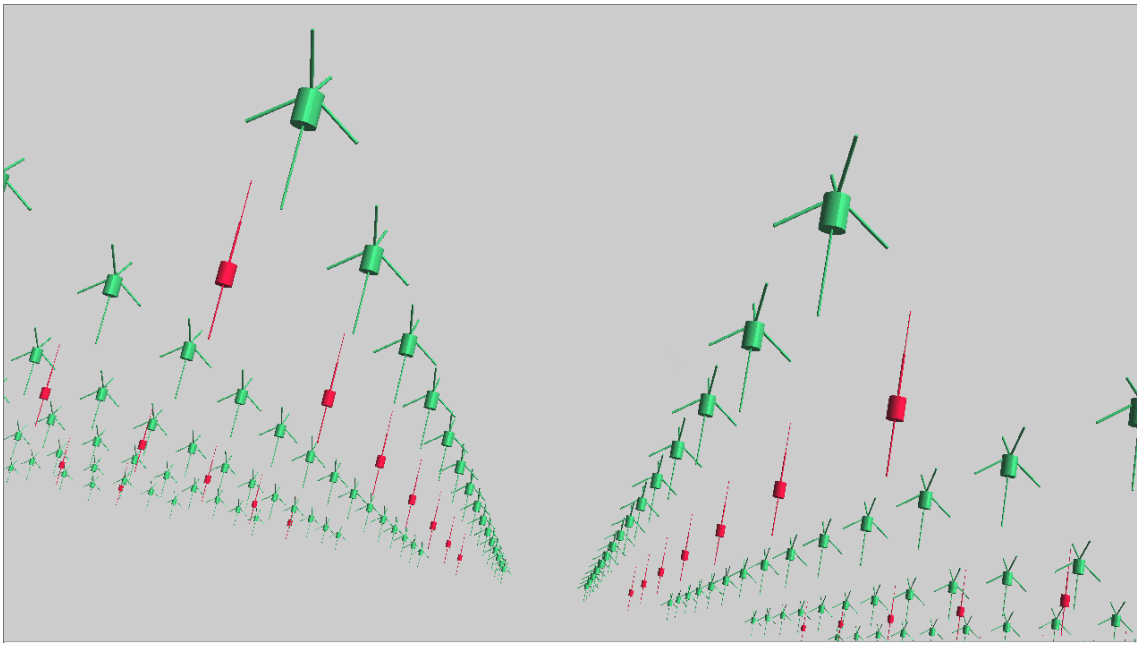

Figure 6.3.: Visualisation of the network: arrangement of excitatory (green) and inhibitory (red) neurons.

Synapses were taken from *neuroConstruct* and were generally modelled as double exponential functions, where the synaptic conductance g followed

$$g(t) = \text{max_cond} \cdot A \cdot (e^{-\frac{t}{\tau_{decay}}} - e^{-\frac{t}{\tau_{rise}}})$$

with the normalisation factor A given by

$$A = e^{-\frac{\tau_{peak}}{\tau_{decay}}} - e^{-\frac{\tau_{peak}}{\tau_{rise}}}$$

and the time τ_{peak} to reach the maximum conductance max_cond given by

$$\tau_{peak} = \frac{\tau_{decay} \cdot \tau_{rise}}{\tau_{decay} - \tau_{rise}} \cdot \ln\left(\frac{\tau_{decay}}{\tau_{rise}}\right).$$

Here, τ_{rise} and τ_{decay} were the time constants for the rise and the decay of the synaptic conductance, respectively.

AMPA receptor kinetics were modelled with a maximum conductance $max_cond = 0.18393972 \cdot 10^{-6}\ mS$ and time constants $\tau_{rise} = 2\ ms = \tau_{decay}$ for connections within the population of excitatory spiny stellate neurons, as provided within the *neuroConstruct* simulation environment.

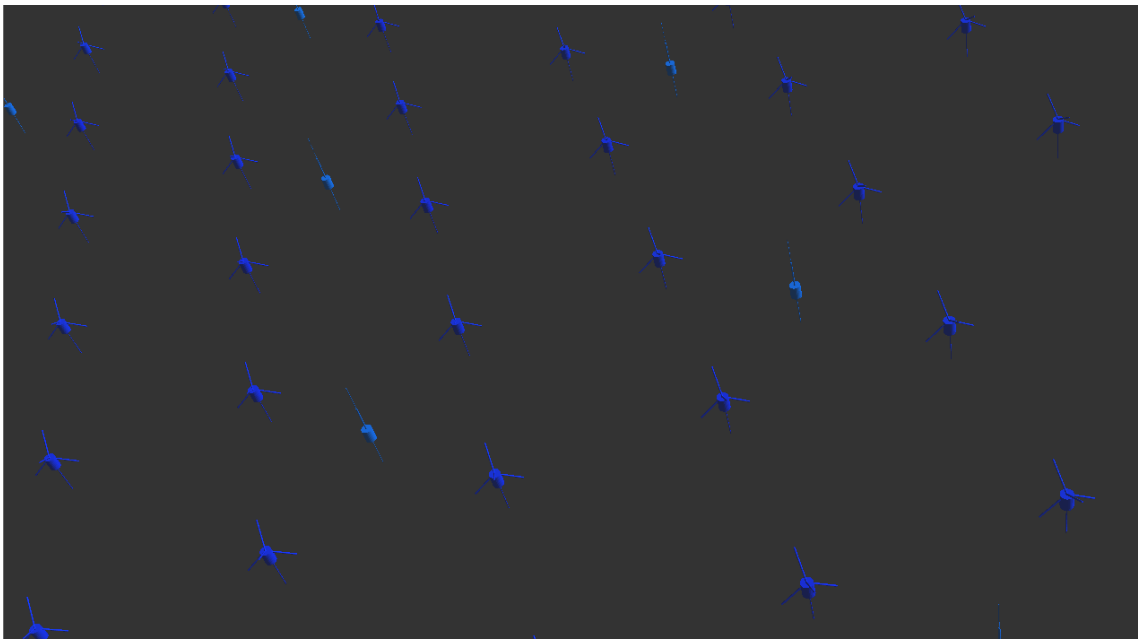

(a)

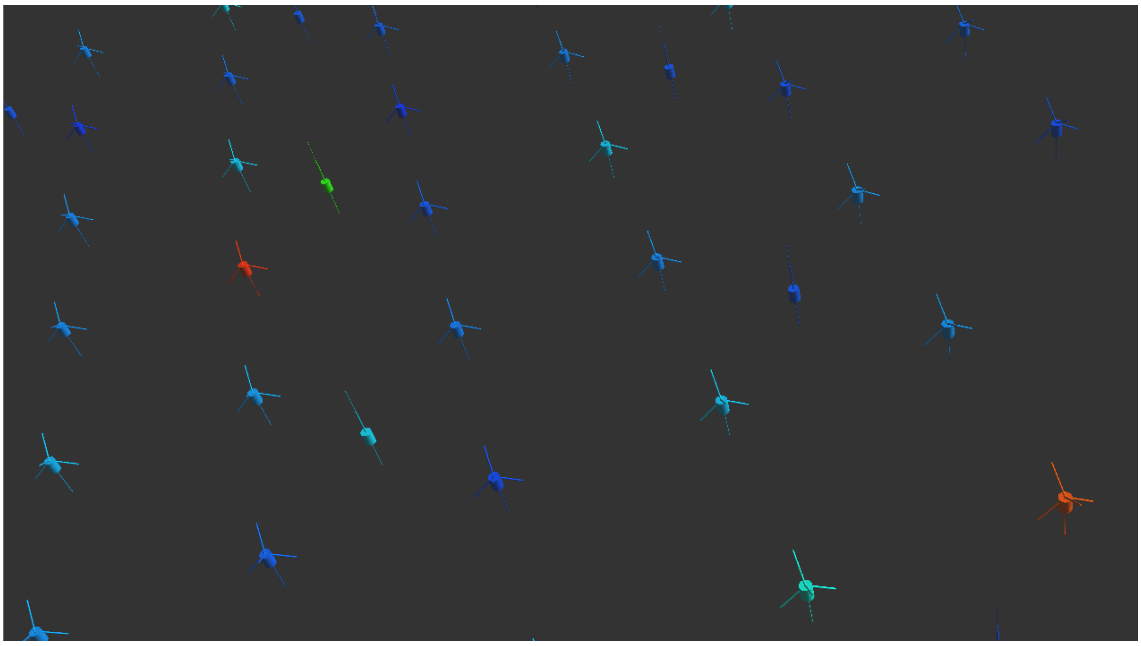

(b)

Figure 6.4.: Visualisation of the network in (a) inactive and (b) active states (membrane potential is colour coded: blue=-90 mV to red=+40 mV).

GABA$_A$ synapses were modelled as single exponentials, which can be obtained with the above-mentioned formulas by formally setting the rise time $\tau_{rise} = 0\ ms$, that is cancelling the second exponential term. As provided within *neuroConstruct*, maximum conductance was set to $max_cond = 1.04 \cdot 10^{-5}\ mS$ and the decay time constant was $\tau_{decay} = 8\ ms$.

NMDA receptor kinetics were modelled according to Maex et al.[134], together with the parameters provided with the *neuroConstruct* package. Importantly, the time constants for rise and decay were chosen to be $1\ ms$ and $133.33\ ms$, respectively.

6.2.1.3. Input Modelling

Sensory Input The thalamic processing of the input gratings was performed by virtual LGN units (arranged in a 44×44 regular grid) and choosing elongated receptive fields within these LGN units for every V1 neuron. The works of Zhu et al.[231] and Tao et al. [204] were followed closely with respective numbers scaled to fit the network size of the model.

Specifically, 4×4 clusters were constructed, having receptive fields with the same width, that is, either one, two or four. These clusters were randomly distributed across the network. As in Zhu et al. [231], one-sixth of the V1 cells had width one, one third had width two and one half had width four. Furthermore, receptive fields were randomly chosen to have even or odd symmetry, that is, to have ON-OFF-ON/OFF-ON-OFF subregions or ON-OFF/OFF-ON subregions (see Figure 6.5).

The preferred orientation of a given neuron determined the axis along which the receptive field of the neuron was aligned. This preferred orientation (between 0° and 180°) was drawn from an artificial orientation map, similar to those previously used [204, 223, 231]. Having assigned an array of LGN cells as ON- and OFF-input for each V1 neuron, as well as a preferred orientation, the input to one V1 neuron was calculated as follows [231]:

$$R_k^{\pm}(t) = \left[R_B \pm \int_0^t ds \int_{\mathbb{R}^2} dx G(t-s) A(|x_k - x|) I(x,s) \right]^+, \tag{6.1}$$

where $\pm$ stood for ON and OFF, respectively. $[\ldots]^+$ stood for rectification, to wit, if R was below zero, it was set to zero. The background firing rate F_B was set to 15 Hz [231]. $I(x,t)$ corresponded to the grey value of the presented grating. The temporal ($G(t)$) and spatial ($A(x)$) kernel of the LGN processing were again taken from Zhu et al. [231] and were as follows:

$$G(t) = \frac{t^5}{\tau_0^6} \left[\exp\left(-\frac{t}{\tau_0}\right) - \left(\frac{\tau_0}{\tau_1}\right)^6 \exp\left(-\frac{t}{\tau_1}\right) \right], \tag{6.2}$$

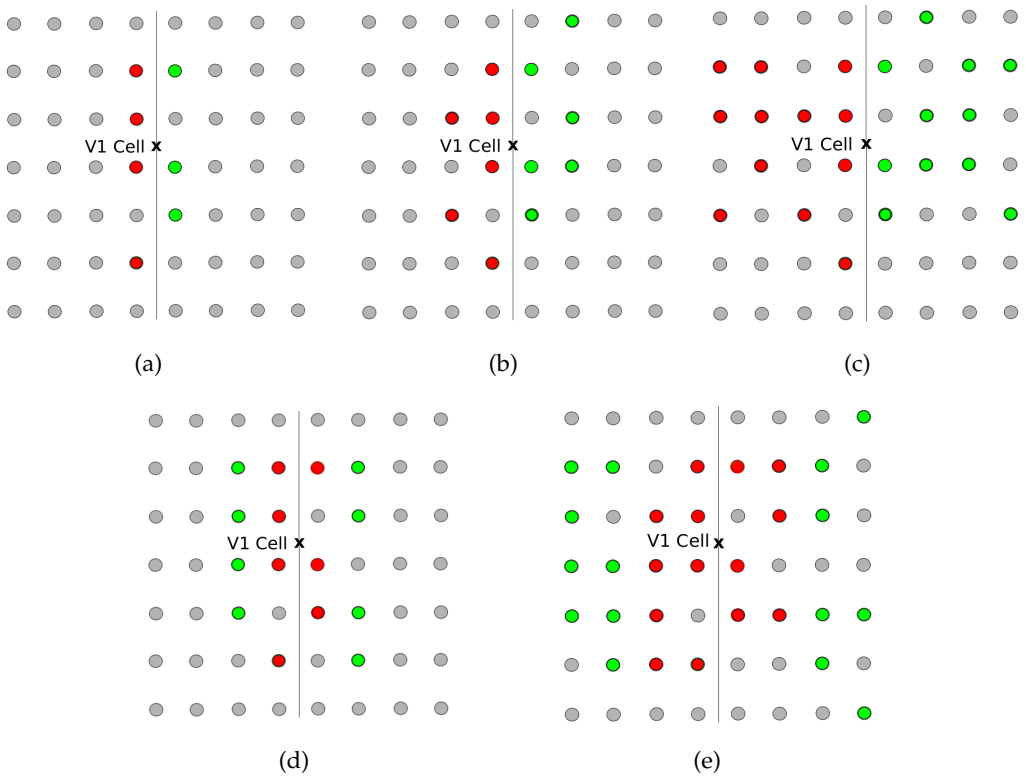

Figure 6.5.: Examples illustrating the various receptive field configurations for the V1 cells: (a) width=1 (b) width=2 and symmetry=odd (c) width=4 and symmetry=odd (d) width=2 and symmetry=even (e) width=4 and symmetry=even. The V1 cell is depicted by a black cross and the black line shows the main axis of the elongated receptive field. Green and red circles represent LGN cells contributing to the receptive field in ON and OFF blocks, respectively. The cells' orientation selectivity was approximately orthogonal to the main axis of its receptive field. The width of the receptive field strongly influenced the spatial frequency preference of the cell.

$$A(x) = \frac{a}{\pi\sigma_a^2}\exp\left(-\left|\frac{x}{\sigma_a}\right|^2\right) - \frac{b}{\pi\sigma_b^2}\exp\left(-\left|\frac{x}{\sigma_b}\right|^2\right). \tag{6.3}$$

The constants $\tau_0 = 3\ ms$, $\tau_1 = 5\ ms$, $\sigma_a = 0.066$, $\sigma_b = 0.093$, $a = 1.0$, and $b = 0.74$ were chosen as in [231] to reflect experimental data.

Background Noise Background noise was introduced as random spike trains arriving at synapses of both excitatory and inhibitory neurons. The random spike trains were based on a Poisson process with a given rate. The rate was chosen such that the resulting spontaneous firing rate in the network, that is, the firing rate when only the noise input was present, resembled experimentally measured spontaneous activity [75, 174].

6.2.2. Single Neurons - Validation I

The correct functioning of the single neuron models was tested. To this end, current pulses were injected into the soma of each model neuron type and the responses were recorded. A variety of different parameters were calculated, based on Nowak et al. [156], to characterise the neuron's behaviour and were compared to their biological counterparts to validate the models.

Inter-spike Interval Histogram In the classification between bursting and non-bursting neurons, the **inter-spike interval histogram (ISIH)** has proven to be very accurate [156]. As can be expected, non-bursting neurons show a unimodal ISIH, because the time difference between consecutive spikes is roughly similar. In contrast, bursting neurons show bimodal ISIHs: the inter-spike intervals during a burst are very small, whereas the inter-spike interval between two bursts is rather long, resulting in two ISIHs peaks. However, Nowak et al. [156] reported that they could improve the classification by means of the histograms of the logarithmic values of the inter-spike intervals (the **log inter-spike interval histogram, logISIH**). logISIHs show similar distributions as ISIHs for non-bursting and bursting neurons, but the distinction between both types is more apparent for the logISIHs [156]. Therefore, logISIHs was used as a classification parameter for non-bursting/bursting and calculated for all cortical model neurons.

Spike Frequency Adaptation Parameter Non-bursting neurons mainly present two types of firing behaviour: RS and FS. Whereas regular spiking neurons often show an adaptation of spike frequency in response to prolonged stimulation, fast spiking neurons hardly show any adaptation.

The adaptation index $\mathbf{Ada}_{50}$ was calculated in order to quantify the adaptation properties of neurons [156]. It was defined as

$$Ada_{50} = \frac{F_{50}}{F_{100}}, \tag{6.4}$$

where F_{50} was the number of spikes in the first half of the stimulation period and F_{100} the number of spikes in the whole period [156]. Neurons without adaptation have an Ada_{50} of $.5$, whereas neurons with stronger adaptation have an Ada_{50} closer to 1.

Spike Width at Half Height Another parameter that distinguishes between regular and fast spiking cells is the **spike width at half height** [156]. While regular spiking cells have broader spikes, fast spiking neurons usually show much narrower spikes and thus have a lower spike width at half height [156]. In the model at hand, **spike width** was computed for different strengths of stimulation currents and averaged over several action potentials. **Spike width at half height** was calculated for both cortical model neurons.

f-I Curve The **f-I curve**, which relates the spike rate (total number of spikes per pulse normalised by pulse duration) to the strength of the injected current, is another parameter used to differentiate between fast from RS cells. Whereas the **f-I curve** of FS cells shows a steep slope, RS cells mostly display far less steep **f-I curves** [156]. In the current model, the slope of a linear regression to the curve was used as a measure for the current frequency relationship of the model neuron.

6.2.3. Classical Receptive Field Properties of Network Model Neurons - Validation II

The first validation section covered essential but basic functions of single cell models. This section goes one step further and contains the main part of the validation of the network model.

The validation of the network model covers a variety of features, which are essential for a model of V1 and which highly discriminate this model from models of other cortical areas. The features investigated in detail are well-known features of V1 neurons, to wit, simple and complex cells, orientation and direction selectivity, spatial frequency selectivity, and temporal frequency selectivity. The simulated results were compared to experimental data as well as simulated data from other models. The network parameters, namely the number of the synaptic connections and their weights, were varied so that the responses best fit the experimental data. This issue is essential, since the model

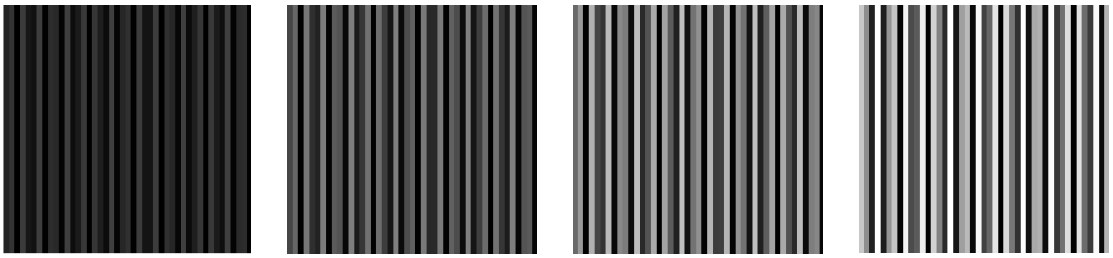

(a) (b) (c) (d)

Figure 6.6.: Sinusoidal grating with an orientation of $0°$ and a spatial frequency of $2\frac{3}{2}c/deg$ at a contrast of (a) $.25$ (b) $.50$ (c) $.75$ (d) 1.0.

was tuned to show these features, so that these are not results from the model, strictly speaking, but a validation step. In contrast, the results presented subsequently on centre-surround suppression and on the influence of different aspects of recurrent inhibition, were obtained with fixed parameters and hence show features resulting from the model, which predict how the visual system should behave, if the model's assumptions hold. These predictions can be used to test the presented model and to explain the mechanism behind the predictions.

In all analyses of receptive field properties, all cells showing a maximum response of less than 8 Hz throughout the stimulations were excluded from further analysis, as in empirical studies. This typically led to an exclusion of around 30% of the cells.

6.2.3.1. Simple and Complex Cells

Neurons were divided into **simple** and **complex** cells according to their F1/F0 ratio [195], where F0 was the mean firing rate in response to a drifting sinusoidal grating with optimal parameters, and F1 was the first harmonic. A cell was classified as simple if $F1/F0 \geq 1$ and as complex if $F1/F0 < 1$.

6.2.3.2. Orientation and Direction Selectivity

The network was stimulated with sinusoidal gratings of different orientations of movement, ranging from 0° to 330° in steps of 30°, to measure the neurons' preference for a specific orientation and direction.

The preference for a specific orientation can then be expressed by the **orientation reaction index (ORI)**

$$ORI = \frac{(max - orth)}{max}, \tag{6.5}$$

where *max* was the response to the optimal orientation, that is, the orientation to which the neuron responded strongest, and *orth* the response to the orientation orthogonal to the optimal one [75]. An ORI $\geq .7$ was considered to characterise an orientation selectivity, whereas $.5 \leq$ ORI $< .7$ was considered to characterise an orientation bias [75]. Note that sometimes the ratio between *orth* and *max* is reported in experimental studies, although this is merely $1 - ORI$.

Another parameter that has been proposed to characterise orientation selectivity is the **circular variance (CV)** [135]. To calculate this, the spike rate responses $r(\theta_i)$, $(i = 1, \ldots, 12)$, were obtained and then the CV was defined as

$$CV = \frac{|\sum_0^{2\pi} r(\theta_i) \exp(2i\theta_i)|}{\sum_0^{2\pi} r}. \tag{6.6}$$

A cell with high selectivity has a CV around 0, whereas a cell without preference has a CV$= 1$ [232]. CV and ORI are highly correlated measures. Still, both were computed in order to be able to compare the results to different experimental and modelling studies.

ORI and CV give global measures of orientation preference. Additionally, the **orientation tuning bandwidth (OBW)** can be used to investigate the local behaviour around the peak and it was calculated as follows

$$OBW = (\theta_{high} - \theta_{low})/2, \tag{6.7}$$

where θ_{high} and θ_{low} were the orientations on both sides of the peak of the linearly interpolated orientation tuning curve, where the response dropped below half the peak response [232].

The preference for a specific direction was measured by the **direction reaction index (DRI)**

$$DRI = \frac{(max - opp)}{max}, \tag{6.8}$$

where *max* was the response to the optimal orientation and *opp* the response to the orientation opposite to the optimal one [75]. Again, if a neuron had a DRI $\geq .7$ it was considered to be direction selective, and for $.5 \leq$ DRI $< .7$ it was considered to have a direction bias.

As argued in Chapter 5, one basic feature of orientation selectivity in V1 neurons is the independence of the contrast of the presented stimuli. Therefore, the oriented gratings were presented with three different levels of contrast $.25$, $.5$ and $.75$, to test contrast-invariance. Examples for a grating at different levels of contrast are shown in Figure 6.6.

Furthermore, it was also tested whether the obtained results were independent from the random choice of the connections and the random choice of the LGN cells contributing to receptive fields. Therefore, the random seeds for both choices were changed and

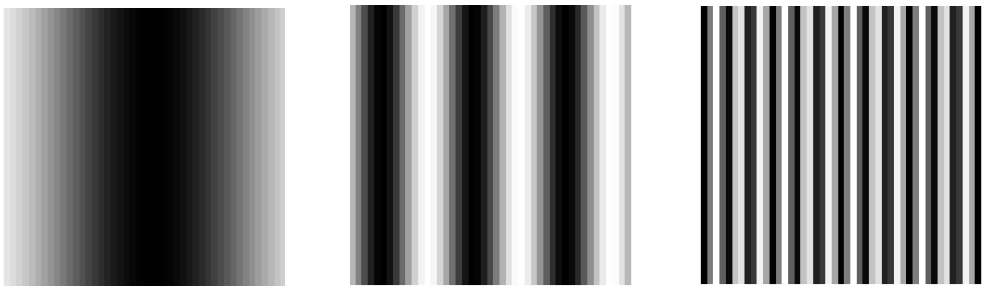

(a) (b) (c)

Figure 6.7.: A sinusoidal input grating with an orientation $0°$, a contrast of 1.0 and a spatial frequency of (a) $0.125c/deg$ (b) $0.5c/deg$ and (c) $2c/deg$.

the orientation selectivity test described above was simulated for the generated seeds. ORI, OBW and CV were computed for these data.

6.2.3.3. Spatial Frequency Selectivity

The spatial tuning of the model neurons within the network was examined using moving sinusoidal gratings with varying spatial frequency (orientation, direction, temporal frequency, grating size and contrast stayed fixed) as shown in Figure 6.7.

A total of 17 spatial frequencies were tested ranging from $2^{-4} = 1/16\ c/deg$ to $2^4 = 16\ c/deg$ in logarithmic steps of one-half order of magnitude. Two measures to describe the spatial frequency tuning properties of the cells were calculated: as a local measure, the **spatial frequency tuning bandwidth** (SBW), and as a global measure, the **low spatial frequency variance** (LSFV) [224, 231]. A difference of Gaussians (DoG) was first fitted for both measures:

$$R(r) = r_0 + k_1 e^{\left(-\frac{(r-\mu_1)^2}{2\sigma_1^2}\right)} - k_2 e^{\left(-\frac{(r-\mu_2)^2}{2\sigma_2^2}\right)} \tag{6.9}$$

to the spike responses r, where all parameters were kept free [182, 224, 232].

The SBW was defined, similarly to the case of orientation tuning curves, as

$$SBW = \log_2(sf_{high}) - \log_2(sf_{low}), \tag{6.10}$$

where again sf_{high} and sf_{low} were the spatial frequencies around the peak, where the response dropped below half the peak response in the fitted response function.

Following Zhu et al. [232], the LSFV was computed using the following equation,

introduced by Xing et al. [224],

$$LSFV = \frac{\sum_{sf_{opt/16}}^{sf_{opt}} r(sf)(log_{16}(sf) - log_{16}(sf_{opt}))^2}{\sum_{sf_{opt/16}}^{sf_{opt}} r(sf)}. \tag{6.11}$$

The LSFV is close to 0 for highly selective cells, whereas it is approximately $.3$ for non-selective, low-pass cells. LSFV shows a high correlation with another measure of low spatial frequency attenuation: the low spatial frequency suppression ratio (LSFSR), which is the ratio between the response at the lowest spatial frequency and the response at the optimal spatial frequency [e.g. 224]. However, the LSFV takes into account all data of the lower limb of the tuning function, whereas the LSFSR only relies on two values and thus does not fully reflect the attenuation at low frequencies. Therefore, only the LSFV was calculated for the spatial frequency tuning data.

6.2.3.4. Temporal Selectivity

The temporal tuning properties of the network neurons was investigated using moving sinusoidal gratings with varying temporal frequency (orientation, direction, spatial frequency, grating size and contrast stayed fixed). A range of 15 temporal frequencies between 1-15 Hz in steps of 1 Hz was tested.

6.2.3.5. Contrast Response

Another important issue in the validation of the network model was the cells' contrast response, since centre-surround suppression was later investigated for different levels of contrast.

Moving sinusoidal gratings of varying contrasts were used and the contrast response functions of the single cells were calculated and then compared to experimental data. Centred gratings of size 10×10 cells with standard orientation ($0°$), spatial frequency ($2^{3/2}$ c/deg) and temporal frequency (3 Hz) were used at four different levels of contrast, namely $.1$, $.2$, $.4$ and $.8$ (as in [226]).

The responses $R(C)$, where $C \in \{.1, .2, .4, .8\}$ represented the level of contrast, were normalised so that the maximum response equalled 1. This normalisation allowed for a better comparability to physiological and psychophysical data. A standard contrast response function:

$$R(C) = \frac{k \cdot C^p}{(1 + a \cdot C^q)}, \tag{6.12}$$

Table 6.4.: Summary of the different parameter sets for the sinusoidal gratings used to test the classical receptive field property stimuli.

	Orientation	Spatial Frequ.	Temporal Frequ.	Contrast	Size
Orientation & Direction Sel. Test	$0°$ - $330°$ 12 steps	fixed at $2^{3/2}\ c/deg$	fixed at $3\ Hz$	1.0	44×44
Spatial Frequency Sel. Test	fixed at $0°$	2^{-4} - $2^{4}\ c/deg$ 17 logarithmic steps of $\sqrt{2}$	fixed at $3\ Hz$	1.0	44×44
Temporal Frequency Sel. Test	fixed at $0°$	fixed at $2^{3/2}\ c/deg$	1-15 Hz 15 steps	1.0	44×44
Contrast Dependence Test	$0°$ - $330°$ 12 steps	fixed at $2^{3/2}\ c/deg$	fixed at $3\ Hz$	$.25 - .75$ 3 steps	44×44

was fitted, where the parameters k, a, p and q were chosen within the ranges reported in physiological and psychophysical studies (see [68, 226]). Boynton et al. proposed a different contrast response function given by

$$R(C) = \frac{c \cdot C^{x+y}}{(C^y + \cdot \sigma^y)}, \tag{6.13}$$

However, as Figure 6.8 shows, both functions are very similar for parameter ranges used in these studies. The ranges are summarised in Table 6.5. This permitted direct comparison between model and experimental data.

6.2.4. Neural Centre-Surround Suppression

After a thorough validation of the network model as described in the previous sections, all model parameters were subsequently fixed in order to explore the emerging centre-surround interactions.

6.2.4.1. Centre-Surround Suppression for Sinusoidal Gratings

The centre-surround suppression properties emerging in response to drifting sinusoidal gratings were explored here. To this end, a moving sinusoidal grating of varying con-

Table 6.5.: Parameter ranges used for the fitting of the contrast response function in 6.12 to the contrast responses. Ranges were taken from physiological and psychophysical studies [68, 226].

Parameter	Range
k	0.5-2
a	0.005-0.05
p	2.2-2.6
q	1.6-2.2

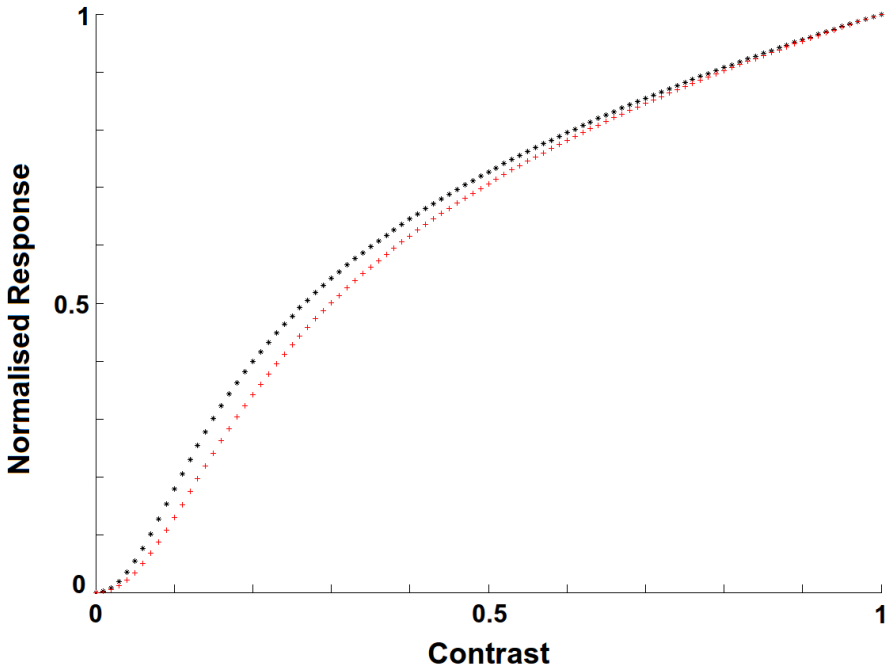

Figure 6.8.: Standard contrast response functions from Equations 6.12 (red) and 6.13 (black). Both are expansive for low contrasts and saturate for higher contrasts. (Parameters: $k = 1$, $a = 0.01$, $p = 2.3$ and $q = 1.9$ for Equation 6.12; $c = 1$, $x = 0.4$, $y = 1.9$ and $\sigma = 0.15$ for Equation 6.13.)

trast ($.1, .2, .4$ and $.8$) and fixed orientation ($0°$), spatial frequency ($2^{3/2}$) and temporal frequency (3 Hz) was presented, to a centred patch of size 10×10 cells. In the surround, an additional drifting sinusoidal grating was presented with the same parameters as the centre grating except for the contrast. The surround grating could have either a low ($.2$ or $.4$) or a high contrast value ($.8$ or $.95$). An additional baseline condition with only the centre patches at the four different contrasts was also acquired. The **suppression index (SI)** for each cell was calculated to quantify the suppression effect:

$$SI = \frac{R_{surround}}{R_{baseline}}, \tag{6.14}$$

where $R_{surround}$ was the firing rate at a certain surround contrast, and $R_{baseline}$ was the firing rate at the same centre contrast but without a surround grating. An SI< 1 indicated suppression whereas, an SI> 1 indicated facilitation.

However, suppression indices were only calculated for a small fraction of the network population. The reason for this was twofold. In the first place, since the main interest lay in centre-surround suppression, only a centre patch of 8×8 cells was selected, because their respective receptive fields lay entirely within the centre grating. This meant that centre-surround effects were only observed for those cells, whereas all others neurons covered parts of the surround grating with their receptive fields and thus did not qualify for the study of centre-surround effects. In the second, since the orientation of the gratings was fixed at $0°$, only cells that lay in a 4×4 region around $0°$ of the artificial orientation map (from which the orientation preference was drawn) were included in the final analysis. This ensured that the orientation of the grating was close to the preferred orientation of the cell.

Summarising, 20 simulations (four baseline simulations at contrasts of $.1, .2, .4$ and $.8$; $16 = 4 \times 4$ surround simulations, for each centre contrast of $.1, .2, .4$ and $.8$, and every surround contrast of $.2, .4, .8$ and $.95$) were performed and, for each surround simulation, suppression indices were acquired for the above-mentioned 4×4 region.

6.2.4.2. Centre-Surround Suppression for Contrast Texture Patterns

Furthermore, in order to compare the behaviour of the model with the experimental data from the study presented in Chapter 7, contrast texture patterns as those used in psychophysical measurements were used here [e.g. 43, 51]. Centre-only texture patterns were used as depicted in Figure 6.9 (b) and (c), the contrast of the patterns was varied, starting from $.05$ going up to $.6$ in steps of 0.025. Additionally, centre-surround texture patterns (Figure 6.9 (a)) with a fixed centre contrast of $.4$ and a fixed surround contrast of $.95$ were

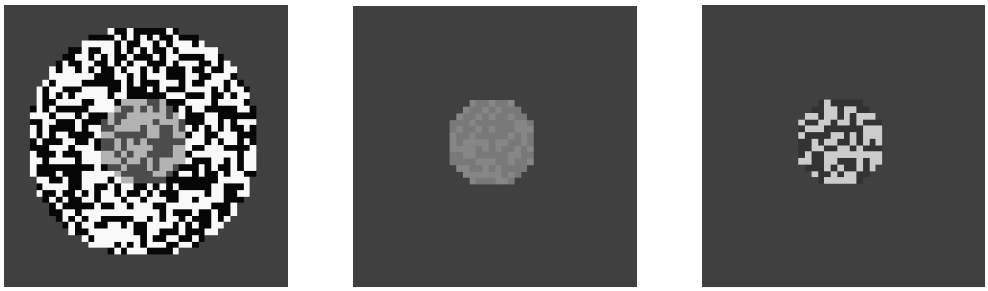

(a) (b) (c)

Figure 6.9.: Example centre-surround and centre-only contrast texture pattern stimuli. (a) Centre-surround stimulus with a centre contrast of $.4$ and surround contrast of $.95$. (b)+(c) Centre-only stimuli with a contrast of $.05$ and $.6$, respectively.

presented in two conditions: a small surround condition, where the surround region was six times larger than the centre region, which encompassed a circle with a diameter of six cells, and a large surround condition, where the surround region was seven times larger. These ratios of surround sizes to centre sizes matched psychophysical experiments [51]. The texture patterns consisted of dark and bright regions, where the dark regions and the bright regions had one specific grey value each, giving the texture a certain contrast. The average intensity, however, was always constant regardless of the contrast of the texture pattern, thus guaranteeing that global intensity differences did not confound the responses.

Here, again, a typical contrast response function was first fitted to the responses of individual neurons, given by

$$R(C) = \frac{k \cdot C^p}{(1 + a \cdot C^q)}, \tag{6.15}$$

where R was the firing rate, k a constant and a, p and q were free parameters. From this fitted response function, the predicted firing rate at $C = .4$ was calculated and compared to the actual values in the two surround conditions ('large' and 'small'). Furthermore, the fitted response function was used in order to compute the contrast C_m at which the predicted response equalled the actual response in each of the two conditions. These contrasts were termed **matching contrasts** for the 'large surround condition' and the 'small surround condition', respectively.

6.2.5. Mechanisms of Emergent Classical Receptive Field Properties

The issues of how strongly the feature selectivity in the model depended on lateral inhibition (i.e. recurrent activity) and how strongly it depended on input tuning (i.e. feed-forward projection) were also of importance. Due to the computational complexity of the model, analysis was restricted to the most important case: orientation selectivity.

In order to calculate the tuning of the input arriving at one excitatory cell, the rate r was calculated from the rates of all LGN cells contributing to this cells receptive field, either ON or OFF. However, adding biophysically detailed models of the LGN cells to the network would have substantially increased the computational complexity and was therefore beyond the scope of this work. Hence, the rate r was translated into spike trains using a simple inhomogeneous Poisson process. A spike train with this time-varying rate $r(t)$ as a firing rate was then simulated by using an inhomogeneous Poisson process $\lambda(t)$. The inhomogeneous Poisson process with time-dependent rate $r(t)$ was implemented by simulating a homogeneous Poisson process $\lambda^\star(t)$ of rate r_{max} with

$$r_{max} = \max_t r(t), \tag{6.16}$$

that is, the maximum rate over time t. Having simulated this homogeneous Poisson process $\lambda^\star(t)$, a spike train with a constant instantaneous firing rate r_{max} was obtained. A spike in this spike train occurring at time t was then accepted with the probability $p(t) = \lambda(t)/\lambda^\star(t)$. This resulted in an inhomogeneous Poisson process with a time-dependent rate $r(t)$, a procedure called the **thinning algorithm** [125]. Having constructed spike trains based on the LGN input received by one cell, the same measures for orientation selectivity could be calculated as for the excitatory cell output spike trains. This allowed for the comparison of orientation tuning before and after recurrent network activity.

Additionally, the influence of the two different types of network inhibition was investigated: feed-forward and feed-back inhibition. The effect of feed-forward inhibition, namely the inhibition triggered by the LGN input to inhibitory neurons, only depended on the weight of inhibitory connections onto excitatory cells. The effect of feed-back inhibition, that is, the inhibition caused by the activation of inhibitory neurons by lateral connections from excitatory neurons, also depended on the weight of the connections from these excitatory cells onto the inhibitory neurons. These different kinds of inhibition were disentangled by varying the weights of both types of connections. Firstly, the weight w_{ie} of inhibitory neurons on excitatory cells was varied, using the values 0.1, 0.2, 0.3, 0.4 and 0.5. The simulations described in Section 6.2.3.2 to test the orientation selectivity of the network cells were repeated. Secondly, the weight w_{ei} of excitatory neurons on inhibitory cells was varied using the values 0.005, 0.01, 0.02, 0.05 and 0.1. The simu-

lations described in Section 6.2.3.2 were then repeated with these changed parameters to test the orientation selectivity of the network cells. Furthermore, the tuning properties of the inhibitory cells were calculated analogously to the case of excitatory neurons.

6.2.6. The Role of Recurrent Inhibition in Classical Receptive Field Properties and Centre-Surround Suppression

To explore the role of recurrent inhibition in classical receptive field properties and centre-surround suppression, different parameters governing recurrent inhibition were systematically varied. Essentially, seven parameters governed the amount of inhibition excitatory cells received in the network model:

1. The weight w_{ie} of inhibitory connections to excitatory cells
2. The weight w_{ei} of excitatory connections to inhibitory cells
3. The number N_i of inhibitory cells
4. The number n_{ie} of inhibitory connections to excitatory cells
5. The number n_{ei} of excitatory connections to inhibitory cells
6. The time constants τ of the GABA_A synapses, that is, the inhibitory synapses on excitatory cells
7. The time constants η of the NMDA synapses, that is, the excitatory synapses on inhibitory cells

Note that, since the weight was multiplied with the maximal conductance in order to calculate the effect on the post-synaptic cell, changing the weight was equivalent to changing the maximal conductance. Furthermore, the NMDA synapse in the model had a long decay time, so that small, physiologically plausible variations thereof were unlikely to have any effect. Therefore, the time constants of the NMDA synapses were not varied.

Otherwise, the above-mentioned parameters were systematically varied to explore their influence on orientation selectivity, as an important CRF property, on contrast response properties and on centre-surround suppression properties (both in response to sinusoidal gratings and contrast texture patterns). The methods used were analogous to those explained in Sections 6.2.3.2, 6.2.3.5, 6.2.4.1 and 6.2.4.2, respectively. However, in the case of orientation selectivity, orientation of the grating was varied at four spatial frequencies and at seven different sizes. The variation of parameters is detailed in Table 6.6.

Table 6.6.: Variations of the six parameters governing inhibition in the network model. The different parameter values tested are shown. Note that in each case only a single parameter was varied while the other parameters were fixed at the standard value.

	Range of Variation	Standard Value
Inhibitory-to-Excitatory Weight w_{ie}	0.1, 0.2, 0.3, 0.4 and 0.5	0.275
Excitatory-to-Inhibitory Weight w_{ei}	0.005, 0.01, 0.02, 0.05 and 0.1	0.01
# Inhibitory Cells N_i	100, 88 and 77 %	100 %=256
# Inhibitory-to-Excitatory Connections n_{ie}	100, 88 and 64 %	100 %=21, 752
# Excitatory-to-Inhibitory Connections n_{ei}	100, 82 and 62 %	100 %=49, 900
Decay Time Constant GABA$_A$ τ	15, 20, 25, 30 and 50 ms	8 ms

6.3. Results [1]

6.3.1. Single Neurons - Validation I

6.3.1.1. Spiny Stellate Neuron

Spiny stellate neurons were modelled to have RS type with frequency adaptation. Figure 6.10 shows the response of a spiny stellate neuron to an injection current of 0.167 nA and 0.333 nA, respectively. The RS behaviour as well as the adaptation of the spike frequency is clearly visible. Moreover, quantitative measures were calculated to categorise the model neurons based on the approach presented in [156]. To this end, 11 simulations were made with varying input currents ranging from 0.1 to 1.1 nA in steps of 0.1 nA. From this data, spike width at half height, the adaptation measure Ada_{50} and the slope of the f-I-curve were calculated (see Section 6.2.2). Table 6.7 summarises the results of the quantitative analysis for the spiny stellate neuron. The average spike width, approximately 0.27 ms, and the gradual slope of the f-I-curve, approximately 104 Hz/nA, fit well with experimental data [156]. The Ada_{50} of approximately .7 showed that the spiny stellate neurons' spike-frequency adaptation was in agreement with experimental values [156].

6.3.1.2. Basket Cell

This cell type has FS firing properties *in vivo*[47]. Figure 6.13 shows the response of a basket cell to an injection of 0.1 nA and 0.3 nA respectively. The fast spiking (FS) behaviour without adaptation was clearly visible. Again, quantitative measures were calculated on

[1] Parts of this section have been published in [146], [147] and [148].

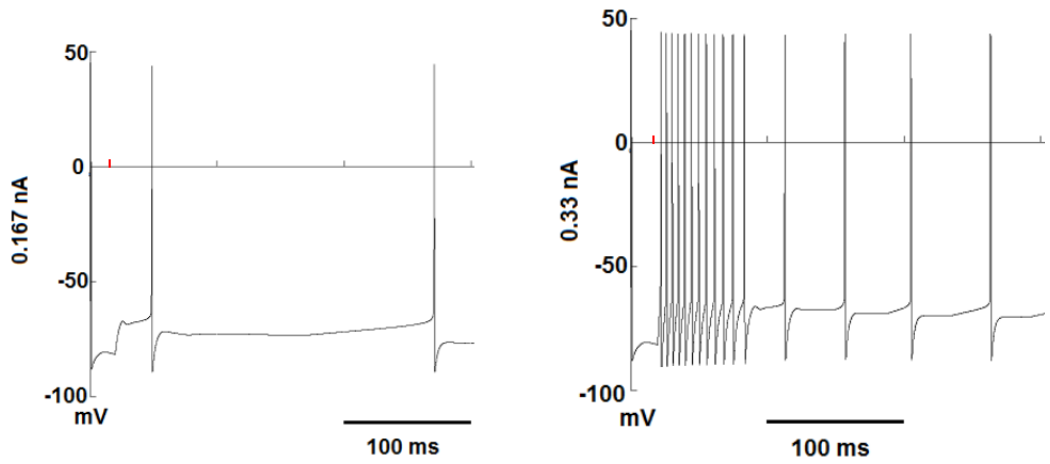

(a) (b)

Figure 6.10.: Firing behaviour of the spiny stellate neurons in layer 4 demonstrating RS behaviour with frequency adaptation. Response of a spiny stellate neuron to somatic input currents of (a) 0.167 nA and (b) 0.333 nA. The onset of the input current is marked in red.

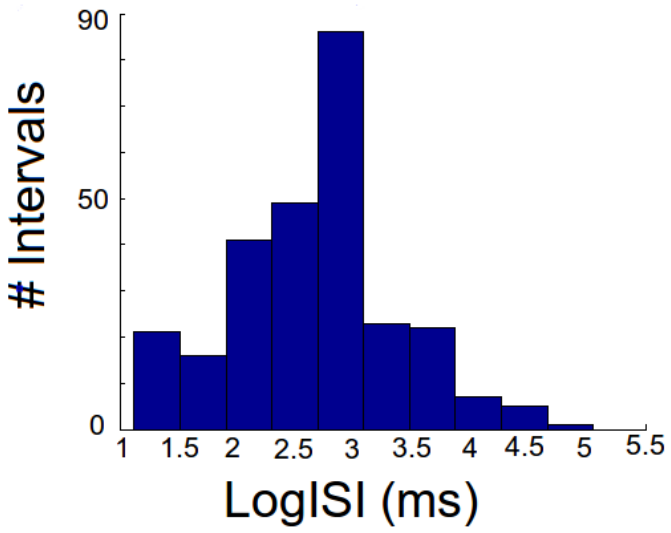

Figure 6.11.: Histogram of the log values of the inter-spike interval of the RS spiny stellate neuron. The distribution in the histogram is clearly unimodal suggesting a non-bursting neuron, as expected for an RS cell.

Table 6.7.: Quantitative parameters characterising this model neuron as an RS cell and comparison with experimental data [156].

	Model	Experimental Range (Nowak et al. [156])
Spike width (ms)	0.2629 (± 0.0076)	0.18 - 1.33
Ada50	.6925 (± .1387)	.41 - .73
f-I slope (Hz/nA)	104.37	45 - 375

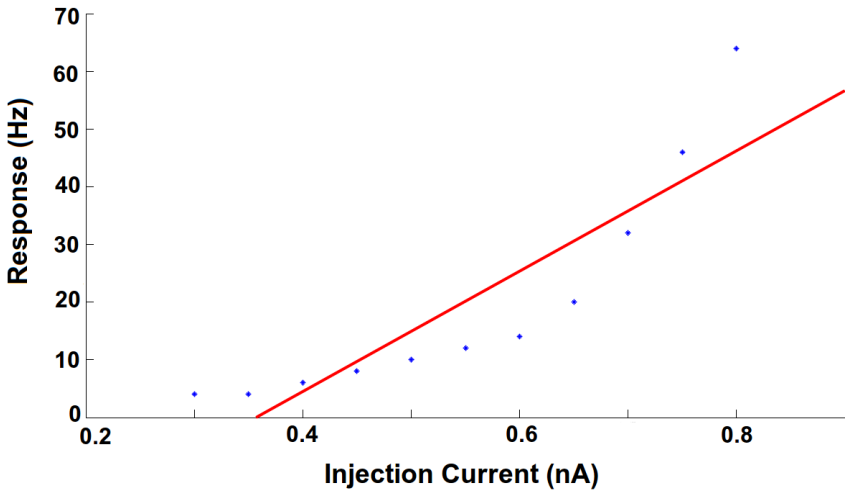

Figure 6.12.: f-I curve of the spiny stellate cell showing RS behaviour. Dots represent firing rates at different input currents and the solid line is a linear fit calculated to estimate the f-I slope in Table 6.7. (Note that, although an exponential fit seemed more appropriate for the data, a linear fit was performed in order to be comparable to the experimental data from Nowak et al. [156].)

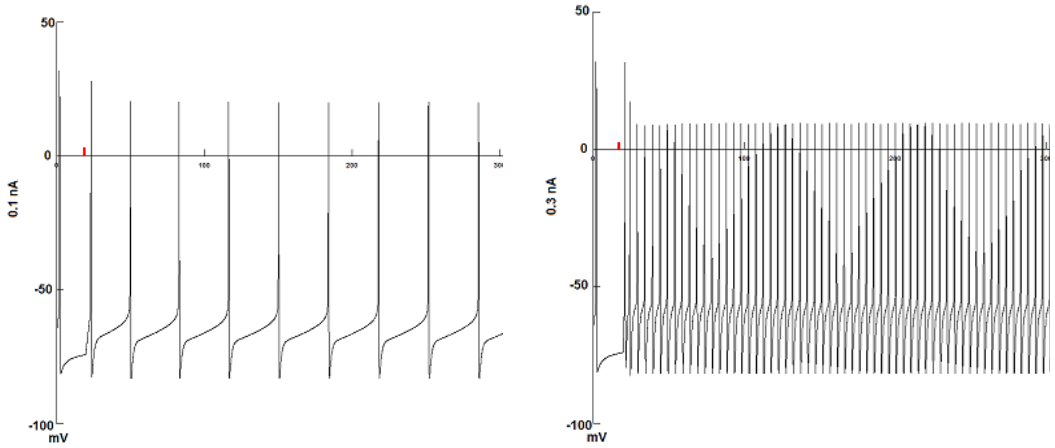

(a) (b)

Figure 6.13.: Firing behaviour of a basket cell demonstrating fast spiking (FS) type. The response of a basket cell to different input currents: (a) somatic input current of 0.1 nA. (b) somatic input current of 0.3 nA. The onset of stimulation is marked in red.

the basis of eleven simulations with input currents ranging from 0.1 nA to 1.1 nA in steps of 0.1 nA (see 6.2.2). The results are shown in Table 6.8. The spike width was smaller than for the RS type spiny stellate cell and the slope of the f-I curve much steeper, overall indicating a fast spiking type neuron. Furthermore, there is no adaptation, as indicated by the adaptation index of approximately 0.51.

Table 6.8.: Quantitative parameters characterising this model neuron as an FS cell. As a reference parameter ranges from experimental data are shown [156]

	Model	Experimental Range (Nowak et al. [156])
Spike width (ms)	0.1913 ($\pm$0.0085)	0.16 - 0.48
Ada50	.5147 ($\pm$ .0241)	.39 - .58
f-I slope (Hz/nA)	595.25	106 - 783

6.3.2. Classical Receptive Field Properties of Network Model Neurons - Validation II

After a validation of the single cell models, the network properties of the neurons were investigated. This meant that, contrary to the previous section, the following properties did not depend solely on the intrinsic properties of the neurons, but crucially depended

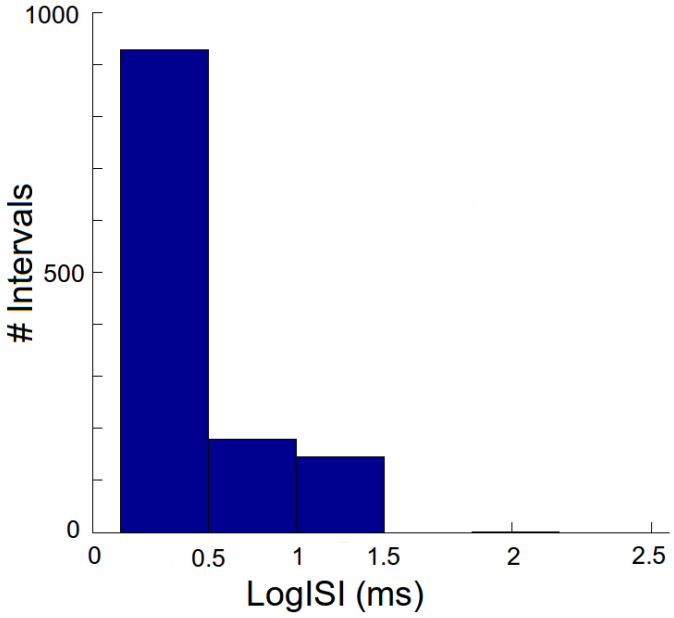

Figure 6.14.: Histogram of the log values of the inter-spike interval of the FS interneuron. The distribution in the histogram is clearly unimodal, suggesting a non-bursting neuron, as expected for an FS cell.

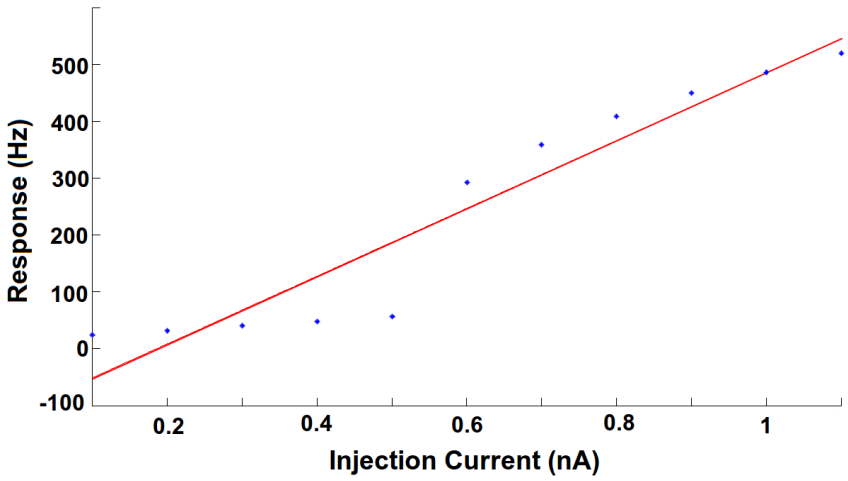

Figure 6.15.: f-I curve of the basket cell showing fast spiking behaviour. Dots represent firing rates at different input currents and the solid line is a linear fit calculated to estimate the f-I slope in Table 6.8.

on the embedding of the neurons in the network. In all subsequent sections of this chapter network properties were tested and explored. Since most experiments only report network properties for excitatory neurons [e.g. 174], all modelling studies mainly investigate network properties for these. Therefore, in the following sections of this chapter all reported parameters describing network properties are for the population of excitatory neurons, unless stated otherwise.

6.3.2.1. Simple and Complex Cells

All cells that showed only weak responses (responses $< 8\,Hz$ for all stimulation conditions) to the stimuli were excluded, resulting in an exclusion of approximately $30\,\%$ of the cells.

Cells were divided into simple and complex, based on the $F1/F0$ ratio, where $F1$ was the fundamental of their response to drifting sinusoidal gratings and $F0$ the mean response [195]. Note that this is not related to the firing behaviour of the neurons discussed in the previous section. Showing simple or complex behaviour is a network property of the neuron and, hence, was only calculated for the excitatory neurons, which were all modelled to show RS firing behaviour.

Figure 6.16 shows the distribution of the ratios in the network model. More simple ($70.97\,\%$) than complex cells ($29.03\,\%$) were found, which is in agreement with experimental data (e.g. $69.32\,\%$ simple cells [190]). However, recent experimental data suggest a slightly larger number of complex cells [174, 232]. Furthermore, a relatively large number of cells with a ratio close to 1 was found, which is not seen experimentally.

6.3.2.2. Orientation and Direction Selectivity

Again the same exclusion criteria for weakly responding cells were used as above.

Orientation selectivity comparable to experimental studies [174, 232] and to other models [160, 232] was found. The results are summarised in Table 6.9. As reported in previous studies, ORI and CV strongly correlated with each other ($r = -.71$, $p < .0001$). Therefore, focus was subsequently mainly set on CV, which is also primarily used by experimentalists and has a broader dynamic range (see [174]). Figure 6.18 shows an example tuning curve of a cell which was sharply tuned, as shown by the high ORI, the low CV and the low OBW. Figure 6.17 shows a comparison of the average CV of the model with the experimental data from Ringach et al. [174]. Both local (OBW) and global measures (ORI and CV) were in good agreement with the experimental data. Furthermore, the average firing rates of the model neurons were also comparable to experimental data.

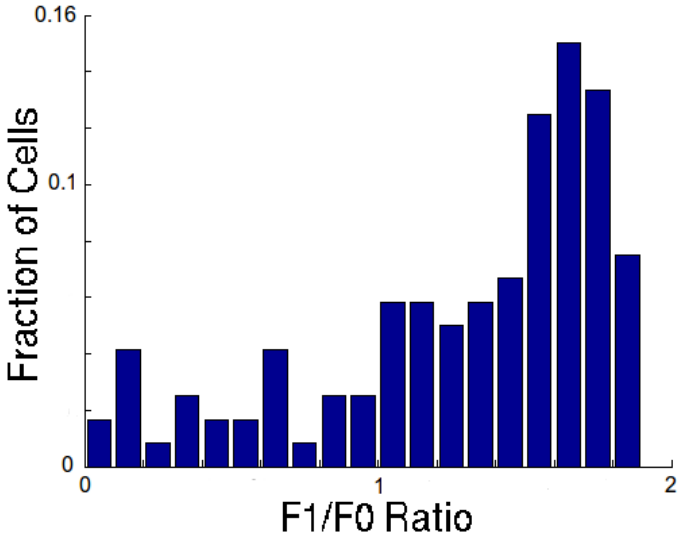

Figure 6.16.: Histogram of the distribution of F1/F0 ratios of the neurons. A ratio < 1 indicated a complex cell whereas a ratio ≥ 1 indicated a simple cell. The distribution was similar to experimentally measured distributions in layer 4Cα [190]. However, the current model had a relatively large proportions of neurons with an F1/F0 ratio around 1.

Further, orientation selectivity was investigated in the model, presenting orientation stimuli at four different spatial frequencies $2^{-\frac{1}{2}}$, $2^{\frac{1}{2}}$, $2^{\frac{3}{2}}$ and $2^{\frac{5}{2}}$ c/deg (note that the distribution of preferred spatial frequencies was very broad, peaking at $2^{\frac{1}{2}}$ c/deg, as seen in Figure 6.25) and at seven different sizes (10×10 to 40×40) of the grating. The trial at the preferred spatial frequency and size of each cell was then chosen, thus resembling experimental procedures. Furthermore, this procedure was very similar to the approach used for the modelling part in Zhu et al. [232]. This procedure led to an increase in selectivity measures in the model, matching experimental data even more closely. $72.32\,\%$ of the cells showed a selective response and a further $12.20\,\%$ showed a biased response. Furthermore, mean ORI ($.77 \pm .25$) and CV ($.52 \pm .24$) were well in agreement with experimental data (see Table 6.9).

$52.76\,\%$ of cells with a bias for orientation also showed a selectivity ($DRI \geq .7$) and another $27.73\,\%$ had a bias ($DRI \geq .5$) for the direction of the moving sinusoidal grating, which fit well with experimentally determined values ($49.10\,\%$ selective cells and $21.62\,\%$ biased cells [55]) . Slightly more selective and biased cells were found in the model compared to previous experiments. However, as can be seen in Figure 6.19, the model had

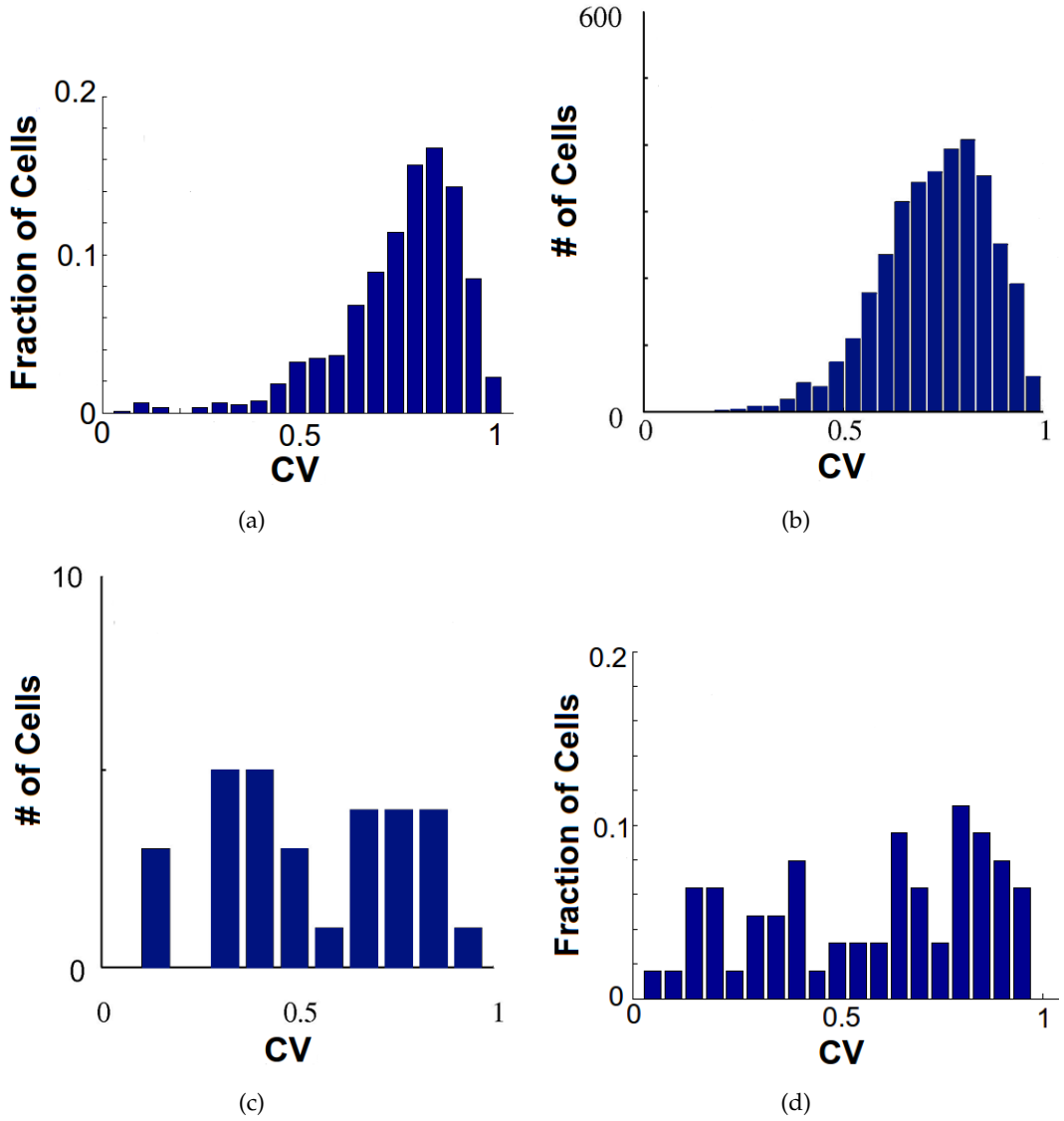

Figure 6.17.: Histogram of the CV of cells in (a) the present network model compared to (b) the model of Zhu et al. [232], (c) the experimental data from Zhu et al. [232], and (d) the experimental data from Ringach et al. [174]. (Images (b) and (c) modified from [232])

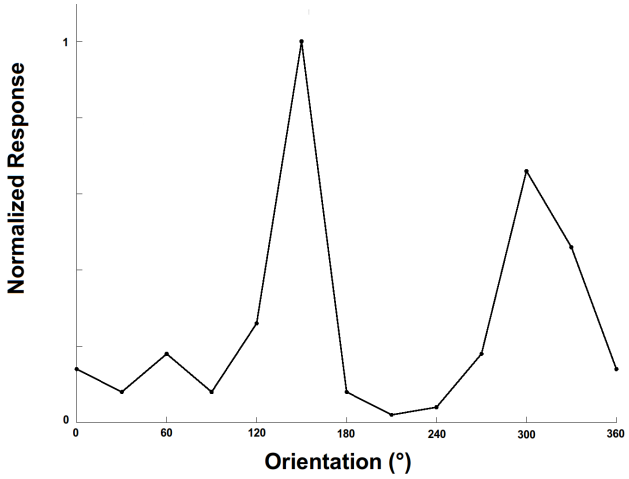

(a)

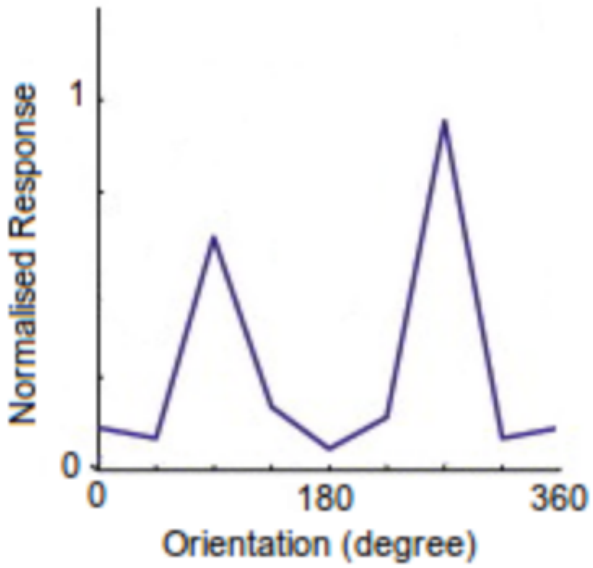

(b)

Figure 6.18.: (a) Example orientation tuning curve for a selective cell in the network model with a preferred orientation of $150°$. The cell ORI=.96, CV=.44 and OBW=12.23°. The cell also showed a bias for direction with DRI=.5. (b) Reference orientation tuning curve from a selective cell (CV=.37) of the network model of Zhu et al. [232]. Note that in both curves the angle of rotation covers a full circle, that is 0-$360°$, which means that each orientation between 0-$180°$ is presented again in the range 180-$360°$ but with the sinusoidal grating moving in opposite direction. Consequently, the tuning curve shows to peaks at approximately the same orientation. (Image (b) modified from [232].)

Table 6.9.: Summarised orientation selectivity data (mean ± std) and comparison to other studies and models. The data were compared to an experimental study of Ringach et al. [174], an experimental study from Gur et al. [81], and an experimental and modelling study from Zhu et al. [232]. Note that only the data from layer 4Cα from the Ringach et al. study were used. Unfortunately, no standard deviation is given in the work of Gur et al.

	Model	Ringach et al.	Gur et al.	Zhu et al. (experiment)	Zhu et al. (model)
ORI	.63 ± .30	.71 ± .25	-	-	-
CV	.74±.21	.58 ± .27	.48 ± -	.54 ± .24	.73 ± .13
Maximum Firing Rate (Hz)	36.5 ± 53.1	45.8 ± 30.0	-	-	-
OBW	23.7 ± 35.7	34.4 ± 29.0	29.0 ± -	-	-

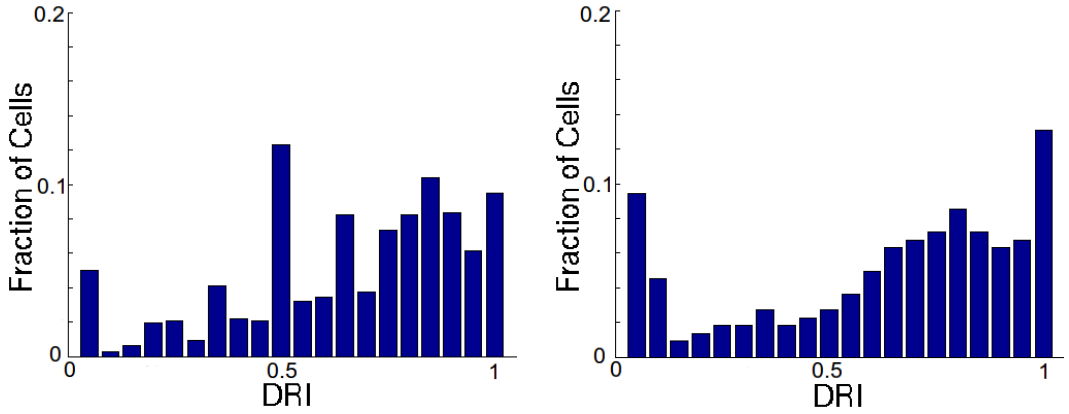

(a) (b)

Figure 6.19.: Histogram of the DRI in (a) the network model compared to (b) experimental data from DeValois et al. [55]. Both histograms show that a large part of the cells were direction selective or biased, but that there was a continual strength distribution of preference for a direction.

approximately $10\,\%$ of cells with a direction bias with a DRI only slightly above $.5$. Figure 6.19 shows the distribution of DRI in the network model compared to the experimental data from DeValois et al. [55].

The network model was tested for the contrast-dependence of orientation selectivity using oriented sinusoidal gratings at three different contrasts: $.25$, $.50$ and $.75$. Again, the orientation was varied from $0°$ to $330°$ in steps of $30°$, and the global selectivity measures ORI and CV, as well as the local measure OBW were calculated, as before. Figure 6.20 shows the results from the orientation selectivity test at the three different levels of contrast. The selectivity increased with increasing contrast for the two global measures ORI and CV, as well as for the OBW. Importantly, as shown in the example in Figure 6.21, the preference for a specific orientation did not strongly change with contrast for most of the cells.

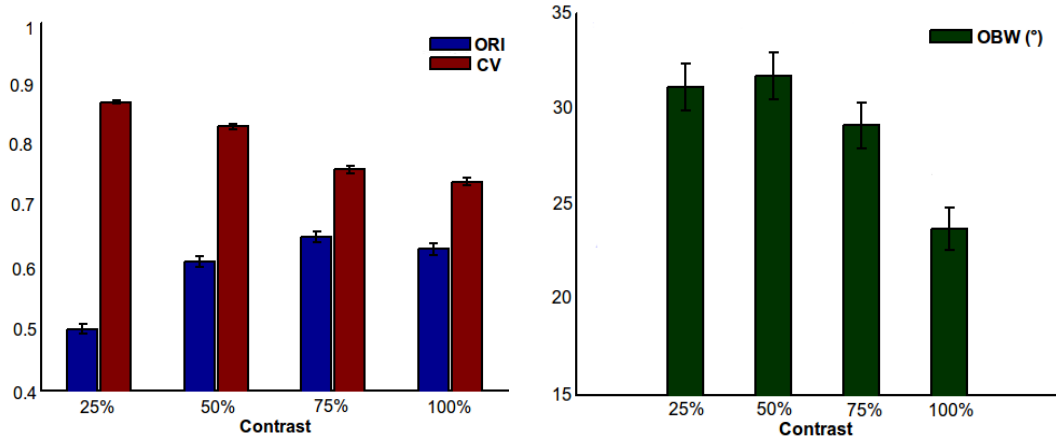

(a) (b)

Figure 6.20.: Orientation selectivity for three different levels of contrasts: $.25$, $.5$ and $.75$. (a) Global measures for orientation selectivity (ORI and CV). (b) Local measure for orientation selectivity (OBW). Mean values and standard errors are shown.

Since the cortical network connectivity of the model, as well as the formation of receptive fields depended on random choices, it was tested whether the specific choice of connectivities and receptive fields, respectively, influenced the results. However, running all the simulations for all feature selectivities and centre-surround suppression tests for different choices of random seeds was not feasible. Thus, exemplary, the influence of the random seed choice on the orientation selectivity, the most important property of our network, was tested. Two additional configurations were chosen for each: the cortical network connectivity and the receptive field mapping, respectively. Figure 6.22 sum-

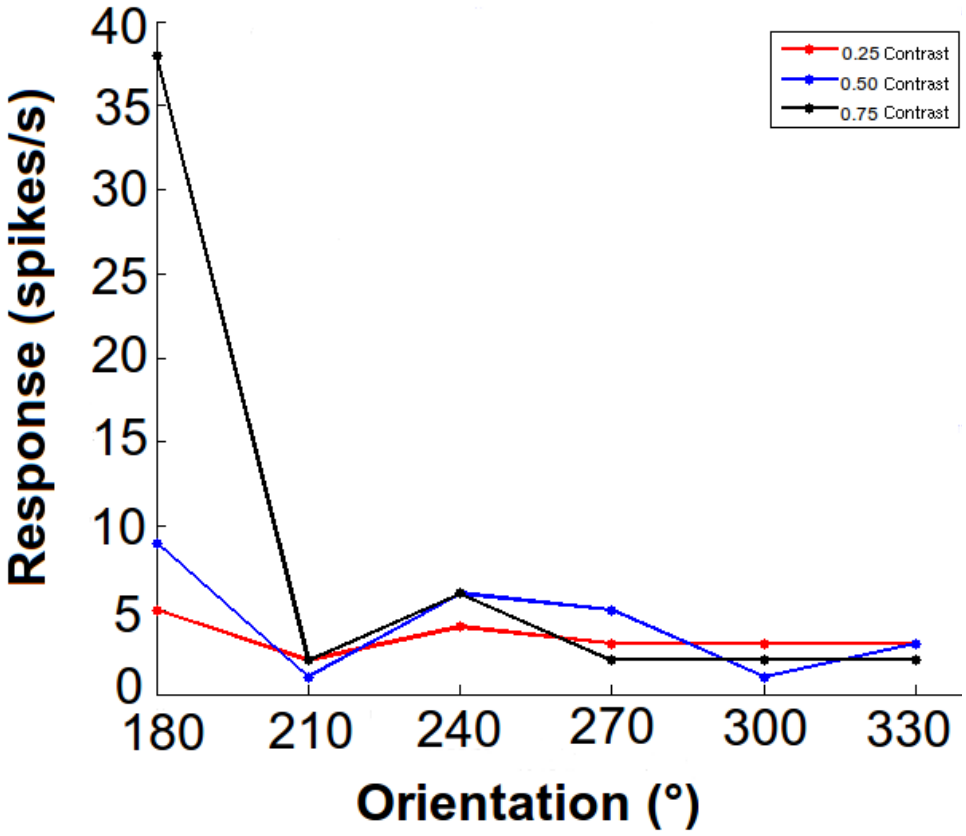

Figure 6.21.: An example orientation tuning curve at three different levels of contrast (.25, .50 and .75). In this cell, the preferred orientation did not change and the tuning strength increased with increasing contrast.

marises the results from this test, showing that both global (a) and local (b) measures did not considerably differ in all four cases and were similar to the standard configuration.

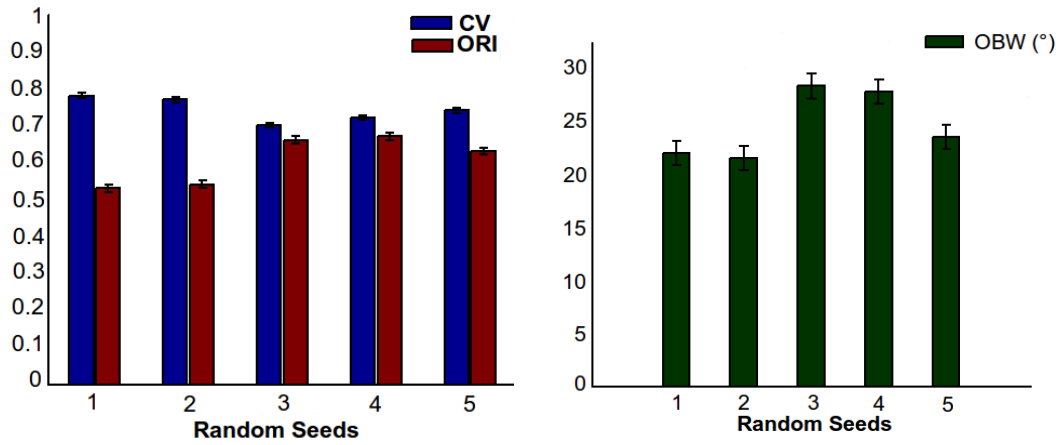

(a) (b)

Figure 6.22.: Orientation selectivity for different random seeds. 1 and 2 depict the variation of the random seed for the cortical connections, 3 and 4 depict the two variations for the random seed in the formation of receptive fields, and 5 depicts the standard configuration. (a) Global measures of orientation selectivity (CV and ORI). (b) Local measure of orientation selectivity (OBW). Mean values and standard errors are shown.

6.3.2.3. Spatial Frequency Selectivity

The spatial frequency selectivity properties of the network model were tested using moving sinusoidal gratings with fixed standard parameters while varying the spatial frequency (see Section 6.2.3.3). Seventeen different spatial frequencies were used, ranging from $2^{-4} = 1/16$ to $2^4 = 16$ in logarithmic steps of one-half order of magnitude. From those data, the LSFV and SBW were calculated, which described the global and the local attenuation at low frequencies as explained in Section 6.2.3.3. Again, all cells showing only weak responses ($< 8\,Hz$ for all stimulation conditions) to the stimuli were excluded (approximately 30 %). Figure 6.23 displays the spatial frequency selectivity of the model, and compares them to experimental and modelling data from other studies [231, 232]. It shows that the model matched well with experimental data and outperformed other modelling studies with respect to the global tuning measured with the LSFV. An example for a spatial tuning curve and a comparison to the model of Zhu et al. [232] is given in Figure 6.24. Furthermore, a high correlation between SBW and LSFV was found (Pear-

son's correlation; $r = .69, p < .0001$), as in experimental studies [224]. This correlation further underpinned the validity of the model, because it showed that the local measure of tuning around the peak (the SBW) agreed with the more global measure (the LSFV). Similar to animal experiments [e.g. 224], about $20\,\%$ of the cells had no measurable SBW. However, the model's SBW (3.34 ± 2.39 octaves) was higher and more diverse than in experimental data (experimental data 1.56 ± 0.19 octaves; estimated from [54], Figure 7)). Another interesting matter was, that the firing rate at optimal parameters (32.90 ± 18.69 Hz) again agreed with experimental data [231]. Figure 6.25 shows the distribution of preferred spatial frequencies in the network model and compares it to experimental data from DeValois et al. [54]. It can be seen that both distributions covered the same range of spatial frequencies and peaked at approximately the same frequency.

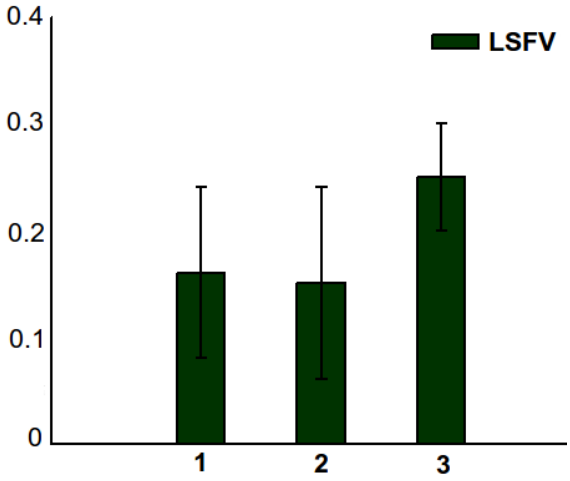

Figure 6.23.: Comparison of the spatial frequency selectivity (the mean LSFV; error bars represent standard deviation) of (1) the network model with (2) experimental and (3) model data from Zhu et al. [231].

6.3.2.4. Temporal Frequency Selection

The temporal frequency selectivity properties of the network neurons were explored using moving sinusoidal gratings with fixed standard parameters (orientation $0°$, spatial frequency $2^{3/2}\,c/deg$, contrast $100\,\%$ and size 44×44). Temporal frequency was varied between 1 and $15\,$Hz. Figure 6.26 shows the results of the temporal frequency selectivity properties of the network model. A broad distribution of preferred temporal frequencies was found between 1 and $9\,$Hz, with an average preferred frequency of $4.66\,$Hz, dovetailing with experimental data (e.g. average preferred temporal frequency $2.9\,$Hz [69]).

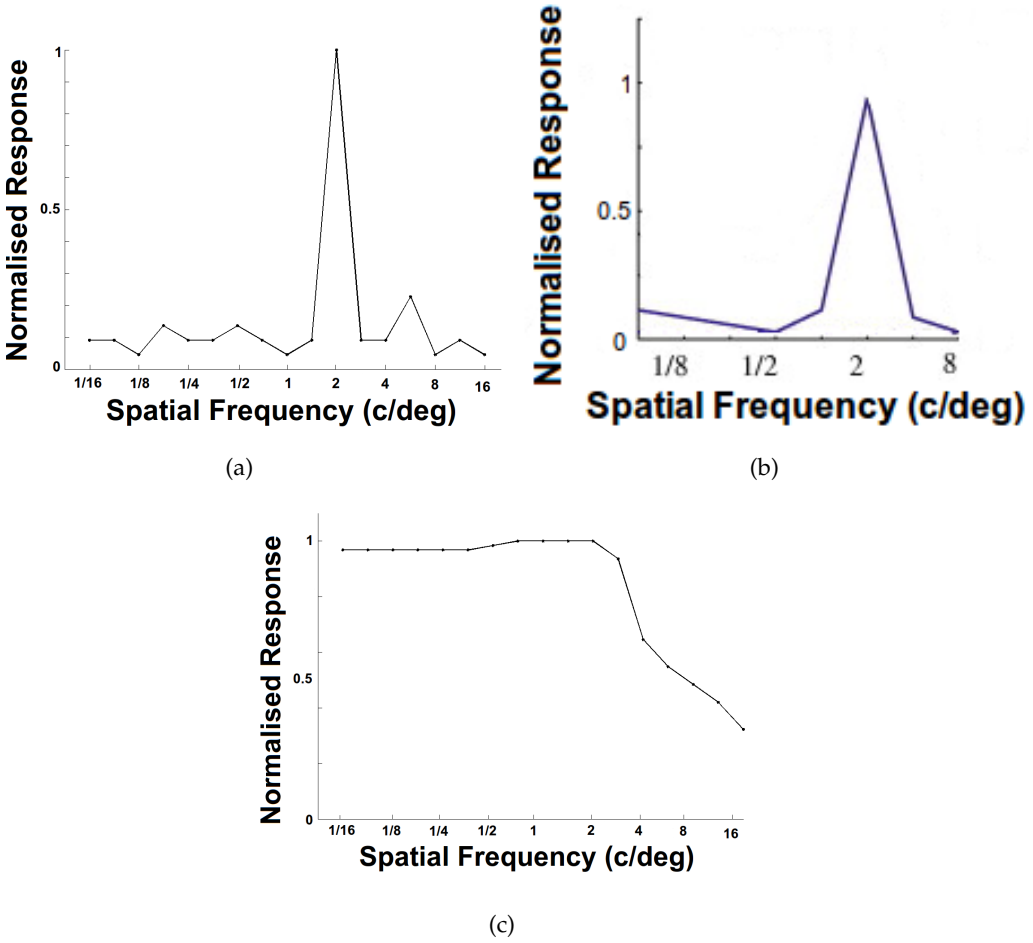

Figure 6.24.: Spatial tuning curves from (a) the present network model, (b) the network model from Zhu et al. [232] and (c) an LGN input neuron. All curves show an attenuation at low spatial frequencies except for the LGN input neuron. Note that in the present network the modelling of the LGN input to the network model was adopted from the model of Zhu et al. [231, 232]. (Images: (b) modified from Zhu et al. [232], (c) after Zhu et al. [231].)

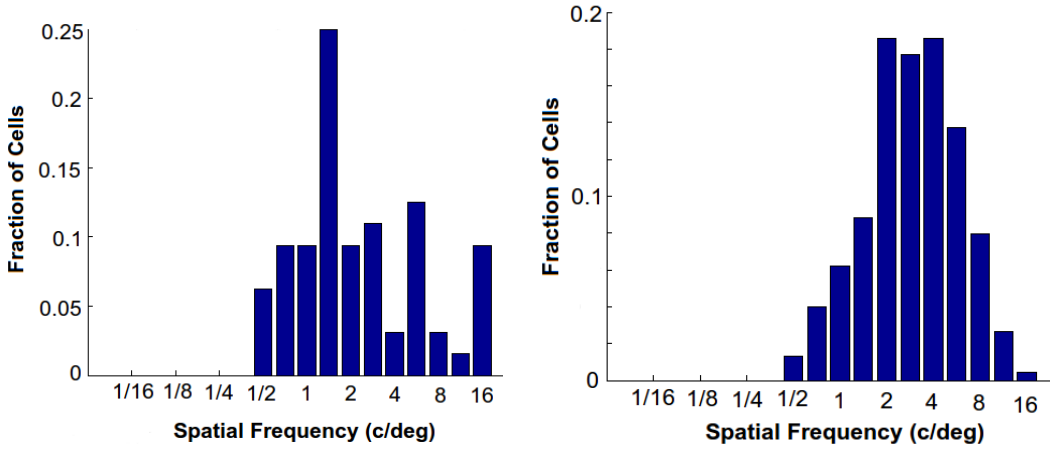

(a) (b)

Figure 6.25.: Spatial frequency preference distributions in (a) the network model compared to (b) experimental data from DeValois et al. [54].

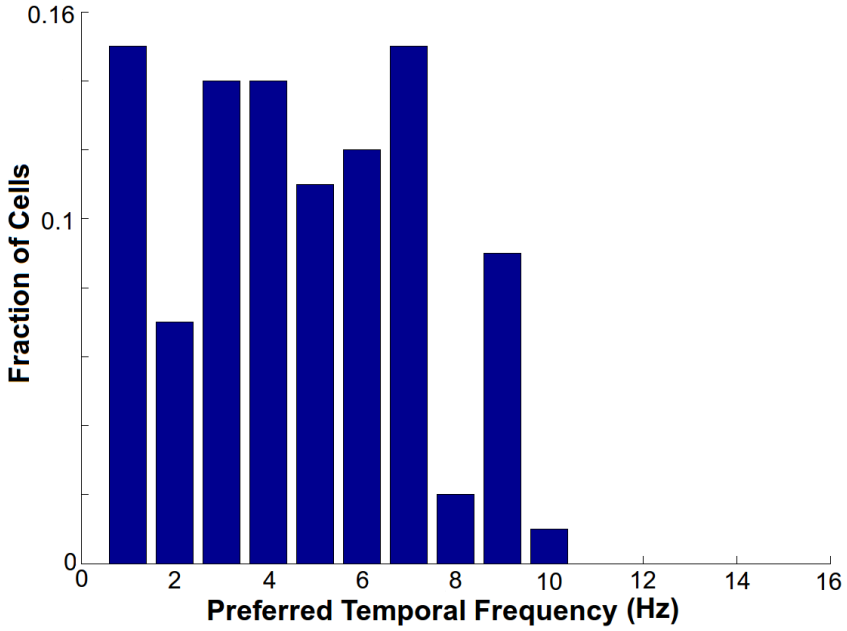

Figure 6.26.: Distribution of preferred temporal frequencies.

Table 6.10.: Resulting parameters (mean $\pm$ std) for the standard contrast response function $R(C) = \frac{k \cdot C^p}{(1+a \cdot C^q)}$ that was fitted to the spiking activity $R(C)$ of single neurons in response to gratings of four different contrasts ($C = .1, .2, .4$ and $.8$).

a	k	p	q	r^2
0.03 ± 0.02	1.74 ± 0.06	2.29 ± 0.16	1.83 ± 0.20	0.88 ± 0.15

Additionally, the sharp cut-off at around 9 Hz was also in good agreement with physiological studies (see also [69]).

6.3.2.5. Contrast Response

The contrast response in the network model was investigated using moving sinusoidal gratings at different levels of contrast as in physiological [24, 68] and psychophysical studies [226]. Four different values were used for the contrast of the sinusoidal grating: $.1$, $.2$, $.4$ and $.8$. A standard contrast response function was then fitted to the responses of each of the 16 cells, which had receptive fields that lay fully within the stimulated 10×10 region and which had a preferred orientation matching the orientation of the presented grating (details see 6.2.3.5). The contrast response function could not be fitted to three cells, because their response was substantially independent from the contrast of the stimulus and thus excluded them from subsequent analyses. Table 6.10 summarises the results for the fitted parameters k, a, p and q, as well as the r^2-value as a measure of the goodness of fit. Contrast response curves were very similar to experimentally observed curves. In general, cells responded weakly to low contrast gratings ($.1$ and $.2$) and responses increased substantially for higher contrasts. Parameters fitted close to experimental data, with exponents p and q around 2.3 and 1.8 (see Table 6.10) and a difference $p - q$ of around 0.45, matching well with experimental data [24, 68]. This is not surprising, the ranges of the fitting parameters were highly restricted to experimentally found values. However, the high average r^2-value (see Table 6.10) shows that, within these bounds, very good fits to the data could be achieved, showing that simulated and experimental data match well.

6.3.3. Neural Centre-Surround Suppression

After the thorough validation of the network model in the previous sections, all model parameters were now fixed and the centre-surround properties of the model were explored.

Table 6.11.: Centre-surround suppression for sinusoidal gratings. Suppression indices for four different centre contrasts in two different surround conditions are shown.

Centre Contrast	.1	.2	.4	.8
Low Surround (SI, mean $\pm$ std)	1.56 ± 0.27	1.36 ± 0.3	1.14 ± 0.42	0.22 ± 0.06
High Surround (SI, mean $\pm$ std)	1.06 ± 0.1	1.29 ± 0.51	0.57 ± 0.15	0.19 ± 0.07

6.3.3.1. Centre-Surround Suppression for Sinusoidal Gratings

Centred moving sinusoidal gratings surrounded by additional sinusoidal gratings of different contrasts were used as explained in Section 6.2.3.5. Suppression indices were calculated for each of the 16 cells with receptive fields that lay fully within the stimulated region (see also 6.2.3.5) for all 16 possible combination of centre and surround gratings (four possible centre contrasts .1, .2, $.4$ and $.8$ and four possible surround contrasts .2, $.4$, $.8$ and $.95$). The results were then divided into two groups based on the contrast of the surround grating: a low surround contrast group, encompassing the results from simulations with surround contrasts of .2 or $.4$, and a high surround contrast group, encompassing the results from simulations with surround contrasts of $.8$ or $.95$. Table 6.11 summarises the results. A high response suppression was found in both low (SI=0.22) and high (SI=0.19) surround conditions for the high centre contrast, which coincides with experimental data [112]. Furthermore, a strong facilitation was observed in the low surround condition with a low centre contrast, also in agreement with experimental findings [226]. This facilitation for low centre contrasts is much weaker for the high surround condition. However, responses at low contrasts have to be interpreted with caution, since they were weak for all cells and the influence of noise fluctuations might have been much stronger, relatively, than for the high centre contrast responses.

6.3.3.2. Centre-Surround Suppression for Contrast Texture Patterns

Centre-surround suppression was additionally tested with a second type of stimulus, consisting of random contrast texture patterns instead of the moving sinusoidal gratings described in the previous section. Contrast texture patterns are also commonly used in psychophysical experiments and thus made it possible to compare the results to a larger body of experimental work. Here, centre-only patterns as described in 6.2.4.2 were used, with varying contrasts, starting from $.05$ going up to $.6$ in steps of $.025$. Additionally, centre-surround patterns with a fixed centre contrast of $.4$ and a fixed surround contrast of $.95$ were presented in two conditions: a small surround condition, where the sur-

Table 6.12.: Centre-surround suppression results. Predicted response at a contrast of $.4$ and the actual responses in the two surround conditions are shown. Furthermore, matching contrasts in the two surround conditions and the prediction are shown.

	Response (Hz) (mean± std)	Match (contrast)) (mean± std)
Predicted 40	15.15 ± 19.96	40
Small Surround	5.93 ± 10.13	$.2083 \pm .1583$
Large Surround	5.67 ± 9.91	$.2097 \pm .1775$

round region was six times larger than the centre region, and a large surround condition, where the surround region was seven times larger (see 6.2.4.2 for more details). A standard contrast response function (see Section 6.2.3.5) was fitted to the spike rates of each cell in response to the centre-only stimuli. A predicted response at a contrast of $.4$ was then calculated from this fit and compared to the actual responses at $.4$ contrast in the two centre-surround conditions. Additionally, the matching contrasts were computed for both surround conditions, that is, the contrast at which the fitted contrast response function predicted a spike rate matching the actual spike rate in the surround condition. This matching contrast gave a measure of the suppression introduced by the surround, since the difference between the matching contrast and the physical contrast of the stimulus ($.4$ in this case) can only be attributed to the surround. Hence, a matching contrast closely below the physical contrast indicates low suppression, whereas a large difference indicates strong suppression. This procedure is commonly used in psychophysical studies [e.g. 51].

$50\ \%(32/64)$ of the cells had to be excluded, either because their response was lower than 4 Hz for all stimuli or because the contrast response function could not be fitted in a reasonable manner (r^2-value lower than .6). Overall, an average r^2-value of $.64 \pm .14$ was obtained indicating that the contrast response function fitted adequately. The predicted response at $.4$ contrast and the response at the two surround conditions are summarised in Table 6.12. The inclusion of a surround markedly reduced the response of the neurons, that is, the predicted response for a contrast of $.4$ was substantially larger than the response in the two surround conditions (see 6.12). Furthermore, a one-tailed t-test was performed between the predicted and the actual responses, to test whether the surround significantly reduced the response strength. An additional t-test was conducted between both surround conditions, to see whether the size of the surround significantly influenced the reduction.There was a significant difference between actual response and prediction

($t(62) = 2.21$, $p < .05$ and $t(62) = 2.36$, $p < .05$ in the small and the large surround condition, respectively). However, the difference between the two surround conditions was not significant ($p = .92$). Additionally, the matching contrasts were calculated for the response in both surround conditions. These were about $.21$ in both cases, dovetailing with psychophysical studies on centre-surround suppression [51].

6.3.4. Mechanisms of Emergent Classical Receptive Field Properties

After the investigation of the centre-surround suppression properties of the network model, the different mechanisms contributing to the emergence of CRF properties were explored in more detail. The main goal was to discern the effects of converging input from LGN at excitatory cells from the effects of recurrent activity from within the cortical layer. Again, the focus was put on orientation selectivity as the most important CRF phenomenon.

In order to estimate the tuning of the input signal to excitatory cortical cells, ORI, CV and OBW were calculated on simulated spike trains based on the input rates of the network neurons (see 6.2.3.2). The classification into selective, biased and non-selective cells was based on the ORI (as explained in 6.2.3.2). Table 6.13 summarises the orientation selectivity of the LGN input to the network neurons. It can be clearly seen that the input arriving at excitatory cells in the network was poorly tuned for orientation, as can be seen in the low ORI, the high CV and the high OBW. This becomes especially apparent in the distribution of the CV depicted in Figure 6.29. Overall, only a few cells received input that was highly selective, whereas the majority of cells received input that was only weakly biased for orientation. Figure 6.28 exemplifies the difference in tuning between the LGN input of one cell and the response of the cell, demonstrating that the poor tuning of the input curve was considerably sharpened in the response curve and that the main effect was a suppression at non-preferred orientations. Table 6.14 shows the tuning of excitatory neurons of the network in comparison to the tuning of the in-

Table 6.13.: Comparison of the orientation tuning of the LGN input to V1 with the tuning of V1 cells.

	ORI (mean $\pm$ std.)	CV (mean $\pm$ std.)	OBW (mean $\pm$ std.)	Selective Neurons	Biased Neurons
LGN Input	.47 $\pm$ .25	.88 $\pm$ .10	64.6 $^\circ$ $\pm$ 35.3 $^\circ$	15.35 %	43.95 %
V1	.63 $\pm$ .30	.74 $\pm$ .21	23.7 $^\circ$ $\pm$ 35.7 $^\circ$	62.03 %	21.30 %

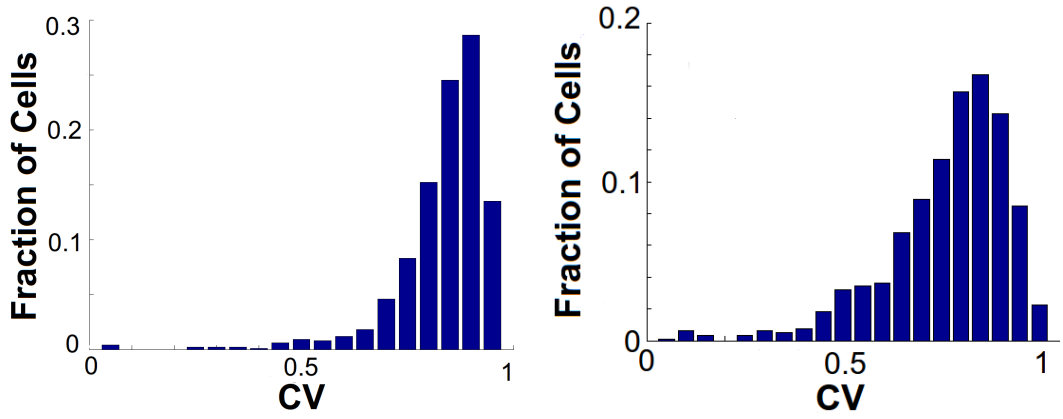

(a) (b)

Figure 6.27.: Comparison of the orientation of the network model with the tuning of the LGN input to the network: (a) CV for the LGN input, and (b) CV for the network . Note that the tuning of the LGN cells themselves is not shown, but the tuning of the input arriving at V1 network cells, thus describing the feed-forward part of the orientation tuning.

Table 6.14.: Comparison of the orientation tuning of excitatory V1 cells with inhibitory V1 cells in the network model.

	ORI (mean ± std.)	CV (mean ± std.)	OBW (mean ± std.)
V1 inh.	.55 ± .26	.85 ± .08	33.5° ± 40.4 °
V1 exc.	.63 ± .30	.74 ± .21	23.7° ± 35.7 °

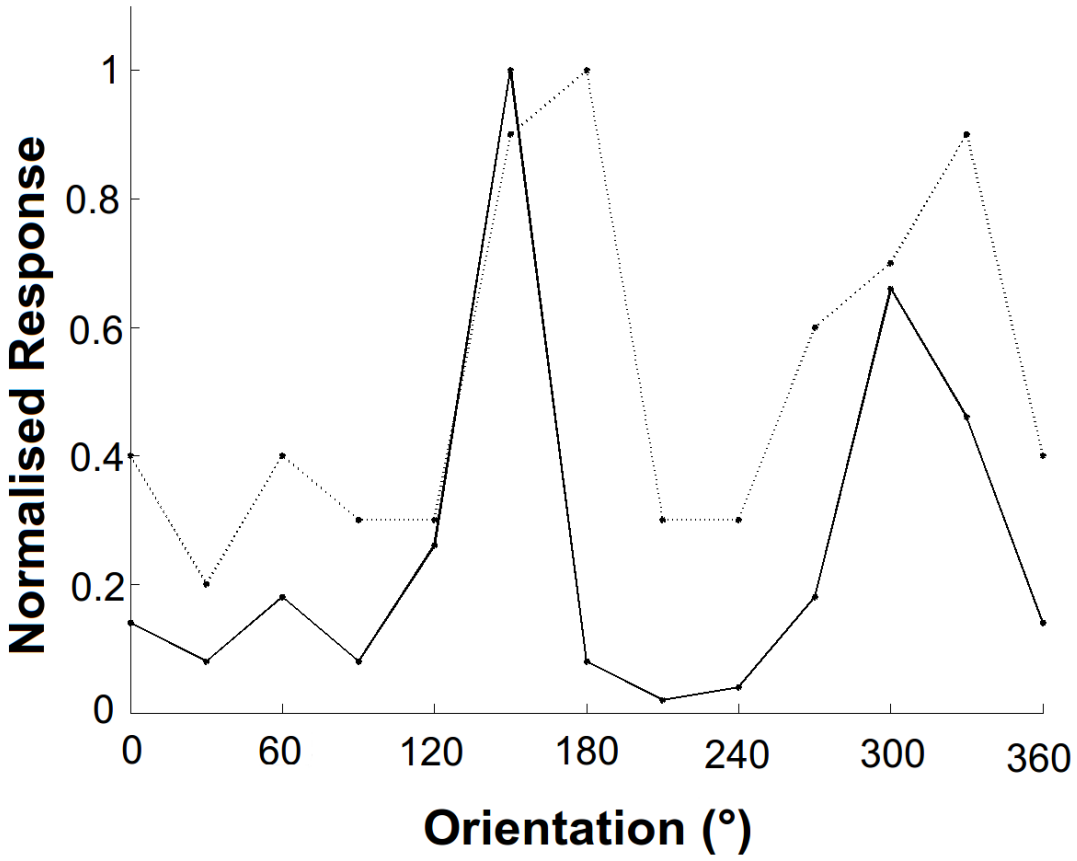

Figure 6.28.: Example orientation tuning curve for a selective cell in the network model having a preferred orientation of 150°. The cell had an ORI of .96, a CV of .44 and an OBW of 12.23°. The cell also showed a bias for direction with a DRI of .5. Overlaid (dashed line) is the normalised strength of the LGN input converging onto this cell (with a CV of .75). Inhibition at non-preferred orientations and sharpening of the tuning was clearly visible.

hibitory population evidencing that excitatory neurons were more sharply tuned, that is, showed a higher ORI, a lower CV and a lower OBW. This result also explains the sharpening of orientation tuning when input and output of excitatory cells were compared. The broader tuning of inhibitory cells was responsible for the suppression of excitatory cells at non-preferred orientations.

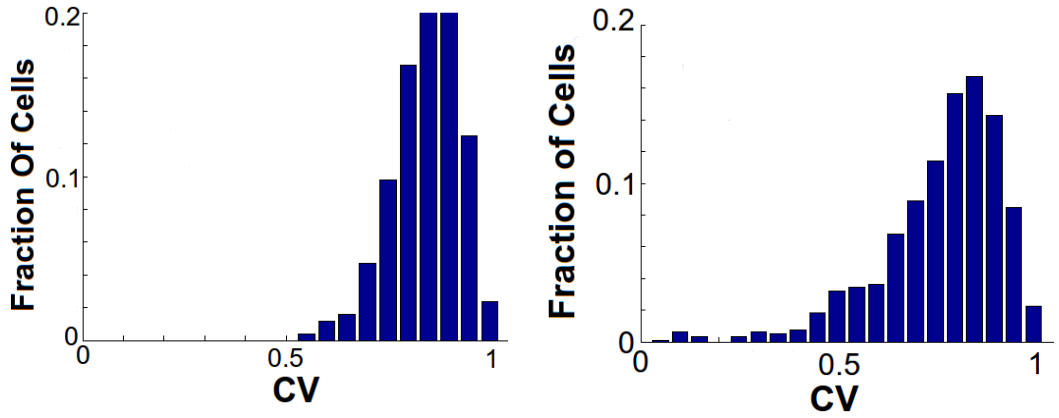

(a) (b)

Figure 6.29.: Comparison of the orientation tuning of the (a) inhibitory cells of the network model with the tuning of the (b) excitatory cells. The distribution of CV is shifted towards higher values for the inhibitory cells, indicating a lower tuning.

Figure 6.30 summarises the influence of the inhibitory weight w_{ie} on the orientation selectivity of the network neurons. The other network parameters were kept fixed, especially the two weights controlling excitatory-to-excitatory and excitatory-to-inhibitory connections were kept constant. The data clearly showed that stronger recurrent inhibition increased orientation selectivity in the network neurons, which was reflected in an increasing ORI, a decreasing CV and a decreasing OBW, as well as increasing percentages of selective neurons. However, this effect is reversed from the point where the weight exceeded 0.3, except for the OBW. Figure 6.31 shows the influence of the weight on the tuning of the population of inhibitory neurons. Again, the tuning of inhibitory neurons was weaker than for the excitatory cells in all conditions. Furthermore, the global tuning increased with inhibition, although, in contrast to excitatory neurons, it did not reach a maximum and then decline but increased monotonically. The local tuning, as reflected by OBW, increased with increasing inhibition, reached its peak at $w_{ie} = 0.4$ and the slightly decreased at $w_{ie} = 0.5$. Figure 6.33 summarises the influence of the excitatory weight on inhibitory neurons w_{ei} on the orientation selectivity of the network neurons. It is clear

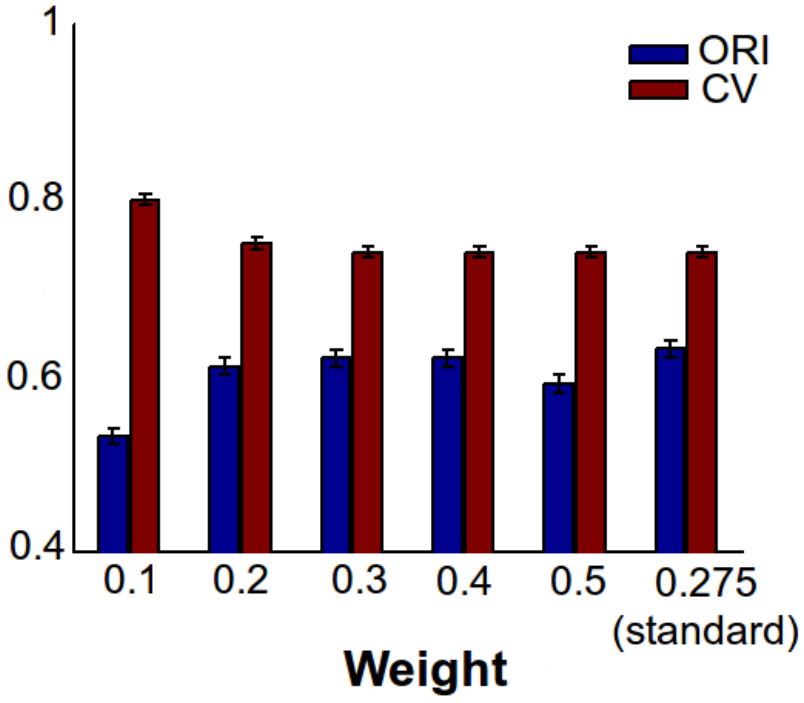

(a)

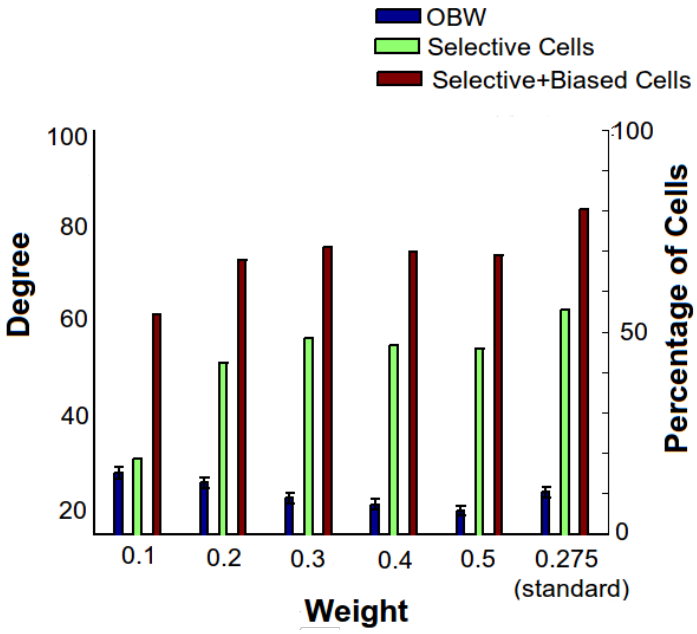

(b)

Figure 6.30.: Evolution of orientation selectivity under increasing strength of inhibition. (a) Global measures of orientation selectivity (CV and ORI). (b) Local measure of orientation selectivity (OBW) and percentage of selective and biased cells. Mean values and standard errors are shown.

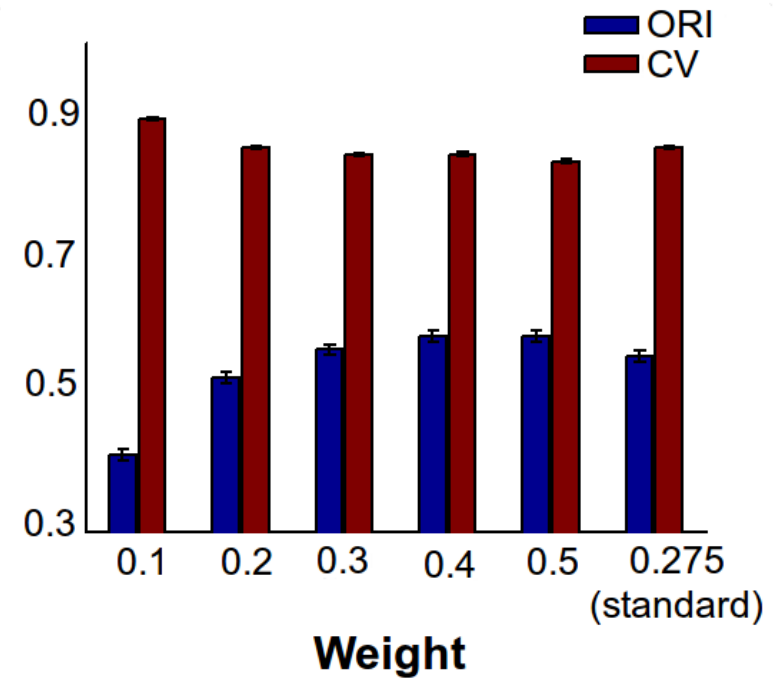

(a)

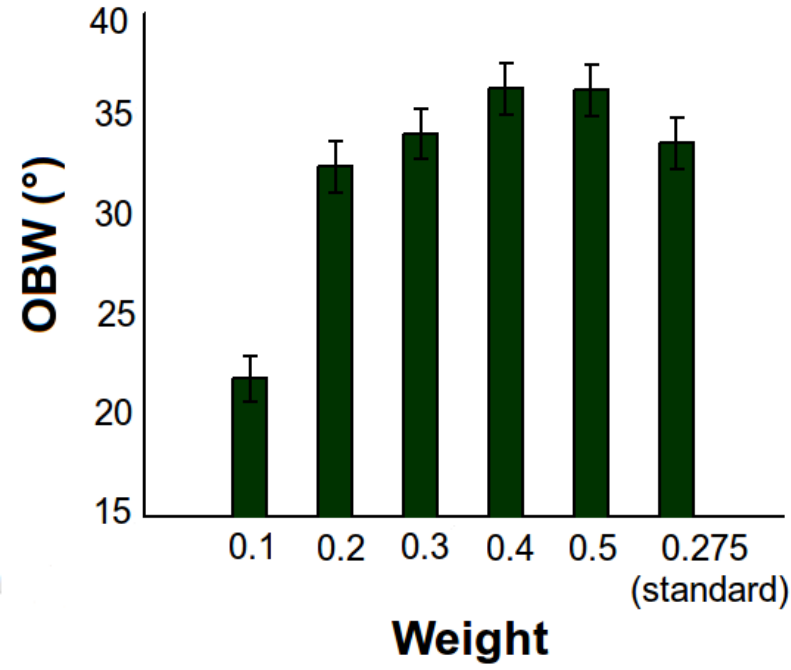

(b)

Figure 6.31.: Evolution of orientation selectivity of inhibitory neurons under increasing strength of inhibition. (a) Global measures of orientation selectivity (CV and ORI). (b) Local measure of orientation selectivity (OBW).

that the influence of the excitation of inhibitory cells, which is controlled by the weight w_{ei}, only had a weak effect on the orientation selectivity of the neurons. ORI and CV for all tested weights were within a narrow range ([.55 .64] and [.73 .74], respectively), and also the number of selective and biased cells did not change substantially. Again, stronger inhibition led to a sharpening of the tuning curve, that is, a decrease in OBW, even though mean ORI and CV again decreased and increased, respectively, and the total numbers of selective and biased neurons also decreased. Figure 6.34 summarises the influence of the excitatory weight on inhibitory neurons w_{ei} on the orientation selectivity of the inhibitory population. While global orientation selectivity decreased (Figure 6.34 (a)), the local tuning around the peak improved (Figure 6.34 (b)).

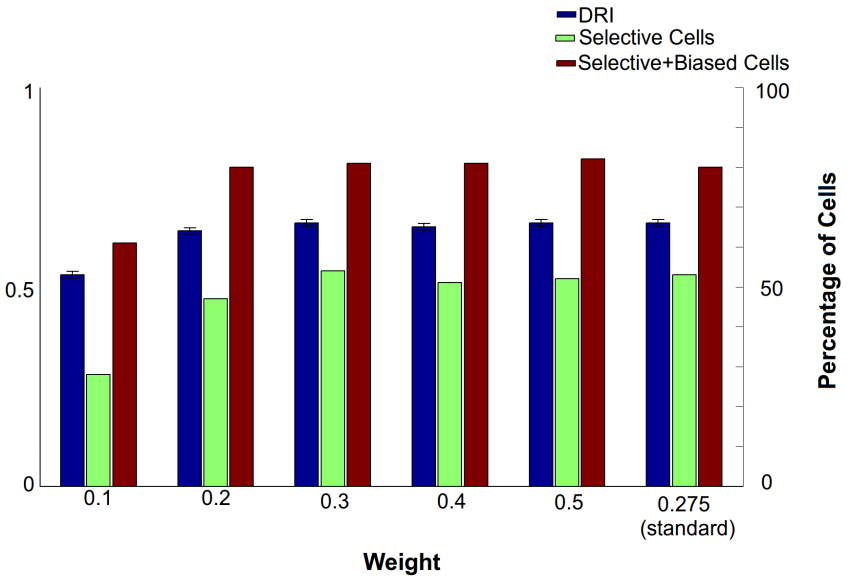

Figure 6.32.: Evolution of direction selectivity under increasing strength of inhibition w_{ie}. Mean value and standard error are reported.

Additionally, it was assessed whether the direction selectivity was also influenced by inhibition. Figure 6.32 shows the evolution of the DRI, as well as the percentage of selective and biased cells with increasing strengths of inhibition. It demonstrates that direction selectivity increased with increasing inhibitory strength and reached a plateau at approximately $w_{ie} = 0.3$. However, the influence was not as strong as in the case of orientation selectivity.

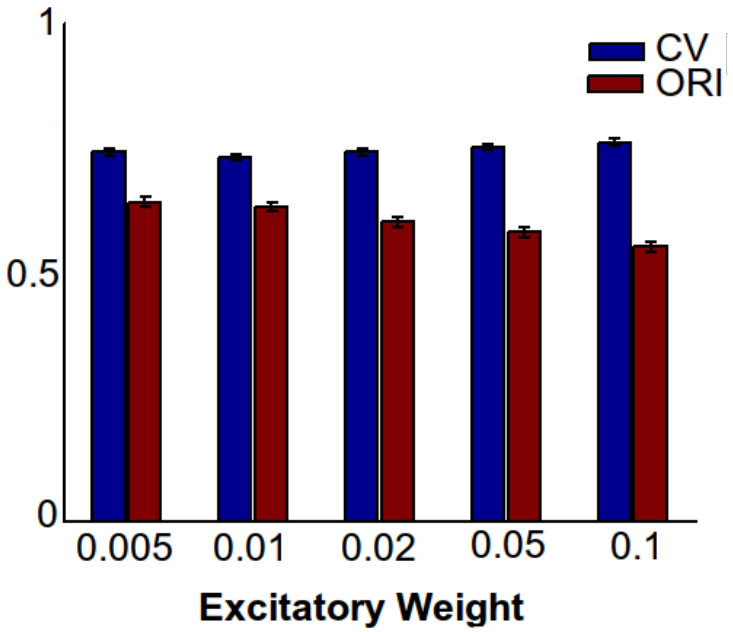

(a)

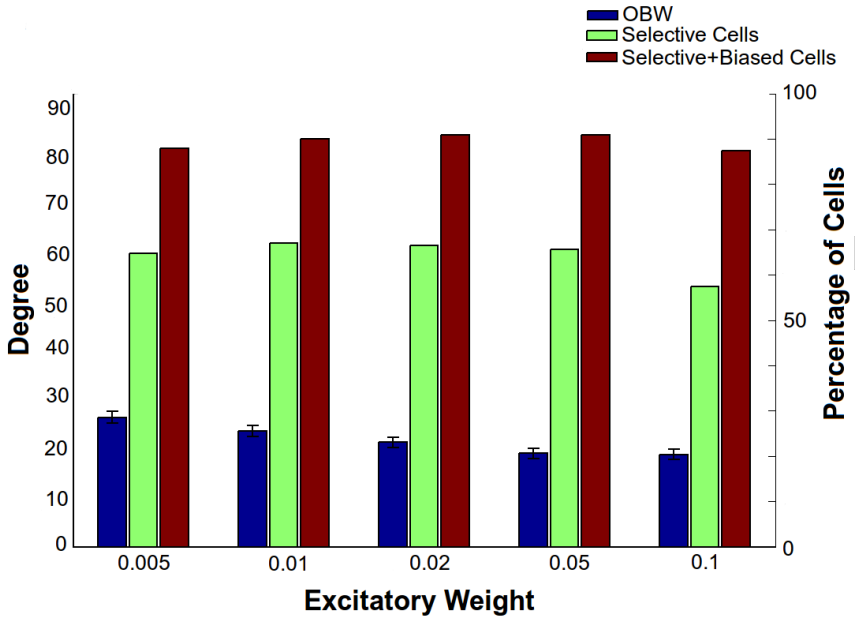

(b)

Figure 6.33.: Evolution of orientation selectivity under increasing strength of excitation of inhibitory neurons. (a) Global measures of orientation selectivity (CV and ORI). (b) Local measure of orientation selectivity (OBW) and percentage of selective and biased cells. Mean values and standard errors are shown.

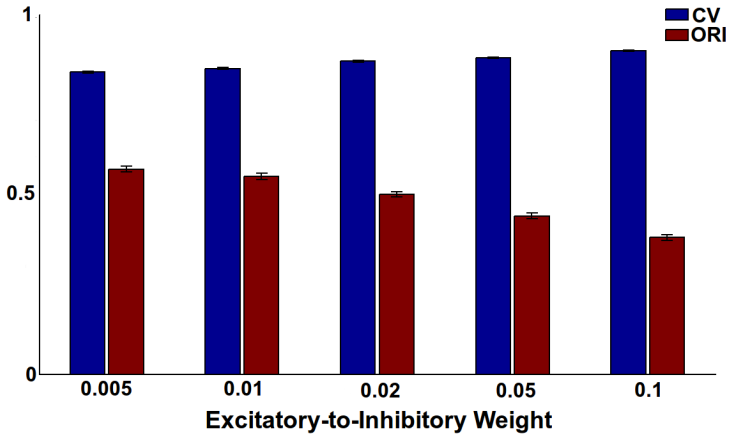

(a)

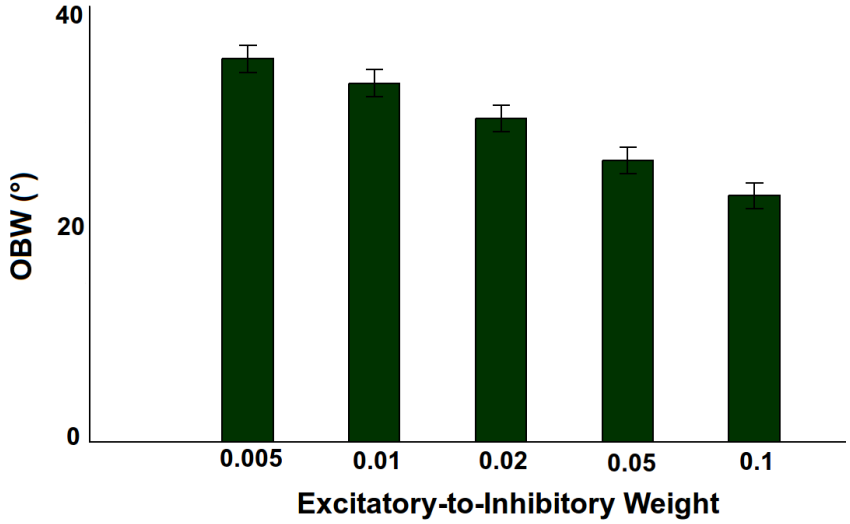

(b)

Figure 6.34.: Evolution of orientation selectivity of inhibitory neurons under increasing strength of excitation of inhibitory neurons. (a) Global measures of orientation selectivity (CV and ORI). (b) Local measure of orientation selectivity (OBW) and percentage of selective and biased cells.

6.3.5. The Role of Recurrent Inhibition in Classical Receptive Field Properties and Centre-Surround Suppression

The previous section dealt with the mechanisms of orientation selectivity in the network model, as the most important CRF property. This section covers how orientation selectivity, contrast response properties and centre-surround properties change as a consequence of variations in GABAergic inhibition. Therefore, the parameters governing GABAergic inhibition were modified as explained in Section 6.2.6, subsequently repeating the simulations testing orientation selectivity, contrast response properties and centre-surround properties in response to sinusoidal gratings and in response to contrast noise patterns, as explained in Sections 6.2.3.2, 6.2.3.5, 6.2.4.1 and 6.2.4.2. This section summarises the results and presents the most important findings. Additional, detailed data are shown in Appendix B.

6.3.5.1. Weight of Inhibitory Connections on Excitatory Cells

The first parameter varied was the weight w_{ie}, controlling the strength of the inhibitory connections onto excitatory cells. Five different values were chosen, ranging from 0.1 to 0.5 in steps of 0.1. Note that the standard value used in the previous simulations was 0.275, which lay roughly in the middle of the chosen interval. All other parameters of the network model were kept fixed at their standard values.

Orientation Selectivity Orientation selectivity properties were tested using moving sinusoidal gratings varying the orientation of the grating at four different spatial frequencies and seven different sizes. The spatial frequency and size of the grating eliciting the maximum response was then identified and only the data at these values were analysed. Measures for orientation selectivity were calculated for the obtained spatial frequency and size, namely the percentage of selective and selective or biased cells, the ORI and the CV. Figure 6.35 (a) shows the orientation selectivity for different weights and compares it to the standard configuration. The orientation selectivity strongly depended on the inhibitory weight. For a small inhibitory selectivity is weak, as indicated by the high CV, the low ORI and the low numbers of selective and selective or biased cells. However, the selectivity reached a plateau at the standard weight $w_{ie} = 0.275$ and stayed approximately constant for higher weights.

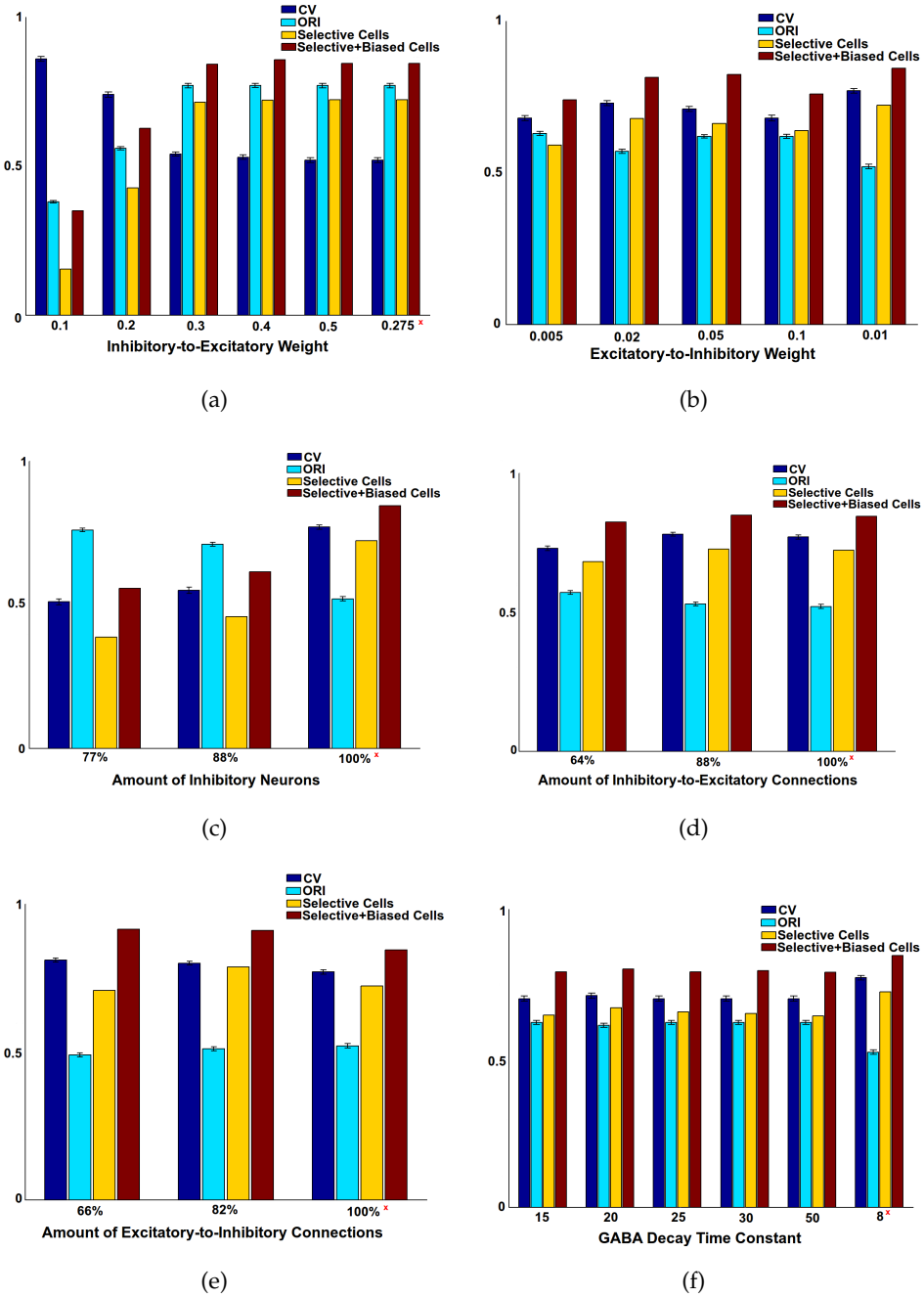

Figure 6.35.: Orientation selectivity measures for different parameters governing inhibition: (a) inhibitory-to-excitatory weight w_{ie}, (b) excitatory-to-inhibitory weight w_{ei}, (c) amount of inhibitory cells N_i, (d) amount of inhibitory-to-excitatory connections n_{ie}, (e) amount of excitatory-to-inhibitory connections n_{ei} and (f) GABA decay time constant τ. For CV and ORI mean values are reported and the error bars show the standard error. For selective and selective or biased cells the fraction of cells in this category are depicted. As a reference, the standard configuration is also shown, marked with a red cross.

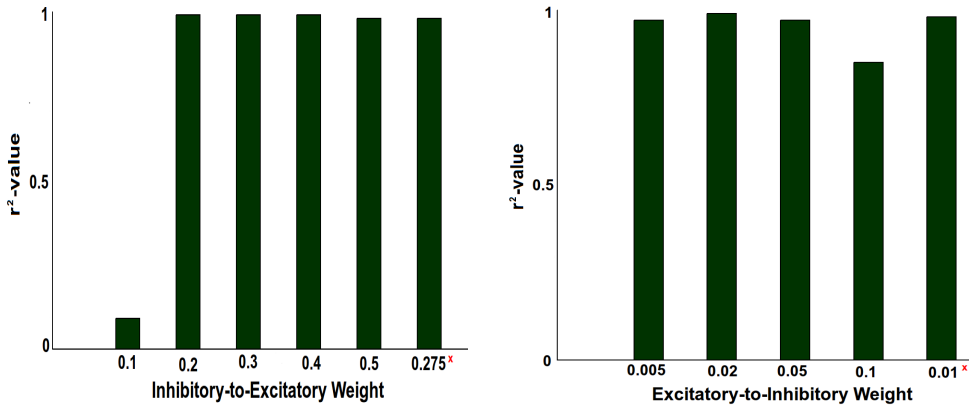

(a)

(b)

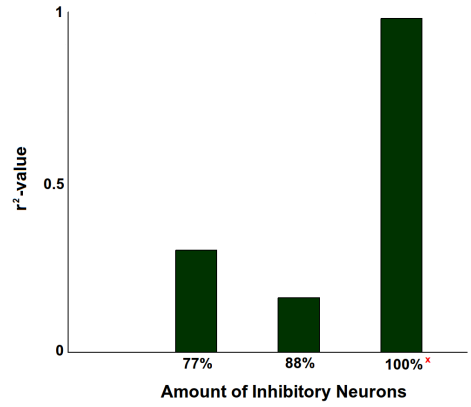

(c)

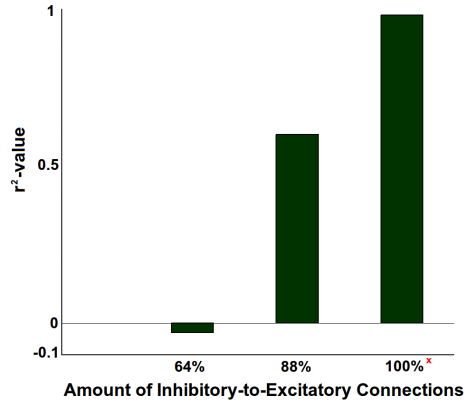

(d)

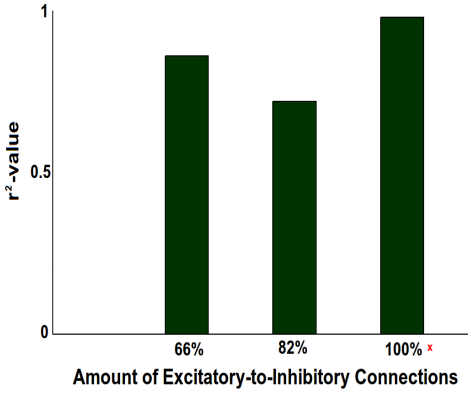

(e)

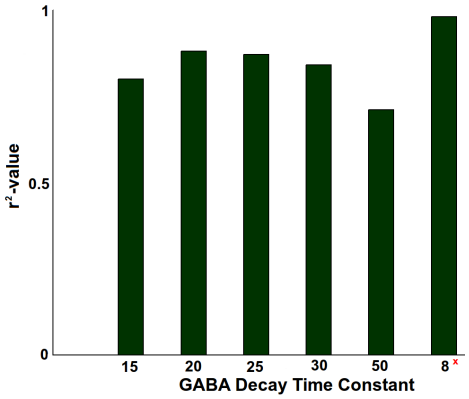

(f)

Figure 6.36.: r^2-values of the fits of the contrast response functions for different parameters governing inhibition: (a) inhibitory-to-excitatory weight w_{ie}, (b) excitatory-to-inhibitory weight w_{ei}, (c) amount of inhibitory cells N_i, (d) amount of inhibitory-to-excitatory connections n_{ie}, (e) amount of excitatory-to-inhibitory connections n_{ei} and (f) GABA decay time constant τ. Standard configurations are shown for comparison and are marked with a red cross.

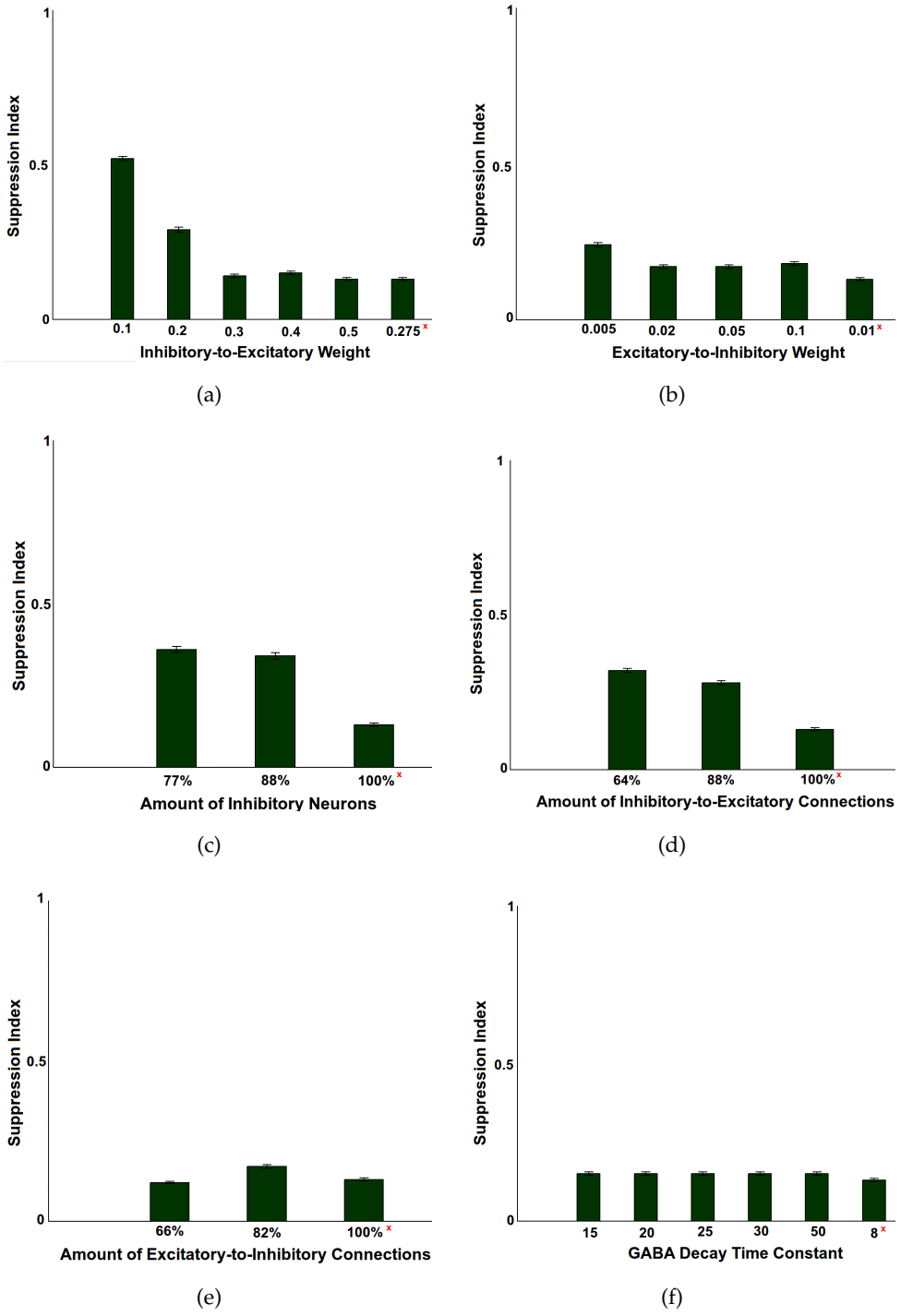

Figure 6.37.: Mean suppression indices (error bars depict standard errors) for the size variation test for different parameters governing inhibition: (a) inhibitory-to-excitatory weight w_{ie}, (b) excitatory-to-inhibitory weight w_{ei}, (c) amount of inhibitory cells N_i, (d) amount of inhibitory-to-excitatory connections n_{ie}, (e) amount of excitatory-to-inhibitory connections n_{ei} and (f) GABA decay time constant τ. Standard configurations are marked with a red cross.

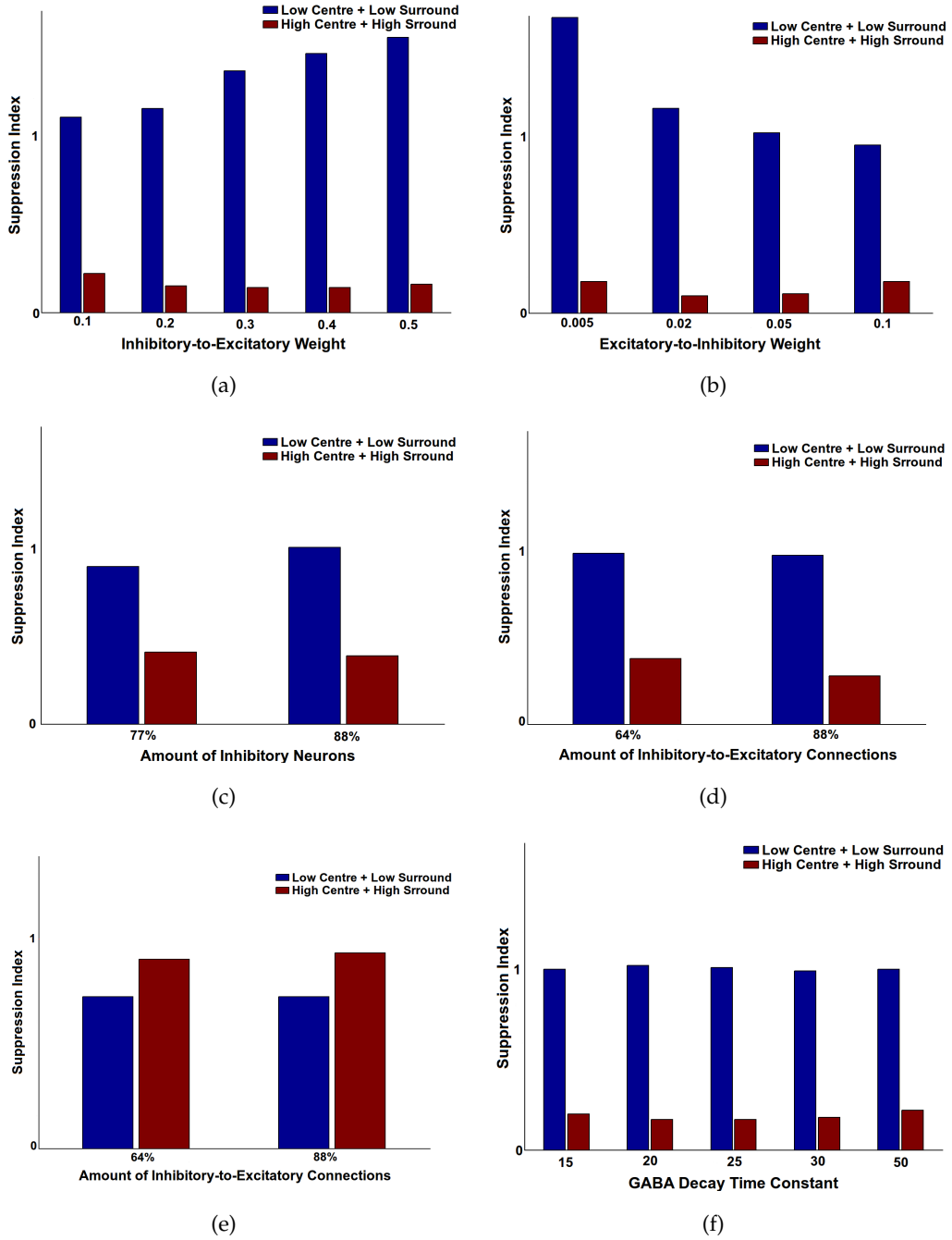

Figure 6.38.: Suppression indices for the two most important conditions ('low-centre/low-surround' and 'high-centre/high-surround') in the centre-surround suppression for sinusoidal gratings test for different parameters governing inhibition: (a) inhibitory-to-excitatory weight w_{ie}, (b) excitatory-to-inhibitory weight w_{ei}, (c) amount of inhibitory cells N_i, (d) amount of inhibitory-to-excitatory connections n_{ie}, (e) amount of excitatory-to-inhibitory connections n_{ei} and (f) GABA decay time constant τ.

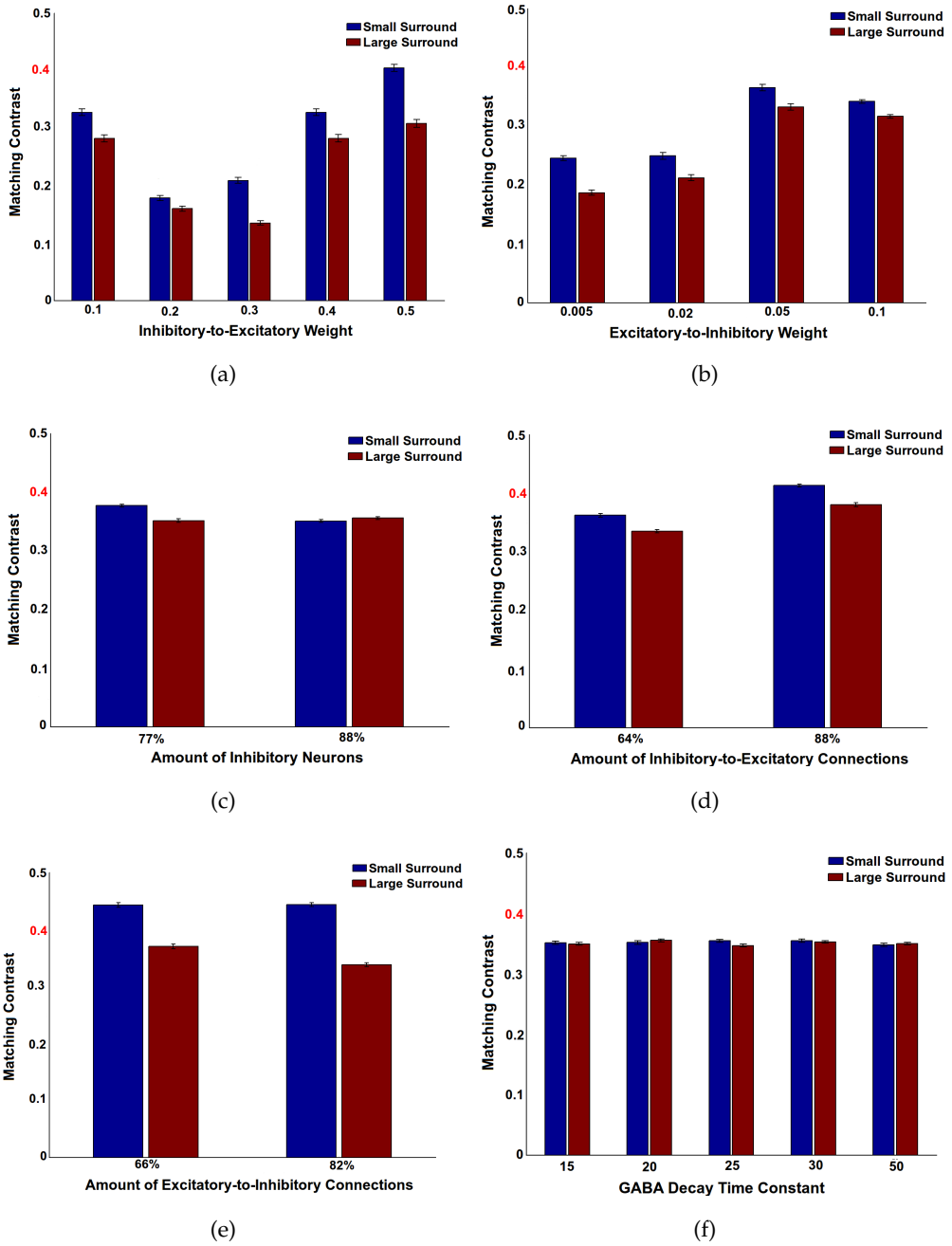

Figure 6.39.: Mean matching contrasts (error bars represent standard errors) for the small and the large surround conditions in the centre-surround suppression for texture patterns test for different parameters governing inhibition: (a) inhibitory-to-excitatory weight w_{ie}, (b) excitatory-to-inhibitory weight w_{ei}, (c) amount of inhibitory cells N_i, (d) amount of inhibitory-to-excitatory connections n_{ie}, (e) amount of excitatory-to-inhibitory connections n_{ei} and (f) GABA decay time constant τ. The actual physical contrast of the stimulus, 0.4, is marked in red.

Contrast Response Properties Again, sinusoidal gratings were used at four different contrasts varying the weight w_{ie} in the network model, and a standard contrast response function was then fitted to the mean of the responses of the 16 cells with receptive fields that lay fully within the stimulated 10×10 region (see 6.2.3.5). Figure 6.36 (a) shows the results for the r^2-value of the fit of the contrast response function to the mean of the responses of the cells, as a measure of the goodness of fit. The contrast response function could be fitted independent from the inhibitory weight w_{ie}. The goodness of fit, as indicated by the r^2 value, was very good in all cases. Detailed fitting parameters are shown in the Appendix in Table B.2.

Centre-Surround Suppression for Sinusoidal Gratings In the size variation test, a certain amount of inhibition was needed, in order to obtain suppression comparable to the standard configuration. A further increase of the inhibitory weight w_{ie}, however, did not further increase suppression (see Figure 6.37 (a)). Centre-surround suppression in the high-contrast surrounding condition was surprisingly unaffected by the inhibitory weight. Only for a low weight $w_{ie} = 0.1$ suppression was notably reduced. Interestingly, centre-surround facilitation for low a centre contrast in the low-surround condition strongly increased with inhibition (see Figure 6.38 (a)). Additional, detailed data for all conditions can be found in Tables B.3 and B.4 in the Appendix.

Centre-Surround Suppression for Contrast Texture Patterns Centre-surround suppression in response to texture patterns, highly depended on the inhibitory weight (see Figure 6.39 (a); full data in Tables B.5 and B.6 in the Appendix). Significant reductions only occurred, when the weight was in a narrow range around the standard configuration. In this range matching contrasts comparable to the standard configuration could be seen and there was no significant difference between the two surround conditions. Interestingly, the number of excluded cells was also very high outside of this range. When the weight was low, cells had a low r^2-value indicating a substantial contribution of inhibition to the contrast response. When the weight was high, cells showed generally weak responses but high r^2-values (Tables B.5 and B.6).

6.3.5.2. Weight of Excitatory Connections on Inhibitory Cells

The weight w_{ei} was varied next, controlling the strength of the excitatory connections onto inhibitory cells. Four different values were chosen: 0.005, 0.02, 0.05 and 0.1. Note that the standard value used in the previous simulations was 0.01. All other parameters of the network model were kept fixed at their standard values.

Orientation Selectivity Orientation selectivity was tested with the different values for the weight w_{ei} in the same way as before. Figure 6.35 (b) shows the orientation selectivity for different weights and compares it to the standard configuration. Orientation selectivity did not change strongly with varying weight.

Contrast Response Properties Figure 6.36 (b) shows the results for the r^2-values of the fits of the contrast response function to the mean response of the cells for different weights. Again, the contrast response properties of the network was independent from the weight. The goodness of fit was also very high (see Figure 6.36 (b)). Fitting parameters are presented in Table B.8 in the Appendix.

Centre-Surround Suppression for Sinusoidal Gratings In the size variation test, suppression was unchanged by changes in the weight (see Figure 6.37 (b)). Similarly, suppression in the high-surround condition was almost independent from the weight. However, facilitation for low centre contrasts in the low-surround condition decreased with the weight (see Figure 6.38 (b)). Data for all tested conditions are summarised in the Appendix (Tables B.9 and B.10).

Centre-Surround Suppression for Contrast Texture Patterns Figure 6.39 (b) shows the evolution of matching contrasts under increasing excitatory-to-inhibitory weight w_{ei}. Interestingly, lower weights led to lower matching contrasts, hence to higher suppression. At low weights (0.005 and 0.02) the matching contrasts were comparable to the standard configuration but only for $w_{ei} = 0.02$ the difference in response was significant. Higher weights resulted in higher matching contrasts and the responses did not significantly differ from each other. The two surround conditions did not produce significantly different results for the tested weight range. The full data is shown in Tables B.11 and B.12 in the Appendix.

6.3.5.3. Number of Inhibitory Cells

Here, the number of inhibitory cells was varied by reducing the number of inhibitory neurons to $88\,\%$ and $77\,\%$ of the standard number of cells. All other parameters of the network model were kept fixed at their standard values.

Orientation Selectivity Orientation selectivity was tested with the different amounts of inhibitory cells in the same way described previously. Figure 6.35 (c) shows the orientation selectivity for different amounts of inhibitory cells and compares it to the standard

configuration. The number of inhibitory neurons had a strong effect on orientation selectivity.

Contrast Response Properties Figure 6.36 (c) shows the results for the fit of the contrast response function to the mean response of the cells. For both conditions, a reasonable fit of the contrast response function was not possible, indicating a fundamental change in contrast response in the network model. Full details of the fitting procedure are shown in Table B.14 in the Appendix.

Centre-Surround Suppression for Sinusoidal Gratings In the size variation test, a strong influence of the number of neurons could be seen (see Figure 6.37 (c)). Further, a strong decrease in both suppression and facilitation was seen in the subsequent tests (Figure 6.38 (c)). Results for all tested conditions are presented in the Appendix (Tables B.15 and B.16).

Centre-Surround Suppression for Contrast Patterns Figure 6.39 (c) shows the matching contrasts for different amounts of inhibitory neurons in the network model. In the $88\,\%$ condition, the matching contrasts for the small surround condition and for the large surround condition did not differ significantly from the actual physical contrast. The matching contrasts for the two conditions also did not differ significantly. In the $77\,\%$ condition, the results were very similar. No significant differences were found either between the two surround conditions and the actual contrast, or between the two conditions. Hence, in both conditions matching contrasts and responses were higher than the standard configuration which implies that the amount of inhibitory neurons is an important factor for centre-surround suppression in this experimental setting. Additional data can be found in the Appendix (Tables B.17 and B.18).

6.3.5.4. Number of Inhibitory Connections to Excitatory Cells

Another factor governing intracortical inhibition in network model was the number n_{ie} of connections from inhibitory to excitatory cells. The influence of the number of inhibitory connections on the excitatory neurons was investigated by reducing the number of connections to roughly $88\,\%$ and $64\,\%$, respectively.

Orientation Selectivity Orientation selectivity was tested with the different amounts of inhibitory connections onto excitatory cells in the same way as before. Figure 6.35 (d)

shows the orientation selectivity for different amounts of inhibitory connections onto excitatory cells and compares it to the standard configuration. The influence of the amount of connections was only weak.

Contrast Response Properties Figure 6.36 (d) depicts the results for the fit of the contrast response function to the mean response of the cells. Again, a reasonable fit of the contrast response function was impossible, indicating a change in contrast response in the network model. All parameters of the fitting procedures are shown in Table B.20 in the Appendix.

Centre-Surround Suppression for Sinusoidal Gratings Suppression decreased with decreasing amounts of connections in the size variation test (see Figure 6.37 (d)). Suppression and facilitation in the two most important conditions also decreased with decreasing amounts of connections in the subsequent test (see Figure 6.38 (d)). An overview over all tested conditions can be found in the Appendix (Tables B.21 and B.22).

Centre-Surround Suppression for Contrast Patterns In Figure 6.39 (e) the matching contrasts for different amounts of excitatory connections are presented. In the $88\,\%$ condition, the matching contrasts for the small surround condition and for the large surround condition did not differ significantly from the actual physical contrast. Furthermore, the matching contrasts did not differ significantly between both conditions. The results were very similar in the $64\,\%$ condition. There were no significant differences either between the two surround conditions and the actual contrast, or between both conditions. Again, the matching contrasts in both conditions differed from the standard configuration. The higher matching contrasts showed that a decrease of inhibitory-to-excitatory connections reduced the centre-surround suppression. Further data are given in the Appendix (Tables B.23 and B.24).

6.3.5.5. Number of Excitatory Connections on Inhibitory Cells

Further the number of excitatory connections on inhibitory cells was reduced to $82\,\%$ and $66\,\%$, influencing mainly feed-back inhibitory effects. Again, all other network parameters were fixed at their standard values.

Orientation Selectivity Orientation selectivity was tested with the different numbers of excitatory connections onto inhibitory cells in the same way as before. Figure 6.35 (e) shows the orientation selectivity for different amounts of inhibitory cells and compares it

to the standard configuration. Interestingly, a reduction of excitatory-to-inhibitory connections further increased the orientation tuning.

Contrast Response Properties Figure 6.36 (e) summarises the results for the fit of the contrast response function to the mean response of the cells. No notable changes in the contrast response properties could be detected for a change in the amounts of connections. All fitting parameters can be found in the Appendix (Table B.26).

Centre-Surround Suppression for Sinusoidal Gratings In the size variation test, the suppression was hardly influenced by the amounts of connections (see Figure 6.37 (e)). Surprisingly, hardly no suppression at all was seen in the high centre and high surround condition (Figure 6.38 (e)). Suppression indices for all conditions of both tests are presented in Tables B.27 and B.28 in the Appendix.

Centre-Surround Suppression for Contrast Texture Patterns In the $82\,\%$ condition, the matching contrasts for the small surround condition and for the large surround condition did not differ significantly from the actual physical contrast (Figure 6.39 (e)). The matching contrasts for both conditions, however, did differ significantly from each other (Figure 6.39 (e); $p = .03$). The results were similar in the $66\,\%$ condition, with no significant differences between the two surround conditions and the actual contrast, but also no difference between the two conditions (Figure 6.39 (e)). All matching contrasts were higher than for the standard configuration, that is, a reduction of excitatory-to-inhibitory connections reduced the centre-surround suppression. Further data can be found in Tables B.29 and B.30 in the Appendix.

6.3.5.6. Decay Times at GABAergic Synapses

The last considered factor that governed inhibition in the cortical network model, was the synaptic decay time constant τ at GABAergic synapses. The time constant τ was changed using five different values, namely 15, 20, 25, 30 and 50, and all other parameters were kept fixed.

Orientation Selectivity Again, orientation selectivity was tested with the different time constants for the inhibitory GABAergic synapses in the same way as before. Figure 6.35 (f) summarises the results for the five conditions. Additionally, for comparison, the results from same simulations are shown, using the standard time constant $\tau = 8\,ms$. The

prolonged time constants reduced the orientation tuning of the cells, the number of selective and biased cells dropped, the ORI decreased and the CV increased, with respect to the standard time constant of $\tau = 8\,ms$. However, the amount of prolongation did not seem to have an effect on the tuning, since all measures did not differ considerably for the prolonged time constants tested.

Contrast Response Properties Figure 6.36 (f) summarises the results for the fit of the contrast response function to the mean response of the cells. The variation of the decay time constant τ hardly influenced the contrast response properties of the network. An overview over all fitting parameters is presented in the Appendix in Table B.32.

Centre-Surround Suppression for Sinusoidal Gratings The results of the size variation test are presented in Figure 6.37 (f). A prolongation of decay times at GABAergic synapses leads to a small decrease in suppression from $87\,\%$ to $85\,\%$. Again, it did not matter by how much the decay time constant was increased, the overall suppression stayed constant. On the contrary, suppression and facilitation were markedly reduced in the second centre-surround suppression test (see Figure 6.38 (f)). Additional data is shown in the Appendix in Tables B.33 and B.34.

Centre-Surround Suppression for Contrast Patterns The matching contrasts for the small surround condition and the large surround condition did not differ significantly from the actual physical contrast for any of the decay time constant manipulations (Figure 6.39 (f)). Similarly, the matching contrasts did not differ significantly between the small and large surround conditions for any of the decay time constants (Figure 6.39 (f)). However, all matching contrasts were higher than the standard configuration, hence, a prolongation of the decay times reduced suppression. Additional data is shown in the Appendix in Tables B.35 and B.36.

7. Experimental Studies

7.1. Introduction

Chapter 1 explained how inhibition as a form of gain control influences the visual properties of single cells, the classical receptive field properties, as well as extra-classical properties such as centre-surround suppression. This chapter will deal with the psychophysical effects of surrounds in humans, that is, the perceptual centre-surround suppression and its neural correlates.

There are two main effects of surrounds in visual perception: surrounds introduce **bias**, that is, the stimuli are perceived different from the physical reality, and they decrease **sensitivity**, that is, they make it harder to detect stimuli. These two effects appear in different modalities. Chubb et al. [43] found an introduction of bias for luminance and, especially, for contrast. They demonstrated that the size of the effect depended on the overlap of spatial frequencies in target and surround stimuli. Furthermore, conditions such as motion [21, 150], size and orientation are known to be biased by a surrounding stimulus. Figure 7.1 shows typical stimuli for luminance, orientation, contrast and size used in human psychophysical studies. These phenomena are attributed to centre-surround suppression [206].

However, centre-surround suppression occurs at different stages of visual processing for the different conditions. Table 7.1 shows the different conditions and the loci where they occur along the visual pathway. Since the focus of this work lies on the interaction of recurrent processing within the primary visual cortex (V1) and feed-forward convergence of lateral geniculate nucleus (LGN) input, the experiments described here concentrate on contrast discrimination and the introduction of bias in this dimension, which takes place in LGN and V1. In addition to psychophysical research on centre-surround suppression, several neuroimaging studies have addressed the relationship of psychophysical effects, blood-oxygenation-level dependent (BOLD) responses and neural activity. Contrast discrimination performance is consistent with responses in V1 obtained with functional magnetic resonance imaging (fMRI) [24]; and the suppressive effect of neighbouring stimuli [114], as well as orientation-specific inhibitory effects have been shown

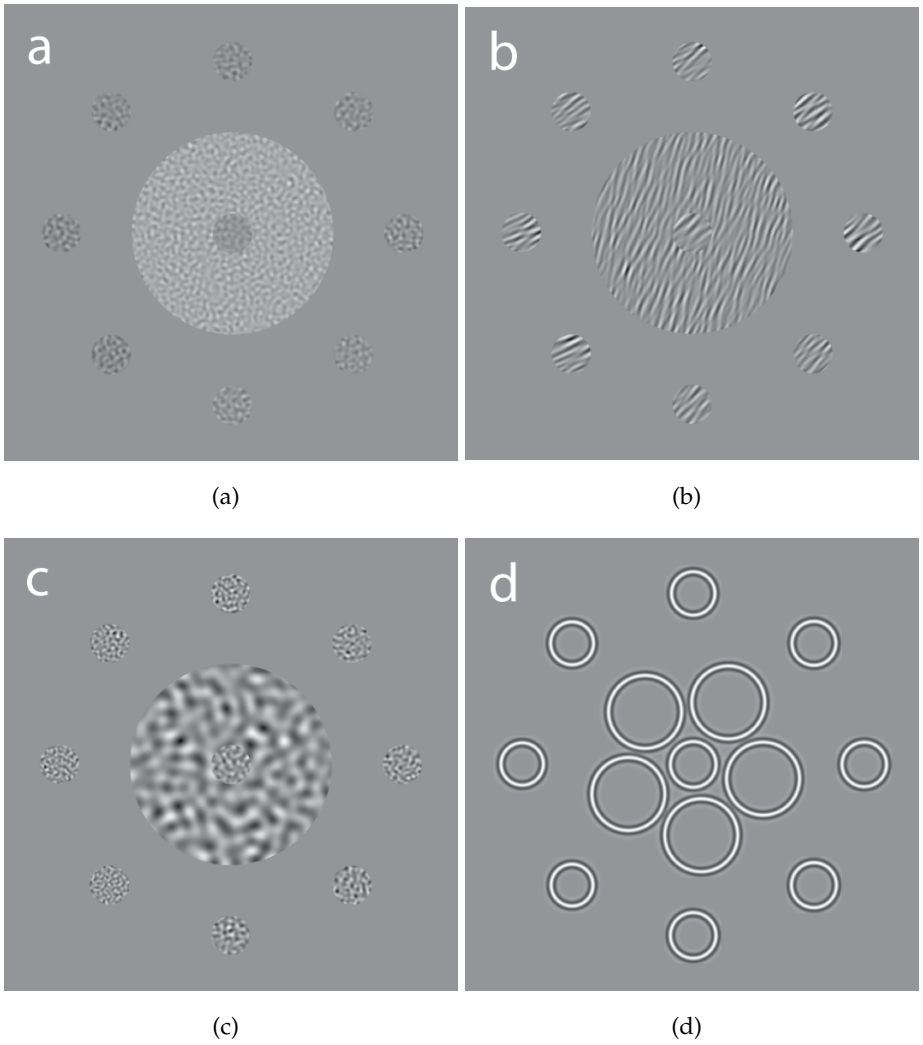

Figure 7.1.: Typical psychophysical stimuli for four of the five conditions producing a perceptual bias in discrimination tasks with surrounds: (a) luminance, (b) orientation, (c) contrast and (d) size. The centre-surround stimulus is depicted in the middle and several centre-only stimuli are placed around it. Usually, centre-surround and centre-only stimuli are shown subsequently and the centre-only stimulus is modified until both stimuli match perceptually. (Image modified from [206]).

Visual Attribute	Locus
Luminance	Retina/LGN
Contrast	LGN/V1
Orientation	V1/V2/V4
Size	V1/V2/V4
Motion	MT/MST

Table 7.1.: The five different conditions producing bias and their apparent locus of processing [e.g. 206].

using fMRI [113]. There is also quantitative agreement between psychophysical surround effects on contrast discrimination, that is, the introduced bias, and the response suppression in V1 obtained by fMRI [230].

Since centre-surround suppression relies on inhibition, it is natural to investigate its link to the neurotransmitter GABA, which is responsible for cortical inhibition. Several electrophysiological and modelling studies have associated the GABAergic system to surround effects [7, 185], and all theories of centre-surround suppression presented in Chapter 3 at least partially attribute centre-surround suppression to inhibition. Furthermore, studies have reported that GABA concentration, measured using magnetic resonance spectroscopy (MRS), is a predictor for BOLD response amplitude in V1 [151] and also in the anterior cingulate cortex [155]. However, neural dynamics strongly depend on the balance between excitation and inhibition, and thus not only the inhibitory neurotransmitter might be important, but also its excitatory counterpart glutamate, as well as the ratio between both.

In summary, centre-surround suppression introduces a bias in the perception of visual stimuli in the presence of surround stimuli. This bias is, at least partially, the result of inhibitory activity elicited by the surround stimulus and is mediated via GABAergic inhibition. Hence, retinotopically reduced BOLD responses appear as neural correlates of centre-surround suppression [230]. Furthermore, the amount of available GABA is a predictor of neural activity in response to stimulation and hence a predictor of centre-surround suppression strength.

Interestingly, the introduction of bias is less pronounced in schizophrenic patients and subjects with schizotypical traits for some conditions, such as contrast [12, 51, 227–229], motion [203] and size [206, 213, 214]. Furthermore, cognitive and perceptual deficits in these patients are sometimes attributed to a compromised GABAergic system: the so-called **GABA-Hypothesis** of schizophrenia [130]. Evidence for reduced GABA levels

comes from studies showing a deficient synthesis of glutamate decarboxylase (GAD67), which is a crucial step in the production of GABA [1, 82, 83, 217]. Indeed, animal experiments where the gene responsible for the production of GAD67 is knocked out, show a significant reduction in GABA levels [8, 41].

Therefore, a disruption of excitatory and inhibitory balance in cortical circuits might lie at the core of schizophrenia, which might manifest itself as a ubiquitous deficit in context processing.

For this reason, centre-surround suppression and its neural correlates were investigated in an experimental study, involving schizophrenic patients and healthy controls. It used a psychophysical paradigm, and measured neurotransmitter concentrations (GABA and glutamate) using MRS and BOLD responses to high contrast stimuli using fMRI. The hypotheses were:

1. **Hypothesis:**
   The concentration of GABA (the ratio of glutamate/GABA) in V1 is reduced (increased) for schizophrenic patients.

2. **Hypothesis:**
   The contrast-evoked BOLD response in V1 is reduced for schizophrenic patients.

3. **Hypothesis:**
   Perceptual centre-surround suppression in schizophrenic patients is reduced in comparison to healthy controls.

4. **Hypothesis:**
   The strength of perceptual centre-surround suppression and the concentration of GABA (the glutamate/GABA ratio) are correlated in V1.

5. **Hypothesis:**
   The visually evoked BOLD response in V1 and the strength of perceptual centre-surround suppression are correlated.

6. **Hypothesis:**
   The visually evoked BOLD response in V1 and the concentration of GABA (the glutamate/GABA ratio) in V1 are correlated.

7.2. Methods

7.2.1. Subjects

Forty patients (21 male) who met DSM-IV criteria for schizophrenia or schizoaffective disorder were recruited from the Department of Psychiatry of the UKSH/University of Lübeck, both from psychiatric inpatient units and from an outpatient treatment unit (most of the latter were former inpatients of the psychiatric hospital). All patients were under treatment with atypical neuroleptics at the time of examination. The Structured Clinical Interview for DSM-IV (SCID) was applied, and the medical recordings were reviewed to determine the diagnosis and rule out patients with co-morbid addiction disorders and severe somatic disorders. Furthermore, patients on benzodiazepine medication within seven days before examination were excluded. All interviews and diagnoses were conducted by the staff of the Department of Psychiatry of the UKSH/University of Lübeck.

Overall, 25 patients had to be excluded from the final analysis (see Figure 7.2 and Table 7.2 for a summary). The mean age of the 15 patients (9 male) included in the final analysis was 34.13 ± 8.76 years, and the mean education time was 11.9 ± 2.78 years (see Figure 7.4). Clinical symptoms were assessed with the Positive and Negative Syndrome Scale (PANSS, [115]). Some of the patients were in an acute state of illness at the time of examination, some suffered of a predominant negative syndrome, while another group could be regarded as remitted according to the criteria of the Remission in Schizophrenia Criteria Working Group [5].

Table 7.2.: Exclusion criteria for the study.

	Threshold
General	Neurological Disorder, Substance Abuse
MRS	Cramer-Rao bound > 30 for GABA or glutamate
fMRI	Severe motion artefacts
Vision	Contrast sensitivity threshold $> 2.5\,\%$ Visual acuity < 0.8 (logMAR)
Psychophysics	Inter-trial variability $> 8.0\,\%$

Twenty-five healthy controls (14 male) with no history of mental illness or neurological disorder were recruited from the community. Thirteen control participants (8 male) were included in the final analysis. The other 12 subjects were excluded on the basis

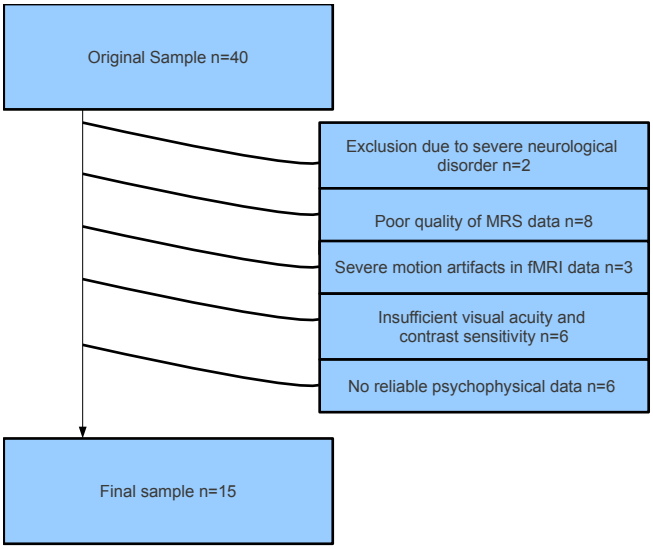

Figure 7.2.: Depiction of the exclusion process in the patient group.

Table 7.3.: Summary of the visual acuity and contrast sensitivity in both groups.

	Patient Group	Control Group	Difference
Visual Acuity (logMAR)	1.28±0.21	1.34±0.32	n.s. $p = .55$
Contrast Sensitivity (% Contrast)	0.87±0.26	0.78±0.29	n.s. $p = .42$

of the same criteria as the patients (see Figure 7.3 for a summary). None of the control subjects were under psychotropic medication. They were matched in age (paired t-test, $p = .29$) and sex (χ^2-test, $p = .89$) with the patient group, although control subjects had a significantly higher education time (paired t-test, $t(26) = 3.42$, $p < .01$, see Figure 7.4). All participants gave written informed consent for their participation and the study was approved by the ethics committee of the UKSH/University of Lübeck.

To address other factors that might affect performance in the psychophysical task, all subjects performed two screening tasks to assess visual acuity and visual contrast sensitivity, respectively. These were measured using the Freiburg Visual Acuity and Contrast Test (FrACT [9]), administered at a viewing distance of 190 cm.

Participants were excluded if they did not have normal or corrected-to-normal vision (a score of less than 0.8 logMAR in the visual acuity task (see Table 7.2)) or were unable to resolve low contrast stimuli (a score of more than $2.5\,\%$ in the contrast sensitivity task

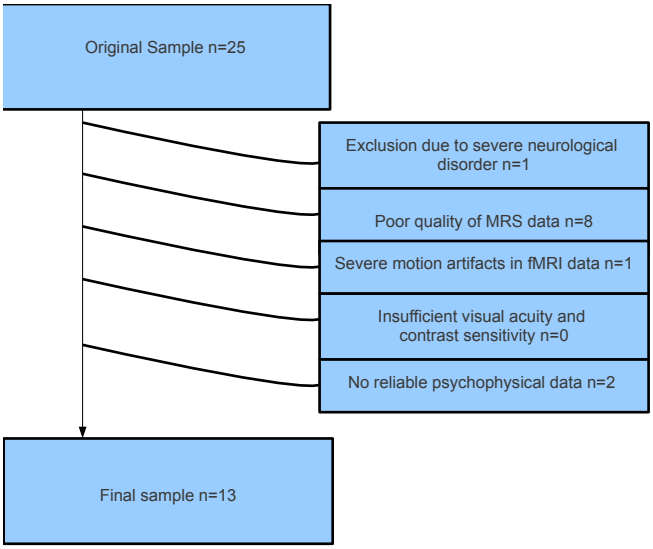

Figure 7.3.: Depiction of the exclusion process in the control group.

(see Table 7.2)). The healthy control group was matched with the patient group regarding visual acuity and contrast sensitivity (see Figure 7.5 and Table 7.3).

7.2.2. MR Spectroscopic Measures of Neurotransmission

Proton magnetic resonance spectroscopy (1H-MRS) is a technique that allows for the identification of selected biochemical compounds, and for the quantification of these compounds. MRS was used to quantify the levels of glutamate and GABA in V1 of the participants. The measurements were performed by the staff of the Department of Neuroradiology of the UKSH.

Apparatus and Experimental Setup MRS was performed using a Philips Achieva 3T scanner with a standard head coil (Philips SENSE-Head-8). A point-resolved spectroscopy (PRESS) sequence was used (TR: $2000\,\text{ms}$, TE: $80\,\text{ms}$, scan duration: $4{:}22.0$ min, spectral resolution: 0.9766 Hz/point) with the TE optimised to reduce the overlapping glutamate and glutamine peaks at around 2.1 and $2.4\,ppm$. A $25 \times 25 \times 25\,mm$ voxel was placed at AP= 65.0, RL= 1.1 and FH= 3.6 bilaterally in the occipital lobe covering area V1 according to probability maps acquired across subjects [63] similar to previous studies [151].

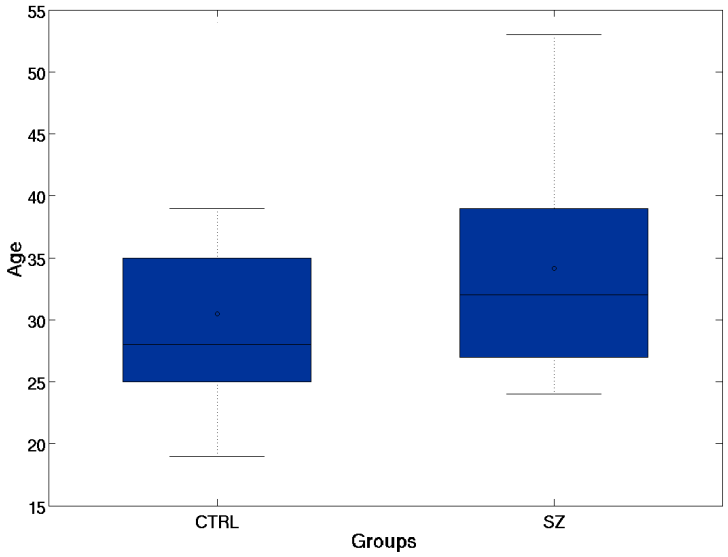

(a)

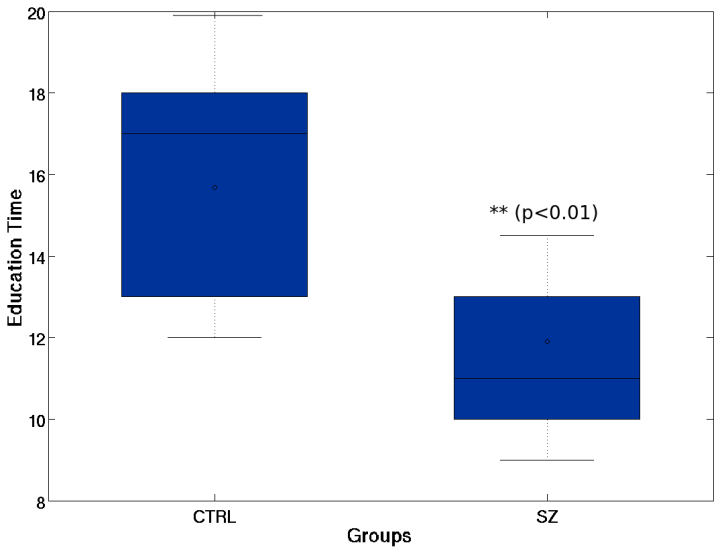

(b)

Figure 7.4.: Demographic data for patient (SZ) and control (CTRL) groups: distributions of (a) age (in years) and (b) education time (in years). On each box, the central mark is the median, the edges of the box are the 25th and 75th percentiles, the whiskers extend to the most extreme data points not considered outliers, and outliers (i.e. values larger than $q_3 + 1.5 \cdot (q_3 - q_1)$ or smaller than $q_1 - 1.5 \cdot (q_3 - q_1)$, where q_1 and q_3 are the 25th and 75th percentiles, respectively) are plotted individually.

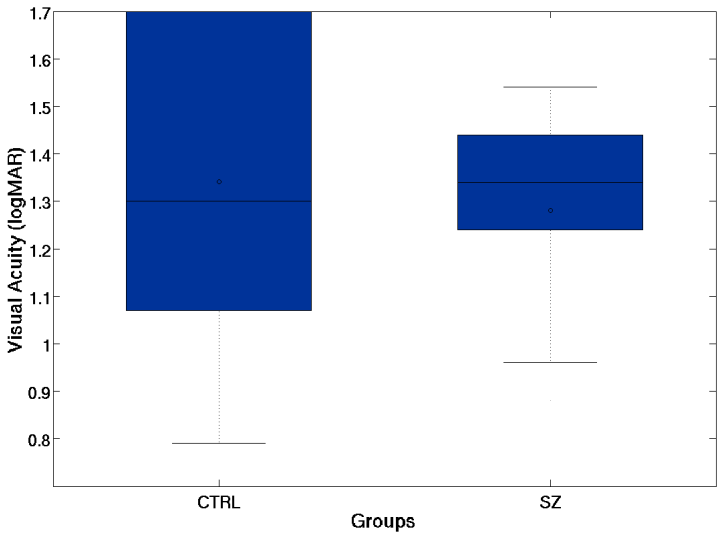

(a)

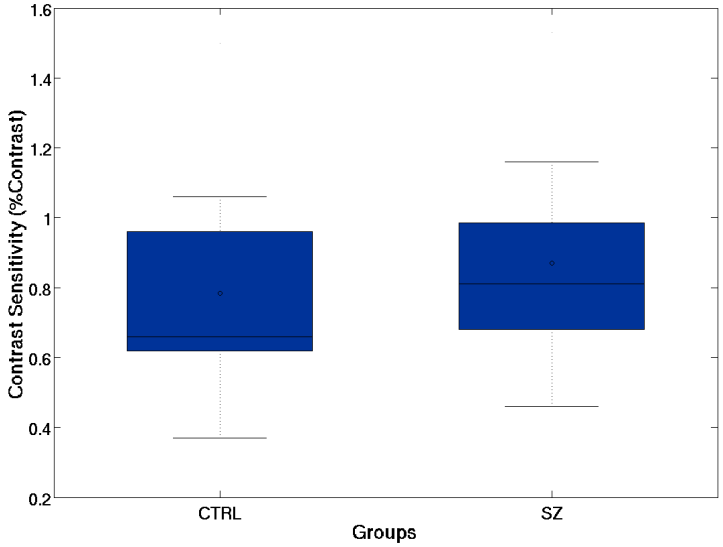

(b)

Figure 7.5.: Performances of the patient (SZ) and control (CTRL) groups in the Freiburg Visual Acuity and Contrast Test (FrACT): (a) visual acuity (Note that the maximum value was 1.7 due to the viewing distance and screen resolution) and (b) contrast sensitivity. On each box, the central mark is the median, the edges of the box are the 25th and 75th percentiles, the whiskers extend to the most extreme data points not considered outliers, and outliers (i.e. values larger than $q_3 + 1.5 \cdot (q_3 - q_1)$ or smaller than $q_1 - 1.5 \cdot (q_3 - q_1)$, where q_1 and q_3 are the 25th and 75th percentiles, respectively) are plotted individually.

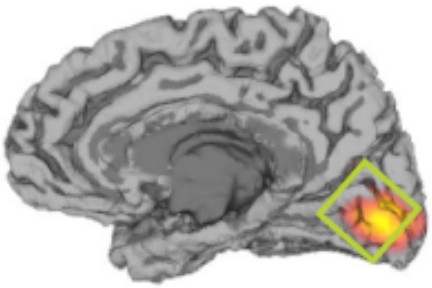

Figure 7.6.: Sagittal view of the voxel positioning for the magnetic resonance spectroscopy (modified from [151]).

Data Analysis LCModel ([167]) was used to analyse the MRS data, a software tool that uses a linear combination of *in vitro* model spectra from different metabolite solutions to quantify metabolites in *in vivo* spectra. This tool offers the advantage of incorporating full model spectra instead of peak information, and a near model-free regularisation method for the estimation. It also requires no user input, thus preventing implicit, subjective user impact on the data.

Statistical analyses of group differences between patients and controls for the absolute GABA and glutamate concentrations, as well as for the GABA and glutamate concentrations normalised with respect to the creatine concentration, using standard parametric (t-test and one-way ANOVA) and non-parametric (Mann-Whitney and Kruskal-Wallis) statistics, where applicable. All statistical analyses were performed using MATLAB [141].

7.2.3. Functional MR Imaging of Contrast Processing

fMRI is a technique to non-invasively measure brain activity using the magnetic properties of the haemoglobin in the blood: oxygenated haemoglobin is diamagnetic, resulting in an increased MR signal; whereas de-oxygenated haemoglobin is paramagnetic, resulting in a decreased MR signal, an effect first described by Ogawa et al. [158, 159]. During a functional scan the participant is placed inside the MR scanner and the brain is imaged repeatedly during the performance of a specific task. The BOLD contrast results from the differences in the images as a function of the amount of de-oxygenated haemoglobin in a certain brain region. When neurons become active, for example, as a result of the participant performing a cognitive task, the supply of oxygenated haemoglobin to those neurons increases, decreasing the amount of de-oxygenated haemoglobin in that area, and thus decreasing the MRI signal loss [131]. In this way, fMRI allows for the local-

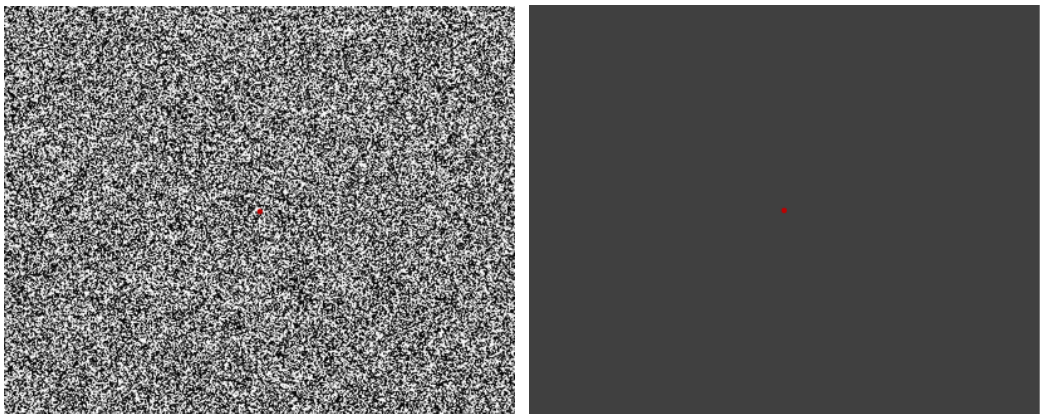

(a) (b)

Figure 7.7.: Stimuli for the fMRI task: (a) contrast texture pattern stimulus presented during ON-blocks, and (b) uniformly grey stimulus for the OFF-blocks. Note that the average luminance level for both stimuli is the same.

isation and the identification of functional networks and even for the classification of psychological or disease states [100].

Apparatus and Experimental Setup fMRI was performed using a Philips Achieva 3T scanner with the standard head coil, as in the MRS experiments. Participants lay in supine position with their heads placed on a head-rest lined with soft foam. Stimuli were presented through a standard binocular goggle system (VisuaStim Digital Goggles,[216]). A standard echo-planar imaging (EPI) sequence was acquired during stimulus presentation (TE: 30 ms , TR: 4000 ms interleaved, 48 slices, slice thickness: 3 mm , voxel size: 3×3 mm^2, 80×79 voxels/slice, scan duration: 7:12.0 min). A 3D T1-weighted anatomical scan was obtained for structural reference. All measurements were performed by the staff of the Department of Neuroradiology of the UKSH.

Procedure A blocked design was used consisting of 21 blocks in total, 10 ON-blocks and 11 OFF-blocks. Each block had a duration of 20s, resulting in a total scan time of approximately seven minutes and a total number of 105 acquired volumes. During the ON-blocks, a high-contrast pattern with a Michelson contrast of $.95$ (see Figure 7.7 (a)) was presented. A red dot in the centre of the image served as a fixation point. Single frames with randomly plotted contrast patterns were replotted each 500 ms. However, the characteristics of the different contrast patterns did not change. During the OFF-blocks (see

Figure 7.7 (b)), a uniformly grey image was shown which had the same average luminance as the contrast patterns. Again, a red dot served as fixation point. The stimuli were presented using the software package *Presentation* [165]. Participants were asked to avoid eye movements and were instructed to keep their eyes fixated on the red dot during the whole fMRI session.

Data Analysis Data from the first three scans were discarded due to T1 saturation effects. A standard pre-processing procedure was then applied to the fMRI time series using the SPM 8 software tool (Wellcome Trust Centre for Neuroimaging, UCL, London, UK, [72]) implemented in MATLAB [141] .

The pre-processing included:

1. Slice-timing correction, to correct for the different acquisition times of slices within each volume.

2. Motion correction, in order to compensate for motion during the fMRI session.(A rigid six-degrees of freedom registration of all volumes to the mean volume)

3. Normalisation to the standard EPI volume provided by SPM and interpolation to a resolution of $2 \times 2 \times 2\,\mathrm{mm}^3$.

4. Smoothing with a Gaussian kernel with a FWHM of $6\,\mathrm{mm}$ in each dimension.

After the pre-processing, any significant changes in regional BOLD signal were estimated at the individual level by contrasting the ON- and OFF-blocks voxel-wise. To analyse the differences between the patient and control groups, the individual statistical maps were inputted in an independent samples t-test, thereby generating a random-effect models, allowing inference to the general population. These statistics were consequently transformed into z-statistics and visualised as colour-coded z-maps.

7.2.4. Psychophysical Measurement of Centre-Surround Suppression

Experimental Set-up and Procedure Perceptual measures of context processing were introduced in the beginning of this chapter, and the question arises how to quantitatively measure the bias caused by the inclusion of surrounds in visual stimuli. A well established approach is to use surrounds that create perceptual illusions, that is to say, that produce a percept of the centre stimulus that is substantially different from the percept without surround. The effect of the surround is quantitatively measured by acquiring

a psychometric function, namely by quantifying the probability of perceiving one stimulus as having a higher contrast than the other as a function of the difference between them. The **point of subjective equivalence (PSE)**, is the point at which two stimuli are perceived to be identical, and is thus defined as the point of the psychometric function where the above-mentioned probability is exactly $50\,\%$. Since the stimuli were designed so that the physical match of the stimuli or, in other words, the **point of objective equivalence (POE)** was known, the bias, or the strength of the **centre-surround suppression (CSS)**, could simply be calculated as the difference between PSE and POE:

$$CSS = PSE - POE. \tag{7.1}$$

This study focused on the contrast-contrast illusion and used stimuli (see Figure 7.8) very similar to those of Chubb et al. [43] and also similar to those of Dakin et al. [51].

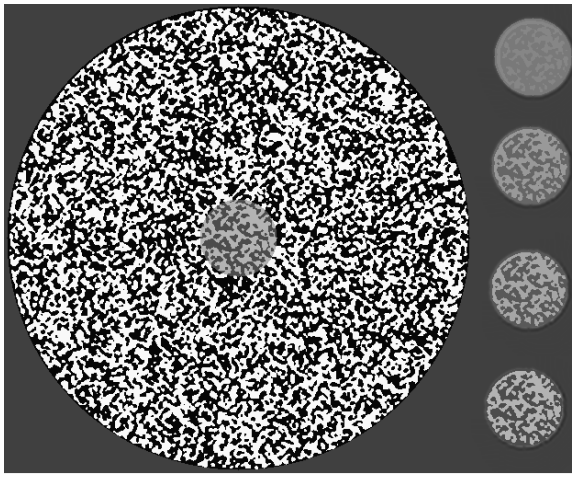

Figure 7.8.: Image of the target stimulus. On the left a centred circle of a noise pattern with a Michelson contrast of .4, surrounded by a disk with a noise pattern of the same characteristics but with a contrast of .95. On the right, four possible reference contrasts with .1, .2, .3 and .4 contrast, respectively. Most subjects' point of subjective equivalence lies between references two or three, although circle four is the exact physical match to the target stimulus. (Note that the surround width and hence the eye-stimulus distance is crucially influencing the effect [32].)

A simple two-interval up-down staircase procedure [123] was used, presenting the fixed .4 contrast target patch with surrounding in the first interval, and a contrast-variable reference patch without surrounding in the second (see Figure 7.9). The start of the first interval was preceded by the appearance of a fixation cross. Both intervals lasted 1000 ms. Subjects made their response by pressing either the left or right mouse button, indicating the first and the second stimulus to have higher contrast, respectively. The range of

contrast to be tested was .05 - .6 and the task was designed to converge to the point of subjective equivalence. Acquisition of individual CSS was achieved by running 12 independent trials, each converging at the PSE. The single CSS acquisitions were averaged for each subject. A large inter-trial variability, that is, a standard deviation of the CSSs of the 12 trials of ≥ 8.0, was considered an exclusion criterion (see 7.2).

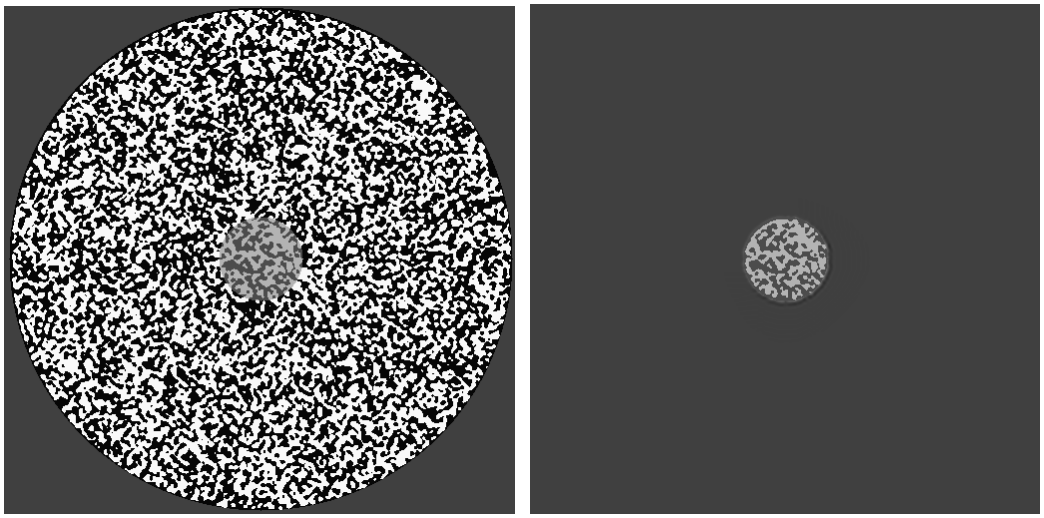

(a) (b)

Figure 7.9.: Stimuli for the psychophysical task. (a) The target stimulus and (b) an example reference stimulus with a contrast of .6 are shown.

7.3. Results

7.3.1. MR Spectroscopic Measures of Neurotransmission

1. Hypothesis:
The concentration of GABA (the ratio of glutamate/GABA) in V1 is reduced (increased) for schizophrenic patients.

^{1}H-MR spectra were acquired from a single voxel in the occipital lobe for all participants of the study using a standard PRESS sequence with a specialised echo time $TE = 80\,\text{ms}$. Table 7.4 shows the results for the neurotransmitter GABA for the control

Table 7.4.: Individual absolute GABA concentrations, GABA/creatine ratios and Cramer-Rao bounds for the control group.

	C1	C2	C3	C4	C5	C6	C7	C8	C9
GABA conc.	1.543	1.625	1.478	1.488	1.571	1.728	1.660	1.606	1.833
GABA/Creatine ratio	0.237	0.249	0.210	0.205	0.247	0.232	0.265	0.213	0.265
Cramer-Rao bound (%SD)	18	23	17	21	19	14	20	17	16

	C10	C11	C12	C13
GABA conc.	1.714	1.839	0.937	1.927
GABA/Creatine ratio	0.252	0.267	0.153	0.262
Cramer-Rao bound (%SD)	16	16	23	17

group. Absolute concentrations as well as GABA/creatine ratios as a normalised measure are reported. The ratio is reported because the absolute concentration depends on the amount of cerebrospinal fluid and grey and white matter in the voxel and also on the signal strength which may vary between participants [53]. Furthermore, the Cramer-Rao bound is also reported for each subject, which gives an estimate on the quality of the spectrum and the fitting used in the analysis [38]. Table 7.5 shows the same data for the patients group. On the whole, a high Cramer-Rao bound can be seen for the GABA estimates, which is due to the spectral overlap of GABA with more prominent metabolites. Nevertheless, the sequence used was able to reliably detect and quantify GABA levels for the studied participants. Figure 7.10 compares the GABA levels for the two groups.

Table 7.6 shows the control group's results for the neurometabolite glutamate. Again, individual absolute concentrations are reported, as well as glutamate/creatine ratios and the Cramer-Rao bounds. Table 7.7 shows the same data for the patients group. A low Cramer-Rao bound for glutamate can be seen here, which is substantially below the exclusion threshold of 30. This demonstrates that the specialised PRESS sequence can detect and quantify glutamate with a high reliability. Figure 7.11 contrasts glutamate levels in both groups. Tables 7.8 and 7.9 report the glutamate/GABA ratios for control and patient groups, respectively, and Figure 7.12 contrasts the ratios in the groups.

Table 7.10 summarises the results of the MRS measurements of neurotransmitter concentrations in both groups. A significant difference can be seen for GABA levels (abso-

Table 7.5.: Individual absolute GABA concentrations, GABA/creatine ratios and Cramer-Rao bounds for the patient group.

	P1	P2	P3	P4	P5	P6	P7	P8	P9
GABA conc.	1.771	1.110	1.339	1.444	1.035	1.400	1.330	1.231	1.422
GABA/Creatine ratio	0.255	0.246	0.172	0.196	0.150	0.204	0.223	0.190	0.214
Cramer-Rao bound (%SD)	17	26	20	19	25	26	21	23	25

	P10	P11	P12	P13	P14	P15
GABA conc.	1.810	1.209	1.591	1.674	1.434	1.089
GABA/Creatine ratio	0.258	0.180	0.207	0.237	0.204	0.147
Cramer-Rao bound (%SD)	18	22	21	20	21	23

Table 7.6.: Individual absolute glutamate concentrations, glutamate/creatine ratios and Cramer-Rao bounds for the control group.

	C1	C2	C3	C4	C5	C6	C7	C8	C9
Glutamate conc.	6.362	6.608	6.104	6.861	6.939	7.805	6.601	6.616	6.926
Glutamate/creatine ratio	0.976	1.014	0.868	0.944	1.090	1.047	1.053	0.877	1.000
Cramer-Rao bound (%SD)	7	9	7	7	7	5	8	6	7

	C10	C11	C12	C13
Glutamate conc.	6.701	6.680	4.981	8.206
Glutamate/creatine ratio	1.004	0.971	0.813	1.117
Cramer-Rao bound (%SD)	7	7	10	9

Table 7.7.: Individual absolute glutamate concentrations, glutamate/creatine ratios and Cramer-Rao bounds for the patient group.

	P1	P2	P3	P4	P5	P6	P7	P8	P9
Glutamate conc.	8.060	4.620	6.174	7.216	6.659	6.755	5.958	6.328	6.850
Glutamate/creatine ratio	1.159	1.019	0.794	0.977	0.968	0.985	0.997	0.976	1.033
Cramer-Rao bound (%SD)	6	10	7	6	6	9	7	7	8

	P10	P11	P12	P13	P14	P15
Glutamate conc.	7.476	6.378	6.680	6.108	6.670	6.000
Glutamate/creatine ratio	1.066	0.949	0.894	0.866	0.950	0.811
Cramer-Rao bound (%SD)	7	7	8	9	7	7

Table 7.8.: Glutamate/GABA ratios for the control group.

	C1	C2	C3	C4	C5	C6	C7	C8	C9
Glutamate/GABA. ratio	4.123	4.067	4.130	4.611	4.417	4.517	3.977	4.120	3.779

	C10	C11	C12	C13
Glutamate/GABA ratio	3.910	3.632	5.316	4.285

Table 7.9.: Glutamate/GABA ratios for the patients group.

	P1	P2	P3	P4	P5	P6	P7	P8	P9
Glutamate/GABA ratio	4.551	4.162	4.611	4.997	6.434	4.825	4.480	5.141	4.817

	P10	P11	P12	P13	P14	P15
Glutamate/GABA ratio	4.130	5.275	4.199	3.649	4.651	5.510

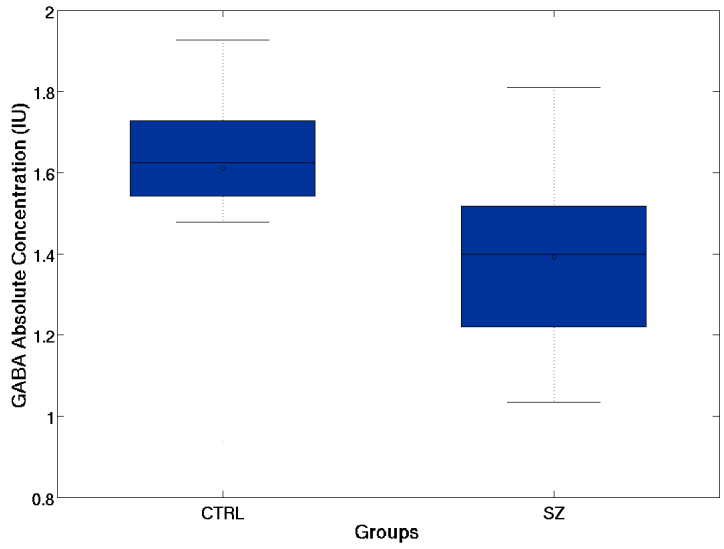

(a)

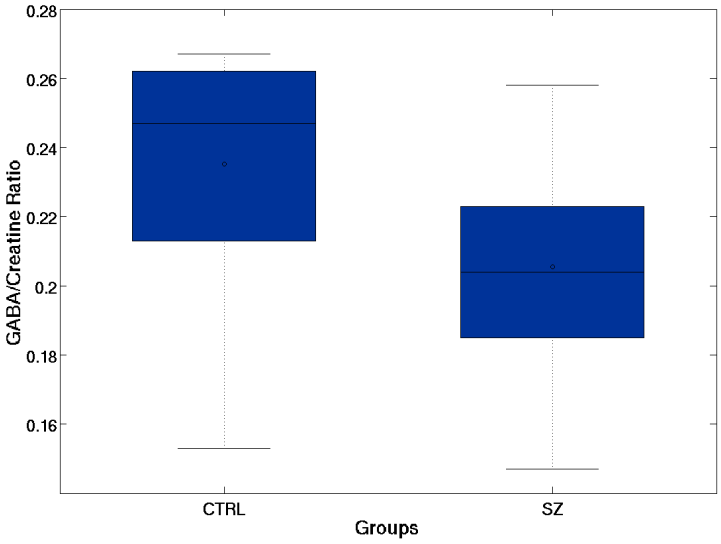

(b)

Figure 7.10.: Box plots of (a) absolute GABA concentrations and (b) GABA concentrations relative to creatine (GABA/creatine ratios) for both patient (SZ) ad control (CTRL) groups.On each box, the central mark is the median, the edges of the box are the 25th and 75th percentiles, the whiskers extend to the most extreme data points not considered outliers, and outliers (i.e. values larger than $q_3 + 1.5 \cdot (q_3 - q_1)$ or smaller than $q_1 - 1.5 \cdot (q_3 - q_1)$, where q_1 and q_3 are the 25th and 75th percentiles, respectively) are plotted individually.

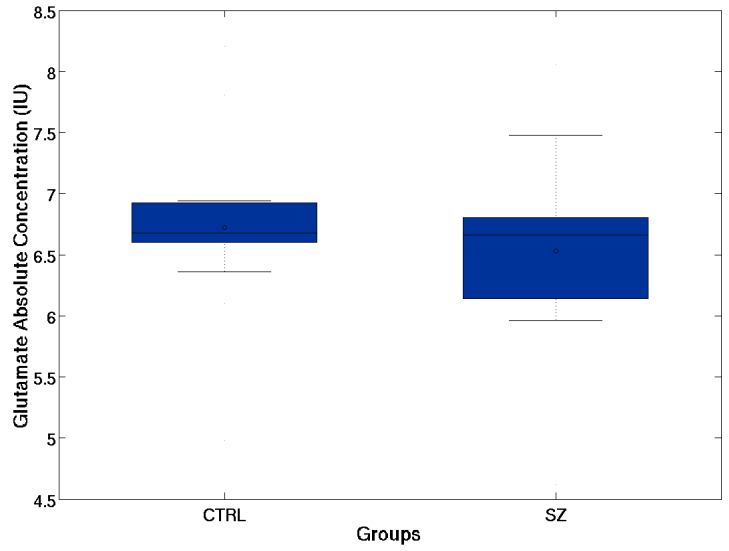

(a)

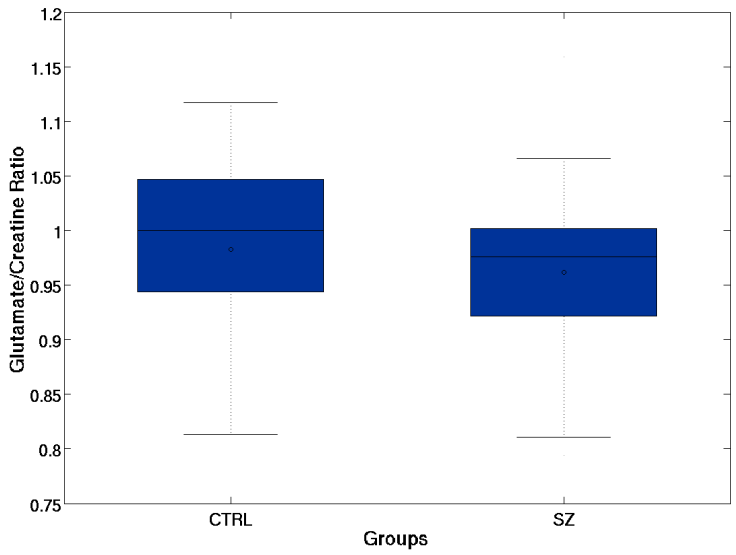

(b)

Figure 7.11.: Box plots of (a) absolute glutamate concentrations and (b) glutamate concentrations relative to creatine (glutamate/creatine ratios) for both patient (SZ) and control (CTRL) groups. On each box, the central mark is the median, the edges of the box are the 25th and 75th percentiles, the whiskers extend to the most extreme data points not considered outliers, and outliers (i.e. values larger than $q_3 + 1.5 \cdot (q_3 - q_1)$ or smaller than $q_1 - 1.5 \cdot (q_3 - q_1)$, where q_1 and q_3 are the 25th and 75th percentiles, respectively) are plotted individually.

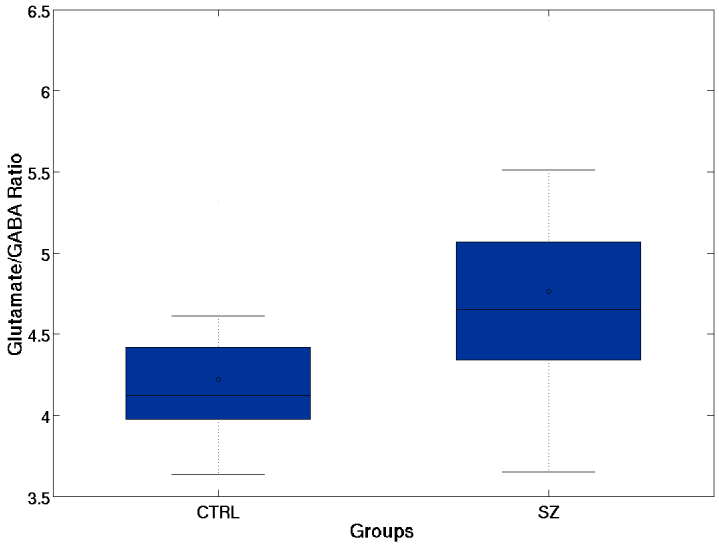

Figure 7.12.: Glutamate/GABA ratios in patient (SZ) and control group (CTRL). On each box, the central mark is the median, the edges of the box are the 25th and 75th percentiles, the whiskers extend to the most extreme data points not considered outliers, and outliers (i.e. values larger than $q_3 + 1.5 \cdot (q_3 - q_1)$ or smaller than $q_1 - 1.5 \cdot (q_3 - q_1)$, where q_1 and q_3 are the 25th and 75th percentiles, respectively) are plotted individually.

lute and GABA/creatine ratio, $p < .05$ and $p < .05$, respectively) as well as a significantly higher glutamate/GABA ratio in the patient group ($p < .05$). The glutamate levels, however, do not differ ($p > .05$).

Furthermore, correlation coefficients were calculated for age and education time with the GABA/creatine, glutamate/creatine and glutamate/GABA ratios, respectively, in order to exclude possible confounders . Results are summarised in Tables 7.11 and 7.13. Given that all correlation coefficients were statistically not significant ($p > .05$), education time was not included as a regressor in the model, although the groups differed statistically regarding education time. However, age significantly correlated with the glutamate/GABA ratio in the patient group, and since there was a significant group difference between the correlation coefficients for age and glutamate/GABA ratios (Fisher z-transform, $z = 2.19$, $p < .05$), an ANCOVA was conducted with age as a covariate. The results are depicted in Figure 7.14 and Table 7.12. A significant difference in glutamate/-GABA ratios between both groups ($p < .01$) and a significant interaction of group with age ($p < .05$) was found.

Additionally, correlation coefficients for visual acuity and contrast sensitivity with the neurotransmitter measures were calculated in order to rule out visual capabilities

Table 7.10.: Comparison of the MRS measurements of glutamate and GABA concentrations in patient and the control groups. An independent two-sample t-test with unequal sample size and unequal variance was used, to test for differences in the mean between both groups. Statistical significance level was set to $p < .05$. Absolute and relative GABA concentrations were significantly reduced in the patient group, whereas the glutamate concentrations were not different. Moreover, the glutamate/GABA ratio was significantly lower in the control compared to the patient group.

	Control Group	Patient Group	Difference
GABA (abs. conc.)	**1.61 ± 0.25**	**1.39 ± 0.24**	*** sign. $p < .03$**
GABA/Cr ratio	**0.24 ± 0.03**	**0.21 ± 0.03**	*** sign. $p < .04$**
Glut (abs. conc.)	6.72± 0.77	6.53 ± 0.78	n.s. $p = .52$
Glut/Cr ratio	0.98± 0.09	0.96±0.09	n.s. $p = .61$
Glut/GABA ratio	**4.22±0.43**	**4.76± 0.67**	*** sign. $p < .02$**

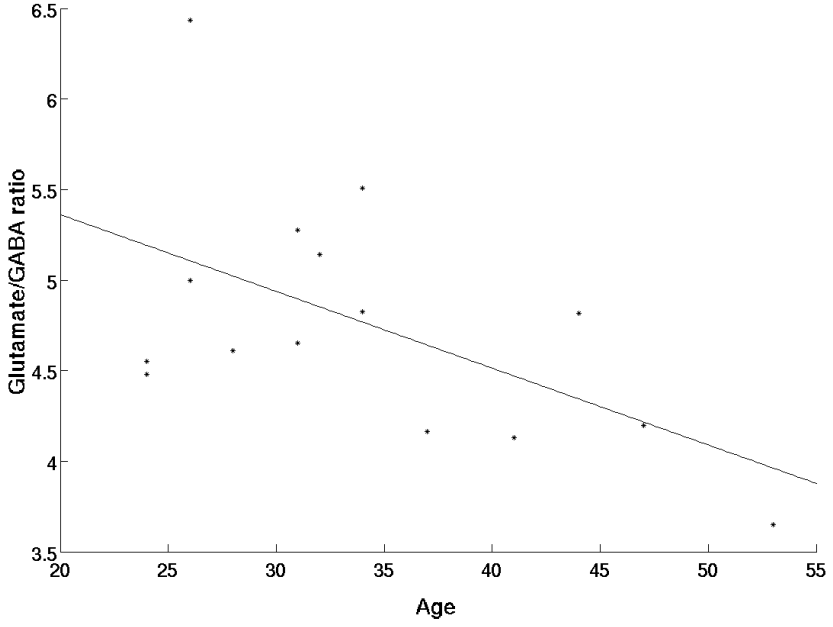

Figure 7.13.: Plot of the correlation between age and glutamate/GABA levels in in the patient group.

Table 7.11.: Summary of the correlations between possible confound age with the neurotransmitter levels and ratios.

	Patient Group	Control Group
Age vs GABA/Creatine Levels	$r = .31, p = .25$	$r = -.30, p = .32$
Age vs Glutamate/Creatine Levels	$r = -.20, p = .47$	$r = -.26, p = .38$
Age vs Glutamate/GABA Ratios	$\boldsymbol{r = -.55, p = .03}$	$r = .37, p = .21$

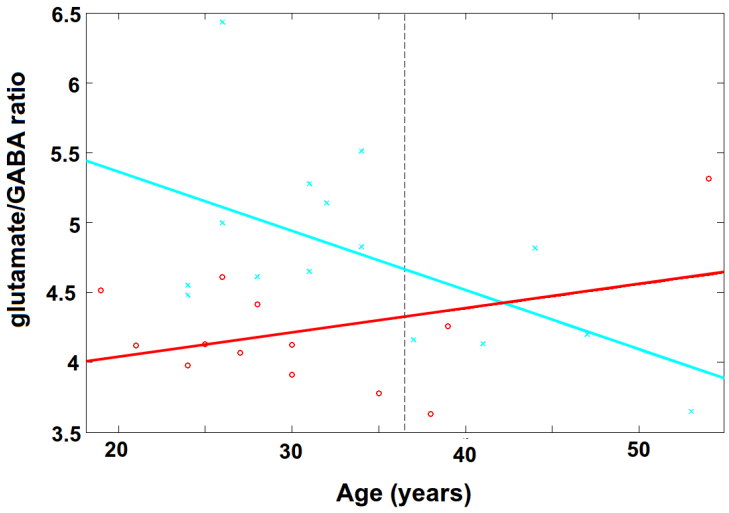

Figure 7.14.: Plot of the ANCOVA of the glutamate/GABA ratio in the two groups with age as a covariate.

Table 7.12.: Results of the ANCOVA of the glutamate/GABA ratio in the two groups with age as a covariate.

	F	p
Group	8.88	.0065
Age	1.39	.2497
Age * Group	7.14	.0133

Table 7.13.: Summary of the correlations of possible confound education time with the neurotransmitter levels and ratios.

	Patient group	Control group
Education Time vs GABA/Creatine levels	$r = 0.26$, $p = 0.35$	$r = 0.22$, $p = 0.47$
Education Time vs Glutamate/Creatine levels	$r = 0.03$, $p = 0.93$	$r = 0.14$, $p = 0.65$
Education Time vs Glutamate/GABA ratios	$r = -0.23$, $p = 0.42$	$r = -0.28$, $p = 0.35$

Table 7.14.: Summary of the correlations between possible confounds visual acuity and contrast sensitivity and the neurotransmitter levels and ratios.

	Patient group	Control group
Visual Acuity vs GABA/Cr levels	$r = .23$, $p = .41$	$r = .40$, $p = .18$
Contrast Sensitivity vs GABA/Cr levels	$r = -.33$, $p = .23$	$r = -.28$, $p = .35$
Visual Acuity vs Glutamate/Cr levels	$r = .31$, $p = .27$	$r = .35$, $p = .24$
Contrast Sensitivity vs Glutamate/Cr levels	$r = -.22$, $p = .43$	$r = -.06$, $p = .86$
Visual Acuity vs Glutamate/GABA ratio	$r = -.15$, $p = .59$	$r = -.30$, $p = .32$
Contrast Sensitivity vs Glutamate/GABA ratio	$r = .36$, $p = .18$	$r = .40$, $p = .18$

as confounders. Results are summarised in Table 7.14. Since none of the correlation coefficients were significant, visual acuity and contrast sensitivity were not included as regressors in the model.

To sum up, significantly reduced GABA concentrations (absolute and relative) as well as an increased glutamate/GABA ration were found for the patient group in comparison to the healthy control group consistent with the hypothesis.

7.3.2. Functional MR Imaging of Contrast Processing

2. Hypothesis:
The contrast-evoked BOLD response in V1 is reduced for schizophrenic patients.

The fMRI experiment was designed to measure the strength of the BOLD signal in response to the contrast stimulus. Figure 7.15 depicts the regions that showed a significantly higher BOLD signal for the ON-blocks ($.95$ contrast) compared to the OFF-blocks (0 contrast) for both groups ($p < .001$, uncorrected). As expected, in both groups the

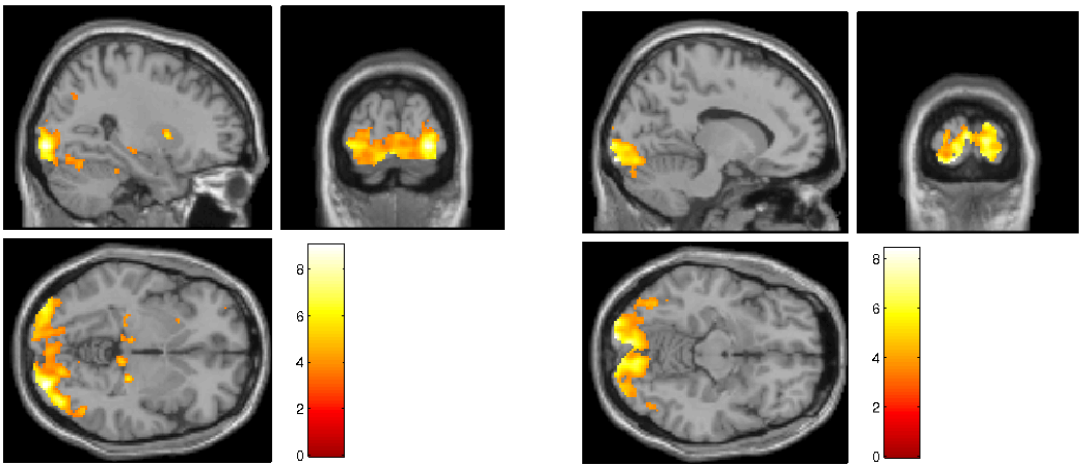

(a) (b)

Figure 7.15.: Contrast of ON- vs OFF-blocks in (a) patient and (b) control groups. The T-maps are projected onto a standard brain (statistical significance threshold $T = 3.50$, $p > .001$, uncorrected, color bars indicate T values above threshold). The main regions of activity lie within the occipital lobe, comprising V1 for both groups.

global maximum lay within the occipital lobe centred on V1. The analysis of the group differences revealed a significantly higher BOLD signal in the primary visual cortex in control participants compared to patients (Figure 7.16). Furthermore, we found a significantly higher activation for the patients in comparison with the control group in the medial temporal lobe (see Figure 7.17).

Again, correlations were calculated between the activity in V1 (the z-value of the most significant voxel in the group analysis), and age, education time, visual acuity and contrast sensitivity, respectively, in order to exclude possible confounds. Results are summarised in Table 7.15. Since there were no significant correlations for age, education time and visual acuity, they were not included as a regressor in our model.

Summarising, a significant group difference of the BOLD signal was found in V1, bilaterally, in response to high contrast stimuli.

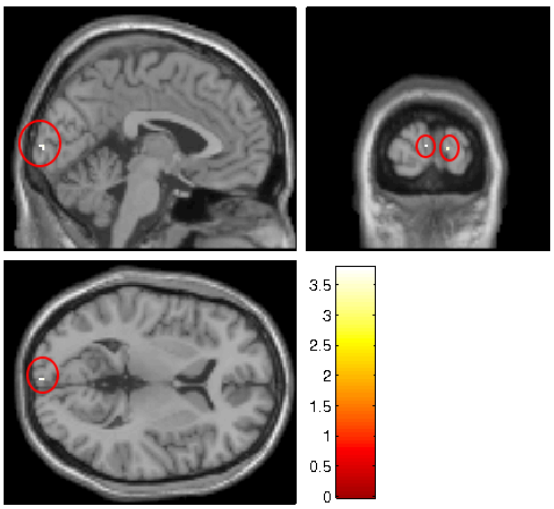

Figure 7.16.: Results of the group analysis. Voxels with a significantly higher response in the control vs. the patient group are shown, colour-coded upon T-values. The highlighted regions lay in V1 on both hemispheres with the global maximum at $x = 14$, $y = -102$ and $z = 4$ in Talairach space (statistical significance threshold $T = 3.50$, $p > 0.001$, uncorrected, colour bar indicates T values).

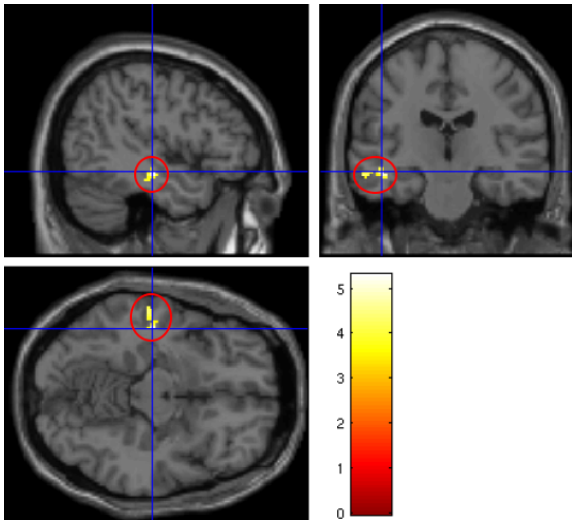

Figure 7.17.: Results of the group analysis. Voxels with a significantly higher response in the patient vs. the control group are shown, colour-coded upon T-value. The highlighted region lies in the medial temporal lobe (statistical significance threshold $T = 3.50$, $p > 0.001$, uncorrected, colour bars indicate T values).

Table 7.15.: Summary of the correlations between BOLD activation and the possible confounds age, education time, visual acuity and contrast sensitivity (all correlations non-significant).

	Patient group	Control group
Age vs BOLD activation	$r = .10$, $p = .73$	$r = -.01$, $p = .98$
Education Time vs BOLD activation	$r = .07$, $p = .81$	$r = -.02$, $p = .94$
Visual Acuity vs BOLD activation	$r = .21$, $p = .45$	$r = .46$, $p = .11$
Contrast Sensitivity vs BOLD activation	$r = .32$, $p = .24$	$r = -.36$, $p = .23$

7.3.3. Psychophysical Measurement of Centre-Surround Suppression

3. Hypothesis:
Perceptual centre-surround suppression in schizophrenic patients is reduced in comparison to healthy controls.

The centre-surround suppression effect was measured for all participants of the control and patient groups, using a two-interval staircase procedure converging to the PSE and calculating the CSS. In Tables 7.16 and 7.17 the results of the psychophysical experiment are shown for the control group and the patient group, respectively. No significant differences were found in suppression strength between both groups ($p = .07$) but a larger intra-subject, inter-trial variability was observed in the patient group ($p < .01$) (see also Table 7.18). This means that patients were less precise in their contrast judgement which dovetails with previous studies [51]. To sum up, no significantly reduced centre-surround suppression strength was found for the patient group contrary to the hypothesis.

Table 7.16.: Average centre-surround suppression and intra-subject, inter-trial variability of the healthy control group. Bias is calculated as average PSE, averaged over all 12 trials, subtracted from POE, here 40%. Intra-subject, inter-trial variability is the standard deviation of the calculated PSEs of the 12 trials.

	C1	C2	C3	C4	C5	C6	C7	C8
Centre-Surround Suppression (% Contrast)	13.88	10.72	9.54	18.49	10.69	9.03	9.93	2.61
Inter-Trial Variability (% Contrast)	5.62	1.34	2.64	4.07	2.29	3.73	1.93	2.34

	C9	C10	C11	C12	C13
Centre-Surround Suppression (% Contrast)	10.34	13.75	16.25	8.37	6.25
Inter-Trial Variability (% Contrast)	3.02	1.58	2.61	1.62	3.02

Table 7.17.: Average centre-surround suppression and intra-subject inter-trial variability of the patient group. Bias and intra-subject, inter-trial variability calculated as above (see 7.16).

	P1	P2	P3	P4	P5	P6	P7	P8
Centre-Surround Suppression (% Contrast)	10.74	32.29	9.28	24.06	18.75	8.75	8.75	19.79
Inter-Trial Variability (% Contrast)	2.47	4.50	3.29	7.78	3.35	3.71	3.87	3.28

	P9	P10	P11	P12	P13	P14	P15
Centre-Surround Suppression (% Contrast)	21.03	13.75	12.84	2.61	15.80	21.02	9.66
Inter-Trial Variability (% Contrast)	3.05	5.54	7.44	4.44	2.57	4.82	3.88

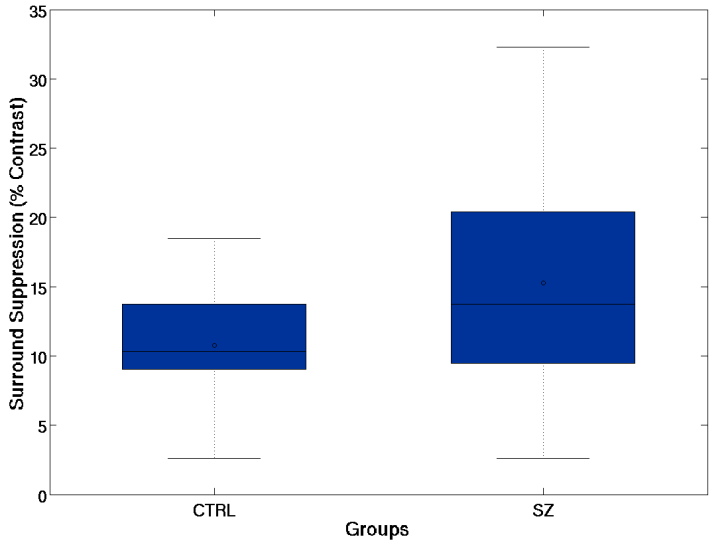

(a)

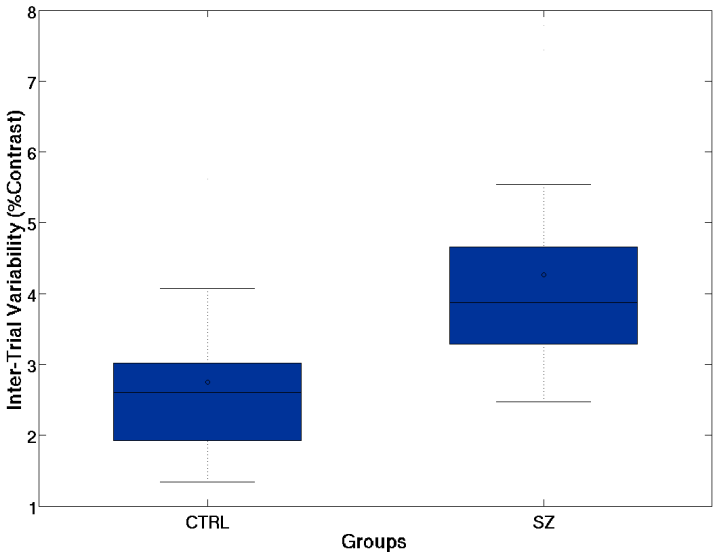

(b)

Figure 7.18.: Box plots of (a) centre-surround suppression strength and (b) inter-trial variability in both patient (SZ) and control (CTRL) groups. On each box, the central mark is the median, the edges of the box are the 25th and 75th percentiles, the whiskers extend to the most extreme data points not considered outliers, and outliers (i.e. values larger than $q_3 + 1.5 \cdot (q_3 - q_1)$ or smaller than $q_1 - 1.5 \cdot (q_3 - q_1)$, where q_1 and q_3 are the 25th and 75th percentiles, respectively) are plotted individually.

Table 7.18.: Summary of the psychophysical experiment. Mean centre-surround suppression and mean intra-subject inter-trial variability of the control and patient groups are shown. Furthermore, group differences were tested using an independent two-sample t-test with unequal sample size and unequal variance. Statistical significance level was set to $p < .05$.

	Patient Group	Control Group	Difference
Centre-Surround Suppression	15.27±7.59	10.76± 4.15	n.s. $p = .07$
Inter-Trial Variability	4.27±1.59	2.75±1.18	*sign. $p < .01$

Table 7.19.: Summary of the post-hoc correlations between the possible confounds visual acuity and contrast sensitivity and surround suppression strength and inter-trial variability (no significances found).

	Patient group	Control group
Visual Acuity vs CSS	$r = -.16, p = .58$	$r = .11, p = .72$
Contrast Sensitivity vs CSS	$r = -.04, p = .90$	$r = .23, p = .45$
Visual Acuity vs Inter-Trial Variability	$r = -.16, p = .57$	$r = -.18, p = .56$
Contrast Sensitivity vs Inter-Trial Variability	$r = -.10, p = .73$	$r = .21, p = .49$

Table 7.20.: Summary of the post-hoc correlations between the possible confounds age and education time and centre-surround suppression strength and inter-trial variability.

	Patient group	Control group
Age vs CSS	$r = -.03, p = .92$	$r = .04, p = .91$
Age vs Inter-Trial Variability	$r = -.18, p = .53$	$r = -.20, p = .51$
Education Time vs CSS	$r = .45, p = .09$	$r = .51, p = .07$
Education Time vs Inter-Trial Variability	$r = -.18, p = .53$	$r = .27, p = .38$

7.3.4. Interactions between Modalities

After considering each of the different, presented modalities separately, the interactions between psychophysical, fMRI and MRS data were analysed. This is particularly interesting because there are known pairwise correlations between all of the three modalities, but, to the author's knowledge, this is the first study addressing all three of them simultaneously. Furthermore, some of the studies reporting pairwise correlations have been conducted with small group sizes and/or only healthy subjects.

4. Hypothesis:
The strength of perceptual centre-surround suppression and the concentration of GABA (the ratio glutamate/GABA) are correlated in V1.

In the first place, correlations between neurotransmitters and centre-surround suppression strength were calculated for both groups separately. Table 7.21 summarises these analyses. No significant correlation was found between surround suppression strength and GABA levels (Figure 7.19), glutamate levels (Figure 7.20) and glutamate/-GABA ratio (Figure 7.21) in either groups, respectively. Summarising, contrary to the

Table 7.21.: Summary of the correlations between neurotransmitter levels and ratios and centre-surround suppression strength.

	Patient group	Control group
GABA/Cr vs CSS	$r = .15, p = .59$	$r = .15, p = .62$
Glutamate/Cr vs CSS	$r = .29, p = .29$	$r = .07, p = .83$
Glutamate/GABA vs CSS	$r = .06, p = .83$	$r = -.15, p = .60$

hypothesis, no significant correlations were found either between centre-surround suppression and GABA concentrations or between centre-surround suppression and glutamate/GABA ratios.

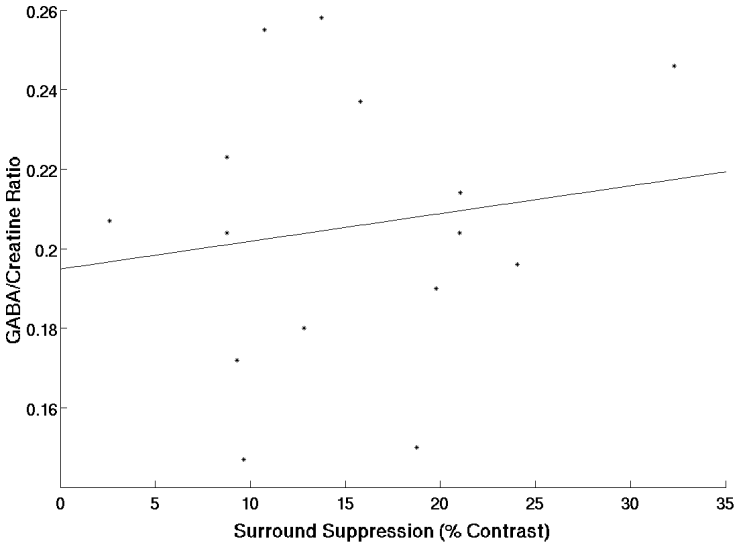

(a)

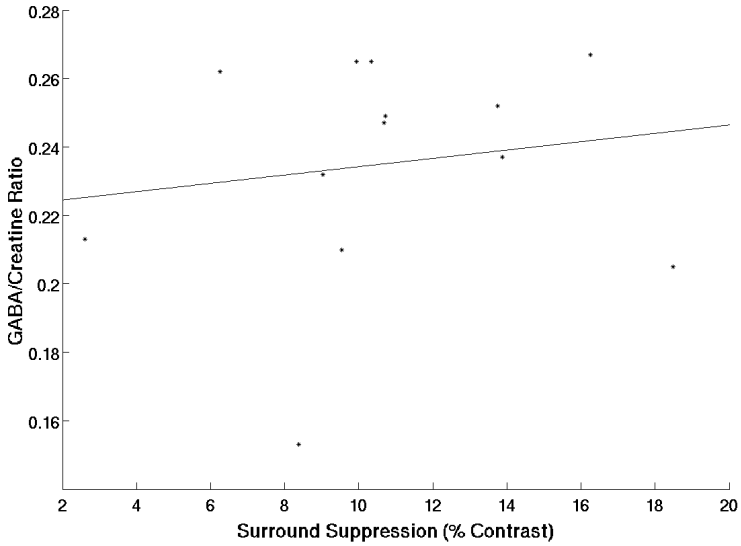

(b)

Figure 7.19.: Plot of the correlation between GABA/creatine ratio and centre-surround suppression in (a) patient and (b) control groups.

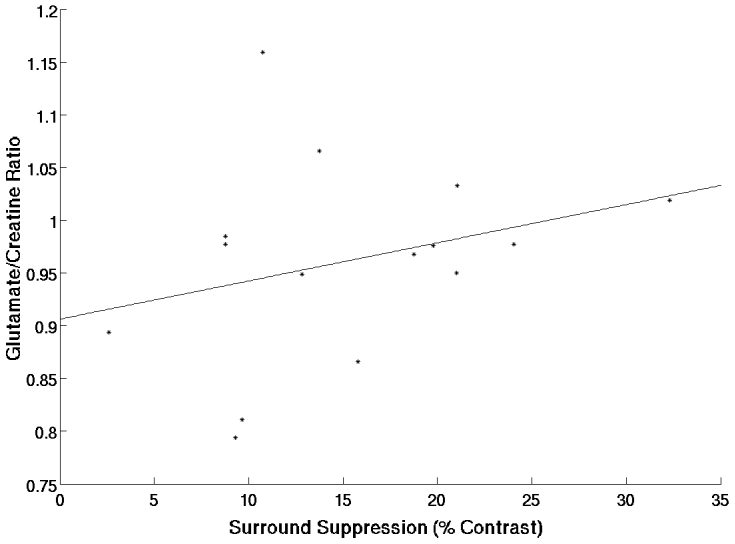

(a)

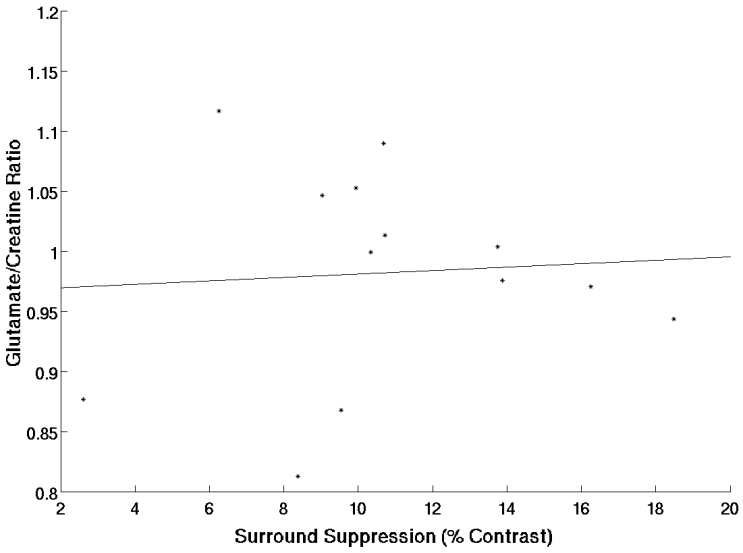

(b)

Figure 7.20.: Plot of the correlation between glutamate/creatine ratio and centre-surround suppression in (a) patient and (b) control groups.

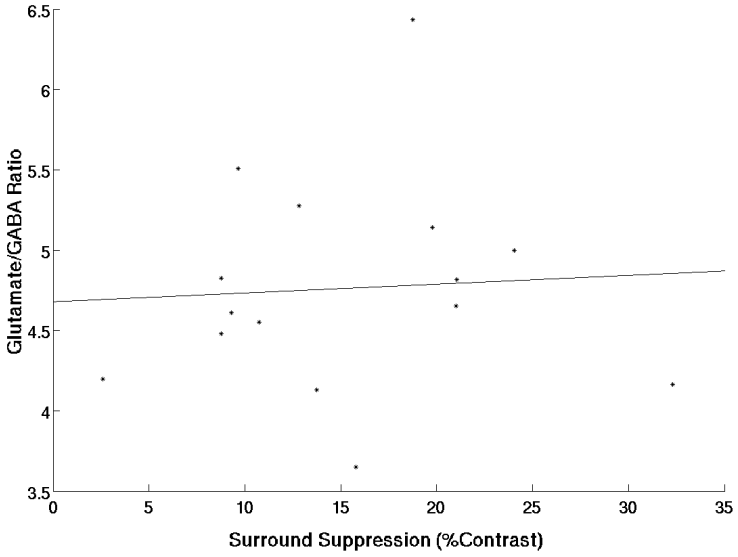

(a)

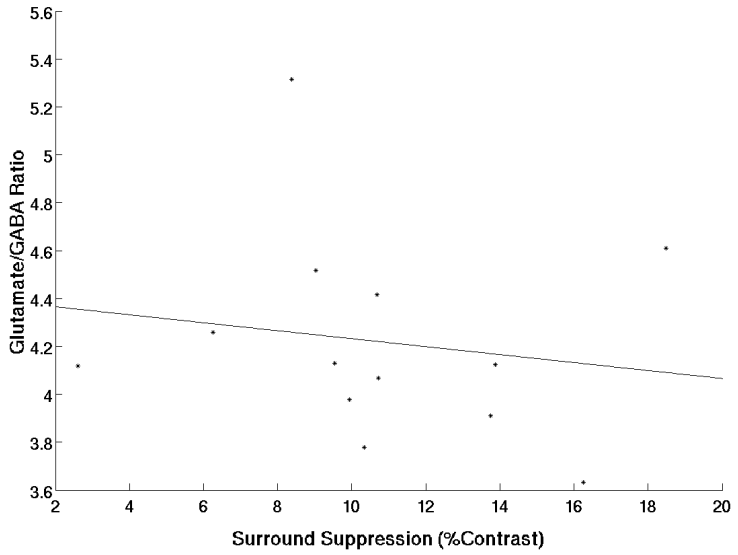

(b)

Figure 7.21.: Plot of the correlation between glutamate/GABA ratio and centre-surround suppression in (a) patient and (b) control groups.

5. Hypothesis:
The BOLD response and the strength of centre-surround suppression are correlated in V1.

In the second place, correlations between centre-surround suppression and the BOLD signal were calculated for both groups. Table 7.22 summarises these results. No significant correlations were found in any case. However, the correlation coefficients for BOLD activation with centre-surround suppression strength was negative for the patient group but positive for the healthy control group (see Figure 7.22). Hence, it was tested whether the correlations for both groups differed significantly, by applying a Fisher z-transformation. There was a marginally significant difference between the correlation coefficients of both groups ($z = 1.88$, $p = 0.06$), which might suggest different relationships between surround integration and neural activation in response to contrast stimuli in the two groups.

Table 7.22.: Summary of the correlations between BOLD activation and centre-surround suppression strength.

	Patient group	Control group
BOLD Signal vs CSS	$r = -.33$, $p = .24$	$r = .46$, $p = .11$

The advantage of fMRI is, that not only can centre-surround suppression strength be correlated with V1 activity, as done above, but other brain regions can also be explored for significant correlations between BOLD activity and centre-surround suppression. Figure 7.23 shows the brain regions where there was a significant interaction between BOLD activation and centre-surround suppression strength in the control group. As already stated above, contrary to the hypothesis, there was no significant correlation between BOLD signal and centre-surround suppression strength within the V1. However, there was a correlation in the thalamus for both groups, bilaterally. Interestingly, the exact localisation of the active regions in the thalamus differed for the two groups (see Figures 7.23-7.25). In the patient group, there was additional activity in another region in the thalamus (see Figure 7.24).

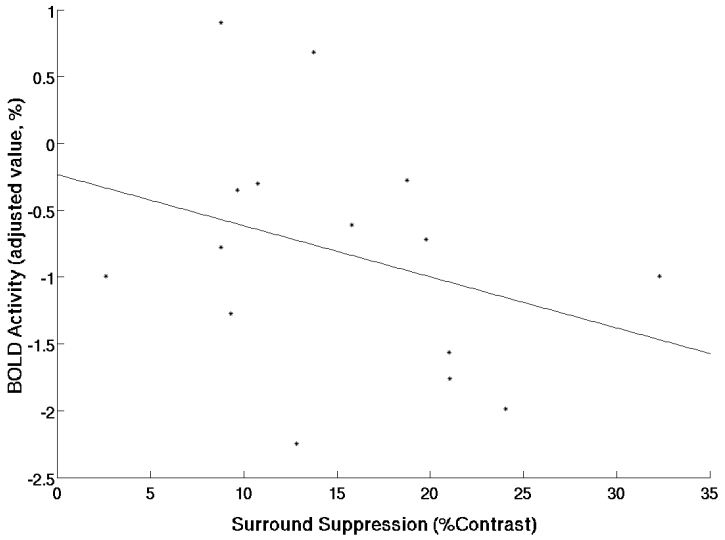

(a)

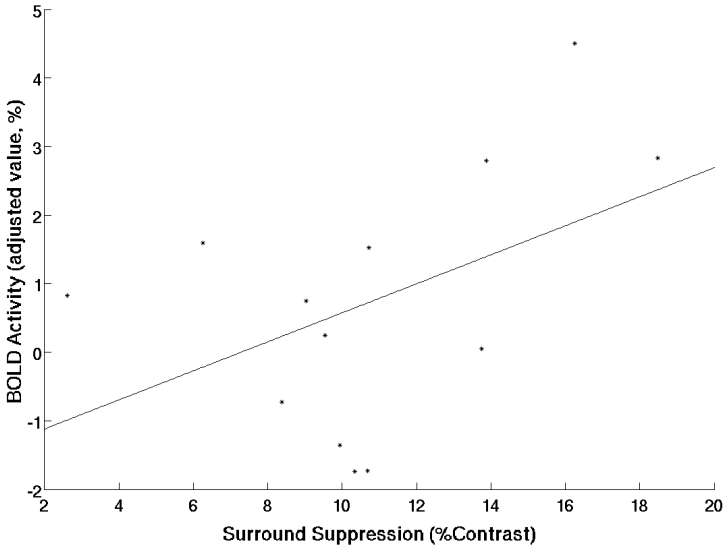

(b)

Figure 7.22.: Plot of the correlation between between BOLD activation and surround suppression in (a) patient and (b) control groups.

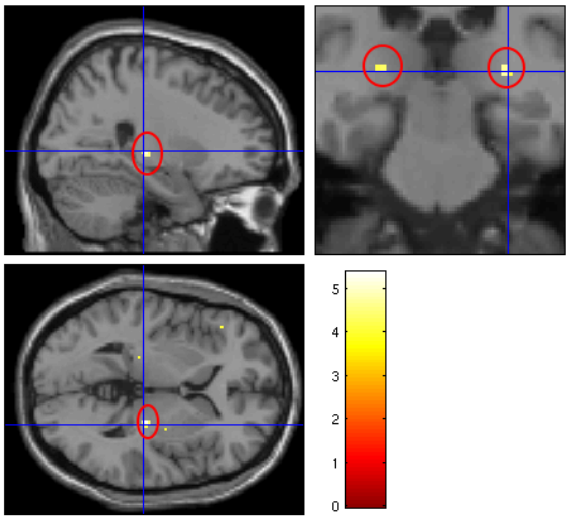

Figure 7.23.: Correlation between BOLD signal and centre-surround suppression in the control group. The T-maps are projected onto a standard brain (statistical significance threshold $T = 3.85$, $p > .001$, uncorrected, color bars indicate T values). The highlighted regions lie within the left and the right thalamus in the LGN (Talairach coordinates $x = 26$, $y = -25$ and $z = 2$, and $x = -26$, $y = -25$ and $z = 2$, respectively).

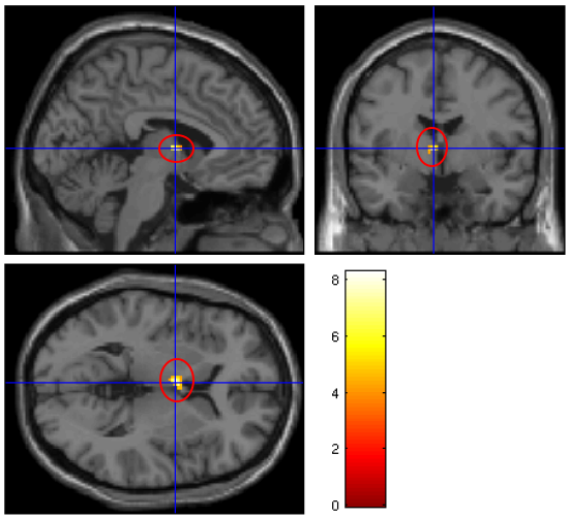

Figure 7.24.: Correlation between BOLD signal and centre-surround suppression in the patient group. The T-maps are projected onto a standard brain (statistical significance threshold $T = 3.85$, $p > .01$, FDR-corrected cluster level, colour bars indicate T values). The highlighted region lies within the left thalamus (Talairach coordinates $x = -4$, $y = -2$ and $z = 4$).

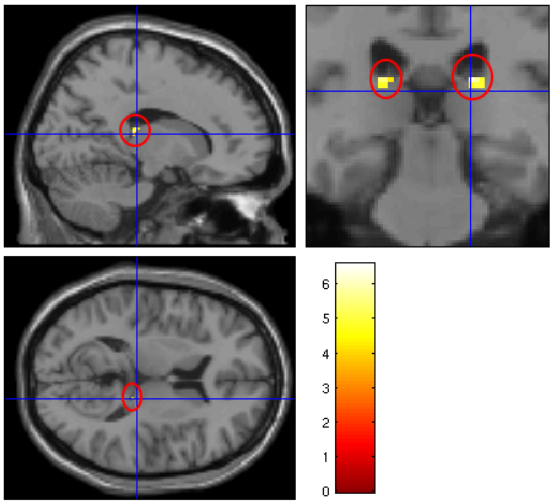

Figure 7.25.: Correlation between BOLD signal and centre-surround suppression in the patient group. The T-maps are projected onto a standard brain (statistical significance threshold $T = 3.85$, $p > .001$, uncorrected, colour bars indicate T values). The highlighted regions lie within the left and right thalami in the pulvinar nucleus (Talairach coordinates $x = 16$, $y = -27$ and $z = 11$ and $x = -16$, $y = -27$ and $z = 11$, respectively).

6. Hypothesis:
The BOLD response and the concentration of GABA (the glutamate/GABA ratio) are correlated in V1.

In the third and final place, the correlations between neurotransmitters and the BOLD signal were analysed. Table 7.23 shows these results. Contrary to the hypotheses, no significant correlations were found between the GABA/creatine levels and the BOLD responses , and between the glutamate/GABA ratios and the BOLD responses There was also no significant correlation between the glutamate/creatine level and BOLD response.

Table 7.23.: Summary of the correlations between neurotransmitter levels and ratios BOLD activation.

	Patient group	Control group
BOLD Activation vs GABA/Creatine Ratio	$r = .23$, $p = .41$	$r = .06$, $p = .84$
BOLD Activation vs Glutamate/Creatine Ratio	$r = .20$, $p = .48$	$r = -.09$, $p = .78$
BOLD Activation vs Glutamate/GABA Ratio	$r = -.07$, $p = .80$	$r = -.19$, $p = .52$

8. Discussion

8.1. Computational Models

In this work, a biologically plausible model of layer 4Cα of the primary visual cortex (V1) has been developed, that not only produces a feature selectivity (orientation, direction and spatial frequency selectivity) close to experimental results, but that also shows neuronal centre-surround suppression resembling experimental data. Two major conclusions can be drawn from this work.

In the first place, the model demonstrates that intracortical inhibition is a crucial factor in feature selectivity and that it consists of two parts: *feed-forward* intracortical inhibition, as a result of broadly tuned thalamic excitation of inhibitory neurons, and *recurrent* intracortical inhibition as a result of recurrent excitation of inhibitory neurons depending on the specific excitatory-inhibitory connectivity pattern of the model. While the *feed-forward* intracortical inhibition is analogous to several previous experimental and modelling studies [e.g. 174, 232], the specific *recurrent* intracortical inhibition profile further sharpens the tuning in the network model, which, compared to other models [e.g. 232], leads to higher selectivity measures that more closely resemble experimental findings. Thus, the model developed here suggests a three stage process of feature tuning in V1 in which feed-forward lateral geniculate nucleus (LGN) input provides a broad tuning of excitatory neurons that is subsequently sharpened by *feed-forward* and *recurrent* intracortical inhibition.

In the second place, the model suggests that intracortical inhibition, both *feed-forward* and *recurrent*, is a crucial factor influencing neuronal centre-surround suppression. Centre-surround suppression emerges in the network solely because of the intracortical connectivity profile without extrastriate input or long-range horizontal connections, similarly to the model of Wielaard and Sajda [222].

8.1.1. Feature Selectivity

In the model, similarly to other models [222, 231, 232], the main mechanism for high feature selectivity is intracortical inhibition, especially *feed-forward* inhibition. This *feed-*

forward inhibition emerges from the tuned input arriving at inhibitory cells from the LGN. As modelled previously [144, 210, 232], inhibition in this model is more broadly tuned than excitation, which leads to a suppression of responses at non-optimal stimuli. Furthermore, this is in agreement with recent experimental data for both orientation selectivity [36, 157] and spatial selectivity [36].

As argued by Zhu et al. [232], this proposed mechanism is different from the classical view, which attributes the emergence of feature selectivity to quasi-linear feed-forward filtering by the convergent LGN input, that is, by the spatiotemporal receptive field [52, 59, 67, 121]. In the model, as well as, the model proposed by Zhu et al. [231, 232], highly selective neurons are a product of non-linear cortical inhibition, dovetailing with recent experimental data on the dynamics of feature selectivity [26, 172, 174, 225]. As in the model of Zhu et al., feature selectivities coexist in the network model, which has not been addressed by most other modelling studies before [144, 204, 210]. It is important to mention here once again that all reported measures of feature selectivity were obtained with the same parameters, specifically the weights of the connections were fixed, and thus the model simultaneously shows feature selectivity in all considered dimensions.

However, the network model proposed in this thesis extends the work of Zhu et al. and other known models in that it yields orientation tuning results very close-fitting to experimentally measured data, due to differences in the factor of *recurrent* intracortical inhibition, which further sharpens orientation tuning [174, 175]. This difference is due to the specific connectivity pattern for recurrent excitatory activation of inhibitory cells, which is different from the pattern in the network models discussed before.

In principle, the network model of Oliveira and Roque [160] should also show feature selectivity results and mechanisms similar to those presented in this work, since both models are based on similar connectivity patterns. Withal, Oliveira and Roque do not test and discuss orientation selectivity in their model in detail, and they also do not investigate spatial frequency selectivity, or the mechanisms underlying these properties.

Orientation Selectivity Orientation selectivity in the network model developed here arises from two major sources. Selectivity is first produced by the convergent LGN input to an excitatory cortical cell, which is determined by its spatiotemporal receptive field this yields a broad selectivity (see Table 6.13), as theoretically predicted [e.g. 187], which is then sharpened by intracortical inhibition, firstly through the activation of inhibitory neurons from the LGN input and secondly through recurrent excitation of inhibitory neurons. This process is also in agreement with experimentally identified components crucially influencing orientation selectivity, namely global, tuned enhancement (reflect-

ing the tuning of the LGN input) followed by tuned (reflecting feed-forward inhibition) and global (reflecting recurrent inhibition) suppression [175]. The sharpening through *feed-forward* inhibition is due to a broader tuning of inhibitory neurons (see Figure 6.29 and Table 6.14), which leads to a suppression of non-preferred orientations (see Figure 6.28). Similarly, *recurrent* inhibition suppresses non-preferred orientations through the spatial distance between connected excitatory and inhibitory neurons, thus further refining the tuning. This refining through intracortical inhibition leads to the high selectivity in the model. Particularly, *recurrent* inhibition sets it apart from other models, in which intracortical inhibition is also the major factor contributing to high selectivity, but that assume a more local recurrent excitation of inhibitory neurons. Therefore, this model and others relying on inhibitory suppression to achieve high selectivity [e.g. 232] predict a significant reduction in selectivity in conditions of experimentally blocked inhibitory synapses, whereas other models do not, for example, purely feed-forward models [e.g. 67]. It is evident that more detailed anatomical data will further help refine and validate the connectivity pattern assumed in the model.

Another important factor is that feature selectivity is very diverse throughout V1 (see Table 6.9 and Figure 6.17), although this aspect of selectivity is often not addressed in modelling studies. The model proposed in this work shows a great diversity within its neuron population, matching experimental findings. This diversity comes from the variation in the receptive fields of each cell, as well as, differences in intracortical connectivity. This is another strong argument in favour of the present model and this diversity is as important as the general high selectivity.

In addition to discerning the mechanisms behind orientation selectivity and investigating the influence of lateral inhibition in the sharpening of tuning, the major factors governing lateral inhibition are systematically varied in the network model. Although the main interest lay in the influence of these variations on the neuronal centre-surround suppression and its link to perceptual centre-surround suppression, this systematic approach also made it possible to explore the effects on orientation selectivity.

There is a strong influence of the inhibitory weight (see Table B.1) and only a weak influence of the excitatory weight (see Table B.7) on the orientation selectivity. Similarly to the inhibitory weight, the number of inhibitory cells strongly affects orientation selectivity in the network model (see Table B.13), whereas the number of connections, both inhibitory (see Table B.19) and excitatory (see Table B.25), does not seem to have a strong influence. However, surprisingly, a reduction of excitatory connections slightly increases the orientation tuning in the network. A prolongation of the decay time constant at GABAergic synapses, reduces orientation tuning, although this is independent from

the amount of prolongation, at least in the tested range (see Table B.31).

Summarising, all parameters governing inhibition in the network model influence orientation selectivity. Not surprisingly, some of the parameters directly affecting inhibition (weight of inhibitory connections, number of inhibitory neurons) have a larger effect than those affecting it only indirectly (weight of excitatory connections, number of excitatory connections). Still, also the number of inhibitory connections and the decay time of inhibitory synapses also merely show a weak effect on selectivity.

Spatial Frequency Selectivity The model shows spatial frequency selectivity matching experimental data (see Figure 6.23). Cells are tuned to a variety of preferred spatial frequencies in the range of 0.5 -$8\,c/deg]$, with variation in their tuning strength (see Figure 6.25). Local and global measures of spatial frequency tuning correspond well to experimental data [26, 54, 59, 69, 224]. These results are also similar to those reported in the works of Zhu et al. [231, 232]; as expected, given that the thalamic processing and the formation of receptive fields were adopted from this work. Once again, this confirms the validity of the network model proposed here.

The influence of cortical inhibition on spatial frequency selectivity was not specifically investigated in this work, since orientation selectivity is more relevant to centre-surround suppression, the central focus of this work, than spatial frequency selectivity. However, since the work of Zhu et al. [231] was followed regarding the mechanisms of spatial frequency selectivity generation, and given the strong influence of cortical inhibition on orientation selectivity in the current network model, cortical inhibition is also expected to be the major factor sharpening spatial frequency tuning. Additionally,low spatial frequency responses of V1 simple cells, recorded intracellularly, do not have much frequency doubling in the membrane potential, which is in accordance with the model of Zhu et al. [231]. Classical feed-forward models without synaptic inhibition predict notably more frequency doubling in the membrane potential, making this another testable difference in the predictions of the two types of models.

The width of the neuron's receptive field is the main factor in generating selectivity for different spatial frequencies in the model. The distribution of receptive field widths thus determines the distribution of preferred spatial frequencies. As argued in [231], the spatial organisation of selectivity is still a matter of debate and is accompanied by controversial experimental data [e.g. 57, 194]. Again, the work of Zhu et al. [231] was followed using their interpretation of the optical imaging data from Sirovich and Uglesich [194]. However, an interesting aspect would be to compare these different interpretations of the optical imaging data and their effects on the spatial tuning properties. The model

presented in this work can be readily used to do so and, in addition, would also permit investigating possible consequences for other receptive field, contrast response and centre-surround suppression properties. However, it was beyond the scope of this work to perform this comparison.

Temporal Selectivity The model presented in this work also agrees well with experimental data regarding temporal frequency selectivity. Neurons respond well to low temporal frequencies up to approximately 9 Hz (see Figure 6.26), which is also reported for V1 neurons in macaques [69, 84]. The temporal tuning characteristics of the network neurons were not investigated in more detail, given this works focus on orientation selectivity and centre-surround suppression. However, a closer investigation of the properties of the network model and a comparison to experimental data could be interesting in order to further the understanding of mechanisms of temporal tuning, that is, including the bandpass nature of frequency-response curves, increases in response amplitude and in cut-off frequency for transient stimuli, and nonlinear temporal summation. Furthermore, an exploration of the correlations of temporal frequency tuning with other properties such as orientation selectivity or spatial frequency tuning, as has been done experimentally [e.g. 69], seems promising.

Simple and Complex Cells The distribution of simple and complex cells in the network model match adequately both experimental data [174, 190, 195] and recent models [204, 231, 232]. The distribution is bimodal, has more simple than complex cells, and shows a continuum of modulation ratios rather than a clear distinction in two groups (see Figure 6.16).

Simple and complex cells emerge in the network model without a hierarchical composition, that is, the two classes of cells are not modelled a priori and intracortical connectivity is isotropical. This dovetails with other models of V1 [204, 231, 232], but contradicts the traditional view of feed-forward models (e.g. Hubel and Wiesel [98]), where simple cells are thought to receive direct LGN input and then project forward onto cells that do not receive LGN input, which in turn show complex responses. As argued in Chapter 5, this view predicts a clear anatomical separation of the two classes and a stronger separation of modulation ratios. However, as mentioned above, experimentally (especially in layer 4C) this strong separation is not observed, supporting the type of model.

The mechanisms underlying the formation of simple and complex cells were not studied in detail in this work. Nonetheless, due to the strong similarities of the construction principles of this network model to those of Tao et al. [204] and Zhu et al. [231, 232], it

is to expect that the crucial factor here is also cortico-cortical inhibition. This inhibition, as argued by Tao et al. [204], allows for nearly linear, simple cell responses despite the highly non-linear drive by LGN cells.

8.1.2. Contrast Response Properties

In addition to classical receptive field properties, the neurons in the network model show contrast response functions well in agreement with electrophysiological studies [2, 35, 186, 207]. The neurons show monotonically increasing activity with increasing contrasts. A standard contrast response function fits reliably to single average firing rates in response to stimuli with varying contrasts. The fact that the free parameters in the fitting of the contrast response function are highly restricted, but still the portion of variance explained by the fitted functions, indicates a close match of the simulated responses to actual experimental data. Furthermore, there is a strong similarity between the contrast response function on the neuronal and on the perceptual level, as indicated by experiments combining electrophysiological or functional magnetic resonance imaging (fMRI) and psychophysical measurements [24, 73, 85, 186, 230].

8.1.3. Centre-Surround Suppression

Centre-surround suppression is researched with the network model for different sets of stimuli, that is, oriented sinusoidal gratings with different contrasts in the centre and the surround, and with contrast texture patterns usually utilised in human psychophysical studies. The main goal is to compare the results to experimental studies investigating centre-surround suppression [e.g. 51, 112, 226, 229, 230]

8.1.3.1. Sinusoidal Gratings

Moving sinusoidal gratings are used at optimal orientation and spatial frequency, and centre-surround suppression is investigated by increasing the grating stimulus beyond its optimal size. An average suppression of 87 % is found in most cells (see Table 6.11). Additionally, centre-surround suppression properties are investigated at four different centre contrasts in two different surround conditions. These manipulations yield three results: The introduction of a surround grating produces either suppression or facilitation of single neuron activity (see Table 6.11). In the second place, this effect depends on the balance between centre and surround contrast. Specifically, for a high centre contrast results in a strong suppression in both, high and low surround conditions, whereas

low centre contrast leads to a facilitation in both surround conditions. Nonetheless, suppression was stronger for the high surround condition, whereas facilitation was much stronger for the low surround condition (see Table 6.11). Finally, in the third place, a medium centre contrast of 0.4, produces facilitation in the low surround condition but suppression in the high surround condition (see Table 6.11).

Comparison to Electrophysiological Studies Using moving sinusoidal gratings and measuring intracellular responses of single cells, Jones et al. [112] report strong suppression, on average $71\,\%$, in layer 4C in V1 of macaques similar to the suppression found in the network. These findings also match with previous reports on centre-surround suppression in macaque V1 using sinusoidal gratings [181, 191, 192]. Additionally, these studies also find facilitation of responses in several cases, but they do not investigate their contrast-dependence. However, these studies show a great complexity of the organisation of spatial regions contributing to the surround interactions, which are beyond the analyses performed in this work. It could be of interest to study the suppressive and facilitatory effects of surround stimuli as well as their spatial organisation, and the proposed model builds an ideal basis for this purpose.

Moreover, the present findings also fit in with other sets of stimuli, such as bars and texture patterns, where suppression is found in the majority of neurons (65-85 %) and the suppression strength varies between 34-69 % of the firing rate at optimal conditions [117, 124]. Furthermore, the higher facilitation in low compared to high surround contrast conditions in the simulations performed for this thesis matches well with the findings of Levitt et al., who report a higher mean facilitation index in high than in low contrast conditions [124]. There is also recent evidence that contrast-dependent centre-surround suppression effects are apparent in response to natural scene stimuli [80].

Comparison to Psychophysical Studies Xing and Heeger [226], have investigated contrast-dependent centre-surround interactions in a human psychophysical study using contras-reversing sinusoidal gratings and developed an analytical model adequately explaining their data. These authors report suppression increasing and enhancement decreasing with increasing surround contrast, in agreement with the data from the model described in this thesis. However, contrary to the findings reported in Chapter 6, the suppression decreased and the enhancement increased with centre contrast. The findings of Xing and Heeger also fit with previous studies of Cannon and Fullenkamp [32] with respect to the dependence of suppression and facilitation on the ratio of centre and surround contrasts. In the model developed here, suppression and facilitation are inde-

pendent from the ratio of centre and surround contrasts, but rather depend on the sum of the contrasts, that is, the lower the sum of the contrasts the more facilitation is seen and the higher the sum the more suppression is observed. Xing and Heeger incorporate two different factors of inhibition in their analytical model: a local inhibition that depends on the centre contrast, and a surround inhibition that depends on the surround contrast. These two different inhibitory mechanisms then account for the observed dependence of suppression and facilitation on the ratio of centre and surround contrasts. A possible explanation for the difference between the findings of this work and those of Xing and Heeger might be that the surround inhibition used in their model is actually mediated via long-range horizontal connections in addition to the short-range intracortical inhibition, whereas the model developed here only utilises short-range intracortical inhibition. Furthermore, Xing and Heeger report that enhancement only depended on the immediate surround and an increase of the surround width had no effect on it, whereas Cannon and Fullenkamp described that an increase in the surround width changed from enhancement to suppression in their measurements. Ultimately, the fact that these studies employed slightly different stimuli (contrast-reversing gratings, in contrast to moving sinusoidal gratings in the current work) and that a direct, quantitative mapping of surround widths is not possible, makes a final assessment of the differences we found very difficult. However, the proposed model builds a basis ideally suited to further investigate these phenomena.

It needs to be noted here that a quantitative comparison of the current model results and those from psychophysical experiments is not possible, since the exact mechanisms by which neural activity in V1 determines contrast perception is poorly understood. Nonetheless, there is a strong link between perceived contrast and neural activity in V1 [85], which allows for a qualitative comparison as has been done in this work.

Influences of Recurrent Inhibition After a discussion of the centre-surround suppression properties of the network model in the standard configuration, the influence of the different parameters governing recurrent inhibition has to be discussed.

In the case of the weight of inhibition on excitatory cells, that the strength of surround suppression increases with weight in the size variation test (see Figure 6.37 and Table B.3) and also for high centre contrasts in the second test (see Figure 6.38 and Table B.4). Furthermore, counterintuitively facilitation increases with inhibitory weight in the low centre and low surround contrast condition (see Figure 6.38 and Table B.4). However, in the low centre and high surround contrast condition, facilitation stays roughly the same. Manipulations of the weight of excitation on inhibitory cells show that the strength

of surround suppression decreases with increasing weight in the size variation test (see Figure 6.37 and Table B.9). In the second test, there is a lower suppression at both ends of the tested range of weights in both the low and the high surround conditions (see Figure 6.38 and Table B.4). Moreover facilitation strongly decreases as a function of the weight (see Figure 6.38 and Table B.4). Changes in the number of inhibitory neurons, result in a strong reduction of suppression (size test: Figure 6.37 and Table B.15; contrast variation test: Figure 6.38 and Table B.16) and facilitation (see Figure 6.38 and Table B.16) with decreasing number of neurons in both conditions. Indeed, facilitation actually disappears and turns into moderate suppression with neuron decrement. This effect is also apparent, albeit weaker, for the number of inhibitory connections on excitatory cells (see Figures 6.37 and 6.38 and Tables B.21 and B.22). Finally, the GABAergic decay time constant hardly has any effect on suppression in the size variation test (see Figure 6.37 and Table B.33),although a slight reduction in suppression and a strong reduction of facilitation is seen in the second test (see Figure 6.38 and Table B.34).

Overall, this demonstrates that suppression in the high centre contrast condition and facilitation in the low centre contrast condition strongly depend on inhibition. Still, each of the considered factors makes a contribution to the net suppression or facilitation, so that one factor cannot simply attributed to one observation.

8.1.3.2. Contrast Texture Stimuli

In addition to the sinusoidal gratings mentioned above, we used stimuli consisting of contrast texture patterns were used, which are commonly used in psychophysical experiments. This enabled comparing the present results to a different body of experimental work. Introducing an additional surround stimulus (in both tested size conditions) to a centre only stimulus significantly reduce the cells' responses (see Table 6.12). Moreover, it results in matching contrasts, which are markedly lower than the actual displayed contrast. This reduction of activity, as well as the lower matching contrasts produced by the introduction of surround stimuli, is in good agreement with experimental data [43, 51]

Withal a substantial number of the cells in the network either do not respond strongly to the texture pattern stimuli, or a standard contrast response function cannot be fitted in a reasonable manner. It needs to be noted that, in contrast to human psychophysical experiments, the simulations did not use static texture patterns, but the pattern in the stimulus changed over the time course of the stimulation in order increase responses (see Section 6.2.4).

These limitations were not present in the case of sinusoidal grating stimuli. This evidences that the current model is missing a mechanism that enables this adaptation. Two

plausible mechanisms might be involved: an increase in responsiveness caused by attentional top-down signals, although attentional effects seem stronger in higher sensory areas (see [58, 215]); an adaptation in the LGN response to texture stimuli.

8.1.3.3. Centre-Surround Mechanisms

The two classical hypotheses explaining the emergence of centre-surround suppression in the visual cortex are fast extrastriate feedback and long-range horizontal connections. In the first case,there is some experimental support for this hypothesis that argues that intracortical connections do not have a spatial extent that is sufficient to generate the surround sizes observed experimentally [6, 10, 37, 182]. Further support comes from experiments investigating the dynamics of surround suppression [10], as well as from tracer injection experiments [6]. In the second case, the argument is similar, now stating that long-range horizontal connections are able to reproduce experimental data but short-range connections cannot [56, 61, 102, 202]. However, the experimental data from these studies only indirectly observe the centre-surround phenomena and, except for the rate-model of Dragoi et al. [61] and a model of Somers et al. [198], no computational support for the hypotheses is available at present. The major reason for this is the great difficulty to experimentally discern the influences of short-range, long-range and extrastriate connections. Recently, a computational model by Wielaard and Sajda showed that centre-surround effects can be reasonably well explained by a model of V1 that only consists of short-range intracortical connections [222]. Additionally, recent experiments demonstrate that short-range connections might be enough to produce surround suppression [161] since it also occurs in layers that do not have long-range connections or do not receive extra-striate feedback.

The network model presented in this work achieves centre-surround suppression without long-range connections and extrastriate feedback in way similar to the model Wielaard and Sajda [222]. In the present model, however, the main factor influencing centre-surround suppression is intra-cortical inhibition, whereas the model of Wielaard and Sajda produces suppression through a mixture of inhibition and reduced excitation. Nevertheles, it has to be noted that the questions that would allow to unequivocally discern between the three above-mentioned hypotheses have not been addressed, since the current network is too small to adequately model horizontal long-range connections and to reliably address the problem of surround sizes. even so, the model could be easily extended to investigate these questions in detail (see also Section 8.1.4.

The importance of a modelling framework for this problem has to be noted. As mentioned earlier, and as argued by Wielaard and Sajda [222], the current experimen-

tal methods do not make it possible to rigorously discriminate the influence of the three proposed mechanisms for centre-surround suppression. In this case, having a computational model that makes all assumptions explicit and that is able to generate predictions that result from these assumptions is an invaluable tool to address this difficult question. The network model is an attempt to provide such a modelling framework.

8.1.4. Modelling Considerations

After addressing receptive field, contrast response and centre-surround suppression properties in the previous sections, the potential and limitations of the proposed network model need to be discussed as well as the chosen modelling approach. The model developed in this work has two major areas of application: The detailed study of mechanisms underlying receptive field phenomena in V1, and the detailed study of mechanisms underlying centre-surround properties in V1.

Receptive Field Phenomena The current model already shows a large variety of features that fit in well experimental data (see Section 6.3.2). Moreover, it displays these features simultaneously, that is, the parameters are not tuned for each feature separately, but the model shows all tested receptive field phenomena with a fixed set of parameters. However, although many important aspects of receptive field phenomena are covered in this work, the amount of experimental data on V1 is enormous and it was not possible to include all of it into the model. Some of these are addressed here, as they seem especially important either with respect to the above-mentioned feed-forward and recurrent theories of feature selectivities in V1, or with respect to the co-existence of feature selectivities (see Chapter 5).

Regarding the emergence of feature selectivities, recent experimental data on the temporal dynamics of orientation selectivity using so-called reverse correlation methods (developed by Ringach et al. [173]) strongly suggest a crucial role of recurrent inhibition [175, 187]. Here, a 'movie' of randomly chosen sinusoidal grating stimuli of varying orientations is displayed, and a probability distribution for orientation is estimated by correlating each spike of the neuron at hand with the orientation of the grating for a specific time offset. This gives different orientation tuning curves for the different time offsets and thus a more detailed description of the temporal dynamics of the orientation selectivity process. A comparison of the dynamics of orientation selectivity in the proposed network model with these experimental data and an investigation of the role of inhibition in this process would be highly interesting. The experimental protocols could be readily transferred to the network modelled here, due to its high flexibility.

Recent experimental and modelling studies have started addressing the co-existence of feature selectivities by exploring the correlations between orientation and spatial frequency selectivity [81, 224, 232]. All studies find strong correlations between orientation selectivity and spatial frequency selectivity measures in both experiments and models. This aspect has not been addressed in the presented work, but similar correlations can be expected in the network, since the mechanisms that produce selectivities are very similar to those used in the mentioned models. Furthermore, the model allows for more detailed analyses than those covered by the scope of this work. For instance, it would be possible not only to relate different selectivity measures to each other, but also to analyse the correlation between feature selectivity and, for example, receptive field width, number of projecting LGN neurons, among others.

Centre-Surround Suppression Centre-surround suppression properties in the network have been explored with sinusoidal gratings and random texture patterns. For both stimulus types, there is a general and strong correspondence with experimental data (see Section 6.3.3). However, several points have not been addressed, such as the surround sizes that can be produced with the local circuitry of the model, the centre-surround suppression in the LGN, the feed-back from other layers and from extrastriate areas (although extrastriate areas do not project to layer 4C), and long-range horizontal connections (although layer 4C hardly receives any horizontal projections).

In order to test the surround sizes produced with the proposed model, the network size would have to be increased to cover a larger area of the visual field, similar to the model of Wielaard and Sajda [222]. An increase in the size of the model would also make it more comparable to human psychophysical studies, since typical centre-surround suppression stimuli used in these studies cover a range of 5-7° of the visual field. An integration of centre-surround suppression in the LGN into the model of thalamic processing could be based on recent experimental data by Solomon et al. [196], but would require changes to the model, although these would be minor, A modelling of feed-back from other layers of V1 would imply a detailed modelling of all layers, which would dramatically increase the complexity of the model and would have to be as rigorously based on experimental data as done in the current model. Although this would greatly improve the model, it would also entail a much larger effort than the current model. An integration of extrastriate feed-back would require an adequate model thereof. However, there is only limited experimental data that measure the extrastriate influence on V1 neurons. As mentioned above, these feed-back projections do not target layer 4C of V1. Therefore, either the other layers of V1 and the extrastriate feed-back projections onto them would

have to be modelled in detail, or a unified, simple model of feed-back from outside of layer 4C would have to be developed. Horizontal connections could also be incorporated into either of these options.

In the end, all these points have to be addressed in order to rigorously test whether the local circuitry in V1 is sufficient to produce centre-surround suppression in all the different experimental conditions. Despite this, the model proposed in this work lays the foundation for a detailed, biophysically grounded, model-based investigation of centre-surround phenomena in V1.

Why detailed modelling? The model offers a big advantage over experimental work in that it allows accessing all parameters at all time, which is not possible in experiments. Admittedly, the model only gives an approximation of the processes in the living brain and, thus, the ground truth can only be provided by experimental data. However, the model provides an invaluable tool to explore the system and generate ideas and hypotheses, which can then be experimentally tested. While the accessibility of parameters is, of course, also true for more abstract models, it is easier to generate new testable hypotheses for detailed models, as the one presented in this work, because the employed neuron models have biophysically meaningful parameters, that is, they directly describe an experimentally measurable quantity. Withal, this comes at the cost of a high computational complexity and long simulation times, a large implementation effort, a non-trivial interpretation of results, due to their complexity.

Concluding, biophysically detailed modelling has become an indispensable tool, which offers great advantages over experimental techniques and more abstract modelling methods, but also has some disadvantages. Therefore, it only unfolds its full potential in combination with more abstract models, tightly linked to the detailed model, and, most importantly, with human or animal experiments.

8.2. Experimental Studies

The second part of this work investigated perceptual centre-surround suppression and its neural correlates in humans in a study that comprised a psychophysical matching task,fMRI and magnetic resonance spectroscopy (MRS). In addition to healthy participants, a group schizophrenic patients was included in the study, because of their documented deficits in centre-surround suppression, as well as known distortions in the GABAergic inhibitory system (see Chapter 7). Six conclusions can be drawn fro this study. In the first place, perceptual centre-surround suppression markedly reduces perceived contrast in the contrast-contrast illusion task. However, centre-surround suppression does not differ significantly between schizophrenic patients and controls. In the second place, in V1, the absolute concentration of γ-amino-butyric acid (GABA) and the GABA/creatine ratio are significantly lower, and the glutamate/GABA ratio is significantly higher in the patient group compared to the healthy control group. In the third place, the contrast-evoked blood-oxygen-level dependent (BOLD) response in V1 is reduced for schizophrenic patients. In the fourth place, neither the GABA/creatine ratio nor the glutamate/GABA ratio correlate with the strength of perceptual centre-surround suppression in V1 in either of the groups. In the fifth place, the BOLD response does not correlate with the strength of perceptual surround suppression in V1 in neither of the groups. Finally, in the sixth place, neither the GABA/creatine ratio nor the glutamate/-GABA ratio correlate with the BOLD response in V1 in neither of the groups.

8.2.1. Psychophysical Measures

The psychophysical data show that the surround lowers the perceived target contrast consistently with previous reports [43]. However, contrary to the hypothesis, the centre-surround suppression is not significantly lower in the patient group than in the control group (see Table 7.18). These findings are in contrast to previous studies using similar centre-surround suppression tasks, which have reported deficits in contextual contrast integration in patients suffering from schizophrenia [12, 51, 206, 227–229]. Furthermore, such deficits have been observed for size in patients with disorganised schizophrenia [213, 214] and for motion in schizophrenic patients [203].

Since the paradigm employed in this study slightly varies from those used in previous studies, the specific experimental set-up could have led to these differences. However, this seems implausible for two reasons: the centre-surround suppression strength for healthy controls (see Table 7.18) is comparable with the above-mentioned reports, and the inter-trial variability in both groups reflects previously reported values (see Table

7.18).

Another factor, that might explain the findings from this study is the heterogeneity of the patient group, which consisted of acutely ill inpatients with first episode of schizophrenia as well as chronically ill outpatients. The previous study by Dakin et al. [51], who report strong effect sizes, only tested chronically ill inpatients; whereas, the studies by Barch et al. [12] and Tibber et al [206], who report weaker effect sizes, consisted only of stable outpatients and of a mixture of stable outpatients, and chronically ill inpatients, respectively. Taken together, there seems to be an influence of the severity and the duration of the illness on centre-surround suppression. Therefore, a correlation analysis with the clinical parameters of duration and severity of the disorder would be convenient in future studies.

Another element that might account for these results is the significant difference in inter-trial variability, which reflects a higher noise level in the patient population. The training time for the participants was relatively short. Whereas this seems sufficient for the control group, it might not be optimal for the patients, as the high variability in the patient group demonstrates. However, a prolonged training time adds to the discomfort and/or drop-out of the patients and is, for practical reasons, hard to achieve.

General visual abilities potentially influence the centre-surround suppression strength. Still, since visual acuity and contrast sensitivity did not differ statistically between both groups (see Table 7.3), it does not appear to be a confounding factor in the current results. The same applies for the demographic factors age and sex (see Figure 7.4). The education level in both groups was significantly different (see Figure 7.4), a possible effect seems unlikely, since there was no correlation of education level with the strength of centre-surround suppression, neither in the patient group nor in the control group.

Antipsychotic medication might also have an effect on the measured centre-surround suppression strength in the patient group. Although the patients did not receive medication directly affecting the GABAergic system, which is thought to mediate centre-surround suppression, atypical neuroleptics typically affect multiple neurotransmitter systems and receptor types and thus might have indirectly influenced the GABAergic system.

Finally, attentional engagement could be a potential confounder. Barch et al [12] have recently demonstrated that group differences in centre-surround suppression levels disappear after controlling for attention. They conclude that the found differences are largely due to attentional impairments in schizophrenic patients. However, the effect reported before controlling for attention is rather weak (Cohen's $d = .27$-$.31$), so that exclusion of non-attentive participants might have simply lowered the power of their anal-

ysis. The study presented in this work did not control for attentional engagement was not executed in the study presented in this work, but the significantly higher inter-trial variability might also indicate a lower attention in the patient group.

Concluding, although there is evidence of a reduced centre-surround suppression strength in schizophrenic patients, the study presented here could not replicate this finding. Nevertheless, possible confounds cannot be excluded with certainty and, especially, the heterogeneity of the patient group, as well as the possible differences in attentional engagement, might have influenced the results.

8.2.2. MR Spectroscopy

The MRS data show, in agreement with the hypothesis, that the absolute GABA concentration and the GABA/creatine ratio in V1 are significantly lower, and the glutamate/-GABA ratio in V1 are significantly higher in the patient group compared to the control group (see Table 7.10). Yoon et al. [229] also report reduced levels of GABA in the visual cortex of schizophrenic patients. Furthermore, these findings match findings in the cingulate cortex [177], where reduced GABA/creatine ratios are also observed and with post-mortem studies that have observed reduced concentrations of cortical GABA [49]. Notwithstanding, these findings are controversial [118, 162]. In the study at hand, no differences between groups are observed in the absolute glutamate and the glutamate/creatine ratio (see Table 7.10). This is also in agreement with previous findings in other brain regions. For instance, Bartha et al. [13] report no differences in glutamate levels between schizophrenic patients and control participants in the left medial prefrontal cortex.

Findings of reduced GABA levels in schizophrenic patients are consistent with the GABA hypothesis of schizophrenia, which attributes symptoms and cognitive deficits to a compromised GABAergic system [130]. Further evidence supporting the GABA hypothesis comes from findings of reduced activity of the glutamate decarboxylase (GAD67), the necessary enzyme for GABA synthesis [18]. However, an alternative hypothesis explaining these results is that the reduced inhibitory activity and the compromised GABAergic system are merely a consequence of a reduced glutamatergic activation of GABAergic interneurons via N-methyl-D-aspartic acid (NMDA) receptors: the so-called NMDA hypothesis of schizophrenia [130]. Evidence in favour of this hypothesis is that: NMDA antagonists found in anaesthetics can induce conditions that resemble schizophrenia [111], and can reproduce negative and positive symptoms, as well as cognitive deficits [120, 180]. However, in the present study no alterations are found in glutamate levels (absolute and relative to creatine) in the current study, which does not support the NMDA hypothesis.

So far, MRS investigations in schizophrenia have mainly targeted the frontal lobe and the hippocampus. However, the findings presented here, support the notion of a compromised GABAergic system throughout the cortex, and might be the neural correlates of ubiquitous changes in cortical function in schizophrenia.

MRS results crucially depend on the image quality. Overall image quality in this study was very good, as indicated by the low Cramer-Rao bounds for the most prominent metabolites (data not shown). This is not surprising since V1 is ideally suited for MRS measurements, due to its proximity to the surface of the head and the relatively large distance to cavities and fatty tissue. However, reliable detection and quantification of GABA is challenging, because it is only present in a low concentration in the human brain and it overlaps with more prominent molecules in the spectrum [168]. In this study, a standard point-resolved spectroscopy (PRESS) sequence used with a modified echo time of 80 ms, in order to resolve the glutamate and glutamine peaks at approximately 2.05-2.50 ppm. This sequence is not optimal for GABA detection and quantification, and thus the Cramer-Rao bounds were relatively high (see Tables 7.4 and 7.5). Therefore, the results reported here have to be treated with caution and more reliable GABA quantification will be necessary for future studies. There are two recent promising approaches to that respect: J-editing MEGA-PRESS sequences [16, 145, 178] and 2-D J-resolved MRS [116]. In contrast, the reliability of the glutamate quantification in this study was very high, as indicated by the generally low Cramer-Rao bounds (see Tables 7.6 and 7.7). The separation of glutamate and glutamine peaks in MRS spectra can be challenging; however, the sequence used in this study was optimised to resolve this issue. Thus, the approach to quantify glutamate taken in this study seems more reliable than approaches using standard sequences.

8.2.3. Functional MR Imaging

The fMRI data of the study show, consistent with the hypothesis of a significantly reduced BOLD response in V1 in response to contrast texture patterns in schizophrenic patients compared to healthy control participants, although, the effect was weak (see Figure 7.16). This finding dovetails with a study by Martinez et al., who report reduced activation in V1 in schizophrenic patients in response to sinusoidal gratings at different levels of contrast [139]. However, other studies have shown normal [11, 25] and even increased [45] BOLD responses to visual stimuli. These ambiguous results might be explained by the nature of the stimuli used in the latter studies, which non-selectively activated magnocellular and parvocellular streams. In contrast, Martinez et al. [139] used stimuli selectively targeting the magnocellular pathway in a narrow spatial frequency band. This

suggests a specific deficiency in the magnocellular pathway in patients suffering from schizophrenia. The texture patterns used in presented in this work, do most probably also mainly target the magnocellular pathway, although not exclusively. Furthermore, the spatial frequencies in the stimuli are restricted to a narrow band similar to those used by Martinez et al. [139]. This might explain the apparent inconsistency of the findings with previous studies. Nevertheless, the study by Martinez et al. [139] found diminished sensitivity especially to low contrast stimuli.

Additionally, schizophrenic patients show a higher BOLD response in the medial temporal lobe in comparison to the control group (see Figure 7.17). Previous studies have found reduced grey matter in the temporal lobe of schizophrenic patients [90, 188]. Furthermore, the role of the temporal lobe in the processing of faces is documented and Holt et al. [92] found an increased BOLD activity in the temporal lobe in schizophrenic patients, when viewing emotional facial expressions. The findings from the study presented here add to the evidence of abnormal structure and function in the temporal lobe in patients suffering from schizophrenia.

8.2.4. Relations Between Neurotransmission, Contrast-Evoked BOLD Signal and Context Perception

In addition to the independent examination of each of the three modalities (psychophysics, MRS and fMRI), the study investigated pairwise correlations between them. This produced three main results. Firstly, GABA/creatine ratios, glutamate/creatine ratios and glutamate/GABA ratios in V1 did not significantly correlate with the strength of centre-surround suppression neither in the patient nor in the control groups (see Table 7.21). Secondly, the strength of the BOLD response in V1 did not significantly correlate with the strength of centre-surround suppression neither in the patient group nor in the control group (see Table 7.22). Nevertheless, there was a marginally significant difference between the correlation coefficients of both groups (see Figure 7.22). Thirdly, the BOLD response in V1 did not significantly correlate with GABA/creatine ratios, glutamate/creatine ratios and glutamate/GABA ratios (see Table 7.23).

The absence of a correlation between GABA/creatine ratios and centre-surround suppression is inconsistent with a previous study of Yoon et al. [229] with schizophrenic patients, which found reduced GABA concentrations, reduced centre-surround suppression and a strong correlation between both. This was interpreted as an underpinning of the GABA hypothesis of schizophrenia. However, there are differences between the two studies. Yoon et al. investigated orientation-specific centre-surround suppression using sinusoidal gratings and studied contrast thresholds instead of the bias introduced

by the grating. Furthermore, the schizophrenic group only consisted of stable outpatients. Therefore, it is likely that, the absence of a correlation in the current study comes from the absence of a group difference regarding centre-surround suppression, despite the fact that reduced GABA concentrations are found. Furthermore, there might not be a correlation between GABA concentrations and non-specific centre-surround suppression measured by bias; this relationship might be limited to the orientation-specific case measured by contrast thresholds. Finally, the perceptual and behavioural consequences of reduced GABA concentrations might differ with respect to severity and duration of the disorder.

The absence of a correlation between BOLD response in V1 and centre-surround suppression is inconsistent with a previous study of Zenger-Landolt et al. [230]. Zenger-Landolt et al. found a positive correlation between BOLD activation in V1 and centre-surround suppression in response to sinusoidal gratings in healthy participants. The absence of the correlation in the patient group in the presented study is likely due to the absence of a reduction in centre-surround suppression in this group, whereas the GABA concentration was significantly reduced, in comparison to the control group. As in the above-mentioned study of Yoon et al. [229], Zenger-Landolt et al. investigated contrast threshold using sinusoidal gratings. Thus, the absence of a correlation in the control group as well as the absence of differences in centre-surround suppression might be task-specific. Still, there was a trend towards a difference between the correlation coefficients describing the relation in both groups. This might suggest a difference in the processing of contrast stimuli between schizophrenic patients and healthy controls. Furthermore, correlations between centre-surround suppression and BOLD response are observed in the thalamus for both groups (see Figures 7.23, 7.24 and 7.25). However, the exact locations are different in both groups, which again suggests a difference in the contrast processing underlying centre-surround suppression. Thus, the trend towards opposing relations between BOLD response and centre-surround suppression might stem from a different processing occurring already at thalamic level.

The presented study does not find correlations between BOLD response and GABA/creatine ratios in V1 in neither group. However, in a recent work Muthukumaraswamy et al. [151] demonstrated a strong negative correlation between GABA concentration and BOLD response in the visual cortex of healthy participants. This finding is supported by several other studies: Firstly, Muthukumaraswamy et al. [152] report a strong negative correlation between GABA concentration and amplitude of the haemodynamic response function in the visual cortex. Secondly, Chen et al. [42] blocked the action of GABA transaminase (GABA-T), which is crucial in breaking down GABA, by administration of

a GABA-T inhibiting drug in the somatosensory cortex of rats. This results in elevated GABA levels as quantified by MRS and, importantly, in a significant decrease in BOLD activation. Lastly, Northoff et al. [155] report a strong correlation between GABA levels and negative BOLD responses in the anterior cingulate cortex in humans. A common interpretation of this relationship is, that the amplitude of the BOLD response strongly depends on the balance of excitation and inhibition, and that increases in GABA shift this balance towards inhibition, thus reducing positive BOLD responses and increasing negative ones. However, it needs to be noted that the GABA level measured by MRS is a bulk concentration and does not necessarily reflect the local effects of GABA on the excitation/inhibition balance. The results presented here, thus indicate that a direct inference on the effects of GABA on local circuit dynamics cannot be readily made from GABA concentrations measured by MRS and that a deeper understanding of the relationship of global GABA levels and excitation/inhibition balances in localised circuits is necessary. The same argument applies to glutamate/creatine and glutamate/GABA ratios. However, to the author's knowledge, no correlation of both of these ratios with BOLD responses in V1 have been reported. This is surprising, because, if the BOLD response depended on the excitation/inhibition balance, changes in glutamate, as well as changes in the glutamate/GABA ratio, should also influence BOLD responses. Most studies, however, do not measure glutamate levels but rather the combined glutamate and glutamine levels because of their strong overlap in the MRS spectrum at the standard echo time $TE = 68\,ms$. The absence of such correlations is then usually explained by the fact that glutamine may contribute with as much as $45\,\%$ to this combined estimate and might mask the correlation between glutamate and the BOLD response [e.g. 151]. However, in the study presented here, the echo time $TE = 80\,ms$ was optimised in order to reliably quantify glutamate. The fact that there still is no correlation between glutamate level and BOLD response, further adds to the issue that global MRS measures of neurotransmitter concentrations might not necessarily reflect effects on the local circuit level.

8.3. Modelling vs. Experiments

In Chapter 6 the present network model was tested with the same contrast texture patterns that were used in Chapter 7 to test centre-surround suppression in humans. One of the ultimate goals of the modelling effort described in this work was to compare these modelling results, that is, the influence of parameters governing inhibition on centre-surround suppression, with the psychophysical and neuroimaging results and then to possibly identify one or several parameters that would allow to discriminate between healthy participants and patients.

However, this comparison is difficult for different reasons: First, due to its complexity, the size of the network was limited in the present work. This implies that a quantitative match between the stimulus sizes used in the model and those used in the psychophysical experiment cannot be given, and thus a quantitative comparison of the matching contrasts cannot be made. However, with the present model, that is, after the thorough and time-consuming validation performed in Chapter 6, an up-scaled version of the model could overcome this limitation. Another option, the use of a more abstract model with lower computational complexity (e.g. integrate-and-fire neurons) seems less favourable since the model would then lose the connection of its parameters to measurable biophysical quantities, which again would prevent quantitative comparisons. Second, the relationship between the parameters tested in the model on the one hand, and the neurotransmitter levels and BOLD signals on the other hand, is still not fully understood. Therefore, a quantitative comparison of these is not yet possible. In summary, there is still a gap in the understanding of the relationships between neural processes on the microcircuit scale and the corresponding phenomena on the perceptual scale.

Despite this, the modelling results of this work are in a general, qualitative agreement with the experimental results presented here and in other psychophysical studies. Furthermore, the present model constitutes a step towards bridging the gap between the neural, microcircuit and the perceptual scale.

9. Conclusion and Outlook

9.1. Contributions

Throughout this work, a biophysically detailed model and experimental results have been presented that advance the understanding of centre-surround suppression on two complementary scales, that is, the local scale of neural circuits and the global scale of perception. One of the main goals of this work was to provide the basis for establishing a link between these two scales.

On the neural circuits scale, a large-scale, biophysically detailed neural network model of the input layer of the primary visual cortex (V1) was developed. The model possesses characteristic features of V1, matching well with experimental data. Furthermore, it extends previous models in that it matches experiments better and has more morphological and biophysical detail. The model allows for an investigation of the mechanisms of feature selectivity in V1 and yields a mechanistic underpinning of the theory explaining the emergence of feature selectivity in terms of recurrent inhibition.

Further, centre-surround suppression and the role of recurrent inhibition in shaping it were explored was performed using the neural network model. The model shows neural centre-surround suppression that concurs with experimental work, allowing for the mechanism underlying the suppression to be identified. Suppression is achieved through recurrent inhibition mediated through the specific pattern of connections. This mechanism is consistent with that, which produces the characteristic feature selectivities. The model demonstrates that various parameters governing recurrent inhibition interplay in neural centre-surround suppression, and additionally, although counterintuitively, that inhibition is also crucial for centre-surround facilitation.

In addition to the investigation of classical receptive field properties and centre-surround suppression mechanisms, the proposed model offers the possibility to perform detailed studies in two other areas of neuroscience: mechanisms of neurological diseases and of pharmacological interventions. An incorporation of models of disease mechanisms and drug mechanisms, respectively, would allow for the study of their effects on the properties of the network model and thus might enable a deeper understanding of these pro-

cesses.

The presented model is explicitly designed to be flexible and easily extensible, and code is available for all common neural simulators as well as in NeuroML, a simulator-independent markup language.

On the perceptual scale, centre-surround suppression and its neural correlates were investigated using a psychophysical task, functional magnetic resonance imaging (fMRI) and magnetic resonance spectroscopy (MRS). In addition to healthy participants, patients suffering from schizophrenia were included in the study, since schizophrenia has been associated with abnormal centre-surround suppression and with an impaired, GABAergic inhibitory system [51, 228, 229].

The study does not confirm previous reports of reduced centre-surround suppression in the heterogeneous patient group that participated. However, it evidences that schizophrenic patients show a reduction in γ-amino-butyric acid (GABA) concentrations and in blood-oxygenated-level dependent (BOLD) response in the visual cortex. Moreover, differences in thalamic processing of contrast related aspects of centre-surround suppression are suggested by an analysis of correlations between centre-surround suppression and BOLD activation. Further correlation analyses between neurotransmitter concentrations (GABA and glutamate) and BOLD responses suggested a more complex relationship between the neurotransmitter concentrations measured by MRS and neural activity on the local neural circuit level than previously assumed.

9.2. Outlook

9.2.1. A Community Model of the Primary Visual Cortex

The model presented in this work is intended to serve as a starting point for a neural network model commonly used by the computational, visual neuroscience research community.

However, several further developments can be implemented in the future of the model to display its full potential. At the moment, the current model only represents the input layer of V1 so far, but a complete understanding of the computations performed by V1, as well as the mechanisms underlying these computations, can only be gained by a full model of all cortical layers. Furthermore, the diversity of neuron types, with respect to morphology and dynamics, is much greater than that implemented in the current model. Since this diversity most certainly fulfils a functional purpose, incorporating of these different types of neurons with greater detail seems necessary. Anatomical and physio-

logical data on which to ground the model already exist [14, 17, 47, 60, 137, 156].

The majority of experimental data used to validate the current model are intracellular recordings in animals, mainly macaque monkeys. However, a simulation of other measures of neural activity, such as fMRI signals, local field potentials (LFP) and optical imaging data, combined with a thorough comparison against experimental work, would not only highly increase the explanatory power of the model, it would also allow for a deeper understanding of the relationships of these different modalities and their dependence on neural processes. Approaches on the modelling of these measures already exist. In the case of fMRI, detailed models have been developed relating neural activity to haemodynamic responses [71, 219], but also coarser approximations have been employed, for example by using summed synaptic activity as measure of the BOLD response [110]. Linden et al. [127–129] have modelled the generation of LFPs as result of the underlying neural activity, and thus, provided the basis for a calculation of LFPs from simulated neural activity. Wielaard and Sajda [221] provide a model to calculate optical imaging signals from membrane potential traces and, as a simplification thereof, from neuronal spike trains. All the above-mentioned models can be readily applied to the proposed network model, since it makes it possible access to all necessary parameters, such as membrane potentials, synaptic currents and conductances, and spatial and connectivity information.

One of the most important property of the brain, the ability to learn and adapt to new circumstances, which is implemented by the plasticity of neural connections, has not been addressed in the current model, due to the additional complexity this would have posed. However, especially the modelling of changes of the inhibitory system has revealed that these adaptation mechanisms need to be considered. Many phenomenological models of short-term depression and facilitation [e.g. 136] and long-term plasticity [e.g. 33, 107, 200], exist and have been applied in large-scale neural network models [107, 110]. The infra-structure for a future inclusion into the proposed model is given.

The further investigation of the mechanisms underlying centre-surround suppression and a thorough testing of the explanatory theories, demands appropriate modelling of long-range horizontal connections and of extrastriate feed-back projections. Again, an experimental basis, that is, fairly detailed anatomical and physiological data, already exists [e.g. 17, 60], so that this could be implemented in future versions of the model.

9.2.2. Theory of Receptive Field Properties

The mechanisms underlying the emergence of receptive field properties in the proposed model support the theory of recurrent inhibition as the primary underlying mechanism.

However, feature selectivity in V1 is still far from being fully explained by this theory and many aspects of feature tuning remain elusive. Recent experiments and models have addressed two important facets: the temporal dynamics [173, 187, 225] and the co-existence of selectivities [224, 232]

The temporal dynamics of feature selectivities have not been addressed in the current model so far. Nevertheless, an implementation of the experimental protocols used in the above-mentioned studies is possible in the current model without further ado. An *in silico* replication of these experimental findings would provide a further underpinning of this theory of classical receptive field properties and allow for a more detailed investigation of the underlying mechanisms.

The study of the co-existence and simultaneous implementation of feature selectivities in V1, would provide further insights into the functions and computations of V1. The theoretical work so far, has mainly focused on the explanation of single feature selectivities. Withal, their interactions and their possible mutual necessitation have been widely ignored. Recent experimental [224] and modelling work [232] has started to address this problem. However, a deeper exploration is needed and the proposed model builds an ideal basis for this.

9.2.3. Theory of Centre-Surround Suppression

The neural mechanisms behind centre-surround suppression are less understood than those of classical receptive field properties, since reliable measurements pose greater challenges to experimenters, and they depend on the incompletely understood classical feature selectivities.

Three competing theories exist at the moment, which ascribe the emergence of centre-surround suppression mainly to local, short-range circuitry [222], horizontal, long-range connections [56, 102], and extrastriate feed-back projections [6, 10, 101, 202], respectively. The evidence for or against any of these theories is controversial, partly because of inadequate experimental methods, partly because of a lack of computational support [222]. A further understanding of this phenomenon and a rigorous testing of the different hypotheses would greatly benefit from a strong computational support, for which the proposed network model builds an ideal starting point.

A. The Visual System

In this chapter the function and organisation of the human visual system is reviewed with a focus on the early stages of visual processing, especially in primary visual cortex. It gives an overview of the anatomy of the visual system

A.1. Functional Neuroanatomy

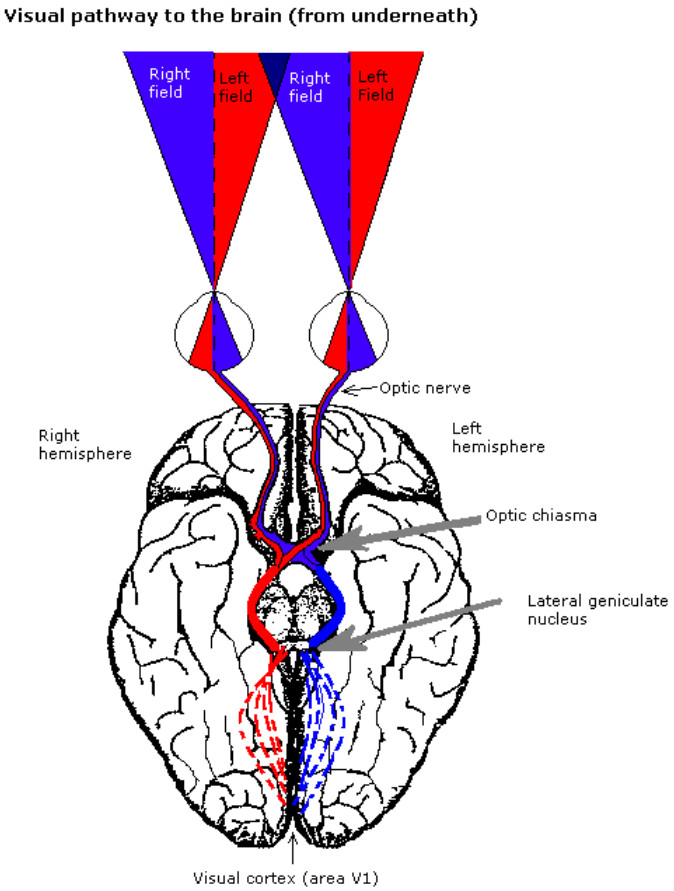

Figure A.1.: Depiction of the visual pathway from the eye to the cortex ([93] License: GFDL).

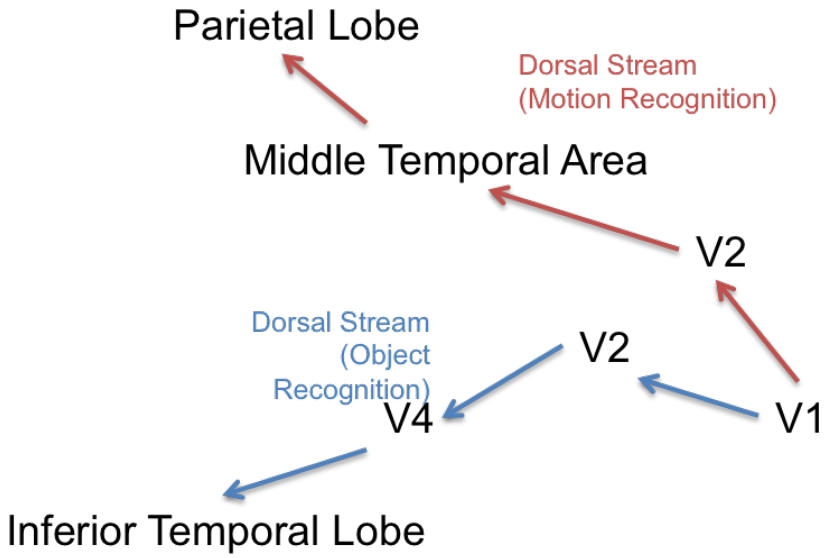

Figure A.2.: The two streams in higher visual processing. The *ventral stream*, also called the *what stream*, and the *dorsal stream*, also called the *where stream*([95] License: GFDL).

Visual processing starts with the input of external stimuli, i.e. light waves hitting the eye and therein the retinal photoreceptors. After a transmission from electromagnetic waves to electric impulses in the retina, the retinal ganglion cells mainly transduce the information to the thalamus, i.e. the dorsal and the ventral part of the lateral geniculate nucleus (LGN). Cells in LGN further relay the sensory information to neurons in the primary visual cortex (also striate cortex, abbrev. V1). In primary visual cortex information is further processed and then fed into two distinct streams, although connections between these two streams exist. The first stream (the so-called *dorsal stream*), is dedicated to the localisation of objects and the detection of motion. It mainly comprises the areas V2, V3, MT (also called V5) and MST and gives us our sense of spatial orientation, movement direction and speed of motion of objects. It fuses information from both eyes to give us depth perception. The second stream (the so-called *ventral stream*) mainly comprises the areas V2, V3, V4 and IT. It is important for perception of shape as well as colour perception [46].

A.1.1. The Eye - Phototransduction and Retinal Processing

The visual system starts with the eye, where the incoming light is directed towards the retina at the back of the eye with the help of an adjustable lens and an iris that controls the amount of light coming in. The retina is a laminar structure dedicated to the

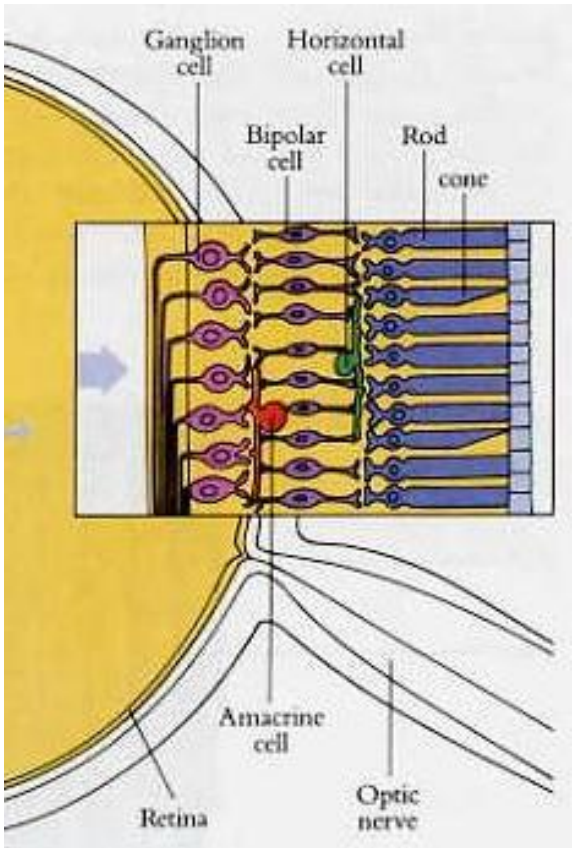

Figure A.3.: Depiction of the layered structure of the retina within the eye ball ([96] with friendly permission from the copyright holder).

transduction of light energy into electric impulses and the processing of the electrical activity. It consists of five different functional units, the *photoreceptors*, the *horizontal cells*, the *bipolar cells*, the *amacrine cells* and the *ganglion cells*. The direct way of information processing goes from the photoreceptors to the bipolar cells and then further to the ganglion cells, which send axons through the optic nerve to the brain. The horizontal cells receive input from photoreceptors and connect laterally to surrounding photoreceptors and bipolar cells and the amacrine cells receive input from bipolar cells and influence ganglion cells, bipolar cells as well as other amacrine cells in the surrounding (see Figure A.3 for a schematic depiction of retinal organisation).

Photoreceptors Light is converted into neural signals via the *photoreceptors*. In the human retina two types of photoreceptors, with different structure and function, exist. The *rod photoreceptors* have long, cylindrical outer segments whereas the *cone photoreceptors* have shorter, tapering outer segments. For both photoreceptors the outer segment contains membranous disks filled with *photopigments*, a light-sensitive substance. The photopigments absorb light, thereby changing the potential of the surrounding membrane and thus transform light energy into neural signals. While the rods have a very high sensitivity to incoming light the smaller outer segments of the cones lead to a significant reduction in light sensitivity. However, only the cones are specifically sensitive to certain wavelength bands and are thus responsible for colour vision. There exist three types of cones sensitive to blue, red and green, respectively.

Bipolar Cells **Bipolar cells** are divided into two groups based on their response to 'light off' or 'light on' conditions. **OFF bipolar cells** respond to 'light off' conditions with a depolarisation due to the increase in glutamate from the photoreceptors, whereas **ON bipolar cells** respond with a depolarisation to 'light on' conditions, i.e. a decrease in glutamate. Bipolar cell receive direct input from a patch of photoreceptors depending on their location in the retina. In the region near the fovea the patches only contain few photoreceptors (down to 1) whereas in the peripheral regions the patches can contain thousands of them. However, this is not the only input to the bipolar cells. Bipolar cells also receive connections from horizontal cells which receive their input from a ring surrounding the patch that directly targets the bipolar cells, thus creating a **receptive field**, i.e. the area of the retina that, when stimulated changes the cell's membrane potential, with a centre-surround structure. The response of the bipolar cell to light falling into the different parts of its receptive field is reversed, i.e. either light falling into the centre causes depolarisation and light falling into the surround causes hyper-polarisation or the

opposite, a mechanism which is seen throughout the visual system.

Horizontal Cells Horizontal cells are connected with photoreceptors in a centre-surround fashion and control the activity of their centre photoreceptor cells based on the activity of the their surround photoreceptor cells. By this mechanism they indirectly induce a centre-surround receptive field in the bipolar cells. This surround effect enhances brightness contrasts to produce sharper images and makes objects appear brighter or darker depending on the background. Furthermore it enables to maintain these contrasts under different levels of illumination.

Amacrine Cells Amacrine cells connect to bipolar cells and ganglion cells. They provide lateral connection in between of these groups, similar to horizontal cells, but also provide links between bipolar and ganglion cells. There exist many different types of amacrine cells (> 20) but little is known about their function. Some amacrine cells have been identified to produce the movement sensitive response of M-type ganglion cells, to enhance the centre-surround receptive field properties in ganglion cells and to connect bipolar cells responding to cone photoreceptors with bipolar cells responding to rod photoreceptors, therefore allowing ganglion cells to respond to the full range of light levels.

Retinal Cells Similar to the bipolar cells, retinal ganglion cells also have centre-surround antagonistic receptive fields. The existence of these **OFF-centre ganglion cells** and **ON-centre ganglion cells**, i.e. cells that have a centre-surround antagonistic receptive field with a centre responding either to dark spot imaged on its receptive field (OFF) or a bright spot (ON), leads to increased neural responses whenever the image shown has light-dark edges. The retina thus can be seen as an edge-detector or as a contrast-enhancing system

There exist three types of retinal ganglion cells: *M-type* (where M stands for *magno* Latin for large) , *P-type* (where P stands for *parvo* Latin for small) and *nonM-nonP* cells. *M-type* ganglion cells are larger, compared with the other ganglion cell types, and have larger receptive fields, conduct action potentials faster and are more sensitive to low-contrast stimulation [46]. Furthermore, the M-type cells respond with transient bursts of activity to a stimulus whereas P-type cells show regular repetitive firing.

A further distinction, which plays an important role in the later visual processing, is the fact that M-type cells are insensitive the wavelength of the incoming light, whereas some of the other ganglion cells are sensitive to changes in the wavelength, i.e. these cells are colour-sensitive. These colour-sensitive cells show a **colour-opponency** in their receptive field. Colour-opponency means that, for example for a cell with red-green op-

ponency (denoted R^+G^--cell) a red light spot in the centre of the receptive field evokes a large response from this cell, but if additionally a green stimulus is presented in the surround region of the cell's receptive field, this leads to a cancellation of the red effect of the red stimulus, thus results in no response from the cell. The same holds for blue and yellow opponencies. The explanation for this phenomenon is that colour-opponency depends on the type of photoreceptors that constitute the cell's receptive field, e.g. a cell where only cones sensitive to blue light contribute to the centre and only cones sensitive to red and green contribute to the surround is a B^+Y^- cell, i.e. has a blue-yellow opponency . This again explains why M-type cells do not show colour-opponency, their receptive fields are so large that they always integrate cones sensitive to all blue, red and green. Furthermore, it explains why humans only see colours in the centre of our visual field, as explained above, the patches of photoreceptors targeting the bipolar cells grow much larger the more peripheral they lie, thus the peripheral ones integrate all types of cones and loose their colour-sensitivity.

A.1.2. The Thalamus

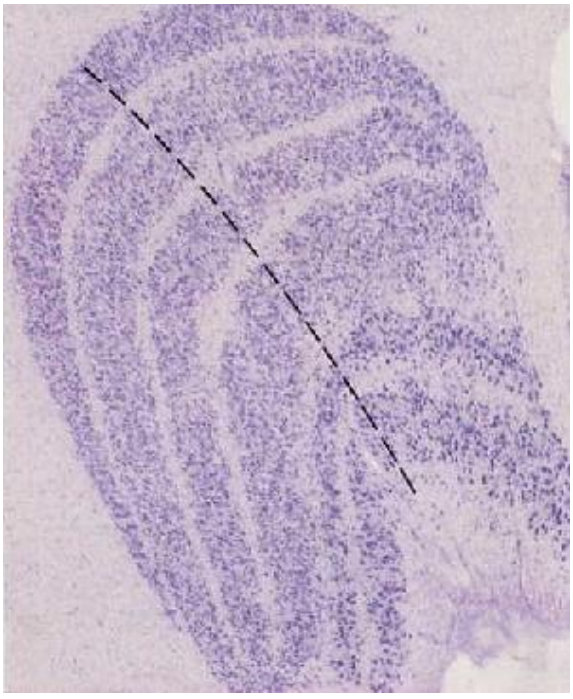

Figure A.4.: Depiction of the layered structure of the LGN ([96] with friendly permission from the copyright holder).

The axons from the retina go along the left and right optic nerve until they reach the optic chiasm, where the information from the right and left visual hemifield, coming from each eye, are separated such that the right optic tract only contains information from the left hemifield and the left optic tract only contains information from the right hemifield. About 80-90 % of the axons in the optic tract target the **lateral geniculate nucleus (LGN)** which is located in the dorsal thalamus bilaterally [46]. The rest of the axons innervate the hypothalamus and the mid-brain. The neurons in thalamus innervate the primary visual cortex and this projection is often called the **optic radiation**. From lesion studies it is known that these projections from LGN to V1 mediate conscious visual perception.

The non-thalamic targets of the optic tract in the hypothalamus and the mid-brain are involved in controlling biological rhythms and the size of the pupil and certain eye movements, respectively.

The thalamic targets of the optic tract, the left and right LGN, is structured in six principal layers of cells which are numbered from 1 to 6 starting in the most ventral layer. It has already been stated that the retinal ganglion can be subdivided into three types of cells. In the thalamus this segregation of these three sub-streams of information persists. The axons from **M-type** ,**P-type** and **nonM-nonP** cells project to different layers of the LGN. The two ventral layers, layer 1 and 2, are called the **magnocellular LGN layers** and the dorsal layers, layer 3 to 6, are called the **parvocellular LGN layers**. The magnocellular layers receive projections exclusively from M-type ganglion cells whereas the parvocellular layers receive projections exclusively from P-type ganglion cells. However, there is a small region of very small neurons between the 6 principal layers of the LGN which receives input projections from the nonM-nonP cells of the retina. These small regions are called the **koniocellular LGN layers**.

But not only the information from the three different retinal ganglion cell types stays segregated in the LGN, but also the information coming from both eyes. In the right LGN, the right (ipsi-lateral) eye cells project to layers 2, 3 and 5 whereas the left (contra-lateral) eye cells send projections to layers 1, 4 and 6 (and vice versa for the left eye).

A.1.3. The Primary Visual Cortex

In primary visual cortex (V1) one finds the laminar 6 layer structure as it is seen throughout cortex. Layer 1 contains only a few cell bodies and mainly consists of dendritic and axonal connections. Layers 2/3 (also called the **supergranular layers**) contain many excitatory projection neurons which mainly target higher visual areas (e.g. V2,V3, V4, MT). Furthermore, layer 2/3 receives very little thalamic input. Layer 4 (the **granular layer**) contains mostly spiny stellate neurons and only few pyramidal cells (as opposed to the

layers 2/3, 5 and 6). It can be subdivided into 4A, 4B and 4C. Layer 4C is the main projection site of innervation from the LGN and can be further subdivided into 4Cα and 4Cβ, where 4Cα receives input only from the M-pathway and 4Cβ only from the P-pathway. This means that the segregation of these two pathways remains also in the visual cortex. Layers 5 and 6 (the **infragranular layer**) contain pyramidal cells that project back to the LGN and provide feedback. Approximately 20% of the neurons in V1 are interneurons. Throughout the layers many types and forms of interneurons, mainly inhibitory, are found. Basket cells, Chandelier cells, neurogliaform cells, double bouquet cells and Cajal-Retzius cells, to name just a few.

A.1.4. Higher Visual Areas

The higher visual areas can be subdivided into two streams the **dorsal stream** and the **ventral stream**, which continues the segregation of M- and P-pathway seen in retinal ganglion cells, LGN and V1. The dorsal stream, often also called the **'where' stream**, goes from V1 through V2 then to the dorso-medial area and area MT (often called V5). It is mainly associated with motion, representation of object location and the control of the eyes and arms. The ventral stream, also called the **'what' stream**, goes from V1 through V2 then to V4 and to inferior temporal cortex. It is mainly associated with object recognition and also involved in storage of long-term memory. Goodale and Milner proposed that the ventral stream performs visual tasks critical for perception whereas the dorsal stream executes tasks related to visual control of skilled actions.

B. Results - The Role of Recurrent Inhibition in Feature Selectivity and Centre-Surround Suppression

B.1. Weight of Inhibitory Connections on Excitatory Cells

and then discusses the functional consequences arising from there.

Table B.1.: Orientation selectivity measures for the five different weights for the inhibitory connections onto excitatory neurons and, as a reference, for the standard configuration of the model.

Weight w_{ie}	Selective Cells	Biased Cells	ORI (mean $\pm$ std)	CV (mean $\pm$ std)
0.1	15.43 %	19.53 %	.38 $\pm$ .26	.86 $\pm$ .14
0.2	42.66 %	19.96 %	.56 $\pm$ .29	.74 $\pm$ .18
0.3	71.43 %	12.75 %	.77 $\pm$ .22	.54 $\pm$ .25
0.4	72.16 %	13.57 %	.77 $\pm$ .25	.53 $\pm$ .22
0.5	72.23 %	12.21 %	.77 $\pm$ .25	.52 $\pm$ .24
0.275 (standard)	72.32 %	12.20 %	.77 $\pm$ .25	.52 $\pm$ .24

Table B.2.: Fitting parameters for the contrast response functions of the mean response of the network neurons for the five different weights of inhibitory on excitatory cells, and for the standard configuration.

Weight w_{ie}	a	k	p	q	r^2
0.1	0.050	1.78	2.10	1.83	0.09
0.2	0.050	1.70	2.20	1.60	0.99
0.3	0.005	1.64	2.22	1.60	0.99
0.4	0.005	1.64	2.20	1.60	0.99
0.5	0.050	1.71	2.20	1.82	0.98
0.275 (standard)	0.050	1.70	2.2	1.8	0.98

Table B.3.: Suppression indices in the size variation test for five different weights of inhibitory connections on excitatory cells and for the standard configuration.

Weight w_{ie}	SI (mean $\pm$ std)
0.1	0.52 ± 0.23
0.2	0.29 ± 0.25
0.3	0.14 ± 0.17
0.4	0.15 ± 0.18
0.5	0.13 ± 0.17
0.275 (standard)	0.13 ± 0.16

Table B.4.: Centre-surround suppression in response to sinusoidal gratings. Suppression indices for the mean responses for five different inhibitory weights in the eight different centre-surround conditions.

Weight: $w_{ie} = 0.1$				
Centre Contrast	.1	.2	.4	.8
Low Surround (SI)	0.82	0.65	0.41	0.38
High Surround (SI)	0.97	0.95	0.65	0.35
Weight: $w_{ie} = 0.2$				
Centre Contrast	.1	.2	.4	.8
Low Surround (SI)	1.15	1.19	0.85	0.26
High Surround (SI)	0.99	0.98	0.36	0.15
Weight: $w_{ie} = 0.3$				
Centre Contrast	.1	.2	.4	.8
Low Surround (SI)	1.36	1.56	0.82	0.17
High Surround (SI)	1.06	0.99	0.36	0.14
Weight: $w_{ie} = 0.4$				
Centre Contrast	.1	.2	.4	.8
Low Surround (SI)	1.46	1.17	0.75	0.14
High Surround (SI)	1.09	1.18	0.39	0.14
Weight: $w_{ie} = 0.5$				
Centre Contrast	.1	.2	.4	.8
Low Surround (SI)	1.55	1.37	0.76	0.14
High Surround (SI)	1.06	1.31	0.36	0.16

Table B.5.: Centre-Surround suppression in response to contrast noise patterns. Responses and matching contrasts for five different inhibitory weights.

Weight: $w_{ie} = 0.1$		
	Response (Hz) (mean± std)	Matching contrast (mean± std)
Predicted 40	17.49 ± 29.27	.4
Small Surround	9.52 ± 16.63	.3271 ± .1866
Large Surround	7.71 ± 14.83	.2819 ± .2037
Weight: $w_{ie} = 0.2$		
	Response (Hz) (mean± std)	Matching contrast (mean± std)
Predicted 40	20.18 ± 22.94	.40
Small Surround	8.33 ± 12.42	.1783 ± .1385
Large Surround	7.38 ± 13.00	.1598 ± .1460
Weight: $w_{ie} = 0.3$		
	Response (Hz) (mean± std)	Matching contrast (mean± std)
Predicted 40	12.86 ± 17.53	.40
Small Surround	5.48 ± 9.09	.2087 ± .1660
Large Surround	4.27 ± 7.64	.1348 ± .1217
Weight: $w_{ie} = 0.4$		
	Response (Hz) (mean± std)	Matching contrast (mean± std)
Predicted 40	8.74 ± 14.63	.40
Small Surround	4.76 ± 8.32	.3272 ± .1867
Large Surround	3.86 ± 7.41	.2821 ± .2039
Weight: $w_{ie} = 0.5$		
	Response (Hz) (mean± std)	Matching contrast (mean± std)
Predicted 40	3.33 ± 5.13	.40
Small Surround	2.82 ± 3.22	.4043 ± .1919
Large Surround	1.96 ± 2.12	.3079 ± .2172

Table B.6.: Centre-Surround suppression in response to contrast noise patterns. r^2 values and percentage of excluded cells, and statistical analysis of the influence of the surround grating on the response for both surround conditions and of the influence of the size of the surround.

Weight w_{ie}	0.1	0.2	0.3	0.4	0.5
r^2-Value	$.60 \pm .14$	$.64 \pm .14$	$.60 \pm .13$	$.60 \pm .14$	$.64 \pm .15$
Excluded Cells	$62.5\,\%$	$25.0\,\%$	$46.9\,\%$	$62.5\,\%$	$73.44\,\%$
Predicted 40 vs Small Surround	n.s. $p = .28$	** $p < .01$	* $p < .05$	n.s. $p = .28$	n.s. $p = .75$
Predicted 40 vs Large Surround	n.s. $p = .18$	** $p < .01$	* $p < .05$	n.s. $p = .17$	n.s. $p = .36$
Small Surround vs Large Surround	n.s. $p = .71$	n.s. $p = .72$	n.s. $p = .57$	n.s. $p = .70$	n.s. $p = .41$

B.2. Weight of Excitatory Connections on Inhibitory Cells

Table B.7.: Orientation selectivity measures the four weights of the excitatory connections onto inhibitory neurons and the standard configuration.

Weight w_{ei}	Selective Cells	Biased Cells	ORI (mean $\pm$ std)	CV (mean $\pm$ std)
0.005	59.15 %	14.95 %	.68±.28	.63±.22
0.02	67.83 %	13.60 %	.73±.26	.57±.22
0.05	66.22 %	16.12 %	$.71 \pm .25$	$.62 \pm .19$
0.1	63.84 %	12.32 %	.68±.29	.62±.22
0.275(standard)	72.32 %	12.20 %	$.77 \pm .25$	$.52 \pm .24$

Table B.8.: Fitting parameters for the contrast response functions of the average response of the network neurons for four different weights w_{ei} and for the standard configuration.

Weight w_{ei}	a	k	p	q	r^2
0.005	0.05	1.73	2.2	1.93	0.97
0.02	0.005	1.76	2.53	1.6	0.99
0.05	0.005	1.78	2.58	1.6	0.97
0.1	0.05	1.70	2.2	1.6	0.85
0.01 (standard)	0.050	1.70	2.2	1.8	0.98

Table B.9.: Centre-surround suppression in response to sinusoidal gratings. Suppression indices in the size variation test for four different weights w_{ei} and the standard configuration.

Weight w_{ei}	SI (mean $\pm$ std)
0.005	0.24 $\pm$ 0.23
0.02	0.17 $\pm$ 0.19
0.05	0.17 $\pm$ 0.19
0.1	0.18$\pm$0.19
0.01 (standard)	0.13 $\pm$ 0.16

Table B.10.: Centre-surround suppression in response to sinusoidal gratings. Suppression indices for four different weights in the eight different centre-surround conditions.

Weight $w_{ei} = 0.005$				
Centre Contrast	.1	.2	.4	.8
Low Surround (SI)	1.79	1.17	0.66	0.23
High Surround (SI)	1.14	0.85	0.27	0.18
Weight $w_{ei} = 0.02$				
Centre Contrast	.1	.2	.4	.8
Low Surround (SI)	1.17	1.03	0.79	0.16
High Surround (SI)	1.04	0.96	0.43	0.10
Weight $w_{ei} = 0.05$				
Centre Contrast	.1	.2	.4	.8
Low Surround (SI)	1.03	1.00	1.00	0.17
High Surround (SI)	1.03	1.00	0.79	0.11
Weight $w_{ei} = 0.1$				
Centre Contrast	.1	.2	.4	.8
Low Surround (SI)	0.96	0.98	1.01	0.25
High Surround (SI)	0.87	0.88	0.89	0.18

Table B.11.: Centre-Surround suppression in response to contrast noise patterns. Responses and matching contrasts for four different weights w_{ei}.

Weight: $w_{ei} = 0.005$		
	Response (Hz) (mean± std)	Matching contrast (mean± std)
Predicted 40	18.76 ± 22.83	.40
Small Surround	11.94 ± 16.71	.2456 ± .1401
Large Surround	9.60 ± 16.30	.1868 ± .1474
Weight: $w_{ei} = 0.02$		
	Response (Hz) (mean± std)	Matching contrast (mean± std)
Predicted 40	10.56 ± 15.56	.40
Small Surround	3.50 ± 5.10	.2494 ± .1883
Large Surround	3.14 ± 4.85	.2121 ± .1625
Weight: $w_{ei} = 0.05$		
	Response (Hz) (mean± std)	Matching contrast (mean± std)
Predicted 40	4.16 ± 7.68	.40
Small Surround	1.88 ± 0.85	.3654 ± .1811
Large Surround	1.89 ± 1.28	.3324 ± .1802
Weight: $w_{ei} = 0.1$		
	Response (Hz) (mean± std)	Matching contrast (mean± std)
Predicted 40	4.50 ± 6.33	.40
Small Surround	2.91 ± 1.49	.3419 ± .1056
Large Surround	2.69 ± 1.47	.3167 ± .0996

Table B.12.: Centre-Surround suppression in response to contrast noise patterns. r^2 values and proportion of excluded cells and statistical analyses of the influence of the surround grating on the response for both surround conditions and, of the influence of the size of the surround.

Weight w_{ei}	0.005	0.02	0.05	0.1
r^2-Value	$.62 \pm .12$	$.60 \pm .14$	$.63 \pm .12$	$.83 \pm .13$
Excluded Cells	$43.75\,\%$	$45.13\,\%$	$39.06\,\%$	$7.81\,\%$
Predicted 40 vs Small Surround	n.s. $p = .16$	* $p < .05$	n.s. $p = .08$	n.s. $p = .07$
Predicted 40 vs Large Surround	n.s. $p = .06$	* $p < .05$	n.s. $p = .08$	* $p < .05$
Small Surround vs Large Surround	n.s. $p = .56$	n.s. $p = .77$	n.s. $p = .96$	n.s. $p = .42$

B.3. Number of Inhibitory Cells

Table B.13.: Orientation selectivity measures for two different amounts of inhibitory neurons and the standard configuration.

Inhibitory Cells (%)	Selective Cells	Biased Cells	ORI (mean ± std)	CV (mean ± std)
77	38.70 %	17.00 %	.51 ± .32	.76 ± .20
88	45.85 %	15.52 %	.55 ± .34	.71 ± .22
100 (standard)	72.32 %	12.20 %	.77 ± .25	.52 ± .24

Table B.14.: Fitting parameters for the contrast response functions of the average response of the network neurons for two different amounts of inhibitory neurons and for the standard configuration.

Inhibitory Cells (%)	a	k	p	q	r^2
77	0.05	1.76	2.2	1.75	0.30
88	0.05	1.78	2.2	1.78	0.16
100 (standard)	0.050	1.70	2.2	1.8	0.98

Table B.15.: Centre-surround suppression in response to sinusoidal gratings. Suppression indices in the size variation test for two different amounts of inhibitory neurons and the standard configuration.

Inhibitory Cells (%)	SI (mean ± std)
77	0.36 ± 0.29
88	0.34 ± 0.32
100 (standard)	0.13 ± .16

Table B.16.: Centre-surround suppression in response to sinusoidal gratings. Suppression indices for two different amounts of inhibitory neurons in the eight different centre-surround conditions..

Number of Neurons = 77 %				
Centre Contrast	.1	.2	.4	.8
Low Surround (SI)	0.90	0.97	1.26	0.62
High Surround (SI)	0.59	0.64	0.62	0.41
Number of Neurons = 88 %				
Centre Contrast	.1	.2	.4	.8
Low Surround (SI)	1.01	1.02	0.91	0.71
High Surround (SI)	1.00	0.98	0.87	0.39

Table B.17.: Centre-Surround suppression in response to contrast noise patterns. Responses and matching contrasts for two different amounts of inhibitory neurons.

Number of Neurons: 88 %		
	Response (Hz) (mean± std)	Matching contrast (mean± std)
Predicted 40	10.92 ± 18.81	.40
Small Surround	7.19 ± 7.71	.3506 ± .0706
Large Surround	7.78 ± 9.65	.3556 ± .0811
Number of Neurons: 77 %		
	Response (Hz) (mean± std)	Matching contrast (mean± std)
Predicted 40	19.21 ± 35.25	.40
Small Surround	14.08 ± 28.39	.3768 ± .0847
Large Surround	13.72 ± 28.34	.3513 ± .0955

Table B.18.: Centre-Surround suppression in response to contrast noise patterns. r^2 values, percentages of excluded cells, and statistical analysis of the influence of the surround grating on the response for both surround conditions and of the influence of the size of the surround for two different amounts of inhibitory neurons.

Inhibitory Cells	88 %	77 %
r^2-Value	.88 ± .09	.91 ± .06
Excluded Cells	6.25 %	12.50 %
Predicted 40 vs Small Surround	n.s. $p = .18$	n.s. $p = .38$
Predicted 40 vs Large Surround	n.s. $p = .28$	n.s. $p = .35$
Small Surround vs Large Surround	n.s. $p = .73$	n.s. $p = .94$

B.4. Number of Inhibitory Connections to Excitatory Cells

Table B.19.: Orientation selectivity measures for different amounts of inhibitory connections on excitatory cells and the standard configuration.

Connection Number (%)	Selective Cells	Biased Cells	ORI (mean ± std)	CV (mean ± std)
64 %	68.11 %	14.23 %	.73 ± .26	.57 ± .22
88 %	72.65 %	12.27 %	.78 ± .23	.53 ± .22
100 %(standard)	72.32 %	12.20 %	.77 ± .25	.52 ± .24

Table B.20.: Fitting parameters for the contrast response functions of the average response of the network neurons for two different amounts of inhibitory connections and for the standard configuration.

Number of Connections (%)	a	k	p	q	r^2
64	0.050	1.79	2.2	1.79	-0.03
88	0.050	1.75	2.2	1.78	0.60
100 (standard)	0.050	1.70	2.2	1.8	0.98

Table B.21.: Centre-surround suppression in response to sinusoidal gratings. Suppression indices in the size variation test for two different amounts of inhibitory connections and the standard configuration.

Inhibitory Connections (%)	SI (mean $\pm$ std)
64	0.32$\pm$0.22
88	0.28$\pm$0.23
100 (standard)	0.13 $\pm$ 0.16

Table B.22.: Centre-surround suppression in response to sinusoidal gratings. Suppression indices for two different amounts of inhibitory connections in the eight different centre-surround conditions.

Number of Connections = 64 %				
Centre Contrast	0.1	0.2	0.4	0.8
Low Surround (SI)	0.99	0.98	1.02	0.41
High Surround (SI)	0.97	1.01	0.86	0.38
Number of Connections = 88 %				
Centre Contrast	0.1	0.2	0.4	0.8
Low Surround (SI)	0.98	0.99	1.05	0.32
High Surround (SI)	0.93	1.03	0.78	0.28

Table B.23.: Centre-Surround suppression in response to contrast noise patterns. Responses and matching contrasts for two different amounts of inhibitory connections.

Inhibitory Connections: 88 %		
	Response (Hz) (mean± std)	Matching contrast (mean± std)
Predicted 40	6.74 ± 1.87	.40
Small Surround	6.90 ± 1.66	.4124 ± .0846
Large Surround	6.48 ± 1.86	.3795 ± .1090
Inhibitory Connections: 64 %		
	Response (Hz) (mean± std)	Matching contrast (mean± std)
Predicted 40	9.12 ± 4.39	.40
Small Surround	8.04 ± 2.18	.3618 ± .0939
Large Surround	7.71 ± 2.45	.3345 ± .0834

Table B.24.: Centre-Surround suppression in response to contrast noise patterns. r^2 values, percentage of excluded cells, and statistical analyses of the influence of the surround grating on the response for both surround conditions and of the influence of the size of the surround, for two different amount of inhibitory connections.

Connection Number	88 %	64 %
r^2-Value	.82 ± .07	.87 ± .08
Excluded Cells	21.88 %	29.69 %
Predicted 40 vs Small Surround	n.s. $p = .68$	n.s. $p = .13$
Predicted 40 vs Large Surround	n.s. $p = .52$	n.s. $p = .05$
Small Surround vs Large Surround	n.s. $p = .27$	n.s. $p = .49$

B.5. Number of Excitatory Connections on Inhibitory Cells

Table B.25.: Orientation selectivity measures for different amounts of excitatory connections onto inhibitory cells and the standard configuration.

Excitatory Connections (%)	Selective Cells	Biased Cells	ORI (mean ± std)	CV (mean ± std)
66	70.76 %	20.74 %	.81 ± .21	.49 ± .21
82	78.73 %	12.35 %	.80 ± .21	.51 ± .22
100(standard)	72.32 %	12.20 %	.77 ± .25	.52 ± .24

Table B.26.: Fitting parameters for the contrast response functions fitted to the mean response of the network neurons for two different amounts of excitatory connections and for the standard configuration.

Excitatory Connections (%)	a	k	p	q	r^2
66	0.050	1.68	2.1	1.6	0.86
82	0.050	1.71	2.1	1.69	0.72
100 (standard)	0.050	1.70	2.2	1.8	0.98

Table B.27.: Centre-surround suppression in response to sinusoidal gratings. Suppression indices in the size variation test for two different amounts of excitatory connections and the standard configuration.

Connection Number (%)	SI (mean ± std)
66	0.12 ± 0.11
82	0.17 ±0 .18
100 (standard)	0.13 ± 0.16

Table B.28.: Centre-surround suppression in response to sinusoidal gratings. Suppression indices for two different amounts of excitatory connections in the eight different centre-surround conditions..

Number of Connections: 82 %				
Centre Contrast	0.1	0.2	0.4	0.8
Low Surround (SI)	0.73	0.69	0.60	0.61
High Surround (SI)	0.93	0.94	0.93	0.94
Number of Connections: 66 %				
Centre Contrast	0.1	0.2	0.4	0.8
Low Surround (SI)	0.73	0.65	0.54	0.56
High Surround (SI)	0.93	0.93	0.93	0.91

Table B.29.: Centre-Surround suppression in response to contrast noise patterns. Responses and matching contrasts for two different amounts of excitatory connections.

Number of Connections: 82 %		
	Response (Hz) (mean± std)	Match (contrast in %) (mean± std)
Predicted 40	6.06 ± 1.55	.40
Small Surround	6.40 ± 1.67	.4437 ± .1058
Large Surround	5.54 ± 1.54	.3383± .1108
Number of Connections: 66 %		
	Response (Hz) (mean± std)	Match (contrast in %) (mean± std)
Predicted 40	5.70 ± 2.13	.40
Small Surround	6.09 ± 2.04	.4430 ± .1293
Large Surround	5.65 ± 2.14	.3700 ± .1347

Table B.30.: Centre-Surround suppression in response to contrast noise patterns. r^2 values, percentages of excluded cells, and statistical analyses of the influence of the surround grating on the response for both surround conditions and of the influence of the size of the surround for two different amounts of excitatory connections.

Connection Number	82 %	66 %
r^2-Value	$.74 \pm .06$	$.73 \pm .08$
Excluded Cells	40.63 %	57.81 %
Predicted 40 vs Small Surround	n.s. $p = .37$	n.s. $p = .53$
Predicted 40 vs Large Surround	n.s. $p = .17$	n.s. $p = .94$
Small Surround vs Large Surround	* $p = .03$	n.s. $p = .49$

B.6. Decay Times at GABAergic Synapses

Table B.31.: Orientation selectivity measures for five different decay time constants τ at inhibitory synapses and the standard configuration.

Time Constant τ τ (in ms)	Selective Cells	Biased Cells	ORI (mean $\pm$ std)	CV (mean $\pm$ std)
15	64.50 %	14.50 %	$.70 \pm .28$	$.62 \pm .21$
20	66.90 %	13.10 %	$.71 \pm .28$	$.61 \pm .22$
25	65.52 %	13.40 %	$.70 \pm .28$	$.62 \pm .21$
30	65.05 %	14.31 %	$.70 \pm .28$	$.62 \pm .21$
50	64.20 %	14.6 %	$.70 \pm .28$	$.62 \pm .22$
8 (standard)	72.32 %	12.20 %	$.77 \pm .25$	$.52 \pm .24$

Table B.32.: Fitting parameters for the contrast response functions fitted to the mean response of the network neurons for five different decay time constants τ at inhibitory synapses and for the standard configuration.

τ (ms)	a	k	p	q	r^2
15	.050	1.72	2.2	1.6	.80
20	.050	1.70	2.2	1.6	.88
25	.50	1.70	2.2	1.6	.87
30	.050	1.71	2.2	1.6	.84
50	.050	1.73	2.2	1.64	.71
8	.050	1.70	2.2	1.8	.98

Table B.33.: Centre-surround suppression in response to sinusoidal gratings. Suppression indices in the size variation test for five different decay time constants τ at inhibitory synapses and the standard configuration.

Time Constant (τ in ms)	SI (mean $\pm$ std)
15	0.15 ± 0.18
20	0.15 ± 0.16
25	0.15 ± 0.18
30	0.15 ± 0.17
50	0.15 ± 0.18
8 (standard)	0.13 ± 0.16

Table B.34.: Centre-surround suppression in response to sinusoidal gratings. Suppression indices for five different decay time constants τ at inhibitory synapses in the eight different centre-surround conditions..

Decay Time Constant: $\tau = 15\,ms$				
Centre Contrast	.1	.2	.4	.8
Low Surround (SI)	1.00	0.96	0.96	0.31
High Surround (SI)	0.86	0.86	0.80	0.20
Decay Time Constant: $\tau = 20\,ms$				
Centre Contrast	.1	.2	.4	.8
Low Surround (SI)	1.02	0.99	0.98	0.26
High Surround (SI)	0.86	0.86	0.80	0.17
Decay Time Constant: $\tau = 25\,ms$				
Centre Contrast	.1	.2	.4	.8
Low Surround (SI)	1.01	1.01	1.01	0.28
High Surround (SI)	0.85	0.86	0.80	0.17
Decay Time Constant: $\tau = 30\,ms$				
Centre Contrast	0.1	0.2	0.4	0.8
Low Surround (SI)	0.99	0.97	0.97	0.28
High Surround (SI)	0.86	0.86	0.81	0.18
Decay Time Constant: $\tau = 50\,ms$				
Centre Contrast	.1	.2	.4	.8
Low Surround (SI)	1.00	0.98	0.98	0.37
High Surround (SI)	0.86	0.86	0.79	0.22

Table B.35.: Centre-Surround suppression in response to contrast noise patterns. Responses and matching contrasts for five different decay time constants τ at inhibitory synapses.

Decay Time Constant: $\tau = 15\,ms$		
	Response (Hz) (mean± std)	Matching contrast (mean± std)
Predicted 40	7.4±6.41	.40
Small Surround	5.73± 2.72	.3511 ± .0905
Large Surround	5.74± 2.92	.3491 ± .0765
Decay Time Constant: $\tau = 20\,ms$		
	Response (Hz) (mean± std)	Matching contrast (mean± std)
Predicted 40	7.48 ± 6.41	.40
Small Surround	5.82 ± 2.79	.3514 ± .0921
Large Surround	6.00 ± 2.79	.3548 ± .0817
Decay Time Constant: $\tau = 25\,ms$		
	Response (Hz) (mean± std)	Matching contrast (mean± std)
Predicted 40	6.94 ± 4.14	.40
Small Surround	5.62 ± 2.55	.3542 ± .823
Large Surround	5.55 ± 2.65	.3465 ± .713
Decay Time Constant: $\tau = 30\,ms$		
	Response (Hz) (mean± std)	Matching contrast (mean± std)
Predicted 40	8.28 ± 11.78	.40
Small Surround	5.80 ± 2.92	.3547 ± .849
Large Surround	5.85 ± 3.02	.3525 ± .707
Decay Time Constant: $\tau = 50\,ms$		
	Response (Hz) (mean± std)	Matching contrast (mean± std)
Predicted 40	8.53 ± 11.86	.40
Small Surround	5.85 ± 2.92	.3478 ± .876
Large Surround	5.95 ± 3.00	.3498 ± .714

Table B.36.: Centre-Surround suppression in response to contrast noise patterns. r2 values, percentages of excluded cells, and statistical analyses of the influence of the surround grating on the response for both surround conditions and, of the influence of the size of the surround, for five different decay time constants τ at inhibitory synapses.

Decay Time Constant (ms)	15	20	25	30	50
r^2-Value	$.86 \pm .10$	$.87 \pm .10$	$.86 \pm .10$	$.86 \pm .10$	$.86 \pm .$
Excluded Cells	12.50 %	10.94 %	12.50 %	12.50 %	12.50 %
Predicted 40 vs Small Surround	n.s. $p = .08$	n.s. $p = .08$	* $p < .05$	n.s. $p = .13$	n.s. $p = .11$
Predicted 40 vs Large Surround	n.s. $p = .09$	n.s. $p = .12$	* $p < .05$	n.s. $p = .14$	n.s. $p = .12$
Small Surround vs Large Surround	n.s. $p = .95$	n.s. $p = .75$	n.s. $p = .88$	n.s. $p = .92$	n.s. $p = .87$

Bibliography

[1] S. Akbarian, J. J. Kim, S. G. Potkin, J. O. Hagman, A. Tafazzoli, W. E. Bunney Jr, and E. G. Jones. Gene expression for glutamic acid decarboxylase is reduced without loss of neurons in prefrontal cortex of schizophrenics. *Archives of General Psychiatry*, **52**(4):258, 1995.

[2] D. Albrecht, S. Farrar, and D. Hamilton. Spatial contrast adaptation characteristics of neurones recorded in the cat's visual cortex. *The Journal of Physiology*, **347**(1):713–739, 1984.

[3] J. Allman, F. Miezin, and E. McGuinness. Stimulus specific responses from beyond the classical receptive field: neurophysiological mechanisms for local-global comparisons in visual neurons. *Annual review of neuroscience*, **8**(1):407–430, 1985.

[4] D. J. Amit and N. Brunel. Learning internal representations in an attractor neural network with analogue neurons. *Network: Computation in Neural Systems*, **6**(3):359–388, 1995.

[5] N. C. Andreasen, W. T. Carpenter, J. M. Kane, R. A. Lasser, S. R. Marder, and D. R. Weinberger. Remission in schizophrenia: proposed criteria and rationale for consensus. *American Journal of Psychiatry*, **162**(3):441–449, 2005.

[6] A. Angelucci, J. B. Levitt, E. J. Walton, J.-M. Hupe, J. Bullier, and J. S. Lund. Circuits for local and global signal integration in primary visual cortex. *The Journal of Neuroscience*, **22**(19):8633–8646, 2002.

[7] A. Angelucci, P. C. Bressloff, et al. Contribution of feedforward, lateral and feedback connections to the classical receptive field center and extra-classical receptive field surround of primate V1 neurons. *Progress in Brain Research*, **154**:93, 2006.

[8] H. Asada, Y. Kawamura, K. Maruyama, H. Kume, R.-G. Ding, N. Kanbara, H. Kuzume, M. Sanbo, T. Yagi, and K. Obata. Cleft palate and decreased brain γ-aminobutyric acid in mice lacking the 67-kDa isoform of glutamic acid decarboxylase. *Proceedings of the National Academy of Sciences U S A*, **94** (12):6496–6499, 1997.

[9] M. Bach. The freiburg visual acuity test-variability unchanged by post-hoc re-analysis. *Graefe's Archive for Clinical and Experimental Ophthalmology*, **245**(7):965–971, 2006.

[10] W. Bair, J. R. Cavanaugh, and J. A. Movshon. Time course and time-distance relationships for surround suppression in macaque V1 neurons. *The Journal of Neuroscience*, **23**(20):7690–7701, 2003.

[11] D. M. Barch, J. R. Mathews, R. L. Buckner, L. Maccotta, J. G. Csernansky, and A. Z. Snyder. Hemodynamic responses in visual, motor, and somatosensory cortices in schizophrenia. *Neuroimage*, **20**(3): 1884–1893, 2003.

[12] D. M. Barch, C. S. Carter, S. C. Dakin, J. Gold, S. J. Luck, A. MacDonald, J. D. Ragland, S. Silverstein, and M. E. Strauss. The clinical translation of a measure of gain control: the contrast-contrast effect task. *Schizophrenia Bulletin*, **38**(1):135–143, 2012.

[13] R. Bartha, P. C. Williamson, D. J. Drost, A. Malla, T. J. Carr, L. Cortese, G. Canaran, R. J. Rylett, and R. W. Neufeld. Measurement of glutamate and glutamine in the medial prefrontal cortex of never-treated schizophrenic patients and healthy controls by proton magnetic resonance spectroscopy. *Archives of General Psychiatry*, **54**(10):959, 1997.

[14] M. Beierlein, J. R. Gibson, and B. W. Connors. Two dynamically distinct inhibitory networks in layer 4 of the neocortex. *The Journal of Neurophysiology*, **90**(5):2987–3000, 2003. DOI: 10.1152/jn.00283.2003.

[15] R. Ben-Yishai, R. Bar-Or, and H. Sompolinsky. Theory of orientation tuning in visual cortex. *Proceedings of the National Academy of Sciences*, **92**(9):3844–3848, 1995.

[16] G. Bielicki, C. Chassain, J. Renou, M. Farges, M. Vasson, A. Eschalier, and F. Durif. Brain GABA editing by localized in vivo1h magnetic resonance spectroscopy. *NMR in Biomedicine*, **17**(2):60–68, 2004.

[17] T. Binzegger, R. J. Douglas, and K. A. Martin. A quantitative map of the circuit of cat primary visual cortex. *The Journal of Neuroscience*, **24**(39):8441–8453, 2004.

[18] J. Bird. Computed tomographic brain studies and treatment response in schizophrenia. *Canadian Journal of Psychiatry*, **30**(4):251, 1985.

[19] A. Bonds. Role of inhibition in the specification of orientation selectivity of cells in the cat striate cortex. *Visual neuroscience*, **2**(1):41–55, 1989.

[20] L. Borg-Graham, C. Monier, Y. Fregnac, et al. Visual input evokes transient and strong shunting inhibition in visual cortical neurons. *Nature*, **393**(6683):369–372, 1998.

[21] R. Born. Center-surround interactions in the middle temporal visual area of the owl monkey. *Journal of Neurophysiology*, **84**(5):2658–2669, 2000.

[22] J. Bower, D. Beeman, and A. Wylde. *The book of GENESIS: exploring realistic neural models with the GEneral NEural SImulation System*. Telos New York, 1995.

[23] J. Bower, D. Beeman, and M. Hucka. The genesis simulation system. *The handbook of brain theory and neural networks*, **2**, 2002.

[24] G. M. Boynton, J. B. Demb, G. H. Glover, and D. J. Heeger. Neuronal basis of contrast discrimination. *Vision research*, **39**(2):257–269, 1999.

[25] D. F. Braus, W. Weber-Fahr, H. Tost, M. Ruf, and F. A. Henn. Sensory information processing in neuroleptic-naive first-episode schizophrenic patients: a functional magnetic resonance imaging study. *Archives of General Psychiatry*, **59**(8):696, 2002.

[26] C. Bredfeldt and D. Ringach. Dynamics of spatial frequency tuning in macaque V1. *The Journal of Neuroscience*, **22**(5318):1976–1984, 2002.

[27] R. Brette. Computing with neural synchrony. *PLoS computational biology*, **8**(6):e1002561, 2012.

[28] R. Brette and W. Gerstner. Adaptive exponential integrate-and-fire model as an effective description of neuronal activity. *Journal of Neurophysiology*, **94**(5):3637–3642, 2005.

[29] D. M. Bryant and K. E. Mostov. From cells to organs: building polarized tissue. *Nature Reviews Molecular Cell Biology*, **9**(11):887–901, 2008.

[30] E. Callaway. Local circuits in primary visual cortex of the macaque monkey. *Annual Review of Neuroscience*, **21**(1):47–74, 1998.

[31] S. R. Campbell, D. L. Wang, and C. Jayaprakash. Synchrony and desynchrony in integrate-and-fire oscillators. *Neural Comput*, **11**(7):1595–1619, 1999.

[32] M. W. Cannon and S. C. Fullenkamp. Spatial interactions in apparent contrast: Individual differences in enhancement and suppression effects. *Vision research*, **33**(12):1685–1695, 1993.

[33] N. Caporale and Y. Dan. Spike timing-dependent plasticity: a Hebbian learning rule. *Annu. Rev. Neurosci.*, **31**:25–46, 2008.

[34] M. Carandini and D. Ferster. Membrane potential and firing rate in cat primary visual cortex. *The Journal of Neuroscience*, **20**(1):470–484, 2000.

[35] M. Carandini, D. J. Heeger, and J. A. Movshon. Linearity and normalization in simple cells of the macaque primary visual cortex. *The Journal of Neuroscience*, **17**(21):8621–8644, 1997.

[36] J. A. Cardin, L. A. Palmer, and D. Contreras. Stimulus feature selectivity in excitatory and inhibitory neurons in primary visual cortex. *The Journal of Neuroscience*, **27**(39):10333–10344, 2007.

[37] J. R. Cavanaugh, W. Bair, and J. A. Movshon. Nature and interaction of signals from the receptive field center and surround in macaque V1 neurons. *The Journal of Neurophysiology*, **88**(5):2530–2546, 2002.

[38] S. Cavassila, S. Deval, C. Huegen, D. Van Ormondt, and D. Graveron-Demilly. Cramer–Rao bounds: an evaluation tool for quantitation. *NMR in Biomedicine*, **14**(4):278–283, 2001.

[39] F. Chance, S. Nelson, and L. Abbott. Complex cells as cortically amplified simple cells. *Nature Neuroscience*, **2**(3):277–282, 1999.

[40] B. Chapman, K. Zahs, and M. Stryker. Relation of cortical cell orientation selectivity to alignment of receptive fields of the geniculocortical afferents that arborize within a single orientation column in ferret visual cortex. *The Journal of Neuroscience*, **11**(5):1347–1358, 1991.

[41] B. Chattopadhyaya, G. Di Cristo, C. Z. Wu, G. Knott, S. Kuhlman, Y. Fu, R. D. Palmiter, and Z. J. Huang. GAD67-mediated GABA synthesis and signaling regulate inhibitory synaptic innervation in the visual cortex. *Neuron*, **54**(6):889–903, 2007.

[42] Z. Chen, A. C. Silva, J. Yang, and J. Shen. Elevated endogenous GABA level correlates with decreased fMRI signals in the rat brain during acute inhibition of GABA transaminase. *Journal of neuroscience research*, **79**(3):383–391, 2005.

[43] C. Chubb, G. Sperling, and J. A. Solomon. Texture interactions determine perceived contrast. *Proceedings of the National Academy of Science U S A*, **86**(23):9631–9635, 1989.

[44] S. Chung, D. Ferster, et al. Strength and orientation tuning of the thalamic input to simple cells revealed by electrically evoked cortical suppression. *Neuron*, **20**(6):1177–1190, 1998.

[45] B. M. Cohen. Greater hemodynamic response to photic stimulation in schizophrenic patients: an echo planar MRI study. *Am J Psychiatry*, **151**(1):1493–1495, 1994.

[46] B. Connors, M. Bear, and M. Paradiso, editors. *Neuroscience - Exploring the Brain*. Lippincott, Williams & Wilkins, 1996.

[47] B. W. Connors and M. J. Gutnick. Intrinsic firing patterns of diverse neocortical neurons. *Trends in Neuroscience*, **13**(3):99–104, 1990.

[48] J. Crook, Z. Kisvárday, and U. Eysel. Evidence for a contribution of lateral inhibition to orientation tuning and direction selectivity in cat visual cortex: reversible inactivation of functionally characterized sites combined with neuroanatomical tracing techniques. *European Journal of Neuroscience*, **10**(6): 2056–2075, 2002.

[49] A. Cross, T. Crow, and F. Owen. Gamma-aminobutyric acid in the brain in schizophrenia. *The Lancet*, **313**(8115):560–561, 1979.

[50] M. O. Cunningham, M. A. Whittington, A. Bibbig, A. Roopun, F. E. N. LeBeau, A. Vogt, H. Monyer, E. H. Buhl, and R. D. Traub. A role for fast rhythmic bursting neurons in cortical gamma oscillations in vitro. *Proceedings of the National Academy of Science U S A*, **101**(18):7152–7157, 2004. DOI: 10.1073/pnas.0402060101.

[51] S. Dakin, P. Carlin, and D. Hemsley. Weak suppression of visual context in chronic schizophrenia. *Current Biology*, **15**(20):R822–R824, 2005. DOI: 10.1016/j.cub.2005.10.015.

[52] P. Dayan and L. Abbott. *Theoretical Neuroscience*, volume 31. MIT press Cambridge, MA, 2001.

[53] R. A. de Graaf. *In vivo NMR spectroscopy. Principles and techniques*. John Wiley and sons Ltd., 2008.

[54] R. De Valois, D. Albrecht, and L. Thorell. Spatial frequency selectivity of cells in macaque visual cortex. *Vision Research*, **22**(5):545–559, 1982.

[55] R. L. De Valois, E. William Yund, and N. Hepler. The orientation and direction selectivity of cells in macaque visual cortex. *Vision research*, **22**(5):531–544, 1982.

[56] G. DeAngelis, R. Freeman, and I. Ohzawa. Length and width tuning of neurons in the cat's primary visual cortex. *The Journal of Neurophysiology*, **71**(1):347–374, 1994.

[57] G. DeAngelis, G. Ghose, I. Ohzawa, and R. Freeman. Functional micro-organization of primary visual cortex: receptive field analysis of nearby neurons. *The Journal of Neuroscience*, **19**(10):4046–4064, 1999.

[58] R. Desimone and J. Duncan. Neural mechanisms of selective visual attention. *Annual review of neuroscience*, **18**(1):193–222, 1995.

[59] R. L. DeValois, B. K. K. D. both Professors, et al. *Spatial Vision*. Number 14. Oxford University Press, USA, 1988.

[60] R. J. Douglas and K. Martin. A functional microcircuit for cat visual cortex. *The Journal of Physiology*, **440**(1):735–769, 1991.

[61] V. Dragoi and M. Sur. Dynamic properties of recurrent inhibition in primary visual cortex: contrast and orientation dependence of contextual effects. *The Journal of Neurophysiology*, **83**(2):1019–1030, 2000.

[62] N. Dudani, S. Ray, S. George, and U. Bhalla. Multiscale modeling and interoperability in MOOSE. *Neuroscience*, **10**(Suppl 1):54, 2009.

[63] S. B. Eickhoff, K. E. Stephan, H. Mohlberg, C. Grefkes, G. R. Fink, K. Amunts, and K. Zilles. A new SPM toolbox for combining probabilistic cytoarchitectonic maps and functional imaging data. *Neuroimage*, **25**(4):1325–1335, 2005.

[64] D. Ferster. Spatially opponent excitation and inhibition in simple cells of the cat visual cortex. *The Journal of Neuroscience*, **8**(4):1172–1180, 1988.

[65] D. Ferster and K. Miller. Neural mechanisms of orientation selectivity in the visual cortex. *Annual Review of Neuroscience*, **23**(1):441–471, 2000.

[66] D. Ferster, S. Chung, H. Wheat, et al. Orientation selectivity of thalamic input to simple cells of cat visual cortex. *Nature*, **380**(6571):249–252, 1996.

[67] I. M. Finn, N. J. Priebe, and D. Ferster. The emergence of contrast-invariant orientation tuning in simple cells of cat visual cortex. *Neuron*, **54**(1):137, 2007.

[68] J. M. Foley. Human luminance pattern-vision mechanisms: Masking experiments require a new model. *JOSA A*, **11**(6):1710–1719, 1994.

[69] K. Foster, J. P. Gaska, M. Nagler, and D. Pollen. Spatial and temporal frequency selectivity of neurones in visual cortical areas V1 and V2 of the macaque monkey. *The Journal of Physiology*, **365**(1):331–363, 1985.

[70] T. Freund, K. Martin, I. Soltesz, P. Somogyi, and D. Whitteridge. Arborisation pattern and postsynaptic targets of physiologically identified thalamocortical afferents in striate cortex of the macaque monkey. *The Journal of Comparative Neurology*, **289**(2):315–336, 2004.

[71] K. J. Friston. Statistical parametric mapping. In *Neuroscience Databases*, pages 237–250. Springer, 2003.

[72] K. J. Friston, A. P. Holmes, K. J. Worsley, J.-P. Poline, C. D. Frith, and R. S. Frackowiak. Statistical parametric maps in functional imaging: a general linear approach. *Human Brain Mapping*, **2**(4):189–210, 1994.

[73] W. S. Geisler, D. G. Albrecht, et al. Visual cortex neurons in monkeys and cats: detection, discrimination and identification. *Visual neuroscience*, **14**(5):897–919, 1997.

[74] W. Gerstner and W. Kistler. *Spiking Neuron Models*. Cambridge University Press, 2002.

[75] S. V. Girman, Y. SauvÃ©, and R. D. Lund. Receptive field properties of single neurons in rat primary visual cortex. *J Neurophysiol*, **82**(1):301–311, 1999.

[76] P. Gleeson, V. Steuber, and R. A. Silver. neuroConstruct: a tool for modeling networks of neurons in 3d space. *Neuron*, **54**(2):219–235, 2007. DOI: 10.1016/j.neuron.2007.03.025.

[77] P. Gleeson, S. Crook, R. Cannon, M. Hines, G. Billings, M. Farinella, T. Morse, A. Davison, S. Ray, U. Bhalla, et al. Neuroml: a language for describing data driven models of neurons and networks

with a high degree of biological detail. *PLoS Computational Biology*, **6**(6):e1000815, 2010.

[78] J. D. Golomb, J. R. McDavitt, B. M. Ruf, J. I. Chen, A. Saricicek, K. H. Maloney, J. Hu, M. M. Chun, and Z. Bhagwagar. Enhanced visual motion perception in major depressive disorder. *The Journal of Neuroscience*, **29**(28):9072–9077, 2009.

[79] A. Grinvald, E. E. Lieke, R. D. Frostig, and R. Hildesheim. Cortical point-spread function and long-range lateral interactions revealed by real-time optical imaging of macaque monkey primary visual cortex. *The Journal of Neuroscience*, **14**(5):2545–2568, 1994.

[80] K. Guo, R. G. Robertson, S. Mahmoodi, and M. P. Young. Centre-surround interactions in response to natural scene stimulation in the primary visual cortex. *European Journal of Neuroscience*, **21**(2):536–548, 2005.

[81] M. Gur, I. Kagan, and D. M. Snodderly. Orientation and direction selectivity of neurons in V1 of alert monkeys: functional relationships and laminar distributions. *Cerebral Cortex*, **15**(8):1207–1221, 2005.

[82] T. Hashimoto, D. W. Volk, S. M. Eggan, K. Mirnics, J. N. Pierri, Z. Sun, A. R. Sampson, and D. A. Lewis. Gene expression deficits in a subclass of GABA neurons in the prefrontal cortex of subjects with schizophrenia. *The Journal of Neuroscience*, **23**(15):6315–6326, 2003.

[83] T. Hashimoto, D. Arion, T. Unger, J. Maldonado-Aviles, H. Morris, D. Volk, K. Mirnics, and D. Lewis. Alterations in GABA-related transcriptome in the dorsolateral prefrontal cortex of subjects with schizophrenia. *Molecular Psychiatry*, **13**(2):147–161, 2007.

[84] M. Hawken, R. Shapley, and D. Grosof. Temporal-frequency selectivity in monkey visual cortex. *Visual neuroscience*, **13**(03):477–492, 1996.

[85] J. D. Haynes, G. Roth, M. Stadler, and H. J. Heinze. Neuromagnetic correlates of perceived contrast in primary visual cortex. *The Journal of Neurophysiology*, **89**(5):2655–2666, 2003.

[86] D. J. Heeger. Normalization of cell responses in cat striate cortex. *Visual neuroscience*, **9**(02):181–197, 1992.

[87] B. Hille. *Ion channels of excitable membranes*, volume 507. Sinauer Sunderland, MA, 2001.

[88] M. Hines. Efficient computation of branched nerve equations. *International Journal of Bio-Medical Computing*, **15**(1):69–76, 1984.

[89] M. L. Hines and N. T. Carnevale. The NEURON simulation environment. *Neural Computation*, **9**(6): 1179–1209, 1997.

[90] Y. Hirayasu, M. E. Shenton, D. F. Salisbury, C. C. Dickey, I. A. Fischer, P. Mazzoni, T. Kisler, H. Arakaki, J. S. Kwon, J. E. Anderson, et al. Lower left temporal lobe MRI volumes in patients with first-episode schizophrenia compared with psychotic patients with first-episode affective disorder and normal subjects. *American Journal of Psychiatry*, **155**(10):1384–1391, 1998.

[91] A. Hodgkin and A. Huxley. A quantitative description of membrane current and its application to conduction and excitation in nerve. *The Journal of Physiology*, **117**(4):500, 1952.

[92] D. J. Holt, L. Kunkel, A. P. Weiss, D. C. Goff, C. I. Wright, L. M. Shin, S. L. Rauch, J. Hootnick, and S. Heckers. Increased medial temporal lobe activation during the passive viewing of emotional and neutral facial expressions in schizophrenia. *Schizophrenia research*, **82**(2):153–162, 2006.

[93] http://commons.wikimedia.org/wiki/File:Constudeyepath.gif, 2013.

[94] http://en.wikipedia.org/wiki/File:Cell_membrane_equivalent_circuit.svg, 2013.

[95] http://wiki.umd.edu/wikivision/index.php?title=File:VentralDorsalStreams.png, 2013.

[96] D. H. Hubel. *Eye, brain, and vision.* Scientific American Library/Scientific American Books, 1995.

[97] D. H. Hubel and M. S. Livingstone. Segregation of form, color, and stereopsis in primate area 18. *The Journal of neuroscience*, **7**(11):3378–3415, 1987.

[98] D. H. Hubel and T. N. Wiesel. Receptive fields, binocular interaction and functional architecture in the cat's visual cortex. *J Physiol*, **160**:106–154, 1962.

[99] D. H. Hubel and T. N. Wiesel. Receptive fields and functional architecture of monkey striate cortex. *J Physiol*, **195**(1):215–243, 1968.

[100] S. A. Huettel, A. W. Song, and G. McCarthy. *Functional magnetic resonance imaging*, volume 1. Sinauer Associates Sunderland, 2004.

[101] J. Hupe, A. James, B. Payne, S. Lomber, P. Girard, and J. Bullier. Cortical feedback improves discrimination between figure and background by V1, V2 and V3 neurons. *Nature*, **394**(6695):784–787, 1998.

[102] J.-M. Hupé, A. C. James, P. Girard, and J. Bullier. Response modulations by static texture surround in area V1 of the macaque monkey do not depend on feedback connections from V2. *The Journal of Neurophysiology*, **85**(1):146–163, 2001.

[103] J.-M. Hupé, A. C. James, P. Girard, S. G. Lomber, B. R. Payne, and J. Bullier. Feedback connections act on the early part of the responses in monkey visual cortex. *Journal of Neurophysiology*, **85**(1):134–145, 2001.

[104] A. Iserles. *A first course in the numerical analysis of differential equations*, volume 44. Cambridge University Press, 2008.

[105] E. Izhikevich. Simple model of spiking neurons. *Neural Networks, IEEE Transactions on*, **14**(6):1569–1572, 2003.

[106] E. Izhikevich. Which model to use for cortical spiking neurons? *Neural Networks, IEEE Transactions on*, **15**(5):1063–1070, 2004.

[107] E. Izhikevich, J. Gally, and G. Edelman. Spike-timing dynamics of neuronal groups. *Cerebral Cortex*, **14**(8):933–944, 2004.

[108] E. M. Izhikevich. Polychronization: computation with spikes. *Neural computation*, **18**(2):245–282, 2006.

[109] E. M. Izhikevich, editor. *Dynamical Systems in Neuroscience - The Geometry of Excitability and Bursting*. The MIT Press, 2007.

[110] E. M. Izhikevich and G. M. Edelman. Large-scale model of mammalian thalamocortical systems. *Proceedings of the national academy of sciences*, **105**(9):3593–3598, 2008.

[111] D. C. Javitt, S. R. Zukin, et al. Recent advances in the phencyclidine model of schizophrenia. *Am J Psychiatry*, **148**(10):1301–1308, 1991.

[112] H. Jones, K. Grieve, W. Wang, and A. Sillito. Surround suppression in primate V1. *Journal of Neurophysiology*, **86**(4):2011–2028, 2001.

[113] A. Karni, K. Bonneh, D. Manor, and T. Kushnir. What Vi sees in textures-an fMRI investigation of the representation of orientation gradients in visual cortex. *Neuroimage*, **9**:S879–S879, 1999.

[114] S. Kastner, P. De Weerd, R. Desimone, and L. G. Ungerleider. Mechanisms of directed attention in the human extrastriate cortex as revealed by functional MRI. *Science*, **282**(5386):108–111, 1998.

[115] S. R. Kay, A. Fiszbein, and L. A. Opler. The positive and negative syndrome scale (PANSS) for schizophrenia. *Schizophrenia Bulletin*, **13**(2):261–276, 1987.

[116] Y. Ke, B. M. Cohen, J. Y. Bang, M. Yang, and P. F. Renshaw. Assessment of GABA concentration in human brain using two-dimensional proton magnetic resonance spectroscopy. *Psychiatry Research: Neuroimaging*, **100**(3):169–178, 2000.

[117] J. J. Knierim and D. C. Van Essen. Neuronal responses to static texture patterns in area V1 of the alert macaque monkey. *Journal of Neurophysiology*, **67**(4):961–980, 1992.

[118] E. R. Korpi, J. E. Kleinman, S. I. Goodman, and R. J. Wyatt. Neurotransmitter amino acids in postmortem brains of chronic schizophrenic patients. *Psychiatry research*, **22**(4):291–301, 1987.

[119] D. E. Koshland, A. Goldbeter, and J. B. Stock. Amplification and adaptation in regulatory and sensory systems. *Science*, **217**:220–225, 1982.

[120] J. H. Krystal, L. P. Karper, J. P. Seibyl, G. K. Freeman, R. Delaney, J. D. Bremner, G. R. Heninger, M. B. Bowers Jr, and D. S. Charney. Subanesthetic effects of the noncompetitive nmda antagonist, ketamine, in humans: psychotomimetic, perceptual, cognitive, and neuroendocrine responses. *Archives of general psychiatry*, **51**(3):199, 1994.

[121] I. Lampl, J. S. Anderson, D. C. Gillespie, D. Ferster, et al. Prediction of orientation selectivity from receptive field architecture in simple cells of cat visual cortex. *Neuron*, **30**(1):263–274, 2001.

[122] L. Lapicque. Recherches quantitatives sur l'excitation electrique des nerfs traitee comme une polarization. *J Physiol Pathol Gen*, **9**:620–635, 1907.

[123] M. R. Leek. Adaptive procedures in psychophysical research. *Perception & Psychophysics*, **63**(8):1279–1292, 2001.

[124] J. B. Levitt and J. S. Lund. Contrast dependence of contextual effects in primate visual cortex. *Nature*, **387**(6628):73–76, 1997.

[125] P. A. Lewis and G. S. Shedler. Simulation of nonhomogeneous poisson processes by thinning. *Naval Research Logistics Quarterly*, **26**(3):403–413, 2006.

[126] G. Li, Y. Yang, Z. Liang, J. Xia, Y. Yang, and Y. Zhou. GABA-mediated inhibition correlates with orientation selectivity in primary visual cortex of cat. *Neuroscience*, **155**(3):914–922, 2008.

[127] H. Lindén, K. H. Pettersen, T. Tetzlaff, T. Potjans, M. Denker, M. Diesmann, S. Grün, and G. T. Einevoll. Estimating the spatial range of local field potentials in a cortical population model. *BMC Neuroscience*, **10**(Suppl 1):P224, 2009.

[128] H. Lindén, T. C. Potjans, G. T. Einevoll, S. Grün, and M. Diesmann. Modeling the local field potential by a large-scale layered cortical network model. In *Frontiers in Neuroinformatics. Conference abstract: 2nd INCF congress of Neuroinformatics*, 2009.

[129] H. Lindén, T. Tetzlaff, T. C. Potjans, K. H. Pettersen, S. Grün, M. Diesmann, and G. T. Einevoll. Modeling the spatial reach of the LFP. *Neuron*, **72**(5):859–872, 2011.

[130] J. E. Lisman, J. T. Coyle, R. W. Green, D. C. Javitt, F. M. Benes, S. Heckers, and A. A. Grace. Circuit-based framework for understanding neurotransmitter and risk gene interactions in schizophrenia. *Trends in Neurosciences*, **31**(5):234–242, 2008.

[131] N. K. Logothetis. The underpinnings of the BOLD functional magnetic resonance imaging signal. *The Journal of Neuroscience*, **23**(10):3963–3971, 2003.

[132] J. S. Lund. Organization of neurons in the visual cortex, area 17, of the monkey (macaca mulatta). *The Journal of Comparative Neurology*, **147**(4):455–495, 1973.

[133] R. MacGregor. *Neural and Brain Modeling*. Academic Press San Diego., 1987.

[134] R. Maex and E. De Schutter. Synchronization of golgi and granule cell firing in a detailed network model of the cerebellar granule cell layer. *Journal of neurophysiology*, **80**(5):2521–2537, 1998.

[135] K. Mardia and K. Mardia. *Statistics of directional data*, volume 5. Academic Press London, 1972.

[136] H. Markram, Y. Wang, and M. Tsodyks. Differential signaling via the same axon of neocortical pyramidal neurons. *Proceedings of the National Academy of Sciences*, **95**(9):5323–5328, 1998.

[137] H. Markram, M. Toledo-Rodriguez, Y. Wang, A. Gupta, G. Silberberg, and C. Wu. Interneurons of the neocortical inhibitory system. *Nature Reviews Neuroscience*, **5**(10):793–807, 2004.

[138] D. Marr and T. Poggio. A computational theory of human stereo vision. *Proceedings of the Royal Society of London. Series B. Biological Sciences*, **204**(1156):301–328, 1979.

[139] A. Martínez, S. A. Hillyard, E. C. Dias, D. J. Hagler, P. D. Butler, D. N. Guilfoyle, M. Jalbrzikowski,

G. Silipo, and D. C. Javitt. Magnocellular pathway impairment in schizophrenia: evidence from functional magnetic resonance imaging. *The Journal of neuroscience*, **28**(30):7492–7500, 2008.

[140] M. Mascagni, A. Sherman, et al. Numerical methods for neuronal modeling. *Methods in Neuronal Modeling*, **2**, 1998.

[141] MATLAB. *Version 7.10.0 (R2010a)*. The MathWorks Inc., Natick, Massachusetts, 2010.

[142] S. McColl and F. Wilkinson. Visual contrast gain control in migraine: measures of visual cortical excitability and inhibition. *Cephalalgia*, **20**(2):74–84, 2000.

[143] C. T. McDonald and A. Burkhalter. Organization of long-range inhibitory connections with rat visual cortex. *The Journal of Neuroscience*, **13**(2):768–781, 1993.

[144] D. McLaughlin, R. Shapley, M. Shelley, and D. Wielaard. A neuronal network model of macaque primary visual cortex (V1): Orientation selectivity and dynamics in the input layer 4cα. *Proceedings of the National Academy of Sciences*, **97**(14):8087–8092, 2000.

[145] M. Mescher, H. Merkle, J. Kirsch, M. Garwood, R. Gruetter, et al. Simultaneous in vivo spectral editing and water suppression. *NMR in Biomedicine*, **11**(6):266–272, 1998.

[146] C. Metzner, A. Schweikard, and B. Zurowski. Context integration in visual processing: A computational model of center-surround suppression in the visual system. In *BMC Neuroscience*, 2010.

[147] C. Metzner, A. Schweikard, and B. Zurowski. Towards realistic receptive field properties in a biologically inspired spiking network model of the mammalian primary visual cortex. In *Front. Comput. Neurosci. Conference Abstract: BC11 : Computational Neuroscience and Neurotechnology Bernstein Conference and Neurex Annual Meeting*, 2011.

[148] C. Metzner, A. Schweikard, and B. Zurowski. Center-surround interactions in a network model of layer 4Cα of primary visual cortex. In *BMC Neuroscience*, 2013.

[149] R. Miikkulainen, J. A. Bednar, Y. Choe, and J. Sirosh. *Computational maps in the visual cortex*. Springer, 2005.

[150] I. Murakami and S. Shimojo. Assimilation-type and contrast-type bias of motion induced by the surround in a random-dot display: evidence for center-surround antagonism. *Vision Research*, **36**(22): 3629–3639, 1996.

[151] S. D. Muthukumaraswamy, R. A. Edden, D. K. Jones, J. B. Swettenham, and K. D. Singh. Resting GABA concentration predicts peak gamma frequency and fMRI amplitude in response to visual stimulation in humans. *Proceedings of the National Academy of Sciences U S A*, **106**(20):8356–8361, 2009.

[152] S. D. Muthukumaraswamy, C. J. Evans, R. A. Edden, R. G. Wise, and K. D. Singh. Individual variability in the shape and amplitude of the BOLD-HRF correlates with endogenous GABAergic inhibition. *Human brain mapping*, **33**(2):455–465, 2012.

[153] S. Nelson, L. Toth, B. Sheth, and M. Sur. Orientation selectivity of cortical neurons during intracellular blockade of inhibition. *Science*, 1994.

[154] A. Nischwitz and H. Glünder. Local lateral inhibition: A key to spike synchronization? *Biological Cybernetics*, **73**:389–400, 1995.

[155] G. Northoff, M. Walter, R. F. Schulte, J. Beck, U. Dydak, A. Henning, H. Boeker, S. Grimm, and P. Boesiger. GABA concentrations in the human anterior cingulate cortex predict negative BOLD responses in fMRI. *Nature Neuroscience*, **10**(12):1515–1517, 2007.

[156] L. G. Nowak, R. Azouz, M. V. Sanchez-Vives, C. M. Gray, and D. A. McCormick. Electrophysiological classes of cat primary visual cortical neurons in vivo as revealed by quantitative analyses. *Journal of Neurophysiology*, **89**(3):1541–1566, 2003. DOI: 10.1152/jn.00580.2002.

[157] L. G. Nowak, M. V. Sanchez-Vives, and D. A. McCormick. Lack of orientation and direction selectivity in a subgroup of fast-spiking inhibitory interneurons: cellular and synaptic mechanisms and

comparison with other electrophysiological cell types. *Cerebral Cortex*, **18**(5):1058–1078, 2008.

[158] S. Ogawa and T.-M. Lee. Magnetic resonance imaging of blood vessels at high fields: in vivo and in vitro measurements and image simulation. *Magnetic Resonance in Medicine*, **16**(1):9–18, 1990.

[159] S. Ogawa, T. Lee, A. Kay, and D. Tank. Brain magnetic resonance imaging with contrast dependent on blood oxygenation. *Proceedings of the National Academy of Sciences*, **87**(24):9868–9872, 1990.

[160] R. Oliveira and A. Roque. A biologically plausible neural network model of the primate primary visual system. *Neurocomputing*, **44-46**:957–963, 2002.

[161] H. Ozeki, O. Sadakane, T. Akasaki, T. Naito, S. Shimegi, and H. Sato. Relationship between excitation and inhibition underlying size tuning and contextual response modulation in the cat primary visual cortex. *The Journal of Neuroscience*, **24**(6):1428–1438, 2004.

[162] T. L. Perry, S. Hansen, and K. Jones. Schizophrenia, tardive dyskinesia, and brain GABA. *Biological psychiatry*, **25**(2):200–206, 1989.

[163] B. Pfleger and A. Bonds. Dynamic differentiation of GABA A-sensitive influences on orientation selectivity of complex cells in the cat striate cortex. *Experimental Brain Research*, **104**(1):81–88, 1995.

[164] V. Porciatti, P. Bonanni, A. Fiorentini, and R. Guerrini. Lack of cortical contrast gain control in human photosensitive epilepsy. *Nature neuroscience*, **3**(3):259–263, 2000.

[165] Presentation. *Version 14.5*. Neurobehavioral Systems Inc., 2010.

[166] N. J. Priebe and D. Ferster. Inhibition, spike threshold, and stimulus selectivity in primary visual cortex. *Neuron*, **57**(4):482–497, 2008.

[167] S. W. Provencher. Automatic quantitation of localized in vivo 1H spectra with lcmodel. *NMR in Biomedicine*, **14**(4):260–264, 2001.

[168] N. A. Puts and R. A. Edden. ¡ i¿ in vivo¡/i¿ magnetic resonance spectroscopy of GABA: A methodological review. *Progress in nuclear magnetic resonance spectroscopy*, **60**:29–41, 2012.

[169] S. Ray and U. Bhalla. PyMOOSE: interoperable scripting in Python for MOOSE. *Frontiers in Neuroinformatics*, **2**(6):1–16, 2008.

[170] S. Ray, R. Deshpande, N. Dudani, and U. Bhalla. A general biological simulator: the multiscale object oriented simulation environment, MOOSE. *BMC Neuroscience*, **9**(1):P93, 2008.

[171] R. Reid, J. Alonso, et al. Specificity of monosynaptic connections from thalamus to visual cortex. *Nature*, **378**(6554):281–283, 1995.

[172] D. Ringach. Spatial structure and symmetry of simple-cell receptive fields in macaque primary visual cortex. *Journal of Neurophysiology*, **88**(1):455–463, 2002.

[173] D. Ringach, M. Hawken, R. Shapley, et al. Dynamics of orientation tuning in macaque primary visual cortex. *Nature*, **387**(6630):281–284, 1997.

[174] D. Ringach, R. Shapley, and M. Hawken. Orientation selectivity in macaque V1: diversity and laminar dependence. *The Journal of Neuroscience*, **22**(13):5639–5651, 2002.

[175] D. L. Ringach, M. J. Hawken, and R. Shapley. Dynamics of orientation tuning in macaque V1: the role of global and tuned suppression. *Journal of Neurophysiology*, **90**(1):342–352, 2003.

[176] J. Robson. Linear and nonlinear operations in the visual system. *Invest Ophthalmol Vis Sci [Suppl]*, **29**: 117, 1988.

[177] I. Rosso, J. Coyle, Y. Ke, S. Gruber, D. Olson, P. Renshaw, and D. Yurgelun-Todd. Cingulate cortex GABA concentration in schizophrenia: a two-dimensional proton magnetic resonance spectroscopy study. In *BIOLOGICAL PSYCHIATRY*. ELSEVIER SCIENCE INC 360 PARK AVE SOUTH, NEW YORK, NY 10010-1710 USA, 2006, pages 151S–151S.

[178] D. L. Rothman, O. Petroff, K. L. Behar, and R. H. Mattson. Localized 1H NMR measurements of

gamma-aminobutyric acid in human brain in vivo. *Proceedings of the National Academy of Sciences*, **90** (12):5662–5666, 1993.

[179] H. Sato, N. Katsuyama, H. Tamura, Y. Hata, and T. Tsumoto. Mechanisms underlying orientation selectivity of neurons in the primary visual cortex of the macaque. *The Journal of Physiology*, **494**(Pt 3): 757–771, 1996.

[180] A. J. Saykin, R. C. Gur, R. E. Gur, P. D. Mozley, L. H. Mozley, S. M. Resnick, D. B. Kester, and P. Stafiniak. Neuropsychological function in schizophrenia: selective impairment in memory and learning. *Archives of General Psychiatry*, **48**(7):618, 1991.

[181] M. P. Sceniak, D. L. Ringach, M. J. Hawken, and R. Shapley. Contrast's effect on spatial summation by macaque V1 neurons. *Nature Neuroscience*, **2**(8):733–739, 1999.

[182] M. P. Sceniak, M. J. Hawken, and R. Shapley. Visual spatial characterization of macaque V1 neurons. *Journal of Neurophysiology*, **85**(5):1873–1887, 2001.

[183] P. Schiller, B. Finlay, and S. Volman. Quantitative studies of single-cell properties in monkey striate cortex. ii. Orientation specificity and ocular dominance. *Journal of Neurophysiology*, **39**(6):1320–1333, 1976.

[184] P. Schiller, B. Finlay, and S. Volman. Quantitative studies of single-cell properties in monkey striate cortex. iii. Spatial frequency. *Journal of Neurophysiology*, **39**(6):1334–1351, 1976.

[185] L. Schwabe, K. Obermayer, A. Angelucci, and P. C. Bressloff. The role of feedback in shaping the extra-classical receptive field of cortical neurons: a recurrent network model. *The Journal of Neuroscience*, **26** (36):9117–9129, 2006.

[186] G. Sclar, J. H. Maunsell, and P. Lennie. Coding of image contrast in central visual pathways of the macaque monkey. *Vision research*, **30**(1):1–10, 1990.

[187] R. Shapley, M. Hawken, and D. Ringach. Dynamics of orientation selectivity in the primary visual cortex and the importance of cortical inhibition. *Neuron*, **38**(5):689–700, 2003.

[188] M. E. Shenton, R. Kikinis, F. A. Jolesz, S. D. Pollak, M. LeMay, C. G. Wible, H. Hokama, J. Martin, D. Metcalf, M. Coleman, et al. Abnormalities of the left temporal lobe and thought disorder in schizophrenia: a quantitative magnetic resonance imaging study. *New England Journal of Medicine*, **327** (9):604–612, 1992.

[189] A. Sillito. The contribution of inhibitory mechanisms to the receptive field properties of neurones in the striate cortex of the cat. *The Journal of Physiology*, **250**(2):305–329, 1975.

[190] A. Sillito. Inhibitory processes underlying the directional specificity of simple, complex and hypercomplex cells in the cat's visual cortex. *The Journal of physiology*, **271**(3):699–720, 1977.

[191] A. Sillito and H. Jones. Context-dependent interactions and visual processing in V1. *Journal of Physiology-Paris*, **90**(3):205–209, 1996.

[192] A. Sillito, K. Grieve, H. Jones, J. Cudeiro, and J. Davls. Visual cortical mechanisms detecting focal orientation discontinuities. *Nature*, 1995.

[193] W. Singer and C. M. Gray. Visual feature integration and the temporal correlation hypothesis. *Annual Review of Neuroscience*, **18**(1):555–586, 1995.

[194] L. Sirovich and R. Uglesich. The organization of orientation and spatial frequency in primary visual cortex. *Proceedings of the National Academy of Sciences*, **101**(48):16941–16946, 2004.

[195] B. Skottun, R. De Valois, D. Grosof, J. Movshon, D. Albrecht, and A. Bonds. Classifying simple and complex cells on the basis of response modulation. *Vision Research*, **31**(7):1078–1086, 1991.

[196] S. G. Solomon, A. J. White, and P. R. Martin. Extraclassical receptive field properties of parvocellular, magnocellular, and koniocellular cells in the primate lateral geniculate nucleus. *The Journal of Neuroscience*, **22**(1):338–349, 2002.

[197] D. Somers, S. Nelson, and M. Sur. An emergent model of orientation selectivity in cat visual cortical simple cells. *The Journal of Neuroscience*, **15**(8):5448–5465, 1995.

[198] D. C. Somers, E. V. Todorov, A. G. Siapas, L. J. Toth, D.-S. Kim, and M. Sur. A local circuit approach to understanding integration of long-range inputs in primary visual cortex. *Cerebral Cortex*, **8**(3):204–217, 1998.

[199] H. Sompolinsky and R. Shapley. New perspectives on the mechanisms for orientation selectivity. *Current Opinion in Neurobiology*, **7**(4):514–522, 1997.

[200] S. Song, K. D. Miller, and L. F. Abbott. Competitive Hebbian learning through spike-timing-dependent synaptic plasticity. *Nature neuroscience*, **3**(9):919–926, 2000.

[201] R. B. Stein. Some models of neuronal variability. *Biophysical Journal*, **7**(1):37–68, 1967. DOI: 10.1016/S0006-3495(67)86574-3.

[202] D. D. Stettler, A. Das, J. Bennett, and C. D. Gilbert. Lateral connectivity and contextual interactions in macaque primary visual cortex. *Neuron*, **36**(4):739–750, 2002.

[203] D. Tadin, J. Kim, M. L. Doop, C. Gibson, J. S. Lappin, R. Blake, and S. Park. Weakened center-surround interactions in visual motion processing in schizophrenia. *The Journal of Neuroscience*, **26**(44):11403–11412, 2006.

[204] L. Tao, M. Shelley, D. McLaughlin, and R. Shapley. An egalitarian network model for the emergence of simple and complex cells in visual cortex. *Proceedings of the National Academy of Sciences*, **101**(1):366–371, 2004.

[205] L. Tao, D. Cai, D. McLaughlin, M. Shelley, and R. Shapley. Orientation selectivity in visual cortex by fluctuation-controlled criticality. *Proceedings of the National Academy of Sciences*, **103**(34):12911–12916, 2006.

[206] M. S. Tibber, E. J. Anderson, T. Bobin, E. Antonova, A. Seabright, B. Wright, P. Carlin, S. S. Shergill, and S. C. Dakin. Visual surround suppression in schizophrenia. *Frontiers in psychology*, **4**, 2013.

[207] D. J. Tolhurst, J. A. Movshon, and A. Dean. The statistical reliability of signals in single neurons in cat and monkey visual cortex. *Vision research*, **23**(8):775–785, 1983.

[208] R. D. Traub, E. H. Buhl, T. Gloveli, and M. A. Whittington. Fast rhythmic bursting can be induced in layer 2/3 cortical neurons by enhancing persistent Na+ conductance or by blocking BK channels. *Journal of Neurophysiology*, **89**(2):909–921, 2003. DOI: 10.1152/jn.00573.2002.

[209] R. D. Traub, D. Contreras, M. O. Cunningham, H. Murray, F. E. N. LeBeau, A. Roopun, A. Bibbig, W. B. Wilent, M. J. Higley, and M. A. Whittington. Single-column thalamocortical network model exhibiting gamma oscillations, sleep spindles, and epileptogenic bursts. *Journal of Neurophysiology*, **93**(4):2194–2232, 2005. DOI: 10.1152/jn.00983.2004.

[210] T. Troyer, A. Krukowski, N. Priebe, and K. Miller. Contrast-invariant orientation tuning in cat visual cortex: thalamocortical input tuning and correlation-based intracortical connectivity. *The Journal of Neuroscience*, **18**(15):5908–5927, 1998.

[211] M. Tsodyks, T. Kenet, A. Grinvald, and A. Arieli. Linking spontaneous activity of single cortical neurons and the underlying functional architecture. *Science*, **286**(5446):1943–1946, 1999.

[212] H. Tuckwell. *Introdcution to theoretical neurobiology*. Cambridge University Press, 1988.

[213] P. J. Uhlhaas, W. A. Phillips, G. Mitchell, and S. M. Silverstein. Perceptual grouping in disorganized schizophrenia. *Psychiatry research*, **145**(2):105–117, 2006.

[214] P. J. Uhlhaas, W. A. Phillips, L. S. Schenkel, and S. M. Silverstein. Theory of mind and perceptual context-processing in schizophrenia. *Cognitive Neuropsychiatry*, **11**(4):416–436, 2006.

[215] S. K. Ungerleider and L. G. Mechanisms of visual attention in the human cortex. *Annual review of neuroscience*, **23**(1):315–341, 2000.

[216] VisuaStim. Advanced Medical Equipment Ltd., Horsham, United Kingdom.

[217] D. W. Volk, M. C. Austin, J. N. Pierri, A. R. Sampson, and D. A. Lewis. Decreased glutamic acid decarboxylase67 messenger RNA expression in a subset of prefrontal cortical {gamma}-aminobutyric acid neurons in subjects with schizophrenia. *Archives of General Psychiatry*, **57**(3):237, 2000.

[218] B. S. Webb, N. T. Dhruv, S. G. Solomon, C. Tailby, and P. Lennie. Early and late mechanisms of surround suppression in striate cortex of macaque. *The Journal of Neuroscience*, **25**(50):11666–11675, 2005.

[219] M. Welvaert and Y. Rosseel. Neural activity with spatial and temporal correlations as a basis to simulate fMRI data. In *15th annual meeting of the organization for human brain mapping, Abstracts*, 2009.

[220] D. Wielaard, M. Shelley, D. McLaughlin, and R. Shapley. How simple cells are made in a nonlinear network model of the visual cortex. *The Journal of Neuroscience*, **21**(14):5203–5211, 2001.

[221] J. Wielaard and P. Sajda. Simulated optical imaging of orientation preference in a model of V1. In *Neural Engineering, 2003. Conference Proceedings. First International IEEE EMBS Conference on*. IEEE, 2003, pages 499–502.

[222] J. Wielaard and P. Sajda. Extraclassical receptive field phenomena and short-range connectivity in V1. *Cerebral Cortex*, **16**(11):1531–1545, 2006.

[223] K. Wimmer, M. Stimberg, R. Martin, L. Schwabe, J. Mariño, J. Schummers, D. C. Lyon, M. Sur, and K. Obermayer. Dependence of orientation tuning on recurrent excitation and inhibition in a network model of V1. *Advances in Neural Information Processing Systems*, **21**:1769–1776, 2009.

[224] D. Xing, D. Ringach, R. Shapley, and M. Hawken. Correlation of local and global orientation and spatial frequency tuning in macaque V1. *The Journal of Physiology*, **557**(3):923–933, 2004.

[225] D. Xing, R. M. Shapley, M. J. Hawken, and D. L. Ringach. Effect of stimulus size on the dynamics of orientation selectivity in macaque V1. *Journal of Neurophysiology*, **94**(1):799–812, 2005.

[226] J. Xing and D. Heeger. Measurement and modeling of center-surround suppression and enhancement. *Vision Research*, **41**(5):571–583, 2001.

[227] E. Yang, D. Tadin, D. M. Glasser, S. W. Hong, R. Blake, and S. Park. Visual context processing in schizophrenia. *Clinical Psychological Science*, **1**(1):5–15, 2013.

[228] J. H. Yoon, A. S. Rokem, M. A. Silver, M. J. Minzenberg, S. Ursu, J. D. Ragland, and C. S. Carter. Diminished orientation-specific surround suppression of visual processing in schizophrenia. *Schizophrenia Bulletin*, **35**(6):1078–1084, 2009.

[229] J. H. Yoon, R. J. Maddock, A. Rokem, M. A. Silver, M. J. Minzenberg, J. D. Ragland, and C. S. Carter. GABA concentration is reduced in visual cortex in schizophrenia and correlates with orientation-specific surround suppression. *The Journal of Neuroscience*, **30**(10):3777–3781, 2010.

[230] B. Zenger-Landolt and D. J. Heeger. Response suppression in V1 agrees with psychophysics of surround masking. *The Journal of Neuroscience*, **23**(17):6884–6893, 2003.

[231] W. Zhu, M. Shelley, and R. Shapley. A neuronal network model of primary visual cortex explains spatial frequency selectivity. *Journal of Computational Neuroscience*, **26**(2):271–287, 2009.

[232] W. Zhu, D. Xing, M. Shelley, and R. Shapley. Correlation between spatial frequency and orientation selectivity in V1 cortex: Implications of a network model. *Vision Research*, **50**(22):2261–2273, 2010.

List of Figures

4.1. Units of a neuron. . . . 9
4.2. Equivalent circuit representation. . . . 12
4.3. Chemical synapse 12
4.4. Equivalent circuit representation of a multi-compartment neuron. . . . 18

5.1. Visual pathway. . . . 28
5.2. Visual streams. . . . 28
5.3. Models of simple/complex cells. . . . 30
5.4. Centre-surround suppression theories. . . . 33

6.1. The model neurons. . . . 39
6.2. 2-d network structure. . . . 42
6.3. Network visualisation. . . . 43
6.4. Visualisation of inactive and active network states. . . . 44
6.5. Receptive field configurations. . . . 46
6.6. Example gratings. . . . 49
6.7. Example gratings 51
6.8. Standard contrast response functions from Equations 6.12 (red) and 6.13 (black). Both are expansive for low contrasts and saturate for higher contrasts. (Parameters: $k = 1$, $a = 0.01$, $p = 2.3$ and $q = 1.9$ for Equation 6.12; $c = 1$, $x = 0.4$, $y = 1.9$ and $\sigma = 0.15$ for Equation 6.13.) 54
6.9. Contrast texture patterns. . . . 56
6.10. Spiny stellate neuron firing behaviour. . . . 60
6.11. LogISI histogram of the spiny stellate neuron. . . . 60
6.12. f-I curve of the RS neuron. . . . 61
6.13. Basket cell firing behaviour. . . . 62
6.14. LogISI histogram of the basket cell. . . . 63
6.15. f-I curve of the FS neuron. . . . 63
6.16. Histogram of F1/F0 ratios. . . . 65
6.17. CV histograms. . . . 66

6.18. Orientation tuning curves. 67
6.19. DRI histograms. 68
6.20. Orientation selectivity at different contrasts. 69
6.21. Orientation tuning curve at different contrasts. 70
6.22. Orientation selectivity for different random seeds. 71
6.23. Spatial frequency selectivity comparison. 72
6.24. Spatial tuning curves. 73
6.25. Spatial frequency preference distributions. 74
6.26. Temporal frequency preference distribution. 74
6.27. CV histogram comparison between LGN and V1. 79
6.28. Orientation tuning curve and LGN input. 80
6.29. CV histogram of excitatory and inhibitory populations. 81
6.30. Evolution of orientation selectivity under increasing strength of inhibition. 82
6.31. Evolution of orientation selectivity of inhibitory neurons under increasing strength of inhibition. 83
6.32. Evolution of direction selectivity under increasing strength of inhibition. . 84
6.33. Evolution of orientation selectivity under increasing strength of excitation of inhibitory neurons. 85
6.34. Evolution of orientation selectivity of inhibitory neurons under increasing strength of excitation of inhibitory neurons. 86
6.35. Orientation selectivity measures for different parameters governing inhibition. 88
6.36. r^2-values of the fits of the contrast response functions for different parameters governing inhibition. 89
6.37. Mean suppression indices for the size variation test for different parameters governing inhibition 90
6.38. Suppression indices in the centre-surround suppression for sinusoidal gratings test for different parameters governing inhibition 91
6.39. Mean matching contrasts in the centre-surround suppression for contrast texture pattern test. 92

7.1. Typical psychophysical stimuli. 100
7.2. Depiction of the exclusion process in the patient group. 104
7.3. Depiction of the exclusion process in the control group. 105
7.4. Demographic data for patient and control groups. 106

7.5. Performances of the patient and control groups in the Freiburg Visual Acuity and Contrast Test. . . . 107
7.6. Sagittal view of the voxel positioning for the magnetic resonance spectroscopy. . . . 108
7.7. Stimuli for the fMRI task. . . . 109
7.8. Image of the target stimulus. . . . 111
7.9. Stimuli for the psychophysical task. . . . 112
7.10. Box plots GABA concentrations. . . . 116
7.11. Box plots glutamate concentrations. . . . 117
7.12. Box plots glutamate/GABA concentrations. . . . 118
7.13. Plot of the correlation between age and glutamate/GABA levels in in the patient group. . . . 119
7.14. Plot of the ANCOVA of the glutamate/GABA ratio in the two groups with age as a covariate. . . . 120
7.15. Contrast of ON- vs OFF-blocks 122
7.16. Results of the group analysis. . . . 123
7.17. Results of the group analysis. . . . 123
7.18. Box plots of centre-surround suppression strength and inter-trial variability. 126
7.19. Plot of the correlation between GABA/creatine ratio and centre-surround suppression in (a) patient and (b) control groups. . . . 129
7.20. Plot of the correlation between glutamate/creatine ratio and centre-surround suppression in (a) patient and (b) control groups. . . . 130
7.21. Plot of the correlation between glutamate/GABA ratio and centre-surround suppression in (a) patient and (b) control groups. . . . 131
7.22. Plot of the correlation between between BOLD activation and surround suppression in (a) patient and (b) control groups. . . . 133
7.23. Correlation between BOLD signal and centre-surround suppression in the control group. . . . 134
7.24. Correlation between BOLD signal and centre-surround suppression in the patient group. . . . 134
7.25. Correlation between BOLD signal and centre-surround suppression in the patient group. . . . 135

A.1. Visual pathway. . . . 163
A.2. Visual streams. . . . 164
A.3. Depiction of the layered structure of the retina. . . . 165

A.4. Depiction of the layered structure of the LGN. 168

List of Tables

4.1. Equilibrium potentials. 11
4.2. Comparison of different neuron models. 20

6.1. Ion reversal potentials. 40
6.2. Membrane conductance densities for the RS neuron 41
6.3. Membrane conductance densities for the FS neuron. 41
6.4. Classical receptive field test parameters. 53
6.5. Contrast Response function fitting parameters. 54
6.6. Variation of inhibitory parameters. 59
6.7. Quantitative parameters of the RS neuron. 61
6.8. Quantitative parameters of the FS neuron. 62
6.9. Orientation selectivity comparison. 68
6.10. Contrast response function fitting parameters. 75
6.11. Centre-surround suppression for sinusoidal gratings. 76
6.12. Centre-surround suppression for contrast texture patterns. 77
6.13. Orientation tuning of the LGN input. 78
6.14. Orientation tuning of excitatory and inhibitory populations. 79

7.1. The five different conditions producing bias and their apparent locus of processing. 101
7.2. Exclusion criteria for the study. 103
7.3. table 104
7.4. GABA concentrations in the control group. 113
7.5. GABA concentrations for the patient group. 114
7.6. Glutamate concentrations for the control group. 114
7.7. Glutamate concentrations for the patient group. 115
7.8. Glutamate/GABA ratios for the control group. 115
7.9. table 115
7.10. MRS data comparison. 119
7.11. 120

7.12. Results of the ANCOVA of the glutamate/GABA ratio in the two groups with age as a covariate. . . . 120
7.13. table . . . 121
7.14. . . . 121
7.15. . . . 124
7.16. Average centre-surround suppression and intra-subject, inter-trial variability of the healthy control group. . . . 125
7.17. Average centre-surround suppression and intra-subject inter-trial variability of the patient group. . . . 125
7.18. Summary of the psychophysical experiment. . . . 127
7.19. Summary of the post-hoc correlations between the possible confounds visual acuity and contrast sensitivity and surround suppression strength and inter-trial variability (no significances found). . . . 127
7.20. Summary of the post-hoc correlations between the possible confounds age and education time and centre-surround suppression strength and inter-trial variability. 127
7.21. Summary of the correlations between neurotransmitter levels and ratios and centre-surround suppression strength. . . . 128
7.22. Summary of the correlations between BOLD activation and centre-surround suppression strength. . . . 132
7.23. Summary of the correlations between neurotransmitter levels and ratios BOLD activation. . . . 135

B.1. Orientation selectivity measures for the five different weights for the inhibitory connections onto excitatory neurons and, as a reference, for the standard configuration of the model. . . . 171
B.2. Fitting parameters for the contrast response functions of the mean response of the network neurons for the five different weights of inhibitory on excitatory cells, and for the standard configuration. . . . 172
B.3. Suppression indices in the size variation test for five different weights of inhibitory connections on excitatory cells and for the standard configuration. . . . 172
B.4. Centre-surround suppression in response to sinusoidal gratings. Suppression indices for the mean responses for five different inhibitory weights in the eight different centre-surround conditions. . . . 173
B.5. Centre-Surround suppression in response to contrast noise patterns. Responses and matching contrasts for five different inhibitory weights. . . . 174

B.6. Centre-Surround suppression in response to contrast noise patterns. r^2 values and percentage of excluded cells, and statistical analysis of the influence of the surround grating on the response for both surround conditions and of the influence of the size of the surround. 175

B.7. Orientation selectivity measures the four weights of the excitatory connections onto inhibitory neurons and the standard configuration. 175

B.8. Fitting parameters for the contrast response functions of the average response of the network neurons for four different weights w_{ei} and for the standard configuration. 176

B.9. Centre-surround suppression in response to sinusoidal gratings. Suppression indices in the size variation test for four different weights w_{ei} and the standard configuration. 176

B.10. Centre-surround suppression in response to sinusoidal gratings. Suppression indices for four different weights in the eight different centre-surround conditions. 177

B.11. Centre-Surround suppression in response to contrast noise patterns. Responses and matching contrasts for four different weights w_{ei}. 178

B.12. Centre-Surround suppression in response to contrast noise patterns. r^2 values and proportion of excluded cells and statistical analyses of the influence of the surround grating on the response for both surround conditions and, of the influence of the size of the surround. 179

B.13. Orientation selectivity measures for two different amounts of inhibitory neurons and the standard configuration. 180

B.14. Fitting parameters for the contrast response functions of the average response of the network neurons for two different amounts of inhibitory neurons and for the standard configuration. 180

B.15. Centre-surround suppression in response to sinusoidal gratings. Suppression indices in the size variation test for two different amounts of inhibitory neurons and the standard configuration. 180

B.16. Centre-surround suppression in response to sinusoidal gratings. Suppression indices for two different amounts of inhibitory neurons in the eight different centre-surround conditions.. 181

B.17. Centre-Surround suppression in response to contrast noise patterns. Responses and matching contrasts for two different amounts of inhibitory neurons. 181

B.18. Centre-Surround suppression in response to contrast noise patterns. r^2 values, percentages of excluded cells, and statistical analysis of the influence of the surround grating on the response for both surround conditions and of the influence of the size of the surround for two different amounts of inhibitory neurons. . . . 182

B.19. Orientation selectivity measures for different amounts of inhibitory connections on excitatory cells and the standard configuration. 182

B.20. Fitting parameters for the contrast response functions of the average response of the network neurons for two different amounts of inhibitory connections and for the standard configuration. 183

B.21. Centre-surround suppression in response to sinusoidal gratings. Suppression indices in the size variation test for two different amounts of inhibitory connections and the standard configuration. 183

B.22. Centre-surround suppression in response to sinusoidal gratings. Suppression indices for two different amounts of inhibitory connections in the eight different centre-surround conditions. 183

B.23. Centre-Surround suppression in response to contrast noise patterns. Responses and matching contrasts for two different amounts of inhibitory connections. . . . 184

B.24. Centre-Surround suppression in response to contrast noise patterns. r^2 values, percentage of excluded cells, and statistical analyses of the influence of the surround grating on the response for both surround conditions and of the influence of the size of the surround, for two different amount of inhibitory connections. . 184

B.25. Orientation selectivity measures for different amounts of excitatory connections onto inhibitory cells and the standard configuration. 185

B.26. Fitting parameters for the contrast response functions fitted to the mean response of the network neurons for two different amounts of excitatory connections and for the standard configuration. 185

B.27. Centre-surround suppression in response to sinusoidal gratings. Suppression indices in the size variation test for two different amounts of excitatory connections and the standard configuration. 185

B.28. Centre-surround suppression in response to sinusoidal gratings. Suppression indices for two different amounts of excitatory connections in the eight different centre-surround conditions.. 186

B.29. Centre-Surround suppression in response to contrast noise patterns. Responses and matching contrasts for two different amounts of excitatory connections. . . 186

B.30. Centre-Surround suppression in response to contrast noise patterns. r^2 values, percentages of excluded cells, and statistical analyses of the influence of the surround grating on the response for both surround conditions and of the influence of the size of the surround for two different amounts of excitatory connections. . 187
B.31. Orientation selectivity measures for five different decay time constants τ at inhibitory synapses and the standard configuration. 187
B.32. Fitting parameters for the contrast response functions fitted to the mean response of the network neurons for five different decay time constants τ at inhibitory synapses and for the standard configuration. 188
B.33. Centre-surround suppression in response to sinusoidal gratings. Suppression indices in the size variation test for five different decay time constants τ at inhibitory synapses and the standard configuration. 188
B.34. Centre-surround suppression in response to sinusoidal gratings. Suppression indices for five different decay time constants τ at inhibitory synapses in the eight different centre-surround conditions.. 189
B.35. Centre-Surround suppression in response to contrast noise patterns. Responses and matching contrasts for five different decay time constants τ at inhibitory synapses. 190
B.36. Centre-Surround suppression in response to contrast noise patterns. r2 values, percentages of excluded cells, and statistical analyses of the influence of the surround grating on the response for both surround conditions and, of the influence of the size of the surround, for five different decay time constants τ at inhibitory synapses. 191

Erklärung an Eides Statt

Ich erkläre hiermit an Eides Statt, dass ich die vorliegende Arbeit selbständig sowie ohne unzulässige Hilfe Dritter und ohne Benutzung anderer als der angegebenen Hilfsmittel angefertigt habe. Die aus anderen Quellen direkt oder indirekt übernommenen Daten und Konzepte sind unter Angabe der Quelle gekennzeichnet.

Weitere Personen waren an der inhaltlich-materiellen Erstellung der vorliegenden Arbeit nicht beteiligt. Insbesondere habe ich hierfür nicht die entgeltliche Hilfe von Vermittlungs- bzw. Beratungsdiensten (Promotionsberater oder anderer Personen) in Anspruch genommen. Niemand hat von mir unmittelbar oder mittelbar geldwerte Leistungen für Arbeiten erhalten, die im Zusammenhang mit dem Inhalt der vorgelegten Dissertation stehen.

Die Arbeit wurde bisher weder im In- noch im Ausland in gleicher oder ähnlicher Form einer anderen Prüfungsbehörde vorgelegt.

Ich versichere an Eides Statt, dass ich nach bestem Wissen die reine Wahrheit gesagt und nichts verschwiegen habe.

(Ort, Datum) (Unterschrift)

Christoph Metzner

Curriculum Vitae

Moislinger Allee 84
23558 Lübeck
✉ *metzner@rob.uni-luebeck.de*
www.rob.uni-luebeck.de

Education

1990–1999 **Abitur**, *Leibniz Gymnasium*, Pirmasens, *Grade: 1.6*.
(grades ranging from 1.0 (best) to 6.0 (worst)).

2000–2009 **Diplom Mathematics**, *Saarland University*, Saarbruecken, *Grade: 1.4*.
The german degree 'Diplom' is a programme equivalent to a Bachelors and a subsequent Masters degree.

2007–2008 **Bachelor Computer Science**, *Saarland University*, Saarbruecken, *Grade: 2.0*.

2009–2014 **PhD Computational Neuroscience**, *University of Luebeck*, Luebeck, *Grade: 1.3, magna cum laude*.

Bachelor thesis

title *Extending the Method of Tumblin/Turk to Tensor Valued Data*

supervisor Prof. Dr. J. Weickert

description The thesis extends image processing methods based on 4th order partial differential equations to tensor valued images which arise e.g. in diffusion tensor imaging. The methods were implemented in C, guaranteeing a high performance since tensor valued images are usually large. A comparison of the methods regarding filter properties such as noise reduction, edge enhancement and contrast enhancement is done.

Diploma thesis

title *Galois-Kohomologie und Isomorphien klassischer Gruppen*

supervisor Prof. Dr. R. Schulze-Pillot

description The thesis elaborates the generic isomorphisms between classical groups in small dimensions. Furthermore, it gives an overview over the k-forms of these groups using Galois-cohomology and illustrates the galois-cohomological interpretations of these isomorphisms.

PhD thesis

title *Centre-surround suppression: Computational models and neural and perceptual correlates in humans*

supervisor Prof. Dr.-Ing. A. Schweikard

description In this thesis a realistic neural network model of layer 4Cα of primary visual cortex is developed. The model is based on recent anatomical and neurophysiological data and shows a diversity of classical and extra-classical receptive field properties. The model is used to explore the influence of different parameters governing GABAergic inhibition on the receptive field properties, especially on center-surround interactions. Furthermore, psychophysical and neuroimaging methods are used to investigate the influence of GABAergic inhibition on a perceptual scale.

Experience

02/2014 – today **Post-Doc Researcher**, Institute for Robotics and Cognitive Systems, University of Luebeck, Luebeck, Germany.

- Modelling neurochemical mechanisms of perceptual deficits in schizophrenia.
- Implementation of a treatment planning system for aortic valve sparing surgery

06/2013 – 11/2013 **Mathematician**, *Research project 'Psychophysical and neurochemical correlates of GABAergic neurotransmission'*, Center for integrative psychiatry - ZIP gGmbH, Kiel, Germany.

- Preparation, execution and analysis of psychophysical and neuroimaging methods to investigate GABAergic neurotransmission in several studies at the ZIP.
- Modelling neurochemical mechanisms of perceptual deficits in schizophrenia.

Workshops, Seminars & Courses

- Latin American Summer School Computational Neuroscience (LASCON), Natal, 2014.
- **Organizer** of the Multiscale Modeling in Computational Neuroscience Workshop, Luebeck, 2012.
- Baltic Autumn School Systems Biology, Luebeck 2011.
- Baltic Autumn School Computational Neuroscience, Luebeck, 2010.
- Barcelona Cognition, Brain and Technology Summer School, Barcelona, 2009.

Awards & Achievements

2014 ***Travel Grant*** **CNS 2014 Quebec, Canada**,
Poster: Computational Multifactoriality in a Detailed Neural Network Model Resembling Centre-Surround Suppression Deficits in Schizophrenia.

2013 ***Travel Grant*** **CNS 2013 Paris, France**,
Poster: Center-Surround Interactions in a Network Model of Layer 4Cα of Primary Visual Cortex.

2012 **Winner *Cureus Fall 2012 Poster Competition, Category Psychiatry***, Poster: Neurochemical Mechanisms of Perceptual Deficits in Schizophrenic Patients - A Spiking Neural Network Approach.

2012 ***Travel Grant* 'Multi-Scale Modeling Workshop' at CNS 2012, Atlanta, US**.

2011 **Winner *'Best Grant Proposal' within the workshop 'Grant Proposal Writing'***, Proposal: Pain Perception in Patients with Obsessive-Compulsive Disorder, together with Daniela Schön.